New Insights into Organization, Assembly and Function of the Export Apparatus of Bacterial Type III Secretion Systems

Dissertation

der Mathematisch-Naturwissenschaftlichen Fakultät

der Eberhard Karls Universität Tübingen

zur Erlangung des Grades eines

Doktors der Naturwissenschaften

(Dr. rer. nat.)

Vorgelegt von

Tobias Dietsche

aus Lörrach

Tübingen 2017

Gedruckt mit Genehmigung der Mathematisch-Naturwissenschaftlichen Fakultät der Eberhard Karls Universität Tübingen

Tag der mündlichen Qualifikation:	07.12.2017
Dekan:	Prof. Dr. Wolfgang Rosenstiel
1. Berichterstatter:	Prof. Samuel Wagner, PhD
2. Berichterstatter:	Prof. Dr. Andreas Peschel

Table of Contents

Abbreviations

2D - two dimensional

ATPase - adenosine triphosphate hydrolase

BN PAGE - blue native polyacrylamide gel electrophoresis

DDM - n-dodecyl beta-D-maltopyranoside

DNA - deoxyribonucleic acid

dSTORM - direct stochastic optical resolution microscopy

EM - electron microscopy

EPEA - EPEA epitope tag

EPEC - enteropathogenic *Escherichia coli*

FLAG - FLAG epitope tag

FRAP - fluorescence recovery after photobleaching

fT3SS - flagella associated type III secretion system

GFP - green fluorescent protein

Halo - Halo epitope tag

LC/MS - liquid chromatography tandem mass spectrometry

LMNG - lauryl maltose neopentyl glycol

LT - lytic transglycosylases

MALLS - multi angle laser light scattering

MS - mass spectrometry

MS-rings - membrane and supramembrane rings

MW - molecular weight

*p*Bpa - *para*-benzoyl-phenylalanine

PE - phosphatidylethanolamine

PEG - polyethylene glycol

PG - peptidoglycan

RNA - ribonucleic acid

SCV - *Salmonella* containing vacuole

SDS PAGE - sodium dodecyl sulfate polyacrylamide gel electrophoresis

SEC - size exclusion chromatography

SIFs - *Salmonella* induced filaments

SPI-1/2 - *Salmonella* pathogenicity island 1/2

SRP - signal recognition particle

T(2-3)SS - type (II-III) secretion system

T4PS - type IV pili system

TMD - transmembrane domain

TMH - transmembrane helix

UV - ultraviolet radiation

WT - wildtype

Symbols and Units

Å - Angstrom

Da - Dalton

h - hour

nm - nanometer

Δ - genetic deletion

Summary

Bacterial type III secretion systems (T3SSs) are big multi-protein complexes which span both membranes of Gram-negative bacteria and are used to translocate effector proteins directly into the cytoplasm of target host cells. The export apparatus, a substructure centrally located in the inner membrane inside of these systems is essential for their proper assembly and functionality. In the *Salmonella* T3SS1, encoded on the Salmonella pathogenicity island 1 (SPI-1), the export apparatus is composed of the five membrane proteins SpaPQRS and InvA. This substructure is also present in the closely related flagella system, which bacteria like *Salmonella* use as a motility device. In the *Salmonella* flagella system the homologs of the export apparatus proteins are FliPQR, FlhB and FlhA. In this work the structural organization and assembly of the core components of this subcomplex from both systems were investigated. It was found that in both systems the homologs SpaP/FliP form a stable complex with SpaR/FliR independently of all other components. SpaP/FliP was identified as T3SS assembly nucleation point, which needs immediate stabilization by SpaR/FliR. This solid subcomplex acts as a platform onto which subsequently SpaQ/FliQ and later on SpaS/FlhB as well as InvA/FlhA get recruited. For the injectisome, the core component SpaP was identified as the pore forming unit in the inner membrane. This protein forms a pentamer with a donut-like shape which allows the passage of molecules with a size of 500 Da, indicating a pore diameter of about 15 Å. For its homolog FliP in the flagella system it was found that this protein forms a hexamer, built by a trimer of dimers. The hexamer is organized, as its respective injectisome homolog, in a donut-like shape, suggesting a similar function. Furthermore, the function of an additional flagella-associated protein FliO was investigated. This bitopic membrane protein is missing in the injectisome and has been reported to be connected to FliP functionality. In this work, it was shown that FliO acts as a chaperone for FliP, preventing its degradation via the Lon pathway and stabilizing its multimerization until FliR gets

recruited. FliO itself builds multimers and is organized in a ring structure with flexible clamp like side arms to which FliP is able to bind.

Zusammenfassung

Bakterielle Typ III Sekretionssysteme (T3SS) sind multi-Protein Komplexe, welche beide Membranen von gramnegativen Bakterien überspannen und genutzt werden, um Effektorproteine aus dem bakteriellen Zytoplasma direkt in Zielzellen zu injizieren. Eine zentrale Struktur im Inneren dieser Systeme ist der sogenannte Exportapparat, welcher essentiell für deren Funktionalität und korrekten Zusammenbau ist. Dieser ist im *Salmonella* SPI-1 T3SS aus den fünf Membranproteinen SpaP, SpaQ, SpaR, SpaS und InvA aufgebaut. Diese fünf Komponenten sind auch Bestandteil des bakteriellen Flagellums, welches der Fortbewegung dient. Die homologen Proteine des Exportapparats im *Salmonella* Flagellum sind FliP, FliQ, FliR, FlhB und FlhA. In dieser Arbeit wurden der strukturelle Aufbau und die Assemblierung dieser Substruktur in beiden Systemen untersucht. Es konnte gezeigt werden, dass in beiden Fällen die jeweiligen homologen Proteine SpaP/FliP und Spar/FliR unabhängig von allen anderen Komponenten einen stabilen Komplex bilden. SpaP/FliP wurde als Initiationspunkt der T3SS Assemblierung ausgemacht, welcher durch SpaR/FliR unmittelbar stabilisiert wird. Dieser Subkomplex stellt die Basisstruktur dar, zu der nachfolgend die Komponenten SpaQ/FliQ und anschließend SpaS/FlhB sowie InvA/FlhA rekrutiert werden. Weiterhin konnte das Virulenz-assoziierte SpaP als die Komponente bestimmt werden, welche in der inneren Membran ein pentameres Multimer mit Porenfunktion ausbildet. Diese Pore ist durchlässig für Moleküle mit einer Größe von bis zu 500 Da, was auf einen Porendurchmesser von ungefähr 15 Å schließen lässt. Für das entsprechende Homolog FliP im Flagellensystem konnte die Bildung eines hexameren Rings gezeigt werden, was eine vergleichbare Funktion vermuten lässt. Darüber hinaus wurde die Funktion der Flagellenkomponente FliO genauer untersucht, für das kein Homolog im Virulenz-assoziierten T3SS nachgewiesen ist. Für FliO konnte bereits zuvor gezeigt werden, dass es mit der Funktionalität von FliP verknüpft ist. In dieser Arbeit konnte FliO als FliP-spezifisches Chaperon identifiziert werden, welches den gezielten FliP

Abbau durch die Lon Protease verhindert und dessen Multimerisierung bis zur Rekrutierung von FliR stabilisiert. FliO selbst ist als Multimer in einem Ring organisiert, an dessen Seiten sich flexible klammerartige Arme befinden, welche in der Lage sind, FliP zu binden.

List of Publications and Personal Contributions

Primary Publications

Publication 1: Dietsche T.*, Tesfazgi Mebrhatu M.*, Brunner M.J., Abrusci P., Yan J., Franz-Wachtel M., Schärfe C., Zilkenat S., Grin I., Galán J.E., Kohlbacher O., Lea S., Macek B., Marlovits T.C., Robinson C.V., Wagner S. (2016). **Structural and Functional Characterization of the Bacterial Type III Secretion Export Apparatus**. PLoS Pathogens, 12(12): e1006071

* Authors contributed equally

Personal contribution: I designed, performed and analyzed *in vivo* photocrosslinking and 2D BN PAGE experiments resulting in figure 2 (panel C-F), figure 3 (A-C), figure 4 and figure 5. Furthermore, I helped to write the original manuscript draft.

Publication 2: Fabiani F.D.*, Renault T.T.*, Peters B.#, Dietsche T.#, Gálvez E.J.C.#, Guse A., Freier K., Charpentier E., Strowig T., Franz-Wachtel M., Macek B., Wagner S., Hensel M., Erhardt M. (2017). **A flagellum-specific chaperone facilitates assembly of the core type III export apparatus of the bacterial flagellum.** PLoS Biology, 15(8): e2002267

*/# Authors contributed equally

Personal contribution: I performed and analyzed BN page and 2D BN PAGE experiments resulting in figure 7 and figure 8. I helped with the methodology for BN PAGE experiments resulting in figure 6. I reviewed and edited the manuscript.

Publication 3: Fukumura T., Makino F., Dietsche T., Kinoshita M., Kato T., Wagner S., Namba K., Imada K., Minamino T. (2017). **Assembly and stoichiometry of the core structure of the bacterial flagellar type III export gate complex.** PLoS Biology, 15(8): 22002281

Personal contribution: I designed, performed and analyzed *in vivo* photocrosslinking experiments resulting in figure 4 (panel A-C).

Additional Publications

Publication 4: Zilkenat S., Dietsche T., Monjarás Feria J.V., Torres-Vargas C.E., Tesfazgi Mebrhatu M., Wagner S. (2017). **Blue Native PAGE Analysis of Bacterial Secretion Complexes.** Methods Mol Biol, Vol. 1615, 321-351

Personal contribution: I wrote the section on crude membrane preparation and 2D BN PAGE methodology.

Introduction

Prolog

Like the human skin, the bacterial cell envelope is of utmost importance for its host. This barrier to the environment is a hot spot for essential processes. Integrity and therefore protection from unfavorable environments, sensing and uptake of nutrients, as well as creating and using ion gradients as energy source are crucial for the survival of the bacterial cell (Silhavy et al., 2010). In order to adapt and interact, communication and exchange with its environment are key tasks of the bacterial cell envelope. To influence their own surroundings, host cells or other competing microbes, bacteria have evolved several secretion systems to translocate specific molecules to their designated target location (Green and Mecsas, 2016). To date, nine different bacterial secretion systems have been found and characterized (Abby et al., 2016; Costa et al., 2015; Lasica et al., 2017). Their occurrence, shape, size, function and mode of action vary greatly.

This work focuses on the type III secretion system (T3SS), a multi membrane-spanning nanomachine of Gram-negative bacteria, which is utilized to inject semi-folded proteins in a one-step mechanism into target host cells (Galán and Collmer, 1999). Due to their function, T3SSs are also called injectisomes. From an evolutionary perspective injectisomes or virulence associated T3SSs have evolved from bacterial flagella systems which harbor a flagella associated T3SS (fT3SS) as their core component (Abby and Rocha, 2012). In the flagella system, the T3SS is used to export several structural components of the flagella filament to the outside, where they assemble and build up a sophisticated nanomachine that enables bacteria to move (Macnab, 2003).

T3SSs - How *Salmonella* Uses Its Major Weapons During Infection

For several enteropathogens, like *Salmonella enterica* serovar Typhimurium, usage of their T3SS is crucial for pathogenesis (Galán and Wolf-Watz, 2006). *Salmonella* expresses two distinct virulence associated T3SSs, depending on the stage of infection. They are expressed from two distinct loci called *Salmonella* pathogenicity islands 1 (SPI-1) and 2 (SPI-2) and are therefore termed T3SS1 and T3SS2. These genetic islands have been acquired via horizontal gene transfer and contribute to the pathogenic abilities of the organism.

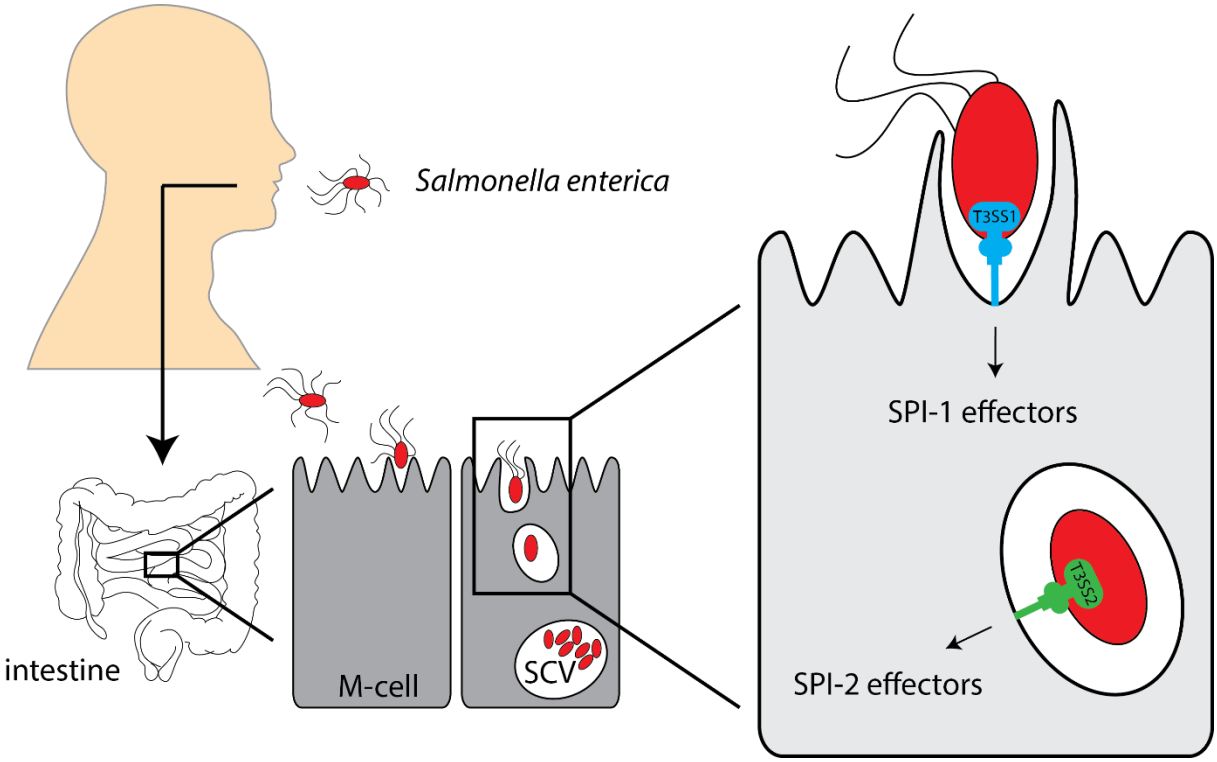

Figure 1: ***Salmonella* infection**. *Salmonella* is taken up with contaminated food or water. In the small intestine it promotes its own invasion into non-phagocytic enterocytes, preferentially M-cells, via various effectors of its T3SS1. For intracellular survival and spreading inside the *Salmonella* containing vacuole (SCV) *Salmonella* secretes another set of effectors via its T3SS2 (Krampen, 2017).

To exert its function as a pathogen, *Salmonella* uses both of its systems to invade, replicate and hide inside host cells to avoid elimination by the host immune system (Fig. 1) (Haraga et al., 2008). The organism causing severe foodborne disease and systemic salmonellosis in immunocompromised patients is taken up with contaminated food or water. A small amount of bacterial cells survive the low pH

environment of the stomach and travel to the distal small intestine (Portillo et al., 1993). At the brush border of the ileum *Salmonella* invades preferentially M-cells, specialized epithelial cells which overlay the gut associated lymphoid tissue (Jones et al., 1994). At the distal small intestine, the microaerophilic environment plus several other factors like high osmolarity, near neutral pH and absence of bile salts lead to the induction of SPI-1 expression (Bajaj et al., 1995; Jones et al., 1994; Prouty and Gunn, 2000). The regulation of SPI-1 gene expression is complex and involves many factors (Altier, 2005). In short, the three AraC-like regulators HilD, HilC and RtsA form a sophisticated feed-forward regulatory loop resulting in induction of the master transcriptional regulator HilA (Ellermeier et al., 2005; Golubeva et al., 2012). This regulator protein contains an OmpR-ToxR family like DNA-binding domain and induces expression of the *prg*/*org* and *inv*/*spa* operons, which encode for all structural components of the T3SS1 (Bajaj et al., 1995).

Salmonella Invades – A Job for T3SS1

When *Salmonella enterica* is in close contact to the epithelium of the small intestine, it adheres to host cells via its various adhesins (Wagner and Hensel, 2011). Once the distance to the target cell is close enough, so that the T3SS needle filament reaches the opposing membrane with its tip, two secreted hydrophobic translocator proteins form a complex on top of the needle tip. This translocator complex integrates into the host cell membrane and forms a pore (Blocker et al., 1999; Collazo and Galán, 1997). Effector proteins from the bacterial cytoplasm can now be translocated via this continuous conduit directly into the host cell cytoplasm.

The T3SS1-secreted proteins exert several functions inside the host cell with the common goal to promote the uptake of *Salmonella*. In detail, several effectors including SopE, SopE2 and SopB activate host Rho-GTPases to induce actin rearrangements of the host cell cytoskeleton (LaRock et al., 2015). SopB furthermore recruits annexin A2 (ANXA2) to the membrane which acts as a platform for the reorganized actin filaments

(Jolly et al., 2014). The SPI-1 T3SS secreted effectors SipA and SipC have the ability to induce actin bundling on their own (Hayward and Koronakis, 1999; McGhie et al., 2001; Zhou et al., 1999). All in all, these actin rearrangements result in membrane ruffling, engulfment of the bacterial cell and the formation of a *Salmonella* containing vacuole (SCV) inside of the cell (Humphreys et al., 2012). After internalization of *Salmonella*, the T3SS1 effector SptP induces the reversion of the cytoskeleton to its native state (Fu and Galán, 1999).

Besides actin restructuring and the resulting invasion of *Salmonella*, many T3SS1 effectors lead to an altered gene expression in the target cell. This alteration can mediate an inflammatory response which indirectly promotes the transmission of *Salmonella* (LaRock et al., 2015). In the case of SopB, it has been shown that this effector promotes the transformation of epithelial cells into M-cells, the preferential invasion target of *Salmonella* (Tahoun et al., 2012). Together this shows how effectively *Salmonella* and other T3SS equipped bacteria manipulate host cells in their favor, using an arsenal of various T3SS effectors in order to induce their uptake and dissemination.

T3SS2 Ensures Intracellular Survival

Inside of the SCV the gene expression profile of *Salmonella* changes drastically. This is induced by the changed environmental conditions inside of the SCV compared to the intestinal lumen. Intracellularly, *Salmonella* has to face several threats, like components of the innate immune system or the acidic pH in the phagocytic vacuole (LaRock et al., 2015). From this point on *Salmonella* switches to its T3SS2. In contrast to the T3SS1, the T3SS2 is needed for intracellular survival and immune system evasion (Cirillo et al., 1998; Hensel et al., 1998). Many factors, including phosphate starvation and low Mg^{2+} or Ca^{2+} concentrations, as they are present inside of the SCV, induce expression of SPI-2 genes (Hansen-Wester and Hensel, 2001). Simultaneously, expression of SPI-1 genes are repressed when SPI-2 inducing conditions are present (Deiwick et al., 1999). The crosstalk between several regulatory elements of both systems is necessary to ensure

a tightly regulated transition of the T3SS1-mediated invasive state to the T3SS2-mediated intracellular survival state (Erhardt and Dersch, 2015). HilD, one of the above-mentioned AraC-like regulators, is for example able to induce either SPI-1 or SPI-2 expression in a growth dependent manner (Bustamante et al., 2008).

Effector proteins specific for the T3SS2 injectisome are specialized to ensure *Salmonella* survival inside of the SCV, but also promote its migration into neighboring epithelial or immune cells (Worley et al., 2006). About 30 different T3SS2 effectors have been characterized until today (Figueira and Holden, 2012). In general, one can distinguish between four different effector targets/functions. Among others, SifA and SseJ have been found to be involved in formation of *Salmonella*-induced filaments (SIFs) and the maintenance of the SCV (Beuzon et al., 2000; Ohlson et al., 2005, 2008; Stein et al., 1996). Localization of the SCV next to the Golgi complex is mediated by SseF and SseG (Deiwick et al., 2006; Salcedo and Holden, 2003). The correct positioning of the SCV next to the Golgi complex was reported to be important for bacterial intracellular replication (Ramsden et al., 2007). Furthermore, T3SS2 effectors are responsible for rearrangements of the cytoskeleton which has returned to its normal morphology after SPI-1 T3SS mediated conformation changes during invasion (Méresse et al., 2001; Miao et al., 2003). This effect is mediated by another set of SPI-2 translocated proteins including SteC (Poh et al., 2008). Another important function is the modulation of the host cell immune response or the NF-κB pathway which leads to a downregulation of cytokine release and the preservation of host cell homeostasis (Mazurkiewicz et al., 2008; Sun et al., 2016).

In immunocompromised patients, *Salmonella* is able to disseminate into other organs like liver and spleen and cause severe life threatening diseases (Mastroeni and Grant, 2011; Santos et al., 2001). All in all, this shows how important T3SSs are for the pathogenesis of many Gram-negative bacteria like *Salmonella*. With the upcoming problems of antibiotic resistances in bacteria and their threat for infected humans, it is necessary to gain detailed insights into the various pathogenicity mechanisms of

bacteria in order to identify new targets for antibiotic or anti-infective therapies. For large and sophisticated virulence factors, like the T3SSs, it is therefore crucial to determine the structure and furthermore the function of all components, in order to understand how the system works and how it might be inhibited.

The Injectisome - Structural Components and Their Function

The Needle Base

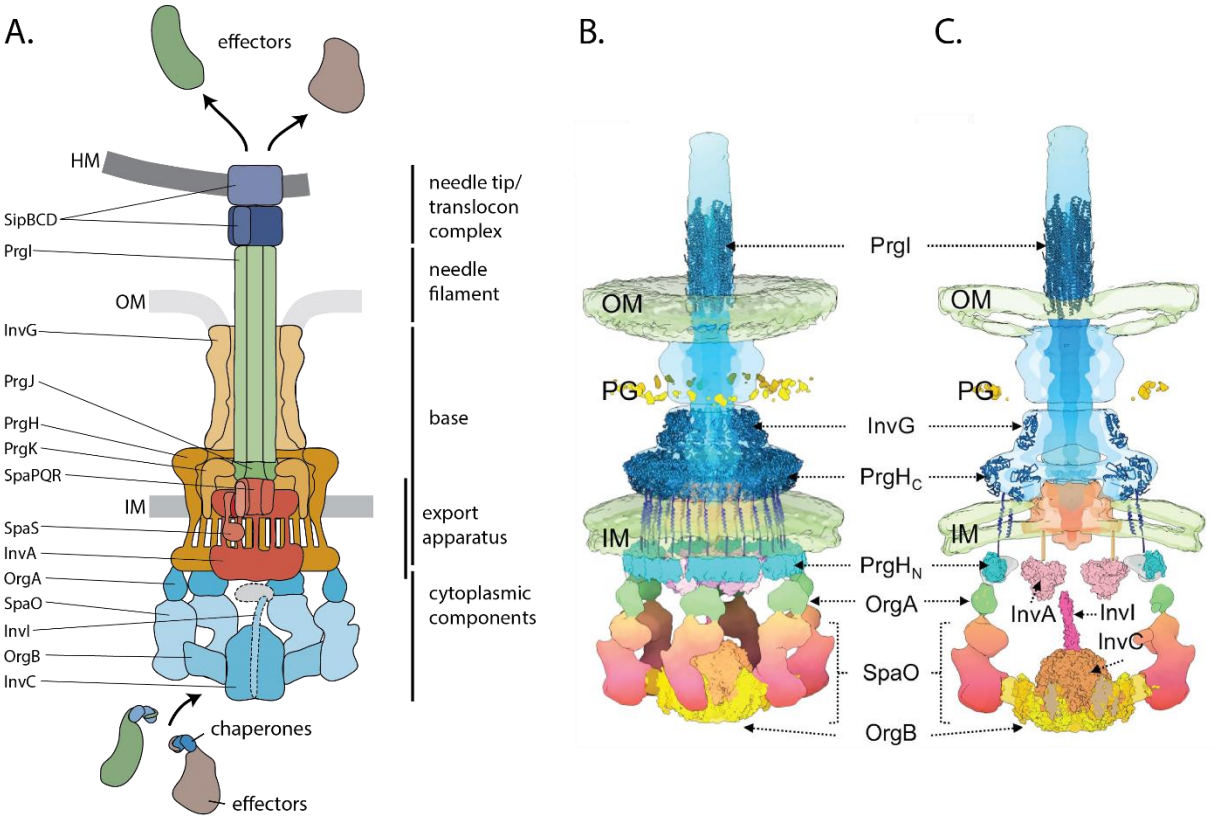

Figure 2: **Structure of the injectisome.** (A.) Cartoon model of the *Salmonella* SPI-1 injectisome (adapted from (Galán et al., 2014)). (B. and C.) Side and cut-through view of the intact injectisome structure. The available atomic structures have been fitted into the structure obtained by *in situ* cryo-electron tomography (Hu et al., 2017). HM: host membrane; OM: outer membrane; IM: inner membrane; PG: peptidoglycan.

Injectisomes have a syringe-like shape and are composed of about 20 different proteins with more than 200 subunits in total (Fig. 2) (Deng et al., 2017; Hu et al., 2017; Zilkenat et al., 2017). The model organism of this study was *Salmonella enterica* serovar Typhimurium. Therefore, all following descriptions and characterizations of T3SS components refer to the T3SS1 of *Salmonella*, if not mentioned otherwise. The prominent core structure spanning both membranes is called needle base. It consists of the outer membrane secretin protein InvG, which forms a 15-mer ring and the two inner membrane proteins PrgK and PrgH (Schraidt and Marlovits, 2011; Schraidt et al., 2010; Worrall et al., 2016). The lipoprotein PrgK as well as the bitopic membrane

protein PrgH form two concentric rings, each composed of 24 subunits (Schraidt and Marlovits, 2011). These two rings in the inner membrane are also called MS rings (membrane and supramembrane), whereby PrgK is termed the inner and PrgH the outer MS ring protein (Kimbrough and Miller, 2000). The secretin ring is connected to the MS ring via direct interactions with the periplasmic domain of the outer MS ring protein PrgH (Schraidt et al., 2010).

Major Focus: Export Apparatus

Another building block of every T3SS is the export apparatus. It is harbored in the inner membrane patch, composed of the five membrane proteins SpaPQRS and InvA and surrounded by the MS rings (Tampakaki et al., 2004; Wagner et al., 2010). The export apparatus substructure is one of the most conserved among all injectisomes and even among all flagella-associated T3SSs. The stoichiometry of all export apparatus components was recently determined for the T3SS1 in *Salmonella* and revealed a stoichiometry of 5 : 1 :1 : 1 : 9 for SpaP : SpaQ : SpaR : SpaS : InvA (Zilkenat et al., 2016). The export apparatus components are divided into two groups, the major and the minor export apparatus. The denotation major export apparatus is derived from the fact that two components, SpaS and InvA, are remarkably bigger than all other components and, besides their transmembrane segments, both consist of large cytoplasmic domains and exert special functions in the system (Berger et al., 2010; Diepold and Wagner, 2014).

The structures for both of these cytoplasmic domains have been solved for SpaS and MixA (InvA homolog) in *Shigella* (Abrusci et al., 2012; Zarivach et al., 2008). SpaS plays a major role in substrate specificity switching (Edqvist et al., 2003). This means that it is involved in shifting T3SS secreted substrate sets from early to intermediate substrates; due to this it is also called the switch protein (Magdalena et al., 2002). The cytoplasmic domain of SpaS and of all other homologous T3SS switch proteins contain an NPTH motif, at which the protein is able to autocatalytically cleave itself (Ferris et

al., 2005; Zarivach et al., 2008). Mutants not able to auto-cleave cannot switch substrate secretion from early to intermediate substrates. However this auto-cleavage is most likely not the switch signal *per se*, but rather gets SpaS into a conformation which then enables it to exert its switch function (Monjarás Feria et al., 2015). The crystal structure of the InvA homolog MxiA revealed that the cytoplasmic domain of this protein forms a nonameric ring (Abrusci et al., 2012). For the InvA homologs FlhA in the flagella system and HrcV in *Xanthomonas*, it was shown that this component interacts with effector proteins and their chaperones, indicating a role in substrate recognition (Büttner et al., 2006; Khanra et al., 2016; Kinoshita et al., 2013).

Like all structural components of the needle complex, the entire export apparatus is essential for a functional T3SS (Sukhan et al., 2001). Due to its central location inside the system it was proposed that the components of the export apparatus might act as a translocation channel through the inner membrane (Aizawa, 2001). Nevertheless, very little is known about the exact structure and function especially of the minor export apparatus components SpaP, SpaQ and SpaR. This discrepancy between the lack of knowledge and the importance of these components for the system was one of the motivations for this thesis. The deeper analysis and characterization of this substructure will help to understand the secretion mechanisms of this highly complex machinery.

The Cytoplasmic Components

Underneath the export apparatus and MS rings the cytoplasmic components of the T3SS are located. This highly organized substructure is composed of the proteins OrgA, OrgB, SpaO, InvI and InvC (Hu et al., 2017). The latter is the ATPase of the system and therefore responsible for energizing the secretion process. The structure of the InvC homolog EscN from *Escherichia* was solved and revealed that the ATPase is organized as hexamers (Zarivach et al., 2007). SpaO and OrgA are organized in hexameric pods (Hu et al., 2017). On the top, OrgA builds the connection of the SpaO

pods to the base structure, most likely via direct interactions with the cytoplasmic N-terminal part of the outer MS ring protein PrgH.

For the SpaO homolog YscQ in *Yersinia,* it was shown that about 22 copies of this protein are present in the assembled system (Diepold et al., 2015). SpaO is present in two forms, due to two distinct translational start sites: a full length form and a version comprised of the C-terminal third of the protein (Bzymek et al., 2012). The two versions of SpaO share some homology with the flagella proteins FliM and FliN, which are reported to be organized in a big ring structure (Zhao et al., 1996). Due to this, SpaO as well as FliM and FliN have been termed C-ring proteins. The large discrepancy between the number of 6 visible pods and the estimated number of 22 for the SpaO homolog YscQ in *Yersinia* might be explained with the high exchange rate of this component in the complex (Diepold et al., 2015). Furthermore, it was shown that SpaO together with OrgA and OrgB forms a sorting platform, ensuring the correct hierarchical order of substrate secretion (Diepold et al., 2017; Lara-Tejero et al., 2011).

Together this suggests that the highly dynamic SpaO might function as a transport protein carrying or guiding secretion substrates with their respective chaperones to the system. On the bottom of SpaO, the stator protein OrgB connects each of the SpaO pods to a subunit of the InvC ATPase complex (Hu et al., 2017). The direct interaction of SpaO with OrgB is essential for a functional injectisome, indicating the importance of both, the close proximity between the ATPase complex and SpaO and the correct organization of the cytoplasmic components (Notti et al., 2015). The small protein InvI sits on top of the ATPase complex (Hu et al., 2017). For the flagella homolog FliJ it has been shown that this protein acts as a positive regulator of the ATPase and moreover connects it via direct interactions to the major export apparatus protein FlhA (InvA homolog) (Minamino et al., 2011). Due to the common architecture, similarities between the ATPase-export apparatus-complex and F- and V-type ATPases have been discussed in literature (Ibuki et al., 2011; Portaliou et al., 2016).

Secreted Structural Components

Once the base components, the export apparatus and the cytoplasmic components have been correctly assembled, the system becomes secretion competent. Besides the cytoplasmic and the membrane associated components several T3SS secreted proteins are also structural components of the fully assembled injectisome. The component contributing the most subunits to the system is the needle filament protein PrgI, which has an α-helical hairpin shape (Wang et al., 2007). In *Salmonella* about 120 copies of PrgI assemble to a right handed helical conduit with an approximate length of about 35 nm (Loquet et al., 2012; Marlovits et al., 2006; Wang et al., 2007). Inside of the needle base the inner rod protein PrgJ is located and it is suggested that this protein somehow connects the needle filament with the export apparatus in the inner membrane (Marlovits et al., 2004). Furthermore, it has been shown that the inner rod protein is partially folded and an interaction of this protein with the needle protein is needed to build fully assembled needles (Cao et al., 2017; Zhong et al., 2012). PrgJ and PrgI share some structural similarities and both proteins are able to polymerize into fibers *in vitro* (Lefebre and Galán, 2014; Loquet et al., 2012; Monlezun et al., 2015).

In injectisomes, secreted substrates are distinguished in a three level hierarchy based on their order of secretion. The filament proteins PrgI, PrgJ as well as the non-structural protein InvJ are termed early substrates. As the name implies, these substrates are the first to be secreted after complete assembly of the secretion competent system. Initiation of secretion leads to a conformational change in the secretin protein InvG. In the closed state, radial projections of a hairpin formed by two β-sheets of each subunit build a periplasmic gate (Worrall et al., 2016). In order to allow passage through the secretin outer membrane pore, these hairpins have to swing out whereby the gate gets into an open state. This assumption is supported by the observation that secreted proteins accumulate in the periplasm, if the needle filament protein is missing (Diepold and Wiesand, 2012). This indicates that the polymerizing

needle filament is needed to open the secretin pore. The secreted protein InvJ, measures in a ruler-like fashion the length of the needle filament and, together with the switch protein SpaS, induces in an unknown mechanism the switch from early to intermediate substrate secretion (Wee and Hughes, 2015).

On top of the needle, the hydrophilic tip protein SipD assembles together with the two hydrophobic translocator proteins SipC and SipB (Lara-Tejero and Galán, 2009). SipBCD are all intermediate secretion substrates, but nevertheless structural components of the fully assembled and functional T3SS. SipD acts as a scaffold for the latter two, which then together form a translocation pore complex in the target host cell membrane (Mueller et al., 2008; Myeni et al., 2013). This results in a continuous channel connecting the *Salmonella* cytoplasm with the target host cell cytoplasm. In a second switch step of substrate specificity, involving the cytoplasmic gatekeeper protein InvE, *Salmonella* shifts its injectisome secreted arsenal towards the so called late substrates or effectors, which act in various ways on the target host cell (Kim et al., 2013; Kubori and Galán, 2002; Roehrich et al., 2016).

Overview on T3SS Assembly

Protein Complex Assembly

For such a sophisticated and highly specialized nanomachine composed of many different components and building blocks, like the injectisome, it is obvious that the correct orchestration of assembly is crucial for the functionality of the whole system. Assembly of homo- and heteromeric multi-protein complexes have been the focus of many studies (Ahnert et al., 2015; Marsh and Teichmann, 2015; Natan et al., 2017). Protein folding in the cytoplasm occurs primarily spontaneous, whereby hydrophobic cores are formed by connections between and among α-helices and β-strands (Levitt and Chothia, 1976). Subsequent oligomerization and complex assembly relies on a large set of various protein-protein interactions and additional assembly factors like chaperones and cofactors (Ellis, 2013; Nooren and Thornton, 2003; Van Vranken et al., 2015).

In contrast to this, assembly of membrane protein complexes is highly constrained, due to the two dimensional spatial limitation of the membrane space. Moreover, insertion as well as folding of proteins in the membrane occurs co-translationally via the Sec, YidC or a pathway combined from both essential machineries, adding a temporal factor to protein complex assembly (Dalbey et al., 2011). For inner membrane proteins and complexes, the interaction of α-helices and the resulting α-helical bundle formation is driven by various amino acid motifs in the α-helical chain (Schneider et al., 2007). Best described example for these motifs is the GXXXG motif, where the glycine of one α-helix provides a flat surfaces onto which side chains of the adjacent α-helix are able to make close contacts (MacKenzie et al., 1997). With this, the GXXXG motif maximizes possible van der Waals interactions and/or hydrogen bonding, resulting in a TMH-TMH right handed crossing (Teese and Langosch, 2015). By formation of α-helical bundles via these specific motifs, TMD-TMD intermolecular interactions can occur which are involved in noncovalent assembly of membrane

protein complexes (Ng et al., 2013). The cytoplasmic and periplasmic domains can also be involved in intermolecular interactions, resulting in stabilized and tightened complex assemblies. Several additional factors have to be mentioned in order to underline the complexity of membrane protein insertion, folding and assembly. It was shown that the phospholipid phosphatidylethanolamine (PE) can be involved in correct folding of certain membrane proteins (Dowhan and Bogdanov, 2009). Furthermore, proper protein complex assembly might require the presence of chaperone proteins or small accessory subunits (Formosa et al., 2017; Kulajta et al., 2006; Stroud et al., 2016). For hetero-oligomeric membrane protein complexes, ordered and non-ordered assembly pathways have been reported. In the ordered model, as reported for the cytochrome bo_3 oxidase or the cell division complex in *E. coli*, assembly of subunits occurs in a defined temporal order (Buddelmeijer and Beckwith, 2004; Stenberg et al., 2007). In contrast to this, a non-ordered assembly was for example reported for maltose transport complex in *E. coli* (Kennedy et al., 2004). In this case, several assembly pathways were reported which showed no sequential accumulation of specific intermediate assembly complexes.

Outside-in or Inside-out?

Characterization and elucidation of the T3SS assembly pathway has been the focus of several studies (Diepold and Wiesand, 2012; Diepold et al., 2010, 2011; Wagner et al., 2010). Based on apparently contradicting results, two distinct assembly pathways have been proposed (Kosarewicz, 2012). An outside-in pathway was suggested, based on the findings in *Yersinia* that the secretin ring in the outer membrane was able to assemble independently of all other components (Diepold et al., 2010). It was shown that the outer MS ring needs the presence of the secretin protein for assembly but not the inner MS ring protein (Diepold et al., 2010). Additionally, the same publication showed that the cytoplasmic components assemble after completion of the MS-rings (Diepold et al., 2010). This study indicated a top-to-bottom assembly starting with the

secretin in the outer membrane followed by the inner membrane components and finally the cytoplasmic parts. Contradictory to this model, it was shown that the proteins of the minor export apparatus are all essential for correct needle complex assembly (Wagner et al., 2010). This proposed an inside-out assembly model with a start point in the inner membrane.

The Bipolar Model

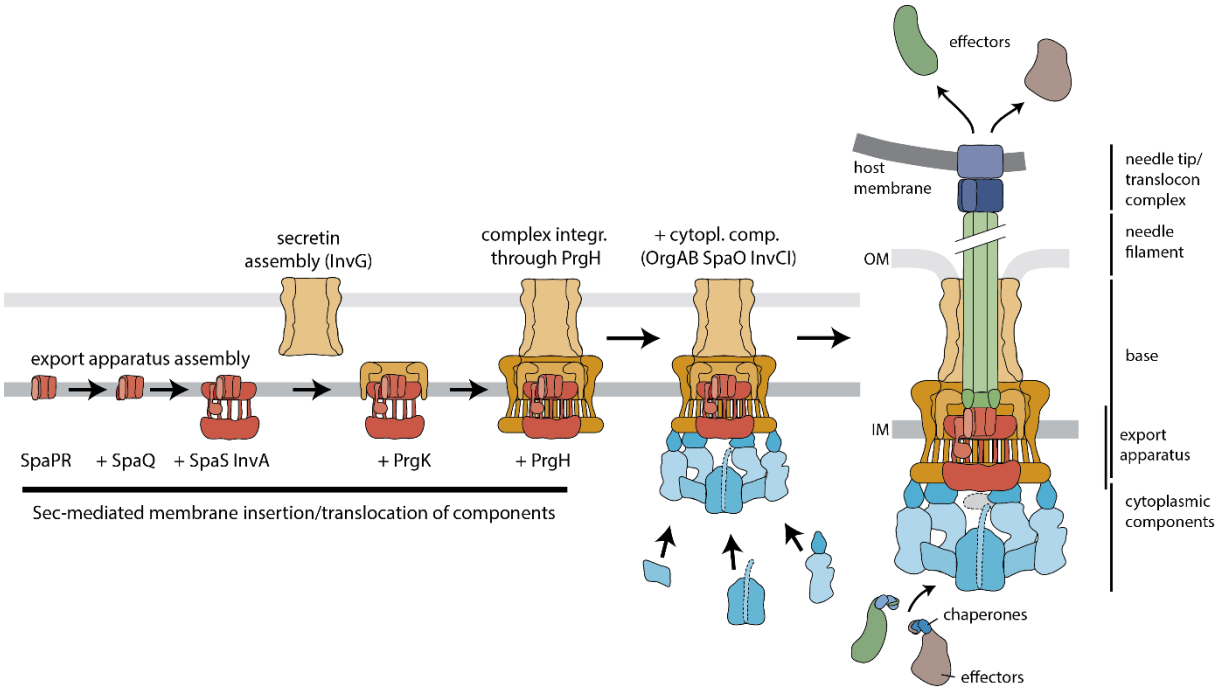

Figure 3: **Assembly of the proposed bipolar model.** In the inner membrane the export apparatus components assemble and recruit the inner MS ring protein PrgK. Simultaneously, the secretin protein InvG assembles in the outer membrane and recruits the outer MS ring protein PrgH. Both subcomplexes get integrated into one holo-complex. In the cytoplasm, components of the sorting platform and the ATPase get recruited. The system gains secretion competence and secretes the inner rod, needle filament, needle tip and translocator proteins. The fully assembled system is now able to translocate effector proteins from the bacterial cytoplasm into the target host cell cytoplasm (adapted from (Diepold and Wagner, 2014)). IM: inner membrane; OM: outer membrane.

The generally accepted working model at the moment is a combination of both approaches to a bipolar assembly pathway with two distinct starting points in the outer and in the inner membrane (Fig. 3) (Diepold and Wagner, 2014). The observation that the export apparatus components can assemble independently of all other components, but seem to float around in the inner membrane in the absence of the

secretin or the MS rings, supports this bipolar model (Diepold et al., 2011). This combined model fulfills not only the integration of all data on T3SS assembly to date but also it shows how quality control of the system can be applied during assembly. Two starting points for different substructures of the T3SS control two distinct functions of the system, which are only useful once they are combined.

In the inner membrane, the export apparatus assembles with the inner MS ring protein and recruits all cytoplasmic components to build a secretion-competent device, but without a connection to the second starting point of assembly, the secretin ring in the outer membrane, the system would secrete all substrates into the periplasmic space and would not be able to form a needle that breaches the outer membrane. Therefore, the second starting point in the outer membrane ensures penetration of this barrier so that secreted needle and other substrates can be translocated efficiently. Vice versa, the outer membrane secretin connected to the outer MS ring protein has to find the substructures in the inner membrane to gain secretion competence.

Nucleation Point Outer Membrane

In detail, the proposed *Salmonella* T3SS1 assembly proceeds in the following order: As described above, there are 15 copies of the secretin protein InvG assembling and forming a ring structure in the outer membrane. Secretins are dynamic channels in the outer membrane of Gram-negative bacteria and are amongst others an important part of several secretion systems like T2SS, T3SS and the type IV pili system (T4PS) (Korotkov et al., 2011). InvG is translocated across the inner membrane in a Sec-dependent manner. Additionally, InvG is dependent on the lipoprotein InvH, which is needed for correct assembly of InvG, as well as its insertion into and anchoring to the outer membrane (Crago and Koronakis, 1998; Daefler and Russel, 1998). InvH itself is directed to the inner leaflet of the outer membrane via the Lol pathway (Worrall et al., 2016). 24 copies of the outer MS ring protein PrgH get recruited to the secretin ring. This statement is based on observations in *Yersinia*, where it was shown that YscD

(PrgH homolog) co-purified with the secretin protein YscC (InvG homolog) in the absence of the inner MS ring protein YscJ (PrgK homolog), but conversely YscJ needed the presence of YscD for co-purification with YscC (Diepold et al., 2010).

Nucleation Point Inner Membrane

Independently, the three minor export apparatus components SpaP, SpaQ and SpaR make up the second nucleation point and assemble in an unknown hierarchical order in the inner membrane (Wagner et al., 2010). All T3SS components of the inner membrane are inserted into the membrane in a Sec-dependent manner (Sukhan et al., 2001). The minor export apparatus recruits the two major export apparatus components SpaS and InvA. As for their flagella associated T3SS homologs, it was proposed that all components of the export apparatus are located in the membrane patch surrounded by the MS rings (Minamino and Macnab, 1999; Tampakaki et al., 2004). The above mentioned observation of an export apparatus assembling independently of MS ring proteins strengthens this suggestion (Diepold et al., 2011).

Before the nonameric stoichiometry of InvA and its homolog MxiA in *Shigella* were determined via an MS-based approach and crystallization of its cytoplasmic domain, it had been already shown that InvA is forming oligomers and that its YscV homolog in *Yersinia* is present in multiple copies in the system (Abrusci et al., 2012; Diepold et al., 2011; Wagner et al., 2010). The limited space of the membrane patch inside the MS rings plus the ring structure of the nonameric InvA with its total predicted 72 transmembrane helices suggest that the InvA oligomer surrounds the rest of the export apparatus components. This assumption is supported by the fact that in *Yersinia,* the InvA homolog YscV co-purified with the inner MS ring protein in the absence of the outer MS ring protein or the secretin (Diepold et al., 2011). This implies that InvA (YscV) is in direct contact to the inner MS ring and therefore has to surround the rest of the export apparatus.

Despite all the progress, which has been made on T3SS assembly, the exact order of export apparatus assembly, the symmetry mismatch of the export apparatus and the connection of the two nucleation points still raise a lot of questions. It seems to be incomprehensible, how the *spa* operon encoded SpaPQRS subcomplex, with its asymmetrical 5:1:1:1 stoichiometry, is able to assemble correctly and subsequently fits into the highly symmetrical InvA nonameric ring. Calculating the approximate space of the membrane patch inside of the MS ring (about 130 Å diameter) shows that about 117 α-helices with an estimated average diameter of 12 Å would fit into the membrane area surrounded by PrgK. The membrane protein topology prediction web server TOPCONS (http://topcons.cbr.su.se/) predicts for InvA 7-8, for SpaP 4-6, for SpaQ 2, for SpaR 6 and for SpaS 4 membrane helices, based on the stoichiometry of these components, resulting in 95-124 membrane helices in total. This shows that the membrane patch inside the MS ring, as well as inside the InvA ring has to be tightly packed and does not give much space for structural flexibility. Additionally, there has to be space for a small pore with a diameter of about 10-15 Å which further tightens the space of the export apparatus components (Radics et al., 2013). Therefore, further investigations on assembly questions, especially concerning the export apparatus, seemed to be necessary.

How to Connect the Two Nucleation Points?

Besides the export apparatus assembly several other steps in the build-up of the T3SSs remain still unclear. One of these other very important open questions is how do both of the just mentioned intermediate complexes in the inner and outer membrane integrate together and form one holo-complex. The export apparatus components surrounded by the 24-mer inner MS ring would not be able to integrate into a fully and stably assembled outer MS ring connected to the secretin ring. This suggests that, although PrgH gets recruited to InvG, the completion of the outer MS ring can only occur if the fully assembled export apparatus plus the surrounding inner MS ring gets

integrated first. This might be due to the tight interaction of PrgH with PrgK which has to occur to stabilize both subcomplexes.

Another important question in this context is how and at which point of assembly the penetration of the peptidoglycan (PG) occurs. For several type III and type IV secretion systems specialized lytic transglycosylases (LT) have been found which are directly associated to the respective secretion system and might facilitate assembly of the translocation complex through the PG layer (Zahrl et al., 2005). In the *Salmonella* SPI-1 system this enzyme is termed IagB. The crystal structure of the IagB homolog EtgA from *E. coli* showed homologies to other LTs and structural features which were similar to lysozyme (Burkinshaw et al., 2015). For several of the associated LTs it was shown *in vivo* and *in vitro* that they efficiently cleave PG (Zahrl et al., 2005). Interestingly, for EtgA it was shown that the enzyme activity was increased when the T3SS inner rod protein was co-incubated (Burkinshaw et al., 2015). Once the two subcomplexes have been correctly built, found and fit together, the resulting fully assembled needle bases are solid and robust structures which can be stably purified and visualized (Kubori et al., 1998).

What Happens in the Cytoplasm?

The cytoplasmic components were for a long time one of the major blind spots on the T3SS assembly map. Those components are easily lost during purification and may have dynamic properties as it was already reported for the C-ring protein SpaO homolog YscQ in *Yersinia* (Diepold et al., 2015). The first study focusing on assembly of the cytoplasmic components was carried out by Diepold *et al.* in 2010. In this publication, it was reported for the *Yersinia* T3SS that the C-ring is only able to assemble when the membrane rings as well as the accessory protein YscK (OrgA homolog), the stator YscL (OrgB homolog) and the ATPase YscN (InvC homolog) are present. Furthermore, it was shown that assembly of the ATPase needed the same components as the C-ring, as well as the C-ring protein itself. Together these data

indicated the formation of a huge ATPase-C-ring complex, which needs all of its components for correct assembly, and a previously finished membrane ring complex which acts as a scaffold for the cytoplasmic parts. Interestingly and contradictory to previously mentioned results on needle base assembly, the presence of the export apparatus components was not needed to detect assembly of the C-ring or the ATPase (Diepold et al., 2010).

All observations in the study of Diepold *et al.* from 2010, are based on the detection of fluorescent spots of green fluorescent protein (GFP) labelled C-ring or ATPase protein tested in the absence of other T3SS components. With this method it is difficult to analyze the exact structural influence of each cytoplasmic component and therefore to distinguish between different assembly states. Key advances have been made by using state-of-the-art cryo-electron microscopy (cryo-EM) and *in situ* cryo-electron tomography to elucidate structural and assembly questions concerning T3SSs (Hu et al., 2017; Worrall et al., 2016). In line with the studies above, these state of the art techniques could confirm that the accessory protein OrgA as well as the stator OrgB and the C-ring protein SpaO are essential for assembly of the cytoplasmic components of T3SS apparatus. Moreover, it was elucidated that the C-ring protein SpaO together with OrgA and OrgB are organized in a 6 pod fashion (Hu et al., 2015, 2017). Interestingly, densities for those pods are also detectable in an ATPase deficient strain, indicating that assembly of those pods is to some extent independent of the presence of the ATPase and furthermore the ATPase is one of the last components assembled to complete the whole system (Hu et al., 2017). A most recent study revealed additionally, that the cytosolic components assemble into a highly dynamic complex in the cytosol, which then gets more stable after binding to the injectisome base components (Diepold et al., 2017).

The Flagella Associated T3SS Export Apparatus

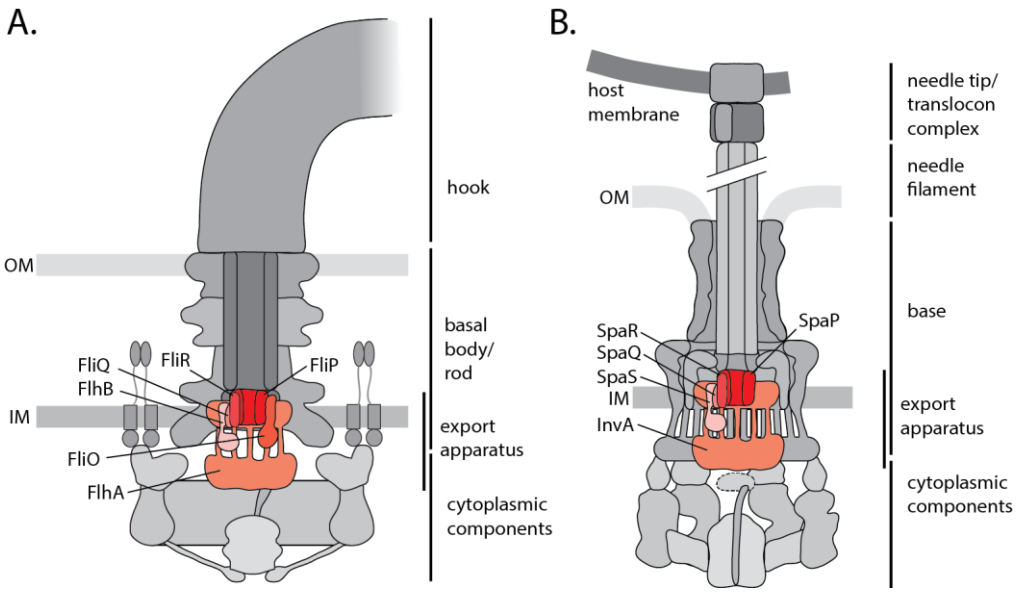

Figure 4: **Structural comparison of the flagellum with the injectisome**. Cartoon models of the structures of the *Salmonella* flagellum (A.) and injectisome (B.). Focus is on the highlighted export apparatus components of both systems.

It was mentioned before that, as the virulence associated injectisome, the bacterial flagellum uses a T3SS for the secretion of some of its components and is therefore crucial for its functionality. The overall structural organization, comparing injectisomes with flagella, is slightly distinct (Fig. 4). Many components of the flagella system, which would be needed to exert its function as a motility device have been lost or exchanged during the evolutionary transition into an injectisome (Abby and Rocha, 2012). A detailed discussion on all structural and functional components of the flagella system would go beyond the scope of this thesis. Only the corresponding fT3SS export apparatus components were of particular interest.

Similarities and Differences

The export apparatus components, also named as export gate complex in fT3SS, are among the most conserved in all T3SS (Macnab, 2004). The genetic organization of the flagella and injectisome export apparatus-encoding genes differ slightly in *Salmonella*. The gene encoding for FlhB, the SpaS homolog in the flagella system, is located outside

the *spaPQR* operon homolog *fliPQR*. The exact genetic organization of the genes encoding for T3SS components varies slightly between different organisms and the different systems but it is always consistent for the mentioned minor export apparatus genes *spaPQR*/*fliPQR* (Fig. 5).

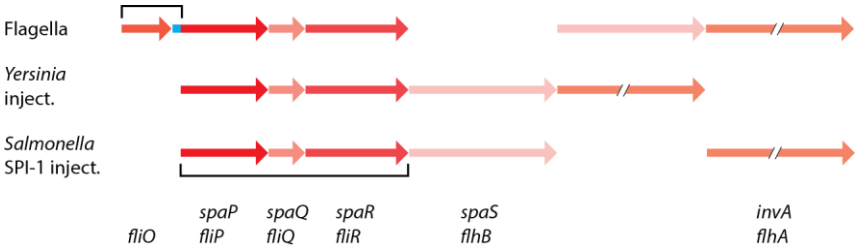

Figure 5: **Genetic organization of the export apparatus genes.** The evolutionary conserved organization of the *fliPQR*/*spaPQR* operon, the additional flagella *fliO* gene as well as the Sec signal sequence of *fliP* (blue) are highlighted.

A more striking difference between the flagella and the injectisome system is the presence of an additional gene upstream of *fliP* and also part of the *fli* operon encoding for FliO. This protein has no homolog in the injectisome system, shows the least conservation among all export apparatus proteins and is even absent in some flagella T3SSs (Barker et al., 2010; Liu and Ochman, 2007). It is a rather small bitopic membrane protein whose exact function had not been elucidated, but it seems to be involved in the functionality of the minor export apparatus component FliP (Barker et al., 2010, 2014). Together, all these results indicated that FliO might be a structural component of the fT3SS.

As mentioned before the degree of conservation between all export apparatus components present in both systems is very high, but still there are minor noteworthy differences. One of those differences is the fact that the N-terminus of FliP harbors a Sec signal peptide, which is essential for the co-translational insertion into the inner membrane via the Sec system and therefore for the functionality of FliP (Pradel et al., 2004, 2005). This Sec signal is missing in SpaP, suggesting that in the SPI-1 injectisome the first transmembrane helix (TMH) of SpaP is recognized by the signal recognition particle (SRP) and by this integrated into the inner membrane in a Sec-dependent manner.

Besides small differences, there have been a lot of similarities observed for the flagella and the injectisome export apparatus. Interestingly, for the fT3SS InvA homolog FlhA a stoichiometry of nine was determined using a fluorescence recovery after photobleaching (FRAP) approach (Morimoto et al., 2014). This result is in line with the observed nonameric crystal structure for the InvA homolog MxiA in *Shigella* (Abrusci et al., 2012). These studies, together with the high degree of conservation between fT3SS and injectisome export apparatus proteins, suggest that overall organization and function might be similar.

Aim of this Work

Despite recent high-resolution structural studies on the injectisome and flagella associated fT3SSs, many aspects concerning architecture, organization and function of these highly complex nanomachines are still blurry. One of these blind spots is the export apparatus, which is located in the inner membrane of every T3SS. Due to the components properties as membrane proteins, structural analyses have been very limited so far. This was particularly the case for the minor export apparatus components. These three proteins are predominantly composed of trans-membrane domains (TMDs) and thus buried inside of the inner membrane. This substructure was the major focus of this thesis. Although these highly conserved proteins are crucial for assembly and secretion competence, still nothing was known about their exact function.

The goal was to analyze different minor export apparatus subcomplexes with focus on their composition and organization. Various purification and interaction studies were designed to investigate the interplay with other T3SS structural components. With this knowledge, it was aimed to obtain detailed insights into the assembly of the export apparatus subcomplexes and subsequently of the whole T3SS. In order to link the components of the minor export apparatus to a specific function, their proposed role as pore-forming unit was of special interest.

The *Salmonella* SPI-1 injectisome as well as the *Salmonella* flagella-associated fT3SS export apparatus components were simultaneously objectives of this thesis. This gave the opportunity to compare these highly conserved and evolutionary related proteins and subcomplexes directly with regard to their structural organization and assembly properties. Furthermore, in this context the outstanding role of FliO in the *Salmonella* fT3SS was of particular interest.

The aim was a detailed hierarchical picture of injectisome, as well as fT3SS, export apparatus assembly.

Results

Publication 1: “Structural and Functional Characterization of the Bacterial Type III Secretion Export Apparatus”

This study focused on the characterization of the minor export apparatus components SpaP and SpaR. Structure and function of these two core components of all T3SSs are still poorly understood. SpaP and SpaR both are essential for needle complex assembly and have been reported to be associated with each other (Wagner et al., 2010). With respect to these results, it was discussed that both components make up one nucleation point of T3SS assembly (Diepold and Wagner, 2014).

Here it was shown that when the *spaPQRS* operon was expressed in the absence of all other structural T3SS components, a stable complex consisting of SpaP and SpaR could be purified. Multi angle laser light scattering (MALLS) combined with size exclusion chromatography (SEC) revealed a complex size of about 160 kDa. In line with this, native mass spectrometry (native MS) analysis of the purified complex determined an exact complex mass of 157.882 kDa. This measurement led to a stoichiometry of 5 SpaP and 1 SpaR (including an additional bound phospholipid) for the purified complex.

Further analyses of both proteins were performed using *in vivo* photocrosslinking. For this, base triplets of choice were mutated to an amber stop codon in order to get incorporation of the artificial photoreactive amino acid para-benzoyl-phenylalanine (*p*Bpa) by a plasmid based suppressor system (Chin and Schultz, 2002; Farrell et al., 2005; Ryu and Schultz, 2006). With this site specific-approach, several amino acid positions in SpaP were identified, which resulted in a five-fold crosslink ladder after UV irradiation. Combining this observed crosslink pattern with the solved stoichiometry led to the assumption that the observed crosslinks might resemble SpaP-SpaP intermolecular interactions. To identify and verify these positions as SpaP-SpaP interaction sites, the photocrosslinking experiment was repeated in *E. coli* BL21 expressing selected SpaP *p*Bpa mutants, which showed ladder crosslinks in *Salmonella*.

In this approach, where all other structural components of the T3SS are absent, the crosslink pattern of the selected SpaP *p*Bpa mutants was unaltered and thereby strengthened the hypothesis of a crosslink identification of several SpaP-SpaP interaction surfaces. To prove this intermolecular interaction, a FLAG-tagged version of wildtype SpaP was expressed from its chromosomal locus and the previous selected *p*Bpa mutants were expressed from plasmid. Probing against the wildtype SpaP version after UV irradiation showed a dimer band, proving a direct SpaP-SpaP interaction.

The SpaPR subcomplex can be detected via blue native polyacrylamide gel electrophoresis (BN PAGE) analysis to considerable amounts, when either both of the components are overexpressed or the needle base assembly is defective (Wagner et al., 2010). This indicates that in these cases there are excessive amounts of SpaPR subcomplexes which accumulate and do not get incorporated into needle complexes. Because of this, it was speculated that the identified SpaP-SpaP interactions might be SpaP or SpaPR subcomplex artifacts. Therefore, 2D BN PAGE analysis of selected SpaP-SpaP crosslinked mutants was performed. With this, it was proven that the observed crosslinks can be detected in the SpaPR subcomplex as well as in the fully assembled needle complex and therefore resemble the functional state of SpaP. Additionally to this, almost all of the initially detected SpaP-SpaP interaction positions were consistent with bioinformatics protein-protein interaction predictions for SpaP based on sequence co-variation analysis.

Besides the observed ladder crosslinks, several other site-specific interactions of SpaP could be detected. Some of these other crosslinks suggested an interaction partner of SpaP, which is slightly bigger than SpaP itself. The possibility that SpaP interacts, as a central component of the export apparatus, with SpaQ, SpaR, SpaS and InvA is high, due to the tight packaging of the export apparatus and the stoichiometry of 5 SpaP. Based on the size of these components, only SpaR and the cleaved membrane inserted part of SpaS were the two possible interaction partners with the highest probability.

Since SpaP was purified in a complex together with SpaR, a possible interaction of these two proteins verified via *in vivo* photocrosslinking was of particular interest. Therefore, to verify possible SpaP–SpaR interactions, a FLAG-tagged version of SpaR was co-expressed with the respective SpaP *p*Bpa mutants. Probing against the prey protein SpaR after UV irradiation confirmed several positions of SpaP, which interact with SpaR. *In vivo* photocrosslinking experiments were expanded and further positions in SpaP as well as SpaR were tested. In the same approach described above, additional interactions of SpaP–SpaS and SpaR–SpaP have been identified. Furthermore MS analysis of crosslink bands revealed SpaQ as interaction partner of SpaP and SpaR.

Surprisingly, additional interactions of SpaP as well as SpaR to the inner rod protein PrgJ were identified via MS. For at least one of these positions, the identified interaction was confirmed by co-detection with a specific antibody against PrgJ in an immunoblot. The inner rod protein PrgJ is a T3SS-secreted early substrate. Due to this, it was checked whether the interaction of SpaP and SpaR with PrgJ is secretion dependent. Therefore, an ATPase hydrolase mutant of InvC was used in a follow up experiment. The InvC K165E point mutation at the active center of the ATPase has been reported to cause a non-secreting phenotype without affecting the proper assembly of T3SS needle complexes (Akeda and Galán, 2005). In this setup, the interaction of PrgJ with SpaP as well as SpaR was abolished, indicating that the SpaPR complex interacts with the inner rod protein after its secretion. Furthermore, it was shown for a SpaR-PrgJ crosslink, using 2D BN PAGE analysis, that this interaction takes place in fully assembled needle complexes.

Due to its location in the inner membrane, it was hypothesized that the export apparatus is involved in pore formation and therefore in the translocation of secreted proteins through the inner membrane. First hints for the correctness of this hypothesis were already derived from preliminary experiments. It was shown that overexpression of the *spaPQRS* operon in *E. coli* was toxic for the cells and mild

expression of the same construct plus addition of several different sized PEGs led to cell lysis (data not shown). In this work, the assumption of a pore formed by the export apparatus was tested with a sophisticated maleimide labelling assay. Furthermore, the goal was to specifically identify the component which acts as pore forming unit in the system.

In this approach, either SpaP alone, SpaPQRS or a vector without insert was expressed in *Salmonella* needle base-deficient cells. After addition of a maleimide-biotin fusion molecule, the cytoplasmic, periplasmic and supernatant fractions were separated and checked via anti-streptavidin immunoblotting for maleimide labeling of free thiol groups from accessible cysteines. In the periplasmic fraction, free thiol groups of every sample including the empty vector control were labeled in the same fashion. Interestingly, the cytoplasmic fractions of cells expressing SpaP or SpaPQRS were labeled similarly, whereas there was no labelling for the vector control without insert. This indicated that already SpaP alone has the ability to form a pore in the inner membrane. Secondary effects, like cell lysis, were excluded because the supernatant fractions showed no labeling at all. Furthermore, there was no altered protein expression pattern when the whole cell contents were separated via SDS PAGE and stained with Coomassie. Additionally, all samples were analyzed via Western Blot against the cytoplasmic enzyme RNA polymerase, showing neither altered protein expression in the cytoplasm, nor secretion into the periplasm.

In line with the results of the labelling experiment, electron microscopy (EM) analysis of negative stained purified SpaPR complexes revealed a ring density with a hole in the middle. In contrast to the EM results, where only SpaPR complexes were analyzed, the maleimide labelling assay indicated that SpaP has the properties to function alone as the pore forming unit. Although the SpaP pentamer is very unstable and refuses to be stably purified on its own, it was shown via BN PAGE analysis of an EPEA tagged version of SpaP, that a homo-SpaP subcomplex can be detected. Deeper analysis of the particles visualized by EM revealed two distinct populations of complexes. One

population, already described above, showed a highly symmetrical donut shaped complex, while there were further complexes visible with an additional density at one side of the ring structure. Therefore, it was speculated that this additional density might in fact represent SpaR, thus the two observed populations were the SpaP pentamer alone and the SpaP pentamer with one associated SpaR molecule.

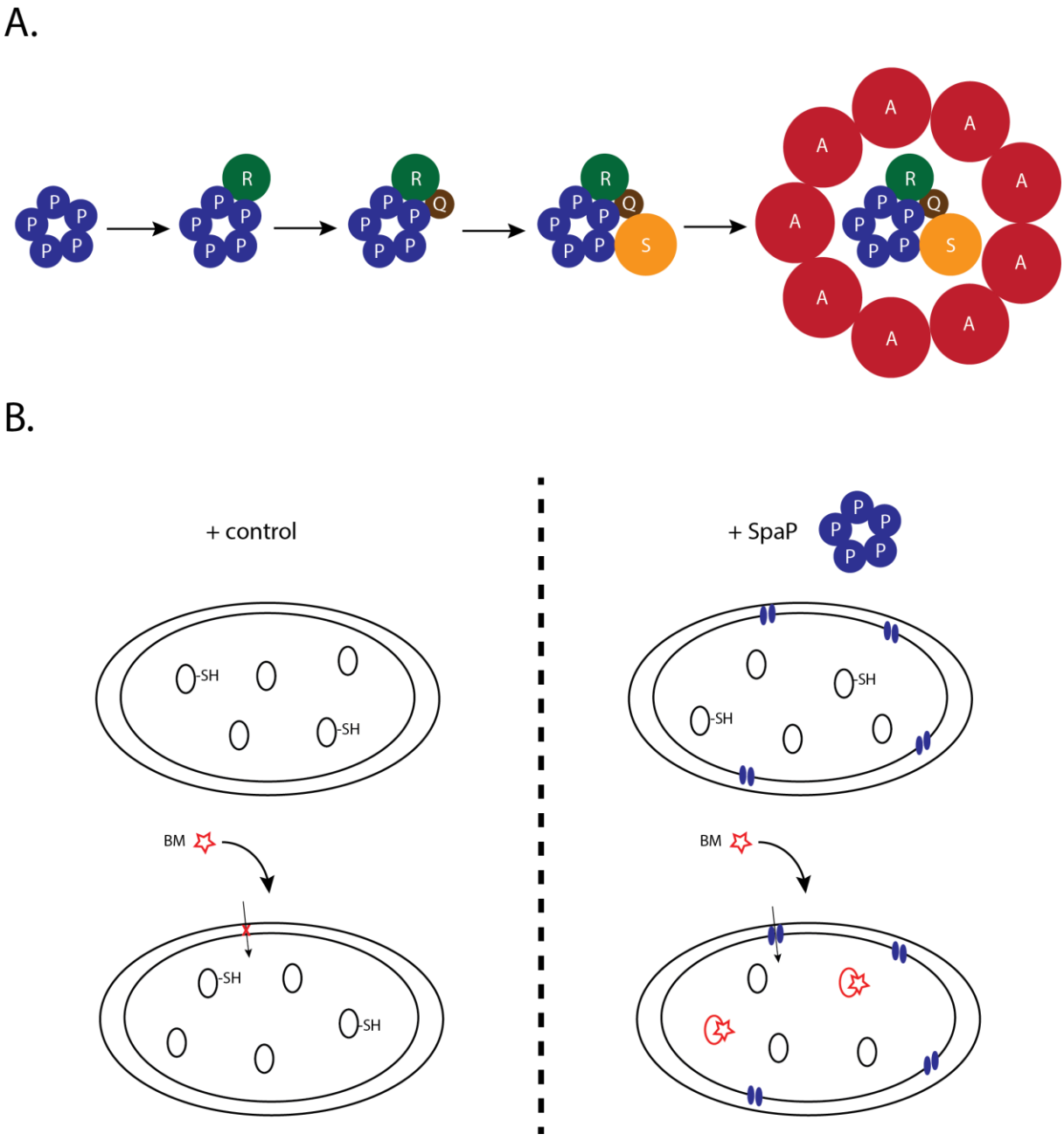

Figure 6: **Graphic summary of publication 1.** (A.) Assembly of the SPI-1 T3SS export apparatus of *Salmonella enterica* serovar Typhimurium. SpaP assembles independently to a pentameric ring. This subcomplex is very unstable and needs stabilization via SpaR. One molecule of SpaR associates with the pentameric ring, forming a stable SpaPR subcomplex. One molecule of SpaQ and subsequently one molecule of SpaS get recruited. Export apparatus assembly is completed with recruitment of the major export apparatus component InvA, forming a nonameric ring encompassing all other components. (B.) SpaP is the pore forming unit in the inner membrane. Biotin-maleimide (BM) labelling assay using cells expressing either SpaP or an empty control. The BM is ony able to lable free thiol groups of cytoplasmic proteins in cells expressing SpaP, proofing a SpaP dependent pore formation. P: SpaP; Q: SpaQ; R: SpaR; S: SpaS; A: InvA; BM: biotin-maleimide.

Publication 2: "A Flagellum-specific chaperone facilitates assembly of the core type III export apparatus of the bacterial flagellum"

In order to corroborate the importance of FliO on flagella assembly and function, extensive phylogenetic analyses of FliO distribution were performed. Pallen *et al.* noticed before that in several cases FliO might be wrongly annotated as FliZ (Pallen et al., 2005). In line with this report, in depth phylogenetic analysis revealed that FliO is more widespread than expected in organisms harboring a flagella system. In fact, it was found that FliO homologs are present in approximately 83% of all flagellated bacteria with a reference genome in the NCBI database. *De novo* predictions of FliO showed that this protein was wrongly annotated in more than half of all genomes harboring a flagella system.

To further analyze the link between FliO and FliP, an experiment was conducted to complement the non-motile phenotype of a Δ*fliO* mutant by overexpression of any other component of the export apparatus. Interestingly, only overexpression of FliP restored motility and secretion. Furthermore, overexpression of neither FliO nor FliP increased motility or secretion in a WT background. This underlined previous observations of the direct connection between FliO and FliP (Barker et al., 2010, 2014). Since extensive amounts of FliP led to a phenotype which compensated the lack of FliO, it was hypothesized that FliO might affect the stability of FliP. Consequentially, higher amounts of FliP could counteract the missing effect of FliO on FliP. In order to test this hypothesis, FliP protein levels were measured after arrest of *de novo* protein synthesis. For the detection time window of 3h the protein level of FliP in the WT background stayed constant, whereas it decreased drastically in a Δ*fliO* mutant strain. To exclude any polar effects of the *fliO* mutation on FliP expression, the same experiment was repeated using a Δ*fliP* strain and a Δ*fliOP* strain, both complemented with a plasmid expressing FliP. The results showed the same effect, protein levels of FliP decreased drastically when FliO was missing. Furthermore, also non-functional

point mutations in FliO decreased FliP levels, indicating that only small contacts of FliO to FliP are needed for FliP stability.

In *Salmonella,* a big difference of the injectisome SpaP protein to the flagella FliP is the presence of a Sec signal peptide harbored at the N-terminus of FliP. This observation raised the question if FliO does not only have an effect on FliP stability but also on the co-translational membrane insertion of FliP. For this, the effect of a Δ*fliO* strain on FliP membrane insertion was tested. Purified membranes were treated with urea, in order to discriminate between properly inserted proteins and aggregated proteins which are only slightly associated to the membrane. As expected, FliP was only detected in the membrane fraction and was unaffected by urea treatment. Comparison of inserted FliP levels showed that deletion of *fliO* had no effect on FliP membrane integration.

Next the degradation of FliP in the absence of FliO was further examined. To gain insights which protein degradation pathway is responsible for FliP degradation, FliP protein levels were measured in a similar approach as before but this time the effect of the absence of several proteases was tested additionally in the presence or absence of FliO. The tested proteases were FtsH, ClpP and Lon. Due to the fact that FtsH, a protease involved in quality control of membrane complexes like the SecYEG translocase, is essential for the cells, using a Δ*ftsH* strain was not an option. For this a strain was used which overexpressed STM1085, a FtsH inhibitor in *Salmonella* (YccA in *E. coli*) (van Stelten et al., 2009). YccA functionality was verified in an experiment, using LamB-LacZ hybrids for displaying FtsH dependent suicidal Sec translocon complex degradation after jamming. For this assay described by van Stelten et al., the Sec signal sequence of the outer membrane protein LamB is fused to LacZ. The presence of maltose leads to the expression of large amounts of hybrid protein and rapid folding of LacZ causes jamming of the Sec complex.

The functional YccA expression construct was now used to test the effect of FtsH on FliO dependent FliP degradation. In this strain no differences in FliP stability were observed in the absence of FliO indicating that FliP is not degraded via the FtsH

protease. Similar results were obtained when FliP stability was analyzed in a Δ*fliO* strain additionally lacking the genes for the protein degradation machinery *clpXP*. Interestingly, in the Δ*lon* mutant, FliP was more stable in the absence of FliO compared to a WT strain lacking *fliO*. This indicates that the Lon protease might be the primary protease responsible for FliP degradation.

As all export apparatus components, FliO is a membrane protein. Due to this and its genetic localization, it was suggested that FliO is also a structural component of the export apparatus and thus located inside of the basal body (Minamino and Macnab, 1999). To test this hypothesis, single molecule super-resolution microscopy was performed to determine the sub-cellular localization of FliO. For this, localization of Halo tagged versions of FliO and FliN protein was revealed by structured illumination microscopy. As reported before, the C-ring protein FliN localized in clusters and it could be shown that this cluster-formation is dependent on MS-ring assembly. FliO was also found to be localized in clusters, however they were smaller and more evenly distributed when compared to those of FliN. Interestingly, in contrast to FliN, the formation of FliO clusters was not affected in MS-ring or fT3SS assembly-defective strains.

Furthermore, single molecule tracking of Halo-tagged FliO and FliN was performed, using direct stochastic optical resolution microscopy (dSTORM). FliN remained stable at the same location in the cell envelope with a diffusion coefficient of 0.03. Compared to this, FliO revealed a much higher movement in the membrane. The measured diffusion coefficient of 0.2 is in the same range of previously reported diffusion rates for freely diffusing proteins in the inner membrane (Dajkovic et al., 2016; Kumar et al., 2010). This result suggests that FliO is not associated with the basal body and exerts its function before basal body assembly is completed. To corroborate this assumption, co-localization studies of the hook protein FlgE and a Halo-tagged version of FliO were performed. An anti-hook immunostaining showed that FlgE is located in big clusters which resemble fully assembled and functional flagella basal bodies, because FlgE

itself has to be secreted via the fT3SS. Staining of FliO with an anti-Halo antibody showed that FliO did not co-localize with the FlgE clusters and therefore not with the assembled basal bodies.

Due to the influence of FliO on FliP stability and the crucial role of FliP on basal body assembly, the effect of FliO on basal body and precursor subcomplex assembly was extensively tested via BN PAGE analysis. It was shown that FliO is required for basal body formation and the assembly of a FliPR precursor complex. Furthermore, an accumulation of FliP monomers and high MW FliP complexes was detected when FliO was absent. It was speculated that these high MW complexes might resemble aggregated FliP-protease complexes, which are formed when FliP monomers are not efficiently assembled into FliP/FliPR subcomplexes. The BN PAGE results were supported by liquid chromatography tandem mass spectrometry (LC/MS) analysis. 2D BN PAGE analyses confirmed the FliO dependent formation of a FliPR precursor complex and additionally showed that FliO itself is not directly associated with this subcomplex.

For the *Salmonella* injectisome SPI-1 system it was shown that the SpaPR complex is the first stable export apparatus assembly subcomplex (publication 1). To investigate the assembly of the flagella export apparatus in more detail, the formation of the FliPR precursor complex was followed in several export apparatus mutants. As shown before, the assembly of this subcomplex was unaffected in an MS-ring-deficient Δ*fliF* mutant, because the formation of the MS-ring occurs upstream of export apparatus assembly. Furthermore, it was also already discussed before that the FliPR complex is unable to assemble without FliO because it is needed to stabilize FliP and therefore initiates the assembly. Deletion of *fliR* led as expected to the loss of the FliPR complex, but interestingly faint bands with distinct sizes were detectable. In contrast to this, a *fliQ* deletion did not have any effect on FliPR precursor complex formation.

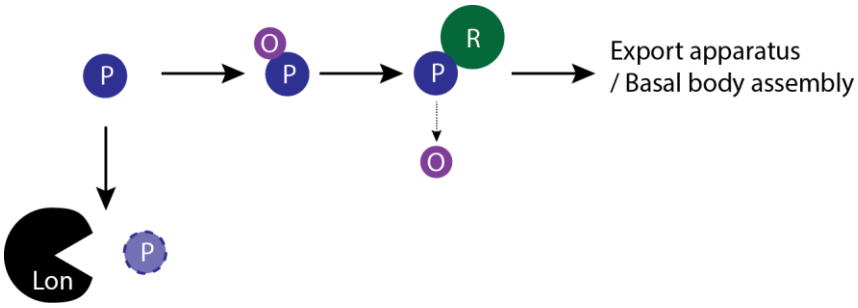

Figure 7: Graphic summary of publication 2. FliO is a flagella specific chaperone, stabilizing the export apparatus component FliP and preventing its Lon dependent degradation. FliR gets recruited and subsequently FliO dissociates form the newly formed FliPR subcomplex. This subcomplex is the basis for further export apparatus and basal body assembly. P: FliP; O: FliO; R: FliR; Lon: Lon protease.

Publication 3: “Assembly and stoichiometry of the core structure of the bacterial flagellar type III export gate complex”

To further analyze the export apparatus assembly in the flagella system, the formation of distinct export apparatus subcomplexes was studied more extensively. The main focus of this study was again on the two proteins FliO and FliP. Purification of FliP complexes resulted in two peaks after SEC. EM analysis of the higher MW complex showed that this protein forms a hexameric ring/donut shaped complex with a diameter of about 10 nm. The latter smaller peak did not show any ring structure at all. When FliO was co-expressed with FliP, a complex consisting of both proteins could be purified besides the FliP hexamer complex. In these FliOP complexes several FliP rings could be detected associated with several FliO molecules. The bitopic membrane protein FliO seems to oligomerize and forms smaller ring-like structures with a diameter of about 5 nm and flexible clamp domains, which then are able to bind the FliP rings. The small MW peak which has been observed when only FliP was expressed and which did not show ring structures was not detectable anymore in this setup. It was noticeable that the purified FliP amounts were significantly increased when FliO was co-expressed. This observation was in line with the results reported in publication 2.

Additionally, three FliP point mutants were included in the purification experiments. These three point mutations were all localized in the big periplasmic loop of FliP and resulted in a FliP loss-of-function phenotype. FliP expression levels of all mutants were comparable to the WT but the secretion of flagella substrates was severely impaired and they all had a non-motile phenotype. When FliO was co-expressed with these three FliP loss of function point mutations, each of the three elution profiles after purification of FliP showed the same peak pattern. Two distinct peaks were detectable, of which the latter one was similar to the small MW peak observed before, when only FliP was expressed. In line with that, this fraction only contained FliP and as mentioned above, there were no ring structures detectable for this peak after EM

analysis. The higher MW peak contained FliO and FliP to less amounts compared to the high MW complex when WT FliP was co-expressed with FliO. EM analysis of this peak showed no detectable FliP hexamers associated to the FliO oligomers. All in all, these results indicated a role in ring formation of all three positions in the FliP loop.

To gain further insights into FliP structure and its hexameric formation, the periplasmic domain of FliP (FliPp) from *Thermotoga maritima* (*Tm*-FliPp) was purified and its crystal structure determined. The FliPp structure was solved to a resolution of 2.4 Å and found to form a homo-tetramer in the crystal (molecules A-D), showing a pseudo D2 symmetry. Two tetramers, whose structures are essentially identical, are organized in an asymmetric unit. All eight *Tm*-FliPp molecules in one asymmetric unit did not show any differences in their structure. The monomers are organized in three α-helices (α1, α2 and α3) with a small unstructured stretch between α2 and α3. Due to the pseudo D2 symmetry of the FliPp tetramer, three different inter-molecular interactions were possible. In order to gain further insights into FliP organization, these three possible interaction interfaces were the focus of deeper analysis. The interface of molecules A to B is hydrophobic, whereas the interactions of molecule A to C were of hydrophobic as well as hydrophilic nature. In contrast, there was no direct contact detectable for the interaction interface of molecule A with molecule D.

The detection of *Salmonella* FliP (*St*-FliP) hexameric rings by EM analysis was inconsistent with the observation of *Tm*-FliPp homo-tetramers from the crystal structure analysis. These contradicting results raised questions concerning the relevance and trustworthiness of these results. Interestingly, stoichiometry analysis of *Tm*-FliPp using sedimentation equilibrium analytical ultracentrifugation measurements already revealed a homo-tetramer formation in solution (Fukumura et al., 2014). Furthermore, it was tested whether dimer units in the observed homo-tetramers might be involved in the hexameric FliP structure by forming trimers of dimers. In the *Tm*-FliPp crystal two distinct dimers are present A-B and A-C which both shared, as described above, hydrophobic as well as hydrophilic interaction

interfaces. The periplasmic domain of *St*-FliP share about 30% sequence identity with *Tm*-FliP, but a homology model of both periplasmic domains based on the tetramer crystal structure of *Tm*-FliPp revealed that although the residues at the interfaces of A to B as well as from A to C are not well conserved, the interface properties remained similar.

When the dimer formation of FliPp is analyzed with respect to the structure of full length FliP and its location in the inner membrane, FliPp dimer formation with an A to C interface can be excluded. The N-terminal part, as well as the C-terminal part of the periplasmic domain both have to be located in close proximity to the membrane, because they are in between TMH2 and TMH3. Based on this, the interaction interface of a possible A-C dimer would be located buried inside the membrane, which is highly improbable. There were no comparable steric hindrances conceivable for the A-B dimer, favoring the suggestion that FliP is organized in trimers of dimers, which lead at the periplasmic interface to intermolecular interactions as described for an A to B dimer.

In order to further determine and verify which FliP dimer is actually present in assembled FliP hexamers, *in vivo* photocrosslinking was used to test FliP-FliP interactions at several positions of both interaction surfaces. Based on previous studies with the injectisome homolog SpaP, two positions were chosen as positive controls for *St*-FliP-FliP interactions (publication 1). As expected, due to the high sequence identity between *St*-FliP and *St*-SpaP, these two designated positive controls for FliP-FliP crosslinks both showed strong additional bands after UV irradiation which correspond to the expected size of a FliP-FliP dimer. Out of the eight additionally tested positions two led to an interaction resulting in a band at the same height as in the FliP-FliP interaction positive controls. Interestingly, both of those positions are located at the A-B interface and therefore strengthens this proposed dimer structure, which occurs in the trimer of dimers formation in FliP hexamers. In line with this, it

was already shown in the FliP purification experiments for one of these positions that this residue was important for FliP hexamer formation.

Extensive photocrosslinking experiments proved that several positions located in the FliP periplasmic loop are interacting with FliO. Additionally, the FliO-FliP crosslinking bands seemed to be weaker when FliQ as well as FliR were co-expressed. From this, it was proposed that the stabilizing effect of FliO on FliP, which has been shown in publication 2, might only be needed until FliR and FliQ bind to this flagella export apparatus assembly nucleation complex.

To study export apparatus subcomplex formation in more detail, several different components were co-expressed and purified. With this, it could be shown that FliR binds to the FliOP complex as expected and furthermore a FliPR complex could be purified to some extent even in the absence of FliO. Additionally, it was shown that the switch protein FlhB can be recruited to a FliOPR subcomplex and that the other major export apparatus protein FlhA forms ring structures together with the MS ring protein FliF, which was stabilized by the C-ring protein FliG. For this, co-expression of the C-ring protein FliG was necessary in order to achieve stabilization of FliF by FliG, which has been reported before (Morimoto et al., 2014). Interestingly, in this setup no other export apparatus component co-purified with FlhA. The loss of FliQ and FlhA during export apparatus purification has been observed before for the corresponding injectisome components SpaQ and InvA (Zilkenat et al., 2016). Adjusting the complex purification protocol by exchanging the detergent n-dodecyl beta-D-maltopyranoside (DDM) with the even milder alternative lauryl maltose-neopentyl glycol (LMNG) changed the elution profile. With this setup, it was shown that FlhA as well as FlhB associate with FliP and FliP itself forms tight complex with FliO as well as with FliR and FliQ.

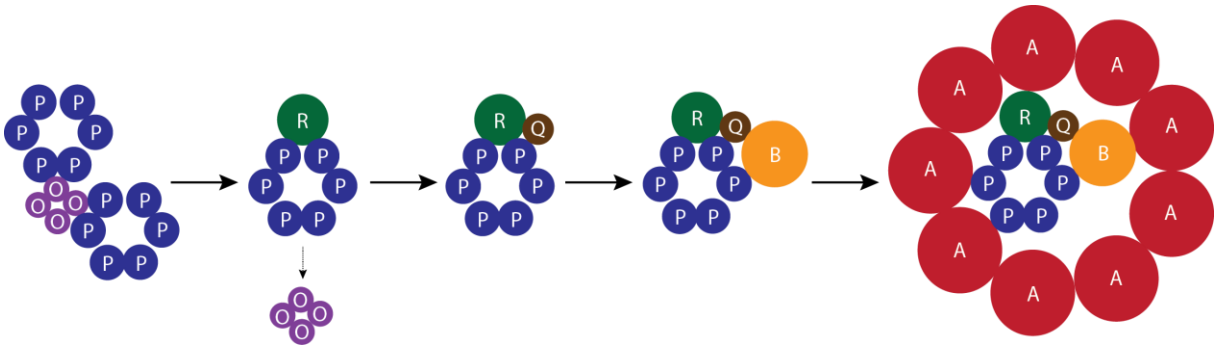

Figure 8: **Graphic summary of publication 3.** Flagella export apparatus assembly is initiated with the binding of FliP complexes to FliO complexes. FliP is organized in hexameric rings composed of trimers of dimers. FliO forms also smaller ring structures with flexible clamps onto which the FliP complexes are able to bind. FliR gets recruited to FliP, leading to the dissociation of FliO. FliQ and subequently FlhB associates to the FliPR complex. Export apparatus assembly is completed with recruitment of the major export apparatus component FlhA, forming a nonameric ring, which encompasses all other components. P: FliP; O: FliO; R: FliR; Q: FliQ; B: FlhB; A: FlhA.

Discussion

Part I: Injectisome Export Apparatus

Bacterial multi protein complexes are fascinating in many ways. Analogous to clockworks, many different parts of various shapes and sizes with distinct features have to fit perfectly into each other in order to exert one or many specialized functions. The correct assembly of such highly sophisticated complexes is crucial and follows some strict hierarchical rules. In the three featured publications of this thesis one common major focus point was the assembly of the T3SS export apparatus. These papers address the export apparatus of the virulence associated injectisome as well as of the flagella system. With different intentions all three studies directed its focus at export apparatus subcomplexes and particularly on its central key component, the minor export apparatus protein SpaP/FliP.

In publication 1 "**Structural and Functional Characterization of the Bacterial Type III Secretion Export Apparatus**" it was shown that five SpaP molecules form a complex with one SpaR molecule. This result was consistent with a previous study, where it was shown that the two export apparatus components are present in five and respectively one copies in fully assembled needle complexes (Zilkenat et al., 2016). Furthermore, this showed that the purified complex resembles the assembly states of SpaP as well as SpaR as they are present in the fully functional system. Until now, protein-protein interaction studies of proteins of the export apparatus were performed using overexpressed purified components in pull-down assays and therefore might not reflect the native situation *in vivo* (Feria et al., 2012; Kinoshita et al., 2013).

In this study, the pentameric conformation of SpaP was confirmed via *in vivo* photocrosslinking experiments. It was shown, that these interactions take place in the fully assembled and functional needle complex. Interestingly, it was shown that positions in SpaP, which were verified as SpaP-SpaP interaction sites, led to crosslink ladders with up to 5 crosslinked proteins after UV irradiation. Exactly the same

crosslinking pattern was detected when SpaP was expressed in the absence of all other structural T3SS components. With this several conclusions can be drawn. First, SpaP has to assemble in a symmetrical ring-like fashion otherwise a crosslink ladder would be impossible to detect. Additionally, this SpaP subcomplex was able to assemble in the absence of all other T3SS components, proving that SpaP has to be the nucleation point of T3SS assembly in the inner membrane.

The method of *in vivo* photocrosslinking was recently used extensively in various studies. For example, with this approach new insight into the multi-protein complex, which mediates biogenesis of β-barrel outer membrane proteins, were gained (Wang et al., 2016). Or it was used to identify interactions in *E. coli* between the ferric enterobactin outer membrane transporter FepA with TonB, an inner membrane protein, which is needed to energize and gate this transporter (Gresock and Postle, 2017). Moreover, this technique helped to determine and verify the stoichiometry of a voltage-gated ion channel to its β-subunit in human tsA201 cells (Murray et al., 2016). Here, it was shown that the technique can be used as a powerful tool for the analysis of structure and assembly intermediates of multi-protein complexes. In this particular case, every attempt to purify a complex composed of only SpaP failed due to missing stabilizing effect of SpaR. Nevertheless, with this method it could be shown that a SpaP pentamer formation can be detected even in the absence of all other T3SS components, indicating that a complex consisting of only SpaP is existent. This result revealed the strength of this method, by combining a very sensitive crosslinking technique with the advantage of not needing any prior purification steps.

Additionally, different structural states of protein in complex can be analyzed. This is supported by the observations that are made when comparing SpaP pentamer crosslink patterns. This ladder pattern can be detected for many different positions but mainly in TMH1 and TMH4. Interestingly, when SpaP was expressed in the absence of SpaR or any other T3SS components it seemed like only the identified positions in TMH1 are forming SpaP-SpaP interactions. In this setup the SpaP ladder pattern at the

identified positions in TMH4 are almost completely lost. This shows that without SpaR, the SpaP subcomplex is in a different structural and maybe more flexible state.

The structural organization of the fully assembled needle complex already indicated a central role for the export apparatus, due to its location in the core of the system. In this thesis the SpaPR subcomplex was identified as the central substructure. It could be shown that both proteins have various connections to several other structural components of the system. Furthermore, both proteins are interacting with the secreted inner rod protein, which is located in the periplasmic space inside the needle base and therefore has to be centrally located. This central status is reflected in the importance of this subcomplex for the assembly of the complete injectisome. The assembly of T3SSs and more precisely of virulence associated T3SSs was the focus of several previous studies (Diepold and Wiesand, 2012; Diepold et al., 2010, 2011; Wagner et al., 2010). In this work, the established crosslinking method was used to monitor subcomplex and respectively assembly intermediate formation in more depth than before.

It was shown that after formation of the SpaPR complex the third minor export apparatus protein SpaQ and the switch protein SpaS get recruited and assemble independently of the needle base. Interactions of SpaP with SpaQ as well as SpaS were unaffected in a background, where the gene encoding for the inner MS ring protein *prgK* was deleted. In contrast to this, it was found that the same interactions were not detectable when *spaPQRS* was expressed in the absence of any other structural components in *E. coli* BL21 cells. This puzzling result seemed to be contradicting to the previous result, which led to the idea that SpaQ as well as SpaS assemble to the SpaPR complex independently of the needle base structure. It seems like export apparatus assembly is more complex than expected and another factor or element is involved in export apparatus intermediate assembly. The most prominent candidate InvA can be excluded, because subsequent analysis revealed that deletion of *invA* did not lead to a loss of either of the two interactions (data not shown). Further explanations might be

the structural flexibility of SpaP and the stability of this intermediate complex. As described above, it has been shown that SpaP - SpaP interactions in TMH4 were lost when the other components of the *spa* operon were not expressed. The detected SpaP - SpaQ and SpaP - SpaS signature crosslinks were at position 203 in SpaP, hence in the mentioned TMH4. In the tested setup all *spa* operon encoded proteins were present, it might be possible that the recruitment of SpaR to the SpaP pentamer leads to the stabilization of SpaP - SpaP interaction surfaces in TMH4. Nevertheless, the SpaQ and SpaS binding site at position 203 is still in a conformational state, where binding of these two proteins is impossible without further stabilization by other structural components. To prove this, it would be interesting to test further SpaP - SpaQ/SpaS interaction positions outside of TMH4 for their dependence on other T3SS components. Therefore, candidates for future further analysis of the assembly of T3SS export apparatus could be position 170 in SpaP or 209 in SpaR. At these positions SpaQ was identified as interaction partner of both proteins via MS analysis. Another approach would be to test the SpaP - SpaQ and SpaP - SpaS crosslinks in a Δ*invA* Δ*prgK* double mutant, in order to check if these components are able to take over the structure stabilizing role of each other. Additionally, there might be a difference in complex assembly or stability between *Salmonella* and *E. coli* which could explain this discrepancy. Despite of this open question, the study was able to deepen the current understanding concerning export apparatus assembly in T3SS.

The identification of PrgJ as interaction partner of SpaP and SpaR was of special interest. Cryo-EM data of mutants lacking all export apparatus components already suggested that these components lead to the absence of a cup structure in the periplasmic space surrounded by the needle base (Wagner et al., 2010). Based on the SpaPR crosslinking it could be shown, as described above, that this subcomplex has to be located in the very center of the inner membrane patch. Therefore, it was assumed that the cup structure might be made up by the SpaPR complex and this acts as a scaffold for the inner rod protein PrgJ. The verification that SpaP and SpaR only

interact with PrgJ when this early substrate is secreted increased the relevance of these interactions. These results indicated indirectly a continuous connection of the inner membrane located SpaPR complex to the needle filament through the inner rod protein PrgJ. This assumption is supported by findings that the inner rod protein needs to interact directly with the needle filament in order to build functional T3SSs (Cao et al., 2017).

If the SpaPR complex builds a continuous conduit with the inner rod proteins and the needle filament, it is highly likely that this subcomplex has to form a pore in the inner membrane. In this work, the SpaPR, and to be more precise the SpaP complex, was identified as the pore forming unit in T3SSs using a biotin-maleimide labelling essay. Based on the size of the conjugated molecule, the SpaP pore was estimated to a diameter size of approximately 15 Å. In line with this, previous cryo-EM studies using a trapped translocation substrate suggested a similar pore size (Radics et al., 2013). This was the first time that the function of protein translocation through the inner membrane was associated with any specific T3SS component.

Although the SpaP pentamer is very unstable and refused to be stably purified on its own, it was shown by BN PAGE using an EPEA-tagged version of SpaP that a homo-SpaP subcomplex exists to some extent. *In vivo* photocrosslinking detection of SpaP pentamers independently of all other components, as described and discussed above, strengthened this statement. Moreover, based on the results of the EM analysis it was speculated that SpaR gets somehow dissociated from the SpaPR complex. Unfortunately the resolution of the pictures derived from the EM analysis was too low for further analysis. To follow up on this hypothesis will be one aspect of future experiments. A promising approach could be a combined experiment of *in vivo* photocrosslinking, complex purification and electron microscopy. The tested hypothesis in this case would be that purification of a SpaPR complex with prior crosslinking of SpaP to SpaR or *vice versa* would shift the population analyzed by EM towards donut shaped complexes with the additional density on one side.

Additionally, the same approach could be repeated with the identified crosslinks of SpaP or SpaR to SpaQ or SpaP to SpaS. Furthermore, sufficient amounts of SpaPR complex were purified to continue with further and deeper structural elucidation by crystallization and cryo-EM studies. This upcoming work will shed light onto many open questions concerning the structure and function of the SpaPR complex and hopefully the entire export apparatus.

Part II: Flagella Export Apparatus

The results reported in publication 1 were the first ever to link any of the minor export apparatus proteins to a specific functional aspect. The high degree of conservation between injectisome and fT3SS associated export apparatus implies the same or at least similar function for the equivalent protein of the respective other system. Nevertheless, it has to be investigated whether there are structural and organizational differences between the two systems. A major blind spot in this context was the protein FliO. As mentioned above this protein is only present in fT3SS and its encoding gene is organized in an operon together with *fliPQR*. FliO was reported and identified as a bitopic membrane protein and is therefore a structural component of the export apparatus. Furthermore, it has been shown that FliO is not *per se* essential for export apparatus and thus for flagella functionality (Barker et al., 2010, 2014). Concurrent point mutations of FliP restored motility of a Δ*fliO* strain and therefore suggested a direct link between the two proteins (Barker et al., 2010, 2014).

The outstanding role of SpaP as the pore forming unit and the nucleation point of injectisome T3SSs assembly was extensively discussed in the first part of this thesis. Focusing on the flagella system, these results raised the question whether similar findings could be observed for FliP. Additionally, the effect of FliO on export apparatus assembly and FliP functionality was assessed in order to shed light onto the question why this component is missing in the injectisome system. In this second part two studies will shed light into these specific questions. Furthermore, the goal was to

analyze the flagella FliP in more detail and gain insights into similarities or differences between the export apparatus of flagella associated T3SS and the injectisome export apparatus.

In publication 2 "**A flagellum-specific chaperone facilitates assembly of the core type III export apparatus of the bacterial flagellum**" it was shown that FliO is more abundant in organisms harboring a flagella system than previously estimated, showing that this protein is more widespread and consequently more important for the system than previously thought. With the quickly increasing amount of data derived from whole genome sequencing, the risk of misannotations of genes and proteins rose simultaneously. A study comparing different annotations of several enzyme superfamily proteins from different protein sequence databases revealed for 10 out of 37 examined families misannotations of above 80% for various databases (Schnoes et al., 2009). Similarly, the results of the FliO analysis showed that this protein was wrongly annotated in more than 50% of all genomes encoding a flagella system. Furthermore, *de novo* predictions of FliO, FliP, FliQ and FliR found some interesting new insights. There were 48 species which were found to express a FliO homolog but no flagellin protein, thus indicating that there might exist FliO homologs which are associated to an injectisome system. From an evolutionary point of view this might indicate an intermediate stage during the transition from flagella evolving to the injectisome system.

With these new findings on the importance of FliO, the influence and function on FliP was further examined. The fact that overexpression of FliP restored a Δ*fliO* phenotype partially suggested that FliO might have a stabilizing effect on FliP. Indeed, it was found that FliO prevents FliP degradation and this effect seemed to be exclusively targeting FliP. This was the first time that such a direct effect of a protein on a T3SS component was described. Furthermore, it was shown that the Lon pathway is responsible for FliO directed FliP degradation. This result was highly unexpected, due to the fact that Lon is a protease that targets cytoplasmic proteins. However, there have

been previous reports that LonB of *B. subtilis* is membrane localized and furthermore it has been shown that the Lon homolog in Yeast degrades mitochondrial membrane proteins (Rep et al., 1996; Simmons et al., 2008). Until now only the ATP-dependent protease ClpXP was reported to be associated with the regulation of flagella synthesis (Tomoyasu et al., 2002). Interestingly, for the Lon protease it was shown that this protease is responsible for down regulation of *Salmonella* SPI-1 genes after invasion of host cells via down regulation of *hilA* (Boddicker and Jones, 2004; Takaya et al., 2002).

Recently single molecule super-resolution microscopy was extensively used to determine exact localization and stoichiometries of several T3SS components or to gain insights into assembly pathways (Diepold et al., 2015, 2017; Zhang et al., 2017). In this work the method helped to reveal that FliO behaves like a freely diffusing protein in the inner membrane and thus is no structural part of the fully assembled basal body. This result underlines the stabilizing function of FliO on FliP, which might only be needed for nucleation of export apparatus assembly and subsequently gets dissociated when this assembly proceeds. Additionally, this indicates that the structure of the fully assembled export apparatus of flagella and injectisome systems might be highly alike. FliO was the major unknown factor, which raised questions on the similarity of export apparatus organization of both structures due to its absence in the injectisome.

Due to these results, the assembly of export apparatus subcomplexes was investigated. It was shown that FliP and FliR form a stable subcomplex whose formation is dependent on FliO. Interestingly, FliO was not directly associated to this subcomplex indicating that the interaction of FliR with FliP is sufficient to stabilize the complex and FliO can dissociate from FliP. The interaction of FliP with FliR and the formation of this subcomplex on which subsequently all other export apparatus components assemble were in line with the results reported in publication 1. Here, FliO was identified as a FliP-specific chaperone which stabilized FliP and prevented its Lon dependent degradation until it associates with FliR. The reason why FliO is not present

in the injectisome system and why SpaP does not get degraded to the same extend as FliP is still puzzling.

The results of this study were backed and expanded in publication 3 "**Assembly and stoichiometry of the core structure of the bacterial flagellar type III export gate complex**". Extensive structural work on FliP provided deepened insights into this export apparatus core component. In EM analysis of FliP complexes, it was shown that FliP forms a hexamer with a donut like shape. This result was slightly different concerning the determined SpaP stoichiometry, but the donut like shape indicated a similar function for both proteins. Purification of the FliP periplasmic loop of *T. maritima* revealed a dimerization of FliP, several identified interaction surfaces were verified by *in vivo* photocrosslinking, leading to a proposed trimer of dimers formation of FliP to obtain the observed hexamers. Although these results were conclusive, the fact that the hypothesis of a trimer of dimers is based on a crystal structure obtained from only a small domain of FliP has to be kept in mind. For example, when a 169 amino acid stretch of the over 350 amino acid long C-terminus of the *Salmonella* injectisome component InvA was crystallized, it was found that this fragment was present as noncrystallographic dimers in the crystals and forms a tetramer in crystal packing (Lilic et al., 2010). Nevertheless, structural analysis of the full C-terminal part of the InvA homolog MxiA in *Shigella flexneri* revealed a nonameric organization of this protein (Abrusci et al., 2012). Furthermore, it is noteworthy that a decent amount of FliP complex particles showed a five-fold or even other symmetries. This could be an indication for FliP flexibility in the absence of FliR, which has been already discussed above for SpaP in the injectisome system.

Comparison of the FliP *in vivo* photocrosslinking results reported in this study with the SpaP interaction picture described above gives insights into similarities but also discrepancies between the structural organizations of both homologs. As already mentioned, two positions in FliP corresponding to proven SpaP-SpaP interacting positions were chosen as positive controls for FliP-FliP interactions. Indeed UV

irradiation of these mutants resulted in crosslink bands with the expected size of a FliP-FliP dimer. This indicates that SpaP-SpaP and FliP-FliP interaction sites are at least partially similar. On the other hand it has to be mentioned that for SpaP-SpaP crosslinked positions in most cases a five-fold crosslink ladder was observed, including both positions used as basis for the FliP-FliP interaction positive controls. In contrast to this, for none of the tested positions in FliP a comparable ladder pattern was detectable. This supports the hypothesized trimer of dimer formation for FliP but at the same time shows a general discrepancy in FliP multimer organization compared to SpaP. Despite of their high sequence degree of conservation, the varying reported stoichiometries for SpaP and FliP are puzzling and require further investigations.

Analysis of different export apparatus protein subcomplexes supported the results of both previously discussed studies. After FliP ring formation is stabilized by FliO, FliR gets recruited and both proteins form the core export apparatus subcomplex. Subsequently FliQ, FlhB and FlhA associate to this core complex. In studies on the injectisome system, like in publication 1, these components get easily dissociated during any purification process. In this work and also in publication 1 and 2, the mild detergent DDM was used for protein purification. LMNG has been recently reported to be a promising alternative detergent for purification of integral membrane proteins (Chae et al., 2010). By using LMNG instead of DDM, it was shown that even supposedly loosely associated components like FliQ and FlhA could be purified together with FliP. These results showed that FliQ co-elutes in a complex with FliP and FliR and therefore proves that all minor export apparatus components assemble to one complex. Furthermore, this experiment revealed explicitly the influence of different detergents on protein purification, which was extensively reported and discussed before (Seddon et al., 2004).

Concluding Remarks

In summary, the combined results of this thesis deepened the current knowledge of T3SS export apparatus assembly. The focus on assembly of the flagella, as well as the injectisome, revealed similarities but also one striking difference between both systems. A combined picture of assembly is depicted in figure 9. In detail, it has been shown that one nucleation point of complex assembly has to be SpaP/FliP. This protein oligomerizes and forms a ring complex in the inner membrane through which substrates can be translocated. The multimeric form of this protein is very unstable and gets easily dissociated. Once one SpaR/FliR molecule gets recruited to the SpaP/FliP multimers, this nucleation complex gets stabilized and builds together with the bound SpaR/FliR a solid platform, where all other components can assemble step by step. In the flagella system, the initiation of export apparatus assembly needs an additional factor. Here, the core component FliP is not only unstable in its multimer state, but also it gets degraded in its monomer form via the Lon pathway as long as its specific chaperone FliO is not present. FliO binds directly to the FliP complex and dissociates after recruitment of FliR. The next step of assembly is the recruitment of one SpaQ/FliQ molecule to the SpaPR/FliPR base. The correct assembly of all three minor export apparatus proteins is crucial for correct assembly of the whole system. Next, the one copy of the switch protein SpaS/FlhB associates and subsequently the biggest component InvA/FlhA builds a nonameric ring, encompassing the whole export apparatus. This ring constitutes the connection between export apparatus with the needle base/basal body. Although both major export apparatus components contribute 10 molecules with at least 70 transmembrane helices in total, it seems like these proteins are not as important for complex assembly as the minor export apparatus components.

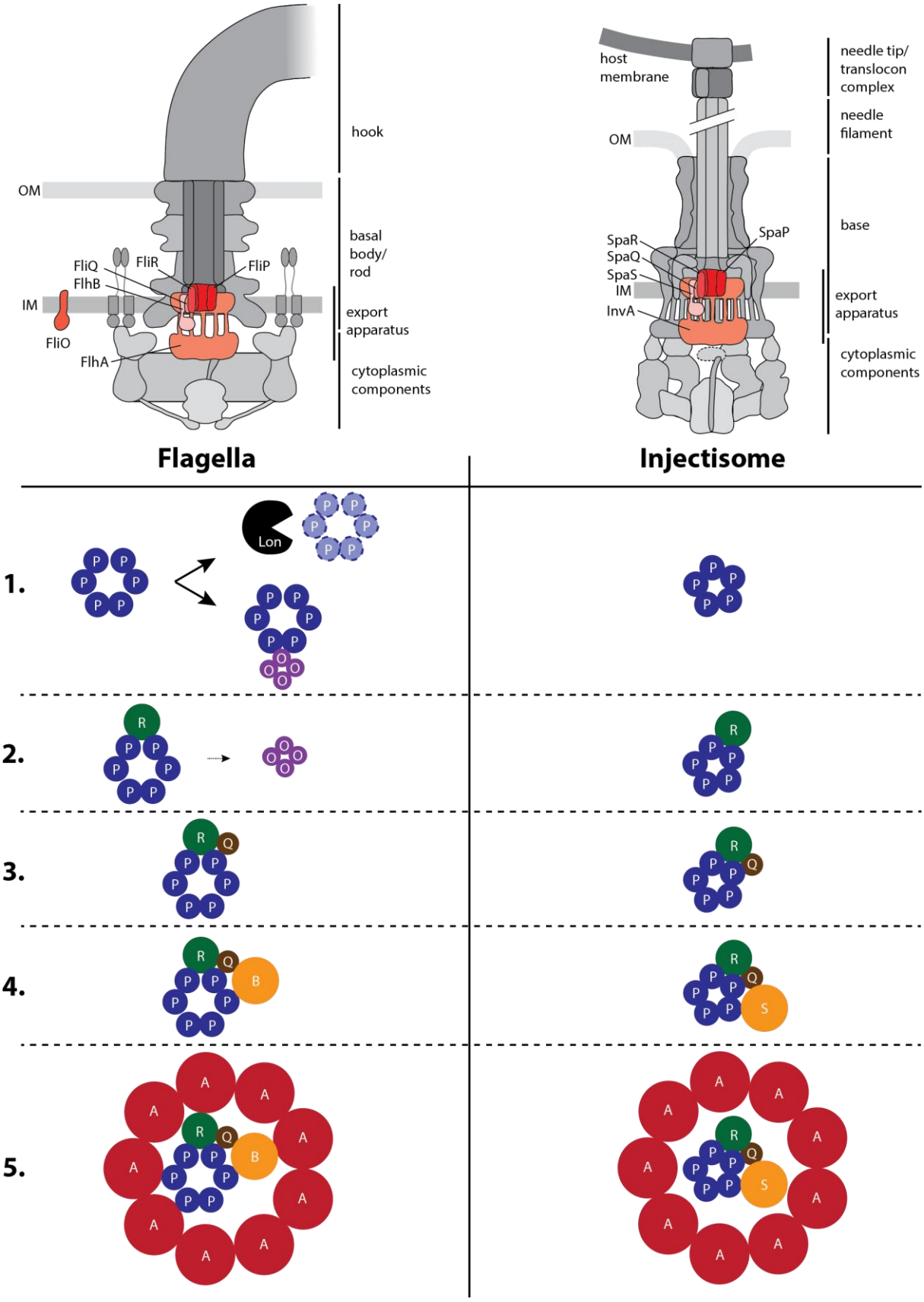
hook
OM
basal body/ rod
FliQ
FlhB
FliR
FliP
IM
export apparatus
FliO
FlhA
cytoplasmic components
host membrane
needle tip/ translocon complex
needle filament
OM
base
SpaR
SpaQ
SpaS
SpaP
IM
export apparatus
InvA
cytoplasmic components
Flagella
Injectisome
1.
Lon
2.
3.
4.
5.

Figure 9: **Graphic summary of all publications and comparison of flagella and injectisome export apparatus assembly.** The multimerization of FliP/SpaP is the nucleation point of export apparatus assembly in both systems. In the flagella system this protein needs the specific chaperone FliO to prevent its degradation via the Lon pathway. FliR/SpaR gets recruited to the FliP/SpaP multimer and a stable FliPR/SpaPR subcomplex is formed. This recruitment leads to the dissociation of FliO in the flagella system. The subsequent assembly of FliQ/SpaQ, FlhB/SpaS and FlhA/InvA occurs in both systems in the same stepwise fashion. Flagella column: P: FliP; O: FliO; R: FliR; Q: FliQ; B: FlhB; A: FlhA; Lon: Lon protease. Injectisome column: P: SpaP; R: SpaR; Q: SpaQ; S: SpaS; A: InvA.

This work will not only help to complete the assembly pathway of flagella and injectisome systems, moreover it may generally facilitate upcoming studies on membrane complex assemblies. Due to the enormous difficulties in analyzing large heteromeric membrane complexes and their assembly *in vivo*, this topic is strongly underrepresented in the current literature. The method of *in vivo* photocrosslinking and especially a combined approach with 2D BN PAGE might help to analyze various membrane protein complexes and their intermediates. The strength of investigating even faint protein-protein interactions in complexes without any necessary purification step can be a huge improvement in the field.

Besides this, the characterization of the specific function for FliO and FliP/SpaP in this work could be the basis for further anti-T3SS drug development studies. Both proteins, with their crucial role for flagella as well as injectisome function are promising targets for new potential anti-infectives. Until now, T3SS inhibitor development focused mainly on the transcriptional activators or the ATPase as targets (Duncan et al., 2012). With the identification of SpaP as pore forming unit, this structure might especially become more and more important for targeted screens. For various applications and diseases, specific pore blocking molecules have been successfully developed and used (Bezrukov and Nestorovich, 2016; Linsdell, 2014). With the emerging problem of antibiotic resistant bacteria, the result of this work could help to find effective alternatives to treat pathogenic bacteria.

Acknowledgements

Früh wurde mir gesagt, dass dies mit der wichtigste und auch meist gelesene Teil meiner Doktorarbeit werden würde. Deshalb an dieser Stelle vielen Dank, an alle die mich während der letzten Jahre so großartig unterstützt haben.

Zunächst möchte ich mich bei Samuel Wagner bedanken. Samuel, du warst stets ein hervorragender Motivator und hattest immer ein offenes Ohr. Vielen Dank, dass ich bei dir so lange Arbeiten und Lernen durfte. Ich werde aus dieser Zeit sehr viel mitnehmen.

In diesem Sinne auch vielen Dank an die ganze AG Wagner, inklusive aller ehemaligen Mitglieder. Sowohl im Labor als auch außerhalb habt ihr mit dafür gesorgt, dass ich die letzten Jahre so genossen habe. Den Postdocs Iwan und Mehari, ihr habt es echt drauf! Danke dass ihr euer Wissen mit allen teilt und ihr jedem so weiterhelft. Dr. Julia und Claudia, auch wenn ihr das hier vielleicht nicht lesen könnt, vielen Dank dass ihr in unsere AG gekommen seid. Es war großartig, euch kennengelernt zu haben. Danke Mexiko! Danke an die ganze Kaffeerunde, dieses tägliche Ritual war häufig Gold wert. Danke an alle Studenten, die in den letzten Jahren bei uns zu Gast waren. Thomas, Michaela und Jialin, danke für die lustigen Tage/Wochen/Monate. Andriko, Simon und Mounir, danke dass ihr mich so bei meinem Projekt mit eurer Arbeit unterstützt habt. Und jetzt zu den wohl wichtigsten Menschen im Labor, Andrea und Melanie, vielen Dank für alles was ihr macht. Ihr haltet den Laden am Laufen! Vor allem Andrea, du hast mir so unglaublich viel geholfen und dafür kann ich dir nicht genug danken.

Dem ganzen Institut der medizinischen Mikrobiologie möchte ich für die schöne Zeit danken. Ich habe es wirklich genossen und es waren immerhin fast 8 Jahre mit euch.

Chris, Marc, Jenni und Felix vielen Dank für eure Freundschaft. Ihr seid einfach ein großartiger Haufen! Amore!

Peter und Wolfi, danke an die beste WG die man sich wünschen kann.

Zum Schluss, tausend Dank an meine Familie. Ihr habt mich immer unterstützt und wart ein fantastischer Rückhalt.

References

Abby, S.S., and Rocha, E.P.C. (2012). The non-flagellar type III secretion system evolved from the bacterial flagellum and diversified into host-cell adapted systems. PLoS Genet. *8*.

Abby, S.S., Cury, J., Guglielmini, J., Néron, B., Touchon, M., and Rocha, E.P.C. (2016). Identification of protein secretion systems in bacterial genomes. Sci. Rep. *6*, 23080.

Abrusci, P., Vergara-Irigaray, M., Johnson, S., Beeby, M.D., Hendrixson, D.R., Roversi, P., Friede, M.E., Deane, J.E., Jensen, G.J., Tang, C.M., et al. (2012). Architecture of the major component of the type III secretion system export apparatus. Nat. Struct. Mol. Biol. *20*, 99–104.

Ahnert, S.E., Marsh, J.A., Hernández, H., Robinson, C. V, and Teichmann, S.A. (2015). Principles of assembly reveal a periodic table of protein complexes. Science (80-.). *350*.

Aizawa, S.I. (2001). Bacterial flagella and type III secretion systems. FEMS Microbiol. Lett. *202*, 157–164.

Akeda, Y., and Galán, J.E. (2005). Chaperone release and unfolding of substrates in type III secretion. Nature *437*, 911–915.

Altier, C. (2005). Genetic and environmental control of salmonella invasion. J Microbiol *43 Spec No*, 85–92.

Bajaj, V., Hwang, C., and Lee, C.A. (1995). *hilA* is a novel *ompR*/*toxR* family member that activates the expression of *Salmonella typhimurium* invasion genes. Mol. Microbiol. *18*, 715–727.

Barker, C.S., Meshcheryakova, I. V., Kostyukova, A.S., and Samatey, F.A. (2010). FliO regulation of FliP in the formation of the Salmonella enterica flagellum. PLoS Genet. *6*.

Barker, C.S., Meshcheryakova, I. V., Inoue, T., and Samatey, F.A. (2014). Assembling

flagella in Salmonella mutant strains producing a type III export apparatus without FliO. J. Bacteriol. *196*, 4001–4011.

Berger, C., Robin, G.P., Bonas, U., and Koebnik, R. (2010). Membrane topology of conserved components of the type III secretion system from the plant pathogen Xanthomonas campestris pv. vesicatoria. Microbiology *156*, 1963–1974.

Beuzon, C.R., Meresse, S., Unsworth, K.E., Ruiz-Albert, J., Garvis, S., Waterman, S.R., Ryder, T. a, Boucrot, E., and Holden, D.W. (2000). Salmonella maintains the integrity of its intracellular vacuole through the action of SifA. Embo J. *19*, 3235–3249.

Bezrukov, S.M., and Nestorovich, E.M. (2016). Inhibiting bacterial toxins by channel blockage. Pathog. Dis. *74*, 1–12.

Blocker, A., Gounon, P., Larquet, E., Niebuhr, K., Cabiaux, V., Parsot, C., and Sansonetti, P. (1999). The Tripartite Type III Secreton of Shigella flexneri Inserts IpaB and IpaC into Host Membranes. J. Cell Biol. *147*, 683–693.

Boddicker, J.D., and Jones, B.D. (2004). Lon Protease Activity Causes Down-Regulation of Salmonella Pathogenicity Island 1 Invasion Gene Expression after Infection of Epithelial Cells. Infect. Immun. *72*, 2002–2013.

Buddelmeijer, N., and Beckwith, J. (2004). A complex of the Escherichia coli cell division proteins FtsL, FtsB and FtsQ forms independently of its localization to the septal region. Mol. Microbiol. *52*, 1315–1327.

Burkinshaw, B.J., Deng, W., Lameignère, E., Wasney, G.A., Zhu, H., Worrall, L.J., Finlay, B.B., and Strynadka, N.C.J. (2015). Structural analysis of a specialized type III secretion system peptidoglycan-cleaving enzyme. J. Biol. Chem. *290*, 10406–10417.

Bustamante, V.H., Martínez, L.C., Santana, F.J., Knodler, L.A., Steele-Mortimer, O., and Puente, J.L. (2008). HilD-mediated transcriptional cross-talk between SPI-1 and SPI-2. Proc. Natl. Acad. Sci. U. S. A. *105*, 14591–14596.

Büttner, D., Lorenz, C., Weber, E., and Bonas, U. (2006). Targeting of two effector

protein classes to the type III secretion system by a HpaC- and HpaB-dependent protein complex from Xanthomonas campestris pv. vesicatoria. Mol. Microbiol. *59*, 513–527.

Bzymek, K.P., Hamaoka, B.Y., and Ghosh, P. (2012). Two translation products of Yersinia yscQ assemble to form a complex essential to type III secretion. Biochemistry *51*, 1669–1677.

Cao, S.Y., Liu, W. Bin, Tan, Y.F., Yang, H.Y., Zhang, T.T., Wang, T., Wang, X.Y., Song, Y.J., Yang, R.F., and Du, Z.M. (2017). An interaction between the inner rod protein YscI and the needle protein YscF is required to assemble the needle structure of the Yersinia type three secretion system. J. Biol. Chem. *292*, 5488–5498.

Chae, P.S., Rasmussen, S.G.F., Rana, R., Gotfryd, K., Chandra, R., Goren, M.A., Kruse, A.C., Nurva, S., Loland, C.J., Pierre, Y., et al. (2010). Maltose-neopentyl glycol (MNG) amphiphiles for solubilization, stabilization and crystallization of membrane proteins. Nat. Methods *7*, 1003–1008.

Chin, J.W., and Schultz, P.G. (2002). In vivo photocrosslinking with unnatural amino Acid mutagenesis. Chembiochem *3*, 1135–1137.

Cirillo, D.M., Valdivia, R.H., Monack, D.M., and Falkow, S. (1998). Macrophage-dependent induction of the Salmonella pathogenicity island 2 type III secretion system and its role in intracellular survival. Mol. Microbiol. *30*, 175–188.

Collazo, C.M., and Galán, J.E. (1997). The invasion-associated type III system of Salmonella typhimurium directs the translocation of Sip proteins into the host cell. Mol. Microbiol. *24*, 747–756.

Costa, T.R.D., Felisberto-Rodrigues, C., Meir, A., Prevost, M.S., Redzej, A., Trokter, M., and Waksman, G. (2015). Secretion systems in Gram-negative bacteria: structural and mechanistic insights. Nat. Rev. Microbiol. *13*, 343–359.

Crago, A., and Koronakis, V. (1998). Salmonella InvG forms a ring-like multimer that

requires the InvH lipoprotein for outer membrane localization. Mol. Microbiol. *30*, 47–56.

Daefler, S., and Russel, M. (1998). The Salmonella typhimurium InvH protein is an outer membrane lipoprotein required for the proper localization of InvG. Mol. Microbiol. *28*, 1367–1380.

Dajkovic, A., Hinde, E., MacKichan, C., and Carballido-Lopez, R. (2016). Dynamic organization of SecA and SecY secretion complexes in the B. subtilis membrane. PLoS One *11*, 1–17.

Dalbey, R.E., Wang, P., and Kuhn, A. (2011). Assembly of Bacterial Inner Membrane Proteins. Annu. Rev. Biochem. *80*, 161–187.

Deiwick, J., Nikolaus, T., Erdogan, S., and Hensel, M. (1999). Environmental regulation of Salmonella pathogenicity island 2 gene expression. Mol. Mcrobiology *31*, 1759–1773.

Deiwick, J., Salcedo, S.P., Boucrot, E., Gilliland, S.M., Henry, T., Petermann, N., Waterman, S.R., Gorvel, J.P., Holden, D.W., and Méresse, S. (2006). The translocated Salmonella effector proteins SseF and SseG interact and are required to establish an intracellular replication niche. Infect. Immun. *74*, 6965–6972.

Deng, W., Marshall, N.C., Rowland, J.L., McCoy, J.M., Worrall, L.J., Santos, A.S., Strynadka, N.C.J., and Finlay, B.B. (2017). Assembly, structure, function and regulation of type III secretion systems. Nat. Rev. Microbiol.

Diepold, A., and Wagner, S. (2014). Assembly of the bacterial type III secretion machinery. FEMS Microbiol. Rev. *49*.

Diepold, A., and Wiesand, U. (2012). Assembly of the Yersinia injectisome: the missing pieces. Mol. Microbiol. *85*, 878–892.

Diepold, A., Amstutz, M., Abel, S., and Sorg, I. (2010). Deciphering the assembly of the Yersinia type III secretion injectisome. EMBO J. *29*, 1928–1940.

Diepold, A., Wiesand, U., and Cornelis, G. (2011). The assembly of the export apparatus (YscR, S, T, U, V) of the Yersinia type III secretion apparatus occurs independently of other structural components and. Mol. Microbiol. *82*, 502–514.

Diepold, A., Kudryashev, M., Delalez, N.J., Berry, R.M., and Armitage, J.P. (2015). Composition, Formation, and Regulation of the Cytosolic C-ring, a Dynamic Component of the Type III Secretion Injectisome. PLoS Biol. *13*, 1–21.

Diepold, A., Sezgin, E., Huseyin, M., Mortimer, T., Eggeling, C., and Armitage, J.P. (2017). A dynamic and adaptive network of cytosolic interactions governs protein export by the T3SS injectisome. Nat. Commun. *8*, 15940.

Dowhan, W., and Bogdanov, M. (2009). Lipid-Dependent Membrane Protein Topogenesis. Annu. Rev. Biochem. *78*, 515–540.

Duncan, M.C., Linington, R.G., and Auerbuch, V. (2012). Chemical inhibitors of the type three secretion system: Disarming bacterial pathogens. Antimicrob. Agents Chemother. *56*, 5433–5441.

Edqvist, P.J., Olsson, J., Lavander, M., Sundberg, L., Forsberg, Å., Wolf-Watz, H., and Lloyd, S.A. (2003). YscP and YscU regulate substrate specificity of the Yersinia type III secretion system. J. Bacteriol. *185*, 2259–2266.

Ellermeier, C.D., Ellermeier, J.R., and Slauch, J.M. (2005). HilD, HilC and RtsA constitute a feed forward loop that controls expression of the SPI1 type three secretion system regulator hilA in Salmonella enterica serovar Typhimurium. Mol. Microbiol. *57*, 691–705.

Ellis, R.J. (2013). Assembly chaperones: a perspective. Philos. Trans. R. Soc. Lond. B. Biol. Sci. *368*, 20110398.

Erhardt, M., and Dersch, P. (2015). Regulatory principles governing Salmonella and Yersinia virulence. Front. Microbiol. *6*, 1–20.

Farrell, I., Toroney, R., Hazen, J., Mehl, R., and Chin, J. (2005). Photo-cross-linking

interacting proteins with a genetically encoded benzophenone. Nat. Methods *2*, 377–384.

Feria, J.M., García-Gómez, E., Espinosa, N., Minamino, T., Namba, K., and González-Pedrajo, B. (2012). Role of escp (Orf16) in Injectisome Biogenesis and Regulation of Type III Protein Secretion in Enteropathogenic Escherichia coli. J. Bacteriol. *194*, 6029–6045.

Ferris, H.U., Furukawa, Y., Minamino, T., Kroetz, M.B., Kihara, M., Namba, K., and Macnab, R.M. (2005). FlhB regulates ordered export of flagellar components via autocleavage mechanism. J. Biol. Chem. *280*, 41236–41242.

Figueira, R., and Holden, D.W. (2012). Functions of the Salmonella pathogenicity island 2 (SPI-2) type III secretion system effectors. Microbiology *158*, 1147–1161.

Formosa, L.E., Dibley, M.G., Stroud, D.A., and Ryan, M.T. (2017). Building a complex complex: Assembly of mitochondrial respiratory chain complex I. Semin. Cell Dev. Biol.

Fu, Y., and Galán, J.E. (1999). A *Salmonella* protein antagonizes Rac-1 and Cdc42 to mediate host-cell recovery after bacterial invasion. Nature *401*, 293–297.

Fukumura, T., Furukawa, Y., Kawaguchi, T., Saijo-Hamano, Y., Namba, K., Imada, K., and Minamino, T. (2014). Crystallization and preliminary X-ray analysis of the periplasmic domain of FliP, an integral membrane component of the bacterial flagellar type III protein-export apparatus. Acta Crystallogr. Sect. Struct. Biol. Commun. *70*, 1215–1218.

Galán, J., and Collmer, A. (1999). Type III secretion machines: bacterial devices for protein delivery into host cells. Science (80-.). *1322*.

Galán, J., and Wolf-Watz, H. (2006). Protein delivery into eukaryotic cells by type III secretion machines. Nature *444*, 567–573.

Galán, J.E., Lara-Tejero, M., Marlovits, T.C., and Wagner, S. (2014). Bacterial Type III

Secretion Systems: Specialized Nanomachines for Protein Delivery into Target Cells. Annu. Rev. Microbiol. *68*, 415–438.

Golubeva, Y.A., Sadik, A.Y., Ellermeier, J.R., and Slauch, J.M. (2012). Integrating Global Regulatory Input Into the Salmonella Pathogenicity Island 1 Type III Secretion System. Genetics *190*, 79–90.

Green, E.R., and Mecsas, J. (2016). Bacterial Secretion Systems – An overview. Microbiol. Spectr. *4*, 1–32.

Gresock, M.G., and Postle, K. (2017). Going outside the TonB box: Identification of novel FepA-TonB interactions in vivo. J. Bacteriol. *199*, 1–16.

Hansen-Wester, I., and Hensel, M. (2001). Salmonella pathogenicity islands encoding type III secretion systems. Microbes Infect.

Haraga, A., Ohlson, M., and Miller, S. (2008). Salmonellae interplay with host cells. Nat. Rev. Microbiol. *6*, 53–66.

Hayward, R.D., and Koronakis, V. (1999). Direct nucleation and bundling of actin by the SipC protein of invasive Salmonella. EMBO J. *18*, 4926–4934.

Hensel, M., Shea, J.E., Waterman, S.R., Mundy, R., Nikolaus, T., Banks, G., Vazquez-Torres, A., Gleeson, C., Fang, F.C., and Holden, D.W. (1998). Genes encoding putative effector proteins of the type III secretion system of *Salmonella* pathogenicity island 2 are required for bacterial virulence and proliferation in macrophages. Mol. Microbiol. *30*, 163–174.

Hu, B., Morado, D.R., Margolin, W., Rohde, J.R., Arizmendi, O., Picking, W.L., Picking, W.D., and Liu, J. (2015). Visualization of the type III secretion sorting platform of Shigella flexneri. Proc. Natl. Acad. Sci. U. S. A. *112*, 1047–1052.

Hu, B., Lara-tejero, M., Kong, Q., Gala, J.E., and Liu, J. (2017). In Situ Molecular Architecture of the Salmonella Type III Secretion Machine. Cell 1065–1074.

Humphreys, D., Davidson, A., Hume, P.J., and Koronakis, V. (2012). Salmonella virulence effector SopE and host GEF ARNO cooperate to recruit and activate WAVE to trigger bacterial invasion. Cell Host Microbe *11*, 129–139.

Ibuki, T., Imada, K., Minamino, T., Kato, T., Miyata, T., and Namba, K. (2011). Common architecture of the flagellar type III protein export apparatus and F- and V-type ATPases. Nat. Struct. Mol. Biol. *18*, 277–282.

Jolly, C., Winfree, S., Hansen, B., and Steele-Mortimer, O. (2014). The Annexin A2/p11 complex is required for efficient invasion of *Salmonella* Typhimurium in epithelial cells. Cell. Microbiol. *16*, 64–77.

Jones, B.D., Ghori, N., and Falkow, S. (1994). Salmonella typhimurium initiates murine infection by penetrating and destroying the specialized epithelial M cells of the Peyer's patches. J. Exp. Med. *180*, 15–23.

Kennedy, K.A., Gachelet, E.G., and Traxler, B. (2004). Evidence for multiple pathways in the assembly of the Escherichia coli maltose transport complex. J. Biol. Chem. *279*, 33290–33297.

Khanra, N., Rossi, P., Economou, A., and Kalodimos, C.G. (2016). Recognition and targeting mechanisms by chaperones in flagellum assembly and operation. Proc. Natl. Acad. Sci. 201607845.

Kim, J.S., Jang, J.I., Eom, J.S., Oh, C.H., Kim, H.G., Kim, B.H., Bang, I.S., Bang, S.H., and Park, Y.K. (2013). Molecular characterization of the InvE regulator in the secretion of type III secretion translocases in Salmonella enterica serovar Typhimurium. Microbiol. (United Kingdom) *159*, 446–461.

Kimbrough, T.G., and Miller, S.I. (2000). Contribution of Salmonella typhimurium type III secretion components to needle complex formation. Proc. Natl. Acad. Sci. U. S. A. *97*, 11008–11013.

Kinoshita, M., Hara, N., and Imada, K. (2013). Interactions of bacterial flagellar

chaperone–substrate complexes with FlhA contribute to co-ordinating assembly of the flagellar filament. Mol. Microbiol. *90*, 1249–1261.

Korotkov, K. V., Gonen, T., and Hol, W.G.J. (2011). Secretins: Dynamic channels for protein transport across membranes. Trends Biochem. Sci. *36*, 433–443.

Kosarewicz, A. (2012). The blueprint of the type-3 injectisome. Philos. Trans. R. Soc. B 1140–1154.

Krampen, L. (2017). Discrimination between membrane protein targeting pathways in Salmonella Typhimurium.

Kubori, T., and Galán, J.E. (2002). Salmonella type III secretion-associated protein InvE controls translocation of effector proteins into host cells. J. Bacteriol. *184*, 4699–4708.

Kubori, T., Matsushima, Y., and Nakamura, D. (1998). Supramolecular structure of the Salmonella typhimurium type III protein secretion system. Science (80-.). *602*.

Kulajta, C., Thumfart, J.O., Haid, S., Daldal, F., and Koch, H.-G. (2006). Multi-step Assembly Pathway of the cbb3-type Cytochrome c Oxidase Complex. J. Mol. Biol. *355*, 989–1004.

Kumar, M., Mommer, M.S., and Sourjik, V. (2010). Mobility of cytoplasmic, membrane, and DNA-binding proteins in Escherichia coli. Biophys. J. *98*, 552–559.

Lara-Tejero, M., and Galán, J.E. (2009). Salmonella enterica serovar Typhimurium pathogenicity island 1-encoded type III secretion system translocases mediate intimate attachment to nonphagocytic cells. Infect. Immun. *77*, 2635–2642.

Lara-Tejero, M., Kato, J., Wagner, S., Liu, X., and Galán, J. (2011). A sorting platform determines the order of protein secretion in bacterial type III systems. Science (80-.). *1188*.

LaRock, D.L., Chaudhary, A., and Miller, S.I. (2015). Salmonellae interactions with host processes. Nat. Rev. Microbiol. *13*, 191–205.

Lasica, A.M., Ksiazek, M., Madej, M., and Potempa, J. (2017). The Type IX Secretion System (T9SS): Highlights and Recent Insights into Its Structure and Function. Front. Cell. Infect. Microbiol. *7*.

Lefebre, M., and Galán, J. (2014). The inner rod protein controls substrate switching and needle length in a Salmonella type III secretion system. Proc. Natl. Acad. Sci. *2013*, 1–6.

Levitt, M., and Chothia, C. (1976). Structural patterns in globular proteins. Nature *261*, 552–558.

Lilic, M., Quezada, C.M., and Stebbins, C.E. (2010). A conserved domain in type III secretion links the cytoplasmic domain of InvA to elements of the basal body. Acta Crystallogr. Sect. D Biol. Crystallogr. *66*, 709–713.

Linsdell, P. (2014). Cystic fibrosis transmembrane conductance regulator chloride channel blockers: Pharmacological, biophysical and physiological relevance. World J. Biol. Chem. *5*, 26–39.

Liu, R., and Ochman, H. (2007). Stepwise formation of the bacterial flagellar system. Proc. Natl. Acad. Sci. *104*, 7116–7121.

Loquet, A., Sgourakis, N.G., Gupta, R., Giller, K., Riedel, D., Goosmann, C., Griesinger, C., Kolbe, M., Baker, D., Becker, S., et al. (2012). Atomic model of the type III secretion system needle. Nature *486*, 276–279.

MacKenzie, K.R., Prestegard, J.H., and Engelman, D.M. (1997). A Transmembrane Helix Dimer: Structure and Implications. Science (80-.). *276*, 131 LP-133.

Macnab, R.M. (2003). How bacteria assemble flagella. Annu. Rev. Microbiol. *57*, 77–100.

Macnab, R.M. (2004). Type III flagellar protein export and flagellar assembly. Biochim. Biophys. Acta - Mol. Cell Res. *1694*, 207–217.

Magdalena, J., Hachani, A., Chamekh, M., Jouihri, N., Gounon, P., Blocker, A., and Allaoui, A. (2002). Spa32 regulates a switch in substrate specificity of the type III secreton of Shigella flexneri from needle components to Ipa proteins. J. Bacteriol. *184*, 3433–3441.

Marlovits, T., Kubori, T., and Sukhan, A. (2004). Structural insights into the assembly of the type III secretion needle complex. Science (80-.). *1040*.

Marlovits, T., Kubori, T., and Lara-Tejero, M. (2006). Assembly of the inner rod determines needle length in the type III secretion injectisome. Nature *441*, 637–640.

Marsh, J.A., and Teichmann, S.A. (2015). Structure, Dynamics, Assembly, and Evolution of Protein Complexes. Annu. Rev. Biochem. *84*, 551–575.

Mastroeni, P., and Grant, A.J. (2011). Spread of Salmonella enterica in the body during systemic infection: unravelling host and pathogen determinants. Expert Rev. Mol. Med. *13*, e12.

Mazurkiewicz, P., Thomas, J., Thompson, J.A., Liu, M., Arbibe, L., Sansonetti, P., and Holden, D.W. (2008). SpvC is a Salmonella effector with phosphothreonine lyase activity on host mitogen-activated protein kinases. Mol. Microbiol. *67*, 1371–1383.

McGhie, E.J., Hayward, R.D., and Koronakis, V. (2001). Cooperation between actin-binding proteins of invasive Salmonella: SipA potentiates SipC nucleation and bundling of actin. EMBO J. *20*, 2131–2139.

Méresse, S., Unsworth, K.E., Habermann, A., Griffiths, G., Fang, F., Martínez-Lorenzo, M.J., Waterman, S.R., Gorvel, J.P., and Holden, D.W. (2001). Remodelling of the actin cytoskeleton is essential for replication of intravacuolar Salmonella. Cell. Microbiol. *3*, 567–577.

Miao, E.A., Brittnacher, M., Haraga, A., Jeng, R.L., Welch, M.D., and Miller, S.I. (2003). Salmonella effectors translocated across the vacuolar membrane interact with the actin cytoskeleton. Mol. Microbiol. *48*, 401–415.

Minamino, T., and Macnab, R.M. (1999). Components of the *Salmonella* flagellar export apparatus and classification of export substrates. J. Bacteriol. *181*, 1388–1394.

Minamino, T., Morimoto, Y. V, Hara, N., and Namba, K. (2011). An energy transduction mechanism used in bacterial flagellar type III protein export. Nat. Commun. *2*, 475.

Monjarás Feria, J. V., Lefebre, M.D., Stierhof, Y.-D., Galán, J.E., and Wagner, S. (2015). Role of Autocleavage in the Function of a Type III Secretion Specificity Switch Protein in *Salmonella enterica* Serovar Typhimurium. MBio *6*, e01459-15.

Monlezun, L., Liebl, D., Fenel, D., Grandjean, T., Berry, A., Schoehn, G., Dessein, R., Faudry, E., and Attree, I. (2015). PscI is a type III secretion needle anchoring protein with in vitro polymerization capacities. Mol. Microbiol. *96*, n/a-n/a.

Morimoto, Y. V., Ito, M., Hiraoka, K.D., Che, Y.S., Bai, F., Kami-ike, N., Namba, K., and Minamino, T. (2014). Assembly and stoichiometry of FliF and FlhA in Salmonella flagellar basal body. Mol. Microbiol. *91*, 1214–1226.

Mueller, C.A., Broz, P., and Cornelis, G.R. (2008). The type III secretion system tip complex and translocon. Mol. Microbiol. *68*, 1085–1095.

Murray, C.I., Westhoff, M., Eldstrom, J., Thompson, E., Emes, R., and Fedida, D. (2016). Unnatural amino acid photo-crosslinking of the IKs channel complex demonstrates a KCNE1:KCNQ1 stoichiometry of up to 4:4. Elife *5*, 1–18.

Myeni, S.K., Wang, L., and Zhou, D. (2013). SipB-SipC Complex Is Essential for Translocon Formation. PLoS One *8*, 1–7.

Natan, E., Wells, J.N., Teichmann, S.A., and Marsh, J.A. (2017). Regulation, evolution and consequences of cotranslational protein complex assembly. Curr. Opin. Struct. Biol. *42*, 90–97.

Ng, S.Y.L., Lee, L.T.O., and Chow, B.K.C. (2013). Receptor oligomerization: From early evidence to current understanding in class B GPCRs. Front. Endocrinol. (Lausanne). *3*,

1–11.

Nooren, I.M.A., and Thornton, J.M. (2003). Diversity of protein-protein interactions. EMBO J. *22*, 3486–3492.

Notti, R.Q., Bhattacharya, S., Lilic, M., and Stebbins, C.E. (2015). A common assembly module in injectisome and flagellar type III secretion sorting platforms. Nat. Commun. *6*, 1–11.

Ohlson, M.B., Fluhr, K., Birmingham, C.L., Brumell, H., Miller, S.I., and Brumell, J.H. (2005). SseJ Deacylase Activity by Salmonella enterica Serovar Typhimurium Promotes Virulence in Mice SseJ Deacylase Activity by Salmonella enterica Serovar Typhimurium Promotes Virulence in Mice. Infect. … *73*, 6249–6259.

Ohlson, M.B., Huang, Z., Alto, N.M., Blanc, M.P., Dixon, J.E., Chai, J., and Miller, S.I. (2008). Structure and Function of Salmonella SifA Indicate that Its Interactions with SKIP, SseJ, and RhoA Family GTPases Induce Endosomal Tubulation. Cell Host Microbe *4*, 434–446.

Pallen, M.J., Penn, C.W., and Chaudhuri, R.R. (2005). Bacterial flagellar diversity in the post-genomic era. Trends Microbiol. *13*, 143–149.

Poh, J., Odendall, C., Spanos, A., Boyle, C., Liu, M., Freemont, P., and Holden, D.W. (2008). SteC is a Salmonella kinase required for SPI-2-dependent F-actin remodelling. Cell. Microbiol. *10*, 20–30.

Portaliou, A.G., Tsolis, K.C., Loos, M.S., Zorzini, V., and Economou, A. (2016). Type III Secretion: Building and Operating a Remarkable Nanomachine. Trends Biochem. Sci. *41*, 175–189.

Portillo, F.G., Foster, J.W., and Finlayl, B.B. (1993). Role of Acid Tolerance Response Genes in Salmonella typhimurium Virulence. Infect. Immun. *61*, 4489–4492.

Pradel, N., Ye, C., and Wu, L.F. (2004). A cleavable signal peptide is required for the full function of the polytopic inner membrane protein FliP of Escherichia coli.

Biochem. Biophys. Res. Commun. *319*, 1276–1280.

Pradel, N., Decorps, A., Ye, C., Santini, C.L., and Wu, L.F. (2005). YidC-dependent translocation of green fluorescence protein fused to the FliP cleavable signal peptide. Biochimie *87*, 191–196.

Prouty, A.M., and Gunn, J.S. (2000). Salmonella enterica serovar typhimurium invasion is repressed in the presence of bile. Infect. Immun. *68*, 6763–6769.

Radics, J., Königsmaier, L., and Marlovits, T. (2013). Structure of a pathogenic type 3 secretion system in action. Nat. Struct. Mol. Biol.

Ramsden, A.E., Holden, D.W., and Mota, L.J. (2007). Membrane dynamics and spatial distribution of Salmonella-containing vacuoles. Trends Microbiol. *15*, 516–524.

Rep, M., van Dijl, J.M., Suda, K., Schatz, G., Grivell, L. a, and Suzuki, C.K. (1996). Promotion of mitochondrial membrane complex assembly by a proteolytically inactive yeast Lon. Science *274*, 103–106.

Roehrich, A.D., Bordignon, E., Mode, S., Shen, D.-K., Liu, X., Pain, M., Murillo, I., Martinez-Argudo, I., Sessions, R.B., and Blocker, A.J. (2016). Steps for Shigella Gatekeeper MxiC Function in Hierarchical Type III Secretion Regulation. J. Biol. Chem. jbc.M116.746826.

Ryu, Y., and Schultz, P. (2006). Efficient incorporation of unnatural amino acids into proteins in Escherichia coli. Nat. Methods *3*, 263–265.

Salcedo, S.P., and Holden, D.W. (2003). SseG, a virulence protein that targets Salmonella to the Golgi network. EMBO J. *22*, 5003–5014.

Santos, R.L., Zhang, S., Tsolis, R.M., Kingsley, R.A., Garry Adams, L., and Bäumler, A.J. (2001). Animal models of *Salmonella* infections: enteritis versus typhoid fever. Microbes Infect. *3*, 1335–1344.

Schneider, D., Finger, C., Prodöhl, A., and Volkmer, T. (2007). From interactions of

single transmembrane helices to folding of alpha-helical membrane proteins: analyzing transmembrane helix-helix interactions in bacteria. Curr. Protein Pept. Sci. *8*, 45–61.

Schnoes, A.M., Brown, S.D., Dodevski, I., and Babbitt, P.C. (2009). Annotation error in public databases: Misannotation of molecular function in enzyme superfamilies. PLoS Comput. Biol. *5*.

Schraidt, O., and Marlovits, T. (2011). Three-dimensional model of Salmonella's needle complex at subnanometer resolution. Science (80-.). *1192*.

Schraidt, O., Lefebre, M.D., Brunner, M.J., Schmied, W.H., Schmidt, A., Radics, J., Mechtler, K., Galán, J.E., and Marlovits, T.C. (2010). Topology and organization of the Salmonella typhimurium type III secretion needle complex components. PLoS Pathog. *6*, e1000824.

Seddon, A.M., Curnow, P., and Booth, P.J. (2004). Membrane proteins, lipids and detergents: Not just a soap opera. Biochim. Biophys. Acta - Biomembr. *1666*, 105–117.

Silhavy, T.J., Kahne, D., and Walker, S. (2010). The bacterial cell envelope. Cold Spring Harb. Perspect. Biol. *2*, 1–16.

Simmons, L.A., Grossman, A.D., and Walker, G.C. (2008). Clp and lon proteases occupy distinct subcellular positions in Bacillus subtilis. J. Bacteriol. *190*, 6758–6768.

Stein, M.A., Leung, K.Y., Zwick, M., Garcia-del Portillo, F., and Finlay, B.B. (1996). Identification of a *Salmonella* virulence gene required for formation of filamentous structures containing lysosomal membrane glycoproteins within epithelial cells. Mol. Microbiol. *20*, 151–164.

van Stelten, J., Silva, F., Belin, D., and Silhavy, T.J. (2009). Effects of antibiotics and a proto-oncogene homolog on destruction of protein translocator SecY. Sci. (New York, NY) *325*, 753–756.

Stenberg, F., von Heijne, G., and Daley, D.O. (2007). Assembly of the Cytochrome bo3

Complex. J. Mol. Biol. *371*, 765–773.

Stroud, D.A., Surgenor, E.E., Formosa, L.E., Reljic, B., Frazier, A.E., Dibley, M.G., Osellame, L.D., Stait, T., Beilharz, T.H., Thorburn, D.R., et al. (2016). Accessory subunits are integral for assembly and function of human mitochondrial complex I. Nature *538*, 123–126.

Sukhan, A., Kubori, T., Wilson, J., and Galán, J. (2001). Genetic Analysis of Assembly of theSalmonella enterica Serovar Typhimurium Type III Secretion-Associated Needle Complex. J. Bacteriol. *183*, 1159–1167.

Sun, H., Kamanova, J., Lara-Tejero, M., and Galán, J.E. (2016). A Family of Salmonella Type III Secretion Effector Proteins Selectively Targets the NF-κB Signaling Pathway to Preserve Host Homeostasis. PLoS Pathog. *12*, 1–19.

Tahoun, A., Mahajan, S., Paxton, E., Malterer, G., Donaldson, D.S., Wang, D., Tan, A., Gillespie, T.L., O'Shea, M., Roe, A.J., et al. (2012). Salmonella transforms follicle-associated epithelial cells into M cells to promote intestinal invasion. Cell Host Microbe *12*, 645–656.

Takaya, A., Tomoyasu, T., Tokumitsu, A., Morioka, M., and Yamamoto, T. (2002). The ATP-Dependent Lon Protease of Salmonella enterica Serovar Typhimurium Regulates Invasion and Expression of Genes Carried on Salmonella Pathogenicity Island 1. J. Bacteriol. *184*, 224–232.

Tampakaki, A.P., Fadouloglou, V.E., Gazi, A.D., Panopoulos, N.J., and Kokkinidis, M. (2004). Conserved features of type III secretion. Cell. Microbiol. *6*, 805–816.

Teese, M.G., and Langosch, D. (2015). Role of GxxxG Motifs in Transmembrane Domain Interactions. Biochemistry *54*, 5125–5135.

Tomoyasu, T., Ohkishi, T., Ukyo, Y., Tokumitsu, A., Takaya, A., Suzuki, M., Sekiya, K., Matsui, H., Kutsukake, K., and Yamamoto, T. (2002). The C1pXP ATP-dependent protease regulates flagellum synthesis in Salmonella enterica serovar Typhimurium. J.

Bacteriol. *184*, 645–653.

Van Vranken, J.G., Na, U., Winge, D.R., and Rutter, J. (2015). Protein-mediated assembly of succinate dehydrogenase and its cofactors. Crit. Rev. Biochem. Mol. Biol. *50*, 168–180.

Wagner, C., and Hensel, M. (2011). Adhesive Mechanisms of Salmonella enterica. In Bacterial Adhesion: Chemistry, Biology and Physics, D. Linke, and A. Goldman, eds. (Dordrecht: Springer Netherlands), pp. 17–34.

Wagner, S., Königsmaier, L., Lara-Tejero, M., Lefebre, M., Marlovits, T.C., and Galán, J.E. (2010). Organization and coordinated assembly of the type III secretion export apparatus. Proc. Natl. Acad. Sci. U. S. A. *107*, 17745–17750.

Wang, Y., Ouellette, A.N., Egan, C.W., Rathinavelan, T., Im, W., and De Guzman, R.N. (2007). Differences in the Electrostatic Surfaces of the Type III Secretion Needle Proteins PrgI, BsaL, and MxiH. J. Mol. Biol. *371*, 1304–1314.

Wang, Y., Wang, R., Jin, F., Liu, Y., Yu, J., Fu, X., and Chang, Z. (2016). A supercomplex spanning the inner and outer membranes mediates the biogenesis of ??-barrel outer membrane proteins in bacteria. J. Biol. Chem. *291*, 16720–16729.

Wee, D.H., and Hughes, K.T. (2015). Molecular ruler determines needle length for the Salmonella Spi-1 injectisome. Proc. Natl. Acad. Sci. *2015*, 201423492.

Worley, M.J., Nieman, G.S., Geddes, K., and Heffron, F. (2006). Salmonella typhimurium disseminates within its host by manipulating the motility of infected cells. Proc. Natl. Acad. Sci. U. S. A. *103*, 17915–17920.

Worrall, L.J., Hong, C., Vuckovic, M., Deng, W., Bergeron, J.R.C., Majewski, D.D., Huang, R.K., Spreter, T., Finlay, B.B., Yu, Z., et al. (2016). Near-atomic-resolution cryo-EM analysis of the Salmonella T3S injectisome basal body. Nature.

Zahrl, D., Wagner, M., Bischof, K., Bayer, M., Zavecz, B., Beranek, A., Ruckenstuhl, C., Zarfel, G.E., and Koraimann, G. (2005). Peptidoglycan degradation by specialized lytic

transglycosylases associated with type III and type IV secretion systems. Microbiology *151*, 3455–3467.

Zarivach, R., Vuckovic, M., and Deng, W. (2007). Structural analysis of a prototypical ATPase from the type III secretion system. Nat. Struct. Mol. Biol. *14*, 131–137.

Zarivach, R., Deng, W., Vuckovic, M., Felise, H.B., Nguyen, H. V, Miller, S.I., Finlay, B.B., and Strynadka, N.C.J. (2008). Structural analysis of the essential self-cleaving type III secretion proteins EscU and SpaS. Nature *453*, 124–127.

Zhang, Y., Lara-Tejero, M., Bewersdorf, J., and Galán, J.E. (2017). Visualization and characterization of individual type III protein secretion machines in live bacteria. Proc. Natl. Acad. Sci. U. S. A. *114*, 6098–6103.

Zhao, R., Pathak, N., Jaffe, H., Reese, T.S., and Khan, S. (1996). FliN is a major structural protein of the C-ring in the Salmonella typhimurium flagellar basal body. J. Mol. Biol. *261*, 195–208.

Zhong, D., Lefebre, M., Kaur, K., McDowell, M.A., Gdowski, C., Jo, S., Wang, Y., Benedict, S.H., Lea, S.M., Galan, J.E., et al. (2012). The Salmonella type III secretion system inner rod protein PrgJ is partially folded. J. Biol. Chem. *287*, 25303–25311.

Zhou, D., Mooseker, M.S., and Galán, J.E. (1999). Role of the S. typhimurium Actin-Binding Protein SipA in Bacterial Internalization. Science (80-.). *283*, 2092–2095.

Zilkenat, S., Franz-Wachtel, M., Stierhof, Y.-D., Galán, J.E., Macek, B., and Wagner, S. (2016). Determination of the Stoichiometry of the Complete Bacterial Type III Secretion Needle Complex Using a Combined Quantitative Proteomic Approach. Mol. Cell. Proteomics *15*, 1598–1609.

Zilkenat, S., Grin, I., and Wagner, S. (2017). Stoichiometry determination of macromolecular membrane protein complexes. Biol. Chem. *398*, 155–164.

Publication 1

PLOS | PATHOGENS

RESEARCH ARTICLE

Structural and Functional Characterization of the Bacterial Type III Secretion Export Apparatus

Tobias Dietsche[1☯], Mehari Tesfazgi Mebrhatu[1☯], Matthias J. Brunner[2,3,4], Patrizia Abrusci[5], Jun Yan[6¤], Mirita Franz-Wachtel[7], Charlotta Schärfe[8], Susann Zilkenat[1], Iwan Grin[1], Jorge E. Galán[9], Oliver Kohlbacher[8,10], Susan Lea[5], Boris Macek[7], Thomas C. Marlovits[2,3,4], Carol V. Robinson[6], Samuel Wagner[1,11]*

1 University of Tübingen, Interfaculty Institute of Microbiology and Infection Medicine (IMIT), Section of Cellular and Molecular Microbiology, Tübingen, Germany, **2** Center for Structural Systems Biology (CSSB), University Medical Center Hamburg-Eppendorf (UKE) and German Electron Synchrotron Centre (DESY), Hamburg, Germany, **3** Institute of Molecular Biotechnology (IMBA), Vienna Biocenter (VBC), Vienna, Austria, **4** Research Institute of Molecular Pathology (IMP), Vienna Biocenter (VBC), Vienna, Austria, **5** Sir William Dunn School of Pathology, University of Oxford, Oxford, United Kingdom, **6** Department of Chemistry, University of Oxford, Oxford, United Kingdom, **7** University of Tübingen, Proteome Center Tübingen, Tübingen, Germany, **8** University of Tübingen, Center for BioinformaticsTübingen, Germany, **9** Yale University School of Medicine, Department of Microbial Pathogenesis, New Haven, Connecticut, United States of America, **10** Max Planck Institute for Developmental Biology, Biomolecular Interactions, Tübingen, Germany, **11** German Center for Infection Research (DZIF), Partner-site Tübingen, Tübingen, Germany

☯ These authors contributed equally to this work.
¤ Current address: Novo Nordisk A/S, Novo Nordisk Park, Måløv, Denmark
* samuel.wagner@med.uni-tuebingen.de

OPEN ACCESS

Citation: Dietsche T, Tesfazgi Mebrhatu M, Brunner MJ, Abrusci P, Yan J, Franz-Wachtel M, et al. (2016) Structural and Functional Characterization of the Bacterial Type III Secretion Export Apparatus. PLoS Pathog 12(12): e1006071. doi:10.1371/journal.ppat.1006071

Editor: Brian K Coombes, McMaster University, CANADA

Received: September 14, 2016

Accepted: November 17, 2016

Published: December 15, 2016

Data Availability Statement: The mass spectrometry proteomics data have been deposited to the ProteomeXchange Consortium via the PRIDE partner repository with the dataset identifier PXD005028. All other data are within the paper and its Supporting Information files.

Funding: The size exclusion chromatography-light scattering/UV/refractive index instrumentation was supported by NIH Award Number 1S10RR023748-01 (www.nih.gov). Work in the laboratory of JEG was supported by Grant AI030492 from the National Institute of Allergy and Infectious Diseases

Abstract

Bacterial type III protein secretion systems inject effector proteins into eukaryotic host cells in order to promote survival and colonization of Gram-negative pathogens and symbionts. Secretion across the bacterial cell envelope and injection into host cells is facilitated by a so-called injectisome. Its small hydrophobic export apparatus components SpaP and SpaR were shown to nucleate assembly of the needle complex and to form the central "cup" substructure of a *Salmonella* Typhimurium secretion system. However, the *in vivo* placement of these components in the needle complex and their function during the secretion process remained poorly defined. Here we present evidence that a SpaP pentamer forms a 15 Å wide pore and provide a detailed map of SpaP interactions with the export apparatus components SpaQ, SpaR, and SpaS. We further refine the current view of export apparatus assembly, consolidate transmembrane topology models for SpaP and SpaR, and present intimate interactions of the periplasmic domains of SpaP and SpaR with the inner rod protein PrgJ, indicating how export apparatus and needle filament are connected to create a continuous conduit for substrate translocation.

(www.niaid.nih.gov). Work performed in the laboratory of SW was supported by a postdoctoral fellowship of the Human Frontiers Science Program (www.hfsp.org), by the Alexander von Humboldt Foundation in the framework of the Sofja Kovalevskaja Award endowed by the Federal Ministry of Education and Research (BMBF) (www.avh.de), by the IZKF of the University Hospital Tübingen through the Nachwuchsgruppenprogramm (www.medizin.uni-tuebingen.de), and by the Deutsche Forschungsgemeinschaft (DFG) as part of the Collaborative Research Center (SFB) 766 Bacterial cell envelope, project B14 (www.dfg.de). The funders had no role in study design, data collection and analysis, decision to publish, or preparation of the manuscript.

Competing Interests: JY was at the Department of Chemistry at the University of Oxford when she performed the experiments described in this paper. She is currently employed by NovoNordisk. All other authors have declared that no competing interests exist.

Author Summary

Many Gram-negative bacteria use type III secretion systems to inject bacterial proteins into eukaryotic host cells in order to promote their own survival and colonization. These systems are large molecular machines with the ability to transport proteins across three cell membranes in one step. It is believed that the only gated barrier of these systems lies in the bacterial cytoplasmic membrane but it was unclear so far how this gate looks like and of which components it is composed. Here we present evidence based on in depth biochemical and genetic characterization that an assembly of five SpaP proteins forms this gate in the cytoplasmic membrane of the type III secretion system of *Salmonella* pathogenicity island 1. We further show that one subunit each of the proteins SpaQ, SpaR, and SpaS are closely associated to the SpaP gate and may function in the gating mechanism, and that the protein PrgJ is attached to this gate on the outside to connect it to the hollow needle filament projecting towards the host cell. Our findings elucidate a hitherto ill-defined aspect of type III secretion systems and may help to develop novel antiinfective therapies targeting these virulence-associated molecular devices.

Introduction

Type III secretion systems (T3SSs) are used by many Gram-negative bacterial pathogens and symbionts to translocate effector proteins in one step across the bacterial envelope and into eukaryotic host cells [1] where they modulate host cell physiology to promote bacterial survival and colonization [2]. The core of T3SSs is formed by the so-called injectisome, a macromolecular machine composed of up to 20 different proteins [1]. The base of the injectisome, consisting of an outer membrane secretin ring and two inner membrane ring components, anchors the system to the bacterial cell envelope [3]. A filamentous needle projects away from the base towards the host cell and serves as conduit for translocated effectors [4,5]. Five cytoplasmic proteins select and unfold the substrates, which are then handed over to the actual export apparatus [6,7] housed in a membrane patch at the center of the inner ring [8,9]. The five export apparatus components are thought to facilitate the actual secretion function of T3SSs, including energy coupling, membrane translocation, and substrate specificity switching [1]. Base, needle filament, and export apparatus are together also termed needle complex.

While analyses by X-ray crystallography and cryo electron microscopy have revealed the structure of most soluble components of injectisomes or of the related flagellar system [10,11], the structure and in particular the function of the hydrophobic transmembrane (TM) domains of the export apparatus components remain poorly defined. In the T3SS encoded within the pathogenicity island 1 (SPI-1) of *Salmonella enterica* serovar Typhimurium (*S*. Typhimurium), the export apparatus is composed of the proteins SpaP, SpaQ, SpaR, SpaS, and InvA in a 5:1:1:1:9 stoichiometry [12]. Of these components, InvA and SpaS are structurally and functionally best characterized: the atomic structures of their soluble cytoplasmic domains have been solved [13,14]. The large cytoplasmic domain of InvA (or its homologs) forms a nonameric ring with a central pore of about 50 Å in diameter [15] and has been proposed to play a role in substrate switching and translocation [16,17] while its 8 predicted TM helices have been proposed to serve in utilization of the proton motive force for secretion [18]. SpaS and its homologs play a role in switching of specificity from secretion of early to intermediate and late substrates [19]. Autocleavage of a highly conserved NPTH motif in the cytoplasmic domain of SpaS is required for this function, possibly to facilitate a high conformational flexibility of this domain for secretion of later substrates [20].

The substantially hydrophobic export apparatus components SpaP, SpaQ, and SpaR and their homologs were shown to be critical for assembly of the needle complex [9,21–23] and essential for secretion function [9,24] but their precise role in secretion is still unknown. It was suggested that SpaP and SpaR form the cup substructure of the needle complex [9]. Given the presumed central location of SpaP and SpaR at the center of the membrane patch of the needle complex and their substantial hydrophobicity, we hypothesized that these two proteins may constitute the actual substrate translocation pore of T3SSs in the bacterial inner membrane, a function that as yet has not been assigned to any T3SS component.

In this study, we have biochemically characterized a stable subcomplex formed by SpaP and SpaR, and mapped its place within the needle complex using *in vivo* photocrosslinking and complementary techniques. We show that an isolated complex of five SpaP and one SpaR forms a donut-shaped structure with an approximately 15Å wide recession at its center. Sole expression of the SpaP pentamer in the bacterial membrane allowed the permeation of compounds of 500 Da into the cytoplasm, suggesting that these proteins form a channel large enough for translocation of secondary structures. We further show that a complex of SpaP, SpaQ, SpaR, and SpaS assembles *in vivo* before incorporation into the needle complex base, and that these four export apparatus components form a compact assembly with multiple reciprocal interactions at TM helices three and four of the SpaP pentamer. We also present evidence that SpaP and SpaR interact on their periplasmic side with the inner rod protein PrgJ, which provides a basis to explain how the substrate translocation conduit is continuous from the export apparatus through the inner rod into the needle filament and suggests that the hitherto unaccounted electron density of the socket substructure is made of the periplasmic domains of SpaP and SpaR, together with PrgJ. In summary, we describe physical interactions among export apparatus components of bacterial T3SSs and identify the components that form its substrate translocation pore. This work will facilitate further structural and functional work on these machines and may help to develop novel antiinfective therapies targeting these virulence-associated molecular devices.

Results

SpaP and SpaR form a stable subcomplex of $SpaP_5R_1$ stoichiometry

We previously showed that a stable complex of SpaP and SpaR can be isolated from *S.* Typhimurium lacking the inner ring components PrgH and PrgK [9]. For further characterization, we expressed the *spaPQRS* operon in *Escherichia coli* and purified the SpaPR complex by immunoprecipitation of epitope-tagged SpaR. The isolated complex eluted as a sharp peak from a size exclusion chromatography column at an apparent size of 400 kDa (Fig 1A). Separation of the protein complex by SDS PAGE followed by Coomassie staining or Western blotting and immunodetection of SpaP and $SpaR^{FLAG}$, respectively, showed that the complex contained more SpaP than SpaR (1B). Since the masses of membrane protein complexes deduced from analysis by size exclusion chromatography are skewed by the presence of bound detergent, we analyzed the fraction of protein and detergent contained in the isolated SpaPR complexes by size exclusion chromatography-multi angle laser light scattering. This analysis determined that the SpaPR peak was monodisperse, corresponding to a size of 311 kDa with a calculated protein content of 160 kDa (Fig 1C, S1 Table, S1 File), suggesting a total of 6 molecules of SpaP (25.2 kDa) and SpaR (31.7 kDa including C-terminal 3xFLAG tag). Given a mean error of 7% (S1 Fig), these data did not allow to distinguish whether the complex composition was 4 SpaP + 2 $SpaR^{FLAG}$ (calc. 164 kDa) or 5 SpaP + 1 $SpaR^{FLAG}$ (calc. 158 kDa). Native mass spectrometry was then performed to assess the exact stoichiometry of a purified $SpaPR^{STREP}$ complex. A major species of complex produced peaks of 157.882 kDa and a minor species of

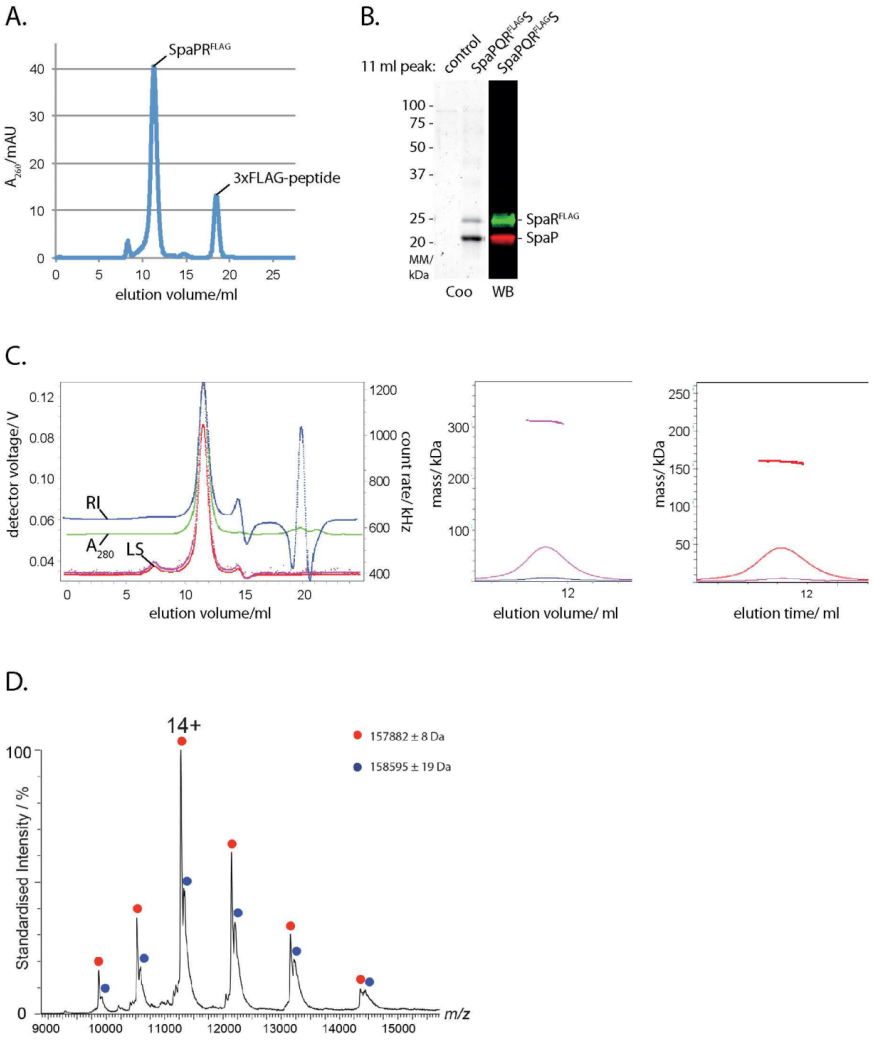

Fig 1. Isolation and stoichiometry analysis of the SpaPR subcomplex of the needle complex. (A) Elution profile of the purified SpaPR^{FLAG} complex run on a Superdex 200 10/300 GL column. The peaks corresponding to the SpaPR^{FLAG} complex and 3xFLAG peptide are indicated. (B) Coomassie-stained SDS PAGE gel of purified SpaPR^{FLAG} complex and of its FLAG-deficient control (left). Immunodetection of SpaP (green) and SpaR^{FLAG} (red) on Western blot from purified SpaPR^{FLAG} complex separated by SDS PAGE (right). (C) Traces of indicated detector signals from size exclusion chromatography—multi angle laser light scattering of purified SpaPR^{FLAG} complex (left). ASTRA-calculated mass profile of total components of peak of purified SpaPR^{FLAG} complex (polypeptides and detergent, middle). ASTRA-calculated mass profile polypeptide components of peak of purified SpaPR^{FLAG} complex (right). (D) Native mass spectrum of the SpaPR^{STREP} complex. Peak series corresponding to the SpaP:SpaR^{STREP} complex in a 5:1 ratio is marked in red, with the most abundant charge state (14+) indicated. The peak series marked in blue corresponds to the same SpaPR complex bound to a ligand with a mass of approximately 710 Da, indicative of an associated phospholipid. Note that the measured mass for SpaPR heterohexamer (157.882 kDa) is heavier than the theoretically calculated mass (157.280 kDa). Abbreviations: Coo: Coomassie stained, WB: Western blot, RI: refractive index, LS: light scattering.

doi:10.1371/journal.ppat.1006071.g001

158.595 kDa. These masses are consistent with a stoichiometry of 5 SpaP and 1 $SpaR^{STREP}$ (calculated molecular mass of 157.280 kDa) with bound phospholipids. In summary, these results show that the isolated SpaPR complex obtained from overexpression in the absence of other needle complex components has the same stoichiometry as SpaP and SpaR assembled into complete needle complexes [12] and indicates that the isolated SpaPR complex is a relevant functional module of the needle complex.

Probing the placement of SpaP and SpaR in the needle complex by *in vivo* photocrosslinking

To further validate the stoichiometry of SpaP and SpaR and to characterize the placing of this module within the assembled needle complex, we employed an *in vivo* photocrosslinking approach based on the genetically encoded UV-reactive amino acid *para*-benzophenylalanine (*p*Bpa) [25]. *p*Bpa was built into the predicted TM helices of SpaP and SpaR, respectively, so that possible interactions at every face of the predicted TM helices were sampled (Fig 2A and 2B). *spaP* or *spaPQRS* deletion mutants of *S*. Typhimurium were complemented with $SpaP^{FLAG}$ or $SpaPQR^{FLAG}S$ containing *p*Bpa at selected positions and expressed from a low copy number plasmid. Complementation of T3SS function of these mutants was assessed by analyzing type III-dependent secretion of substrate proteins into the culture supernatant (S2 Fig). Crosslinking of *p*Bpa to nearby interactors was induced by UV irradiation of intact bacterial cells immediately after harvesting. Subsequently, crude membranes were isolated and crosslinking patterns were analyzed by SDS PAGE and immunodetection of the FLAG-tagged bait protein. Crosslinked adducts of different sizes were identified at various positions of SpaP and SpaR (Fig 2C and 2D). To exclude crosslinking artifacts resulting from plasmid-based complementation, *p*Bpa positions that produced representative crosslinking patterns were also introduced into the chromosome-encoded genes, and crosslinking was performed accordingly. Notably, for all tested chromosomal positions the quality of previously identified crosslinks could be confirmed while the efficiency of crosslinking improved in some cases, possibly due to a more efficient complex assembly achieved by expression of *p*Bpa-containing proteins from its native context (Fig 2E and 2F). To identify the nature of crosslinked adducts, needle complexes with *p*Bpa-containing $SpaP^{FLAG}$ or $SpaR^{FLAG}$ were purified, UV-irradiated, resolved by SDS PAGE, and gel slices of the positions of the crosslinks were analyzed by mass spectrometry (S3 Fig). This analysis identified crosslinks between SpaP and the export apparatus components SpaS and SpaQ, and between SpaP and the inner rod protein PrgJ. Furthermore, crosslinks between SpaR and SpaP, SpaQ, and PrgJ were also identified (S2 Table, Fig 2C and 2D). The detailed validation and interpretation of the crosslinking analysis is presented in the following three sections.

Crosslinking of the SpaP pentamer

UV-irradiation of $SpaP^{FLAG}$-containing *p*Bpa at positions L7, L10, A12, F13, S14, T15, M187, S189, I193, and T195 showed a ladder of crosslinks at 40 kDa, 70 kDa, 120 kDa, and 200 kDa (Fig 2C and 2E). We reasoned that this crosslink ladder might correspond to a homo-oligomeric crosslinking of the SpaP pentamer. Two further experimental results supported this hypothesis: First, crosslinking of $SpaP_{T15X}{}^{FLAG}$ expressed in *E. coli* in the absence of other T3SS components showed the same crosslink ladder (Fig 3A); and second, crosslinking plasmid-complemented $SpaP_{T15X}$ in an *S*. Typhimurium strain with chromosome-encoded $SpaP^{FLAG}$ also produced the 40 kDa FLAG-containing crosslink, which proved at least a bipartite $SpaP_{T15X}$-$SpaP^{FLAG}$ interaction (Fig 3B). Several of the SpaP *p*Bpa mutants that produced a ladder upon crosslinking (A12X, T15X, M187X, S189X, I193X) were non-functional (S2 Fig).

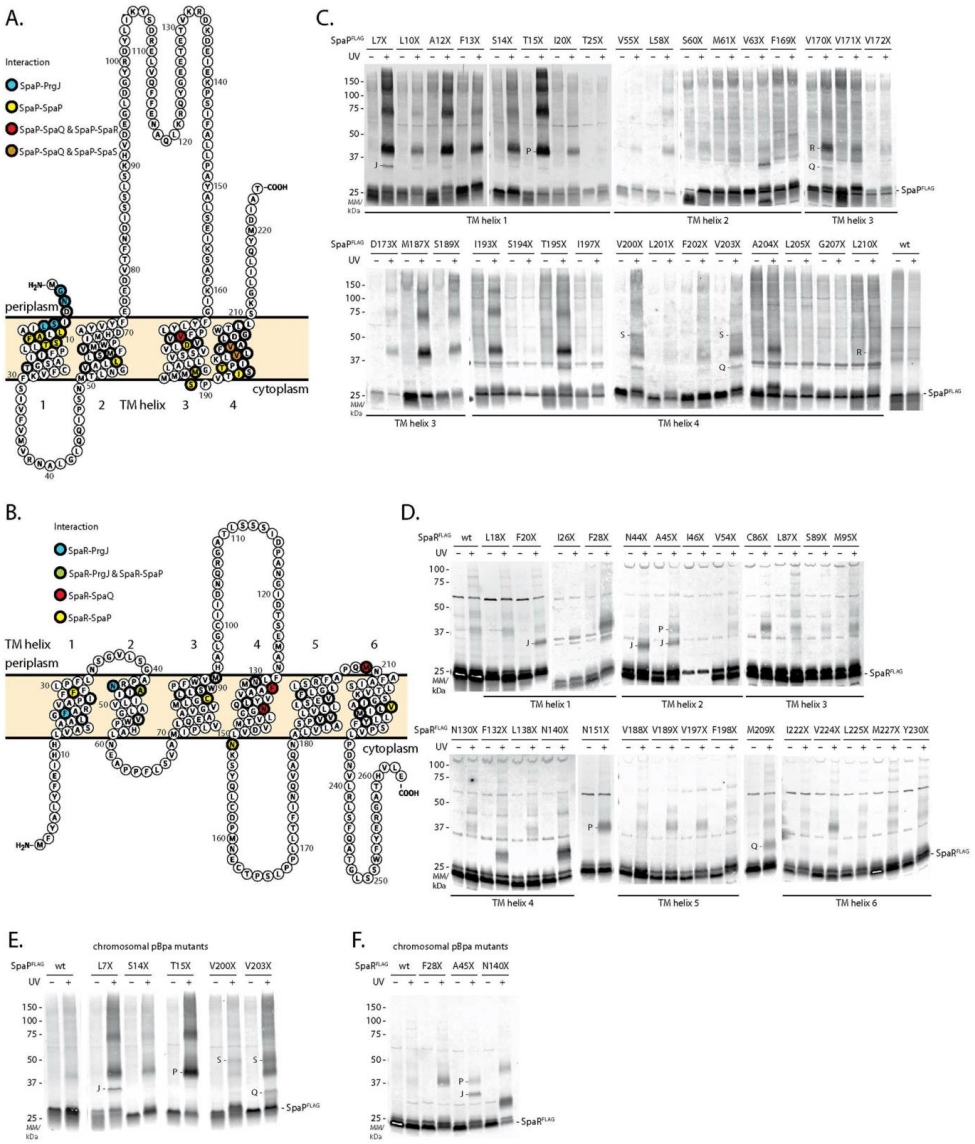

Fig 2. Screen of protein-protein interactions of SpaP and SpaR by *in vivo* photocrosslinking. (A) Protter visualization of SpaP presenting predicted TM topology, positions analyzed by *in vivo* photocrosslinking (thick stroke), and identity of interactions (colored). (B) As in (A) but showing SpaR. (C) Immunodetection of $SpaP^{FLAG}$ on Western blots of crude membrane samples of *S.* Typhimurium expressing indicated plasmid-complemented SpaP-*p*Bpa mutants separated by SDS PAGE. *p*Bpa mutations are denoted as "X". Each sample is shown with and without UV-irradiation to induce photocrosslinking of *p*Bpa to neighboring interaction partners. Since the running behavior of

crosslinked proteins often deviates from the calculated mass due to incomplete unfolding and since membrane proteins like SpaP often show an aberrant running behavior, the position of a crosslink on a gel does not easily allow drawing direct conclusions on the size of the crosslinked adduct. Crosslinked proteins identified by mass spectrometry or Western blotting are indicated. Other highlighted interactions shown in A and B were based on comparable SDS PAGE band pattern. (D) As in (C) but showing SpaR complemented from a low-copy number plasmid expressing SpaPQR^{FLAG}S. (E) As in (C) but expression of SpaP-*p*Bpa mutants from their chromosomal location. (F) As in (D) but expression of SpaR-*p*Bpa mutants from their chromosomal location. Abbreviations: J—PrgJ, P—SpaP, Q—SpaQ, S—SpaS.

doi:10.1371/journal.ppat.1006071.g002

Analysis of two of these *p*Bpa mutants (T15X and M187X) by 2-dimensional blue native/SDS PAGE indicated that the observed SpaP-SpaP interaction occurred between SpaP assembled into the complete needle complex as well as between SpaP molecules that had not yet been yet incorporated into this structure (Fig 3C). These results suggest that the loss of function of

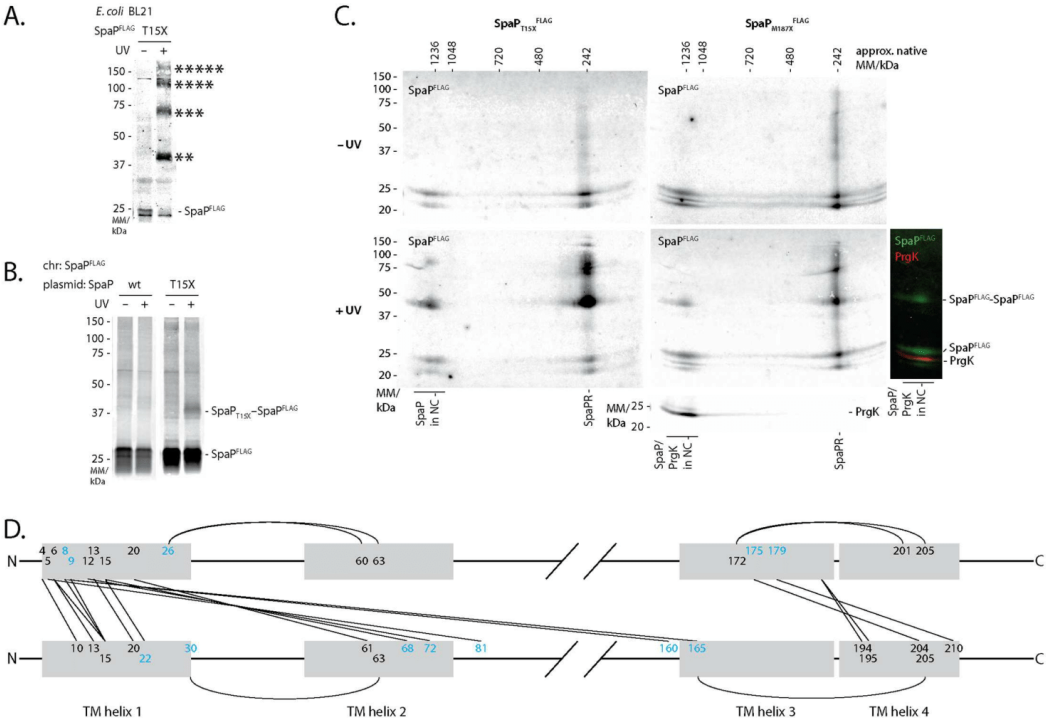

Fig 3. SpaP-SpaP interactions analyzed by *in vivo* photocrosslinking and sequence co-variation. (A) Immunodetection of SpaP^{FLAG} on Western blots of crude membrane samples of *E. coli* BL21 (DE3) expressing SpaP$_{T15X}^{FLAG}$ in the absence of all other T3SS components. The sample is shown with and without UV-irradiation to induce photocrosslinking of *p*Bpa to neighboring interaction partners. (B) Immunodetection of chromosome-encoded SpaP^{FLAG} on Western blots of crude membrane samples of *S.* Typhimurium expressing plasmid-encoded SpaP$_{T15X}$. (C) Immunodetection of SpaP^{FLAG} and the inner MS ring protein PrgK on Western blots of crude membrane samples of *S.* Typhimurium expressing indicated SpaP-*p*Bpa mutants separated by 2-dimensional blue native/SDS PAGE. Full 2D gels are only shown for SpaP^{FLAG} scanned in the 800 nm channel. The 2D gel showing SpaP$_{M187X}^{FLAG}$ +UV has been re-probed with antibody for PrgK and scanned in the 700 nm channel. PrgK indicates the position of the assembled needle complex. An overlay of FLAG and PrgK signals is shown on the right. The relevant slice of the 700 nm image showing PrgK at 25 kDa and the overlay of both channels showing the needle complex-associated bands have been aligned to the corresponding 2D image. (D) Interaction map of SpaP. Lines indicate predicted interactions with a normalized coupling score > 0.8 (S3 Table) at positions with experimentally identified SpaP-SpaP crosslinks (at least from one side). Positions with experimentally observed SpaP-SpaP interactions are shown in black, target positions only predicted are shown in light blue. Grey shading indicates TM helices. Only positions within or in close proximity to TM helices are shown. Abbreviations: chr—chromosomal.

doi:10.1371/journal.ppat.1006071.g003

these mutants is unlikely due to improper folding or assembly but rather due to subtle conformational changes that alter their function.

Overall, these results indicate that TM helix one and to a smaller extent the cytoplasmic face of TM helix three and four are involved in protomer contacts in the SpaP homopentamer while only few homotypic interactions were observed at positions of TM helices two and three.

To cross-validate the experimental findings, we performed an independent prediction of SpaP-SpaP interactions based on analysis of sequence co-variation using the software EV couplings [26–28]. 27 of the experimentally tested SpaP positions were predicted to be involved in SpaP-SpaP interactions with a normalized coupling score >0.80 (S3 Table). 18 of the 27 experimentally tested positions yielded indications of SpaP-SpaP interactions, 2 positions were experimentally ambiguous because of very low expression levels of the mutated proteins, and 7 positions showed no signs of SpaP-SpaP interactions. As used, EV couplings does not distinguish between intra and intermolecular interactions. 6 of the predicted but experimentally negative positions are likely to be involved in intramolecular interactions, which are not detectable by the *in vivo* photocrosslinking approach used (Fig 3D). Many intermolecular interactions at experimentally tested SpaP positions were predicted to connect two TM helices 1 or TM helix 1 and 3 in a parallel fashion, and TM helices 1 and 2 or TM helices 3 and 4 in an antiparallel fashion (Fig 3D), supporting a SpaP topology as depicted in Fig 2A, while only the coupling prediction of $SpaP_{S189}$ (to L11) opposed this model. Overall, the bioinformatic analysis supports our experimental results, strengthens the topology model of SpaP, and provides a first picture of the buildup of the SpaP pentamer.

SpaQ, SpaR, and SpaS assemble independently of other T3SS components onto the SpaP pentamer and closely interact with each other

Mass spectrometry analysis of crosslinked SpaP and SpaR adducts produced evidence for multiple interactions among the export apparatus components SpaP, SpaQ, SpaR, and SpaS (Fig 2, S3 Fig, S2 Table). To validate these results by immunoblotting, we assayed the SpaP-SpaR as well as the SpaP-SpaS interactions by FLAG-tagging the target instead of the *p*Bpa-containing bait protein. We found that SpaP interacts with $SpaR^{FLAG}$ through its residues V170 and L210 but not through V203 and A204 (Fig 4A) and that SpaR contacts $SpaP^{FLAG}$ via its residue N151 (Fig 4B). Using an autocleavage-deficient FLAG-tagged variant of the switch protein SpaS, we could further validate interactions between SpaS and $SpaP_{V200X}$/$SpaP_{V203X}$ (Fig 4C). In summary, these crosslinking data indicate that, consistent with our previous report [12], 1 SpaQ, 1 SpaR, and 1 SpaS form a closely interconnected assembly that contacts SpaP at TM helix three (V170: SpaQ, SpaR) and TM helix four (V200/203: SpaQ, SpaS). The interaction of these four proteins seems to be integrated by SpaQ as this small protein makes contacts to all other three proteins (*in vivo* photocrosslinking-identified SpaS-SpaQ contacts communicated results of J. Monjarás Feria).

Previous results showed that SpaQ is critical for efficient formation of the needle complex base but due to technical limitations of the blue native PAGE approach used at the time, it was not clear whether assembly proceeds through a pre-assembled complex of all four minor export apparatus components before integration into the base or whether these components only interact upon base integration [9]. To examine the early events of the assembly of the T3SS export apparatus components, we probed the SpaP-SpaQ, SpaP-SpaS, and SpaR-SpaQ interactions identified by the crosslinking studies in strains deficient in the inner ring protein PrgK. These mutants are deffective for base assembly thus allowing to prove the requirement of a fully assembled base for the assembly of the export apparatus. Indeed, we detected

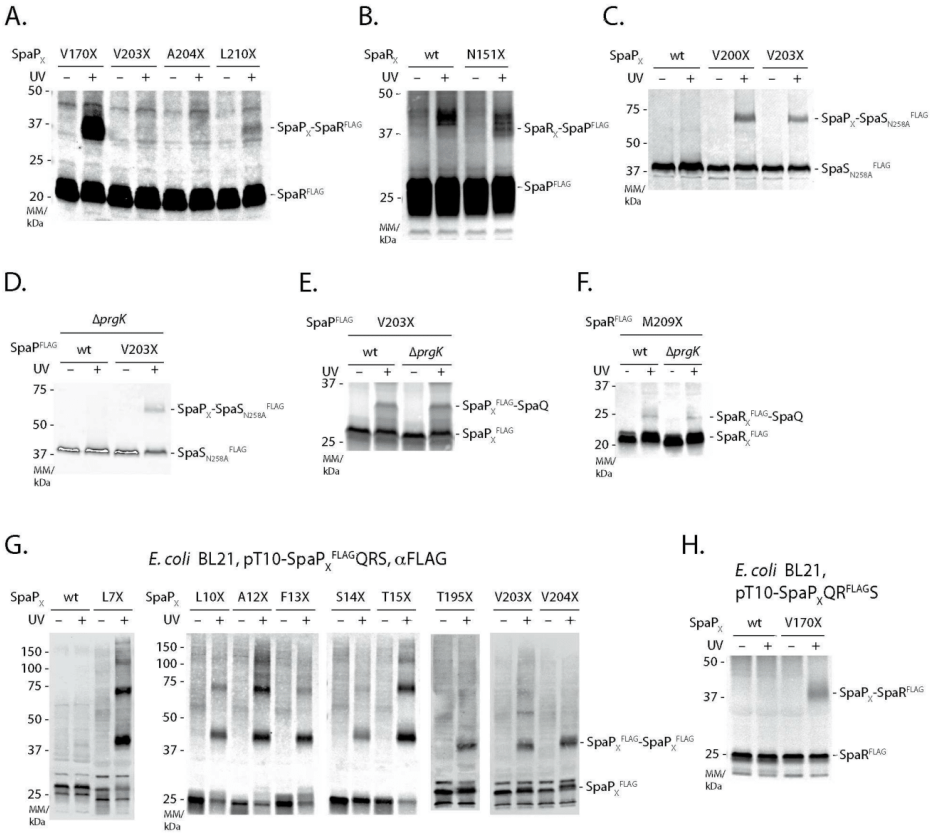

Fig 4. Interactions among the export apparatus components SpaP, SpaQ, SpaR, and SpaS. (A) Immunodetection of SpaR^{FLAG} on Western blots of SDS PAGE-separated crude membrane samples of Δ*spaPQRS S.* Typhimurium expressing indicated SpaP-*p*Bpa mutants from a pT10-*spaPQR*^{FLAG}*S* plasmid. (B) Immunodetection of SpaP^{FLAG} on Western blots of SDS PAGE-separated crude membrane samples of Δ*spaPQRS S.* Typhimurium expressing indicated SpaR-*p*Bpa mutants from a pT10-*spaP*^{FLAG}*QRS* plasmid. (C) Immunodetection of SpaS$_{N258A}^{FLAG}$ on Western blots of SDS PAGE-separated crude membrane samples of *S.* Typhimurium expressing indicated plasmid-complemented SpaP-*p*Bpa mutants. (D) As in (C) but assessing the SpaP-SpaS interaction in absence of the inner ring protein PrgK. (E) Immunodetection of SpaP^{FLAG} on Western blots of SDS PAGE-separated crude membrane samples of *S.* Typhimurium expressing chromosome-encoded indicated SpaP-*p*Bpa mutants in the presence or absence of the inner ring protein PrgK. (F) As in (E) but showing SpaR$_{M209X}^{FLAG}$. (G) Immunodetection of SpaP^{FLAG} on Western blots of crude membrane samples of *E. coli* BL21 (DE3) expressing indicated SpaP-*p*Bpa mutants together with SpaQRS to form the SpaPR complex. (H) As in (F) but expressing SpaP$_{V170X}$QR^{FLAG}S to reveal the SpaP-SpaR interaction in *E. coli.*

doi:10.1371/journal.ppat.1006071.g004

SpaP-SpaQ and SpaP-SpaS interactions at SpaP$_{X203}$ in the absence of PrgK (Fig 4D and 4E), and SpaR-SpaQ interactions at SpaR$_{X209}$ (Fig 4F). SpaP-SpaP and SpaP$_{V170X}$-SpaR crosslinks were also identified when plasmid-encoded SpaPQRS were expressed in *E. coli* BL21, lacking all other T3SS components (Fig 4G and 4H). Altogether, these results indicate that assembly of the export apparatus precedes and is independent of base assembly.

The inner rod protein PrgJ locates close to the inner membrane and directly contacts the periplasmic domains of SpaP and SpaR

UV-irradiation of SpaP^{FLAG} with *p*Bpa at position L7 or SpaR^{FLAG} with *p*Bpa at positions F20, N44, and A45 resulted in an 8 kDa mobility shift of these proteins in SDS-PAGE (Fig 2C, 2D and 2E). Mass spectrometry analysis of the shifted bands identified PrgJ in both cases (S3 Fig, S2 Table). In an effort to characterize the extent of the SpaP-PrgJ interaction in more detail, we also noted the same mobility shift of SpaP after UV-irradiation of SpaP^{FLAG} with *p*Bpa at positions G2, N3, D4, I5, and S6, where crosslinked PrgJ was confirmed by immunodetection (Fig 5A). To rule out potential artifacts due to overexpression of the plasmid-borne constructs, we confirmed the crosslinks of SpaP$_{G2X}^{FLAG}$ and SpaP$_{S6X}^{FLAG}$ after expression from their native chromosomal context (Fig 5B). 2-dimensional blue native/SDS PAGE analysis of the crosslinks resulting from UV-irradiation of SpaR$_{A45X}^{FLAG}$ showed that the observed SpaR-PrgJ interaction is only observed when SpaR is incorporated into the needle complex (Fig 5C). Furthermore, SpaP-PrgJ as well as SpaR-PrgJ interactions were not observed in an ATPase activity-deficient InvC$_{K165E}$ mutant, demonstrating that the detected interactions dependent on active type III secretion, which is consistent with the observation that incorporation of PrgJ into the needle complex and inner rod assembly require a functional type III secretion system (Fig 5D). Taken together, these results indicate that the periplasmic domains of SpaP and SpaR serve to anchor the inner rod protein PrgJ to the export apparatus, thus creating a continuous conduit for substrate translocation from the export apparatus to the needle filament.

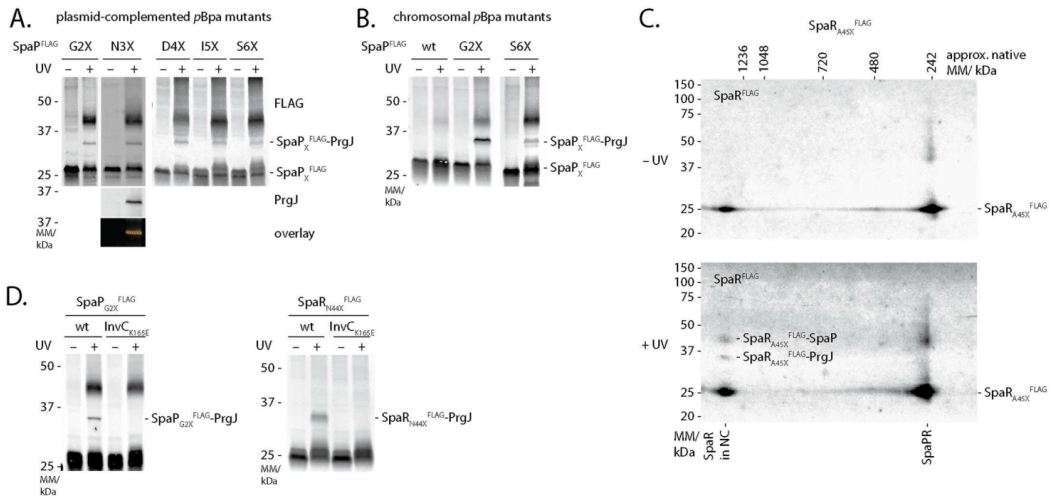

Fig 5. Interactions of SpaP and SpaR with the inner rod protein PrgJ. (A) Immunodetection of SpaP^{FLAG} on Western blots of crude membrane samples of *S*. Typhimurium expressing indicated plasmid-complemented SpaP-*p*Bpa mutants separated by SDS PAGE. The Western blot of SpaP$_{N3X}^{FLAG}$ was re-probed with PrgJ antibody to show the presence of SpaP and PrgJ in the same band. (B) Immunodetection as in (A) but detailing chromosome-encoded *p*Bpa-containing mutants of SpaP^{FLAG}. (C) Immunodetection of SpaR^{FLAG} on Western blots of crude membrane samples of *S*. Typhiumurium expressing SpaR$_{A45X}^{FLAG}$ separated by 2-dimensional blue native/SDS PAGE. (D) Immunodetection of SpaP^{FLAG} or SpaR^{FLAG} on Western blots of SDS PAGE-separated crude membrane samples of *S*. Typhimurium expressing SpaP$_{G2X}^{FLAG}$ or SpaR$_{N44X}^{FLAG}$ in wild type or in InvC ATP-hydrolysis mutants, which are unable to secrete.

doi:10.1371/journal.ppat.1006071.g005

SpaP forms a donut-shaped structure with a pore conducive to molecules of 500 Da

The location of the $SpaP_5R_1$ complex at the center of the needle complex base, right underneath and connected to the filamentous conduit formed by the inner rod and needle proteins, suggests that this complex forms the T3SS's substrate translocation pore in the bacterial inner membrane.

To obtain structural evidence for its putative pore-forming function, we analyzed the purified, negative-stained $SpaPR^{FLAG}$ complex by electron microscopy. 11202 individual particles were classified and aligned into 91 class averages (S4 Fig). A number of class averages showed a symmetric, donut-shaped complex with an iconic recession at its center (Fig 6A). The diameter of these particles was about 80 Å and the diameter of the recession was about 15 Å. Other class averages showed a more asymmetric shape with an extra density outside of the ring-structure or a mushroom-like shape (Fig 6A). Even though the sample analyzed consisted of a homogeneous population of $SpaPR^{FLAG}$ complexes, it cannot be ruled out that SpaP and $SpaR^{FLAG}$ partly dissociated during sample preparation so that a mixture of $SpaP_5$ and $SpaP_5R_1$ complexes was imaged, explaining the diversity of observed classes. It is therefore possible that the donut-shaped particles represent $SpaP_5$ complexes and the asymmetric extension the SpaP-bound $SpaR^{FLAG}$. Overall, the particles' shape and dimensions conformed well with the structure of the cup region of assembled bases reported previously (3).

We reasoned that the recession at the center of the observed particles might represent the protein translocation pore of the T3SS. To probe the conducting properties of the SpaPR complex, we assessed its ability to allow the access of biotin maleimide (BM, molecular mass = 500 Da) into the bacterial cytoplasm, an approach that has been used previously to test the gating

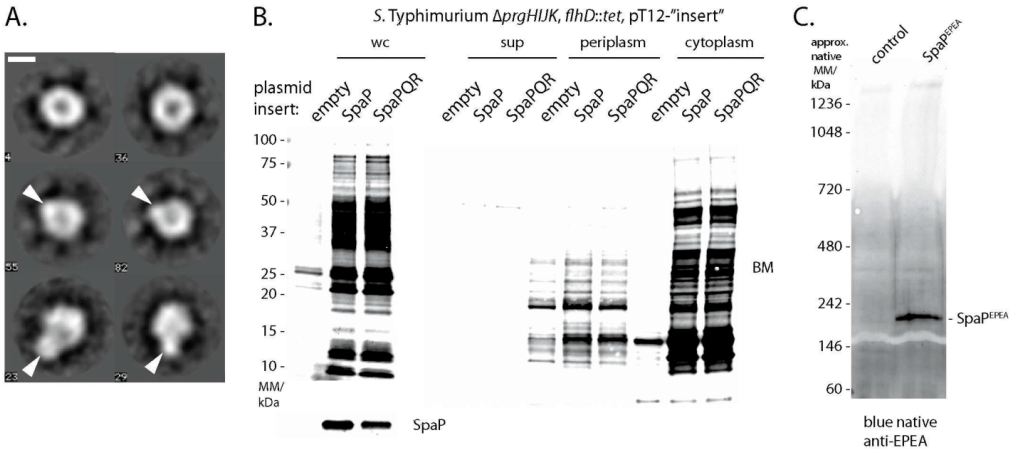

Fig 6. Visualization and characterization of the pore formed by SpaP and SpaR. (A) Six selected class averages (4, 23, 29, 36, 55, 82) of negative-stained isolated SpaPR complexes imaged by electron microscopy. The length of the scale bar represents 50 Å. The two class averages at the top represent the $SpaP_5$ complex. Arrowheads in the class averages in the middle and at the bottom represent the anticipated position of SpaR on the $SpaP_5$ ring. The complete picture of all class averages can be seen in S4 Fig. (B) Fluorescent streptavidin detection of SDS PAGE-separated biotin maleimide-labeled proteins of whole cell lysates, cell culture supernatant, periplasmic fraction, or cytoplasmic fraction of *S.* Typhimurium Δ*prgHIJK*, *flhD::tet* moderately overexpressing indicated proteins from a medium copy number plasmid (pT12). (C) Blue native PAGE and immunodetection of a high molecular weight complex formed by EPEA-tagged SpaP alone.

doi:10.1371/journal.ppat.1006071.g006

of the Sec-translocon [29]. The maleimide moiety of BM can only react with and biotinylate free thiol groups of cysteine residues of cytoplasmic proteins if BM can penetrate the inner bacterial membrane through a sufficiently large pore. The extent of biotinylation can then be detected on a Western blot by utilizing streptavidin. Strong BM labeling of proteins was observed in whole cell lysates when SpaPR or SpaP alone were overexpressed from a medium copy plasmid (Fig 6B). Cell fractionation of the expression host showed that only cytoplasmic proteins were differentially labeled by BM upon expression of SpaPR and SpaP, labeling of periplasmic proteins, however, was almost indistinguishable in control and expressing bacteria (Fig 6B). General lysis of the expression host could be ruled out to cause the observed phenotype as neither the cytoplasmic protein RNA polymerase nor the periplasmic maltose binding protein were observed in the culture supernatant of SpaPR or SpaP expressing bacteria (S5A and S5B Fig). Formation of a sizable, ungated pore by these complexes was also indicated by the strong impact even modest overexpression of SpaP and SpaPR had on the viability of the expression host (S5C Fig). Altogether, these results suggest that BM accessed the cytoplasm of the expression host through a pore formed by the expressed proteins. Since SpaP expression alone led to BM labeling of cytoplasmic proteins, it is conceivable that SpaP alone is sufficient to form the actual substrate translocation pore. In line with this idea, overexpressed $SpaP^{EPEA}$ was observed to assemble into high molecular weight complexes when analyzed by blue native PAGE (Fig 6C), however, we were not able to isolate and investigate stable SpaP-only complexes. The access of 500 Da BM to the cytoplasm through the pore of the SpaP pentamer suggests a pore diameter of about 15 Å, which is consistent with the diameter of the recession observed by electron microscopy of the isolated $SpaP_5R_1$ complexes.

Discussion

The export apparatus of bacterial T3SSs is its central unit that facilitates translocation of substrates across the bacterial inner membrane and likely the only gated barrier of these one-step secretion devices. While functions have been proposed for some export apparatus components, the components forming the actual substrate translocation pore in the bacterial inner membrane have not been defined.

In this study we present evidence that a homopentamer of the minor hydrophobic export apparatus component SpaP is a central component of the translocation pore in the inner membrane of the injectisome T3SS encoded by *Salmonella* pathogenicity island 1. We purified a stable complex of 5 SpaP and 1 SpaR that under electron microscopy exhibited a donut-like shape of about 80 Å in diameter and a 15 Å wide central recession. Expression of the components of this complex in *E. coli* rendered the bacterial cells permeable to 500 Da compounds, supporting the notion that it may work as translocation channel. Extensive mapping of protein-protein interactions of the TM domains of SpaP and SpaR by *in vivo* photocrosslinking revealed that SpaQ, SpaR, and SpaS form a compact assembly connected to the central pentamer formed by SpaP. We further demonstrated that assembly of this complex does not require its incorporation into the needle complex. We also detected crosslinks between SpaP and SpaR and the inner rod protein PrgJ showing that the inner rod makes direct contact with the export apparatus.

Previous analysis by blue native PAGE showed that SpaP and SpaR form stable complexes in an *S*. Typhimurium mutant unable to assemble the needle complex [9]. We now present evidence based on size-exclusion chromatography-multi angle laser light scattering and native mass spectrometry that this complex is composed of 5 SpaP and 1 SpaR. The stoichiometry of the isolated $SpaP_5R_1$ complex is consistent with the stoichiometry of SpaP and SpaR in the context of a fully assembled needle complex [12], which indicates that the isolated complex

represents a relevant intermediate of needle complex assembly. This notion is further supported by the good match of the dimensions of the observed SpaPR complex with the dimensions of the cup substructure of the needle complex [30], which we previously showed to be composed of SpaP and SpaR [9]. Electron micrographs of the isolated $SpaP_5R_1$ complex and BM permeation experiments suggested a pore size of the substrate translocation channel of about 15 Å. Within the range of uncertainty, this diameter conforms with the 10 Å that were reported for the dimensions of the channel of an assembled *S*. Typhimurium *S*PI-1 needle complex containing a trapped translocation intermediate [5]. A tight seal during substrate translocation is expected to be important for T3SS to avoid leakage of ions through the open pore, so it is conceivable that the pore diameter closely resembles the dimensions of extended polypeptides or alpha helices. However, a larger pore diameter in its fully open state cannot be excluded given that the herein investigated isolated $SpaP_5R_1$ complex most certainly lacks the necessary elements for gating of the pore.

We detected extensive crosslinks of up to five consecutive SpaP at TM helix one and at the cytoplasmic face of TM helices three and four, suggesting that these regions form the major contact area between protomers of the SpaP pentamer. This notion was supported by results of a sequence co-variation-based prediction of residue-residue interactions of SpaP. The formation of these crosslinks was independent of the presence of other needle complex components, supporting the notion that the SpaP pentamer nucleates assembly of the needle complex. Interestingly, the presence of SpaP pentamer crosslinks at TM helices three and four correlated with secretion defects of the respective *p*Bpa mutants, a phenomenon also seen for $SpaP_{A12X}$ and $SpaP_{T15X}$. The secretion defect was not due to defects in their incorporation into assembled needle complexes, suggesting that these residues may play a critical role in protein translocation.

The recently reported stoichiometry of SpaP, SpaQ, SpaR, and SpaS of 5:1:1:1 [12] suggests that these export apparatus components form an asymmetric assembly within the needle complex. We show here that SpaQ, SpaR, and SpaS contact the SpaP pentamer at its TM helices three and four. We further demonstrate that SpaQ interacts with SpaP and SpaR. These observations, together with the observation that a fusion of SpaR and SpaS homologs retains function [31], suggest that SpaQ, SpaR, and SpaS are not wrapped around the SpaP pentamer but form a compact assembly at one side of SpaP, with SpaQ as the central component that makes contacts to all other components (Fig 7A and 7B). Besides SpaR's contribution in anchoring the inner rod protein PrgJ, the assembly formed by SpaQ, SpaR, and SpaS might also facilitate gating of the SpaP pore, a critical aspect to prevent detrimental effects of nutrient and ion leakage across the bacterial inner membrane.

The assessment of the dependence of crosslinks between SpaP, SpaQ, SpaR, and SpaS on the presence of the inner ring protein PrgK allowed us to refine a model for the early steps of export apparatus assembly (Fig 7C). We propose that assembly starts with the formation of the SpaP pentamer. This initially unstable complex is stabilized upon binding SpaR. The high stability of the resulting $SpaP_5R_1$ intermediate suggests that this complex is the major nucleus of further needle complex assembly. Next, SpaQ and SpaS associate with the $SpaP_5R_1$ complex but presumably with weaker affinity since this complex could only be captured after *in vivo* crosslinking. InvA would then be recruited to the SpaPRQS complex although it is not clear whether its recruitment occurs prior or after this complex initiates the assembly of the needle complex rings. Subsequently, association of the outer membrane secretin InvG and the inner ring protein PrgH would lead to formation of the completed base-export apparatus holo-complex [21,23].

Beyond interactions among the export apparatus components, we also identified crosslinks between the periplasmic domains of SpaP and SpaR and the inner rod protein PrgJ. The close

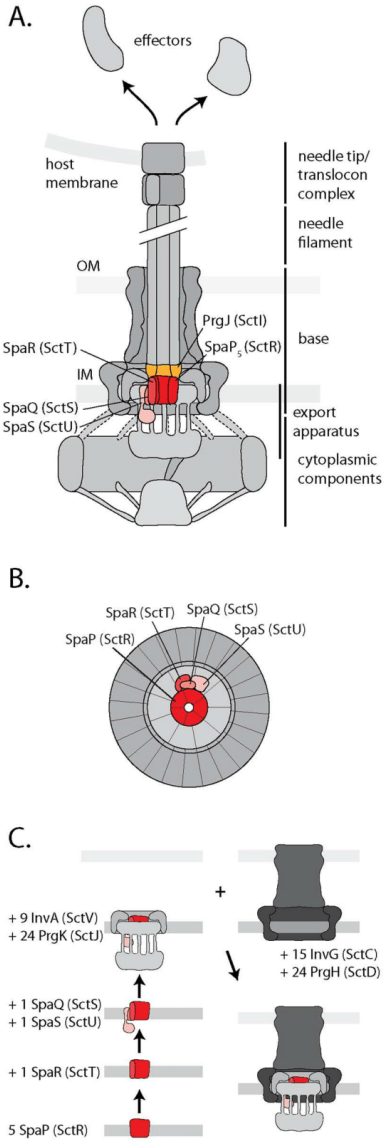

Fig 7. Models of SpaP, SpaR, SpaQ, SpaS, and PrgJ in the T3SS needle complex and its assembly. (A) Model of the central SpaP complex with surrounding export apparatus components SpaQ, SpaR, and SpaS, and direct connection to the inner rod formed by PrgJ. These results suggest that SpaP, SpaR, and PrgJ form the socket structure on the periplasmic side of the inner membrane patch of the base. (B) Model of a view of the membrane patch of the needle complex from the cytoplasmic side highlighting SpaP, SpaQ, SpaR, and SpaS. (C) Model of needle complex assembly. The unified Sct nomenclature [23] is shown in parenthesis.

doi:10.1371/journal.ppat.1006071.g007

interaction of SpaP, SpaR, and PrgJ is likely to create a continuous conduit for substrate translocation, where PrgJ might serve as an adapter to connect the flat translocation pore of the inner membrane with the helical needle filament. Analysis of the needle complex by cryo-electron microscopy revealed a central juxtamembrane structure at the periplasmic interior of the base, which was termed socket [30], however, no protein could be assigned to contribute to this density. Our results suggest that the socket is composed of the periplasmic parts of SpaP and SpaR, together with the inner rod protein PrgJ. The mass of six PrgJ [12] and the periplasmic domains of five SpaP and one SpaR could well account for the observed density of the socket structure. Our observation now opens the door for further investigations of the relevance of the export apparatus-PrgJ interaction for needle length control, substrate specificity switching, and host cells sensing, functional roles that were suggested for PrgJ [32,33].

The positions of SpaP and SpaR that interact with PrgJ also help to consolidate the TM topology models of these two export apparatus proteins. SpaP is predicted to contain four TM helices (Fig 2A) and the presence of a cleavable signal sequence in flagellar homologs suggests an N-out/C-out TM orientation [34]. This model is supported by the interaction between the N-terminus of SpaP and the periplasmic inner rod detected in this study. Further support for this topology model comes from the presented sequence co-variation-based analysis of SpaP residue-residue interactions, which strongly predicted antiparallel interactions between TM 1 and 2, and between TM 3 and 4 (Fig 3D). The TM topology predictions of SpaR and its homologs are very uncertain, ranging from five to eight TM helices with mostly N-out orientation (Fig 2B, S6 Fig) [34,35]. A C-in orientation, on the other hand, was suggested based on the report of a functional protein fusion of the flagellar SpaR and SpaS homologs of *Clostridium*, given that the N-terminus of SpaS and its homologs is strongly predicted to reside in the cytoplasm [31,35,36]. Here we presented interactions of SpaR F20, N44, and A45 with the periplasmic protein PrgJ. These residues are predicted to be located within SpaR's first two TM helices, however, our results rather suggest a periplasmic localization of this part of SpaR. This notion is supported by rather high ΔG values for membrane partitioning of the predicted TM helices one, two, and four (S6B Fig), so that a SpaR model comprising an N-out/C-in topology with only three TM helices is conceivable (S6C Fig).

In summary, we have presented evidence that a pentamer of SpaP forms the substrate translocation pore of T3SSs in the bacterial inner membrane. We show that this pentamer closely interacts with the export apparatus components SpaQ, SpaR, and SpaS in the plane of the membrane, an accessory assembly that may facilitate gating of the export pore. We further show that SpaP and SpaR intimately contact the periplasmic inner rod protein PrgJ and propose that the inner rod serves as an adapter to connect the flat export pore and the helical needle filament, thus creating a continuous conduit for substrate translocation from the bacterial cytoplasm into the host cell.

Materials and Methods

Materials

Chemicals were from Sigma-Aldrich unless otherwise specified. Detergent n-dodecyl-maltoside (DDM) was from Affimetrix-Anatrace. para-benzophenylalanine was from Bachem. SERVA Blue G and SERVAGel TG PRiME 8–16% precast gels were from Serva. NativePAGE Novex Bis-Tris 3–12% gels were from Life Technologies. Primers are listed in S5 Table and were synthetized by Eurofins and Integrated DNA Technologies. Polyclonal rabbit anti-MBP antibody were from New England Biolabs. Monoclonal mouse anti-RNApol antibody was from BioLegend. Monoclonal M2 anti-FLAG antibody, M2 anti-FLAG agarose beads, and 3xFLAG peptide were from Sigma-Aldrich. CaptureSelect-biotin, Streptavidin DyLight 800,

and secondary antibodies goat anti-mouse IgG DyLight 800 conjugate and goat anti-rabbit IgG DyLight 680 conjugate were from Thermo-Fisher.

Bacterial strains and plasmids

Bacterial strains and plasmids used in this study are listed in S4 Table. Primers for construction of strains and plasmids ere listed in S5 Table. The position and sequence of epitope tags introduced into SpaP, SpaR, and SpaS is shown in S7 Fig. All *Salmonella* strains were derived from *S*. Typhimurium strain SL1344 [37]. Bacterial cultures were supplemented as required with streptomycin (50 μg/mL), tetracycline (12.5 μg/mL), ampicillin (100μg/mL), kanamycin (25 μg/mL), or chloramphenicol (10 μg/mL).

Expression and purification of SpaPR complex

The SpaP, and SpaPR complexes were expressed in *E. coli* BL21 (DE3) from rhamnose-inducible medium copy number plasmids encoding $SpaP^{EPEA}$, $SpaPQR^{FLAG}S$, or $SpaPQR^{STREP}$, respectively. Expression was autoinduced by over night growth at 37˚C in TB medium. Bacterial cells were harvested, crude membranes purified as described previously [9], and membrane proteins were extracted with 1% DDM in PBS. After removal of unsolubilized material by ultracentrifugation for 30 min at 100.000 x g, complexes were immunoprecipitated according to the manufacturers instructions using CaptureSelect affinity gel for $SpaP^{EPEA}$, M2 anti-FLAG agarose beads for $SpaPR^{FLAG}$, and Strep-Tactin sepharose (IBA) for $SpaPR^{STREP}$. Complexes were natively eluted with 150 ng/ml SEPEA or 3xFLAG peptides, respectively, or with 2.5 mM desthiobiotin, each in PBS/0.04% DDM. The $SpaP^{EPEA}$ and the $SpaPQR^{FLAG}S$, complexes were subsequently purified by anion exchange (Mono Q 5/50 GL, GE), while this step was omitted for the $SpaPQR^{STREP}$ complex. Samples were further purified by size exclusion (Superdex 200 10/300 GL, GE) chromatography, and concentrated to 1 mg/ml using Amicon Ultra 100 k cutoff spin concentrators (Merck Millipore). Purified SpaP and SpaPR complexes were stored in liquid nitrogen until further use.

Size exclusion chromatography—multi angle laser light scattering analysis

The detergent and polypeptide content of the purified $SpaPR^{FLAG}$ complex in PBS/0.04% DDM was determined by size exclusion chromatography—multi angle laser light scattering and analysis by the ASTRA software (Wyatt, Santa Barbara, CA) as previously described [38].

Native mass spectrometry of isolated native SpaPR complex

Purified $SpaPR^{STREP}$ complex was concentrated to 20 μM in PBS/0.04% DDM, and buffer exchanged to 250 mM ammonium acetate, pH 7.5, complemented with 0.01% polyoxyethylene(9)dodecyl ether (C12E9) prior to native mass spectrometry analysis. Buffer exchange was carried out using Amicon Ultra 0.5 ml centrifugal filters with a 100-kDa cut-off (Millipore UK Ltd, Watford UK). Mass measurements were carried out on a Synapt G1 HDMS (Waters Corp., Manchester, UK) Q-ToF mass spectrometer [39]. The instrument was mass calibrated using a solution of 10 mg/ml cesium iodide in 250 mM ammonium acetate. 2.5 μL aliquots of samples were delivered to the mass spectrometer by means of nano-electrospray ionization via gold-coated capillaries, prepared in house [40]. Instrumental parameters were as follows: source pressure 6.0 mbar, capillary voltage 1.40 kV, cone voltage 150 V, trap energy 200 V, transfer energy 10 V, bias voltage 5 V, and trap pressure 1.63x10-2 mbar.

Membrane protein topology prediction

SpaP and SpaR TM topology was predicted using TOPCONS (http://topcons.cbr.su.se) [41]. The extent of the hydrophobic regions constituting TM helices was predicted using dGpred full portein scan (http://dgpred.cbr.su.se) [42] setting the minimal helix length to 18 and the maximal helix length to 31 aa. For visualization, the online tool PROTTER (http://wlab.ethz.ch/protter/start/) was used [43].

Secretion assay

Analysis of type III-dependend secretion of proteins into the culture medium was carried out as described previously [20].

Immunoblotting

For protein detection, samples were subjected to SDS PAGE using SERVAGel TG PRiME 8–16% precast gels, transferred onto a PVDF membrane (Bio-Rad), and probed with primary antibodies anti-SipB, anti-InvJ, anti-PrgJ, anti-SpaP, anti-MBP, anti-RNApol, and M2 anti-FLAG. Secondary antibodies were goat anti-mouse IgG DyLight 800 conjugate and goat anti-rabbit IgG DyLight 680. EPEA-tagged SpaP was visualized using CaptureSelect-biotin anti C-Tag conjugate and Streptavidin DyLight 800. Scanning of the PVDF membrane and image analysis was performed with a Li-Cor Odyssey system and image Studio 2.1.10 (Li-Cor).

In vivo photocrosslinking

S. Typhimurium strains were grown at 37˚C in LB broth supplemented with 0.3 M NaCl with low aeration to enhance expression of genes of SPI-1. For *in vivo* photocrosslinking of $SpaP^{FLAG}$ in *Escherichia coli* BL21 (DE3), bacteria were cultured at 37˚C in LB broth. Cultures were supplemented with 500 μM rhamnose to induce expression of $SpaP^{FLAG}$, $SpaP^{FLAG}$QRS or SpaPQR^{FLAG}S from low copy number pTACO10 plasmids [9]. To boost general SPI-1 expression, *S.* Typhimurium strains were transformed with pBAD24-hilA. Expression of the SPI-1 master regulator HilA was induced by addition of 0,05% arabinose to the cultures. Additionally the cultures were supplemented with the artificial amino acid para-benzoyl phenyl alanine (pBpa) to a final concentration of 1 mM and afterwards incubated for 5.5 h. 2 ODU of bacterial cells were harvested and washed once with 1 mL cold PBS. Cells were resuspended in 1 mL PBS and transferred into 6-well cell culture dishes. UV irradiation with λ = 365 nm was done on a UV transilluminator table (UVP) for 30 min.

Crude membrane preparation

10 OD units of bacterial lysates of *S.* Typhimurium or *E. coli*, respectively, were resuspended in 750 μl buffer K (50 mM triethanolamine, pH 7.5, 250 mM sucrose, 1 mM EDTA, 1 mM $MgCl_2$, 10 μg/ml DNAse, 2 mg/mL lysozyme, 1:100 protease inhibitor cocktail), and incubated for 30 min on ice. Samples were bead milled and beads, unbroken cells and debris were removed by centrifugation for 10 min at 10.000 x g and 4˚C. Crude membranes contained in the supernatant were precipitated by centrifugation for 45 min at 55,000 rpm and 4˚C in a Beckman TLA 55 rotor. Pellets containing crude membranes were frozen until use.

Blue native PAGE

1-dimensional blue native PAGE and 2-dimensional blue native/SDS PAGE of crude membranes was carried out as previously described [9].

Needle complex purification

S. Typhimurium Δ*spaP* or Δ*spaPQRS* mutants, respectively, transformed with pSUP, pSB3292, and pSB3398-based rhamnose-inducible low copy number plasmids containing $SpaP^{FLAG}$ amber mutants or SpaPQRS with $SpaR^{FLAG}$ amber mutants, respectively, were grown in 200 ml LB broth supplemented with 0.3M NaCl, 1 mM *p*Bpa, 500 μM rhamnose, 0.02% arabinose, and appropriate antibiotics for 5 h at low aeration to express *S*PI-1 and assemble needle complexes. Purification of needle complexes was carried out as published previously [4,20,12] but LDAO was replaced by DDM (0.7% for lysis/extraction, 0.1% for maintenance) for lysis of cells and extraction of needle complexes throughout the protocol. Furthermore, an initial concentration of 35% (wt/vol) of CsCl was used to prepare the gradient. Purified needle complexes containing $SpaP^{FLAG}$ or $SpaR^{FLAG}$ with *p*Bpa at desired positions were irradiated with UV light (365 nm) for 30 min to induce photocrosslinking to nearby proteins. Samples were subsequently analyzed by SDS PAGE, Western blotting, and immunodetection with M2 anti-FLAG antibodies. For MS analysis of crosslinked adducts, gel pieces at positions of observed crosslinks of *p*Bpa-containing and control samples were cut out of Coomassie-stained SDS PAGE gels and subjected to in gel digestion.

Protein in-gel digestion for analysis of crosslinked interaction partners

For identification of crosslinked proteins, the area of a Coomassie-stained gel corresponding the position of the crosslinked band detected by Western blotting were excised and in-gel digested with trypsin [44]. For a better recovery, remaining proteins in the gel were again subjected to another tryptic digestion step. After each step extracted peptides were desalted using C_{18} StageTips [45]. Corresponding eluates were combined and subjected to LC-MS/MS analysis.

Mass spectrometry for analysis of crosslinked interaction partners

LC-MS/MS analyses were performed on an EasyLC II nano-HPLC (Proxeon Biosystems) coupled to an LTQ Orbitrap Elite mass spectrometer (Thermo Scientific) as decribed elsewhere [46] with slight modifications: The peptide mixtures were injected onto the column in HPLC solvent A (0.5% acetic acid) at a flow rate of 500 nl/min and subsequently eluted with a 106 min gradient of 5–33% HPLC solvent B (80% ACN in 0.5% acetic acid). During peptide elution the flow rate was kept constant at 200 nl/min. For proteome analysis, the 20 (Orbitrap Elite) most intense precursor ions were sequentially fragmented in each scan cycle using collision-induced dissociation (CID). In all measurements, sequenced precursor masses were excluded from further selection for 90 s. The target values for MS/MS fragmentation were 5000 charges and 10^6 charges for the MS scan.

Mass spectrometry data processing for analysis of crosslinked interaction partners

The MS data were processed with MaxQuant software suite v.1.2.2.9 as described previously [47–49] with slight modifications. Database search was performed using the Andromeda search engine [48], which is part of MaxQuant. MS/MS spectra were searched against a target database consisting of 10,152 protein entries from *S.* Typhimurium and 248 commonly observed contaminants. In database search, full tryptic specificity was required and up to two missed cleavages were allowed. Carbamidomethylation of cysteine was set as fixed modification, protein N-terminal acetylation, and oxidation of methionine were set as variable modifications. Initial precursor mass tolerance was set to 6 parts per million (ppm) and at the

fragment ion level 0.5 dalton (Da) was set for CID fragmentation. The MS data have been deposited to the ProteomeXchange Consortium (http://proteomecentral.proteomexchange.org) via the PRIDE partner repository with the data set identifier PXD005028.

EVfold coupling analysis

Sequence co-variation analysis was performed using EVcouplings [26–28] with pseudo-maximum likelihood approximation [50–52]. The multiple sequence alignment used as input for the model inference was created by jackhmmer 3.1 [53] (5 iterations) using the full sequence of Salmonella SpaP (UniProt: SPAP_SALTY, residues 1–224) as query against the November 2015 release of the UniProt Reference Cluster database (UniRef100) [54]. Sequences with more than 30% gaps are subsequently removed from the alignment. We then excluded alignment columns that contained 50% or more gaps from model inference and subsequent couplings predictions. Lastly, sequences were clustered at 80% sequence identity and then downweighted according to the cluster size to reduce redundancy. This resulted in an alignment of 5663 unique sequences with an effective number of 1080.4 non-redundant sequences (sequences/alignment length = 4.8) included in model inference and coupling prediction. The coupling scores of residue pairs were further normalized by estimating the background noise analogously to the procedure described in Hopf et al., 2014 [28]. Evaluation of the co-evolution prediction was done in the light of topology predictions obtained from deltaG, resulting in four predicted TM segments: (7, 38), (50, 75), (163, 193), (194, 211). Python (Python Software Foundation, http://www.python.org) and Ipython/Jupyter notebooks [55] were used for data analysis. The multiple sequence alignment, EC scores file, a contact map of the strongest couplings and an Ipython notebook of the analysis are available as supplement (S3 Table, S8 Fig, S2 and S3 Files).

Electron microscopy and image analysis

Isolated SpaPR^{FLAG} complexes were deposited on glow-discharged carbon coated copper-palladium grids and stained with 0.75% uranyl formate. Micrograph acquisition was performed on a FEI Tecnai F30 Polara at 300 kV, equipped with a Gatan Ultrascan 4000 UHS CCD (4k x 4k pixels, physical pixel size of 15 μm), using the LEGINON automated image acquisition system [56]. The corrected magnification was 71950x, resulting in a pixel size of 2.08 Å/pixel. 11202 particles were picked from the micrographs with EMAN2 boxer [57]. Particle images were first subjected to a maximum-likelihood classification and alignment (ML2D) in XMIPP [58] and then further processed in IMAGIC-5 (Image Science Software GmbH) through multi-reference alignment and classification by multi-variate statistical analysis.

SpaPR pore assessment by biotin maleimide labeling

SpaP or SpaPQR^{FLAG} were moderately overexpressed in *S*. Typhimurium strain SB1770 (Δ*prgHIJK*, *flhD*::*tet*) from a rhamnose-inducible medium copy number plasmid by induction with 20 μM rhamnose. BM labeling was performed essentially as previously described [29], with minor modifications: After 3 h of induction, 0.2 ODU of bacterial cells were transferred to a fresh reaction tube and brought to the same volume by addition of fresh LB broth. Cells were labeled by addition of BM (EZ-link maleimide-PEG2-biotin, Thermo Pierce, final concentration 0.4 mM) for 30 min at room temperature with gentle agitation. The reaction was quenched by addition 2M β-mercaptoethanol to a final concentration of 10 mM. Cells were pelleted, re-suspended in SB buffer and incubated at 70˚C for 10 min. BM labeling of proteins was analyzed by SDS PAGE, Western blotting, and detection of BM with streptavidin DyLight

800 dye (Thermo pierce). Scanning of the PVDF membrane and image analysis was performed with a Li-Cor Odyssey system and image Studio 2.1.10 (Li-Cor).

For subcellular fractionation, BM-labeled bacterial cells were pelleted by centrifugation. The culture supernatant was harvested and TCA precipitated. The bacterial cell pellet was resuspended and used to prepare the periplasmic and cytoplasmic fractions as described elsewhere. Briefly, pellets were resuspended by pipetting gently in ice-cold spheroplast buffer (40% sucrose, 33 mM Tris-HCl, pH 8.0) with freshly prepared lysozyme to a final concentration of 200 μg/ml, 50 μg/ml DNAse and 1.5 mM EDTA. The mixture was left on ice for 30 min with gentle stirring. Spheroplasts were stabilized by adding 20 mM $MgCl_2$ and centrifuged at 3000 x g for 10 min at 4˚C. The supernatant was transferred to ultracentrifugation tubes and centrifuged at 30 krpm for 30 min at 4˚C in a Beckman TLA55 rotor to remove insoluble material. The supernatant (periplasmic fraction) was collected into fresh tube. The cytoplasmic fraction was prepared by resuspending the pellet of spheroplasts in 1 ml of 20 mM Tris-HCl, pH 8.0 and subsequent lysis by bead milling as described above. Lysates were transferred to ultracentrifugation tubes and centrifuged at 55 krpm for 45 min at 4˚C in a Beckman TLA55 rotor. The supernatant (cytoplasmic fraction) was collected into fresh tubes.

Supporting Information

S1 Table. Raw data of the size exclusion chromatography-multi angle laser light scattering analysis of the purified SpaPR complex.
(XLSX)

S2 Table. Crosslinked adducts identified by mass spectrometry.
(XLSX)

S3 Table. EC scores of coupling prediction.
(XLSX)

S4 Table. Strains and plasmids.
(XLSX)

S5 Table. Oligonucleotides.
(XLSX)

S1 Fig. Three detector calibration of the SEC-MALLS equipment and error calculation.
(PDF)

S2 Fig. Functional analysis of SpaP and SpaR *p*Bpa mutants. (A) Type III dependent secretion into the culture supernatant of indicated *p*Bpa mutants of SpaP and SpaR, respectively, was assayed by SDS PAGE and immunodetection of the early substrate InvJ and the intermediate substrate SipB. For two of the secretion-deficient SpaP mutants (T15X, M187X), assembly of SpaP into the needle complex was confirmed by 2-dimensional blue native/SDS PAGE (Fig 3C). Further, many secretion-defective *p*Bpa mutants showed productive crosslinks to other needle complex components. These results suggest that secretion-deficiency was not due to gross structural defects but rather the result of subtle conformational changes. (B) As in (A) but detailing secretion profiles of chromosome-encoded SpaP-*p*Bpa mutants.
(TIF)

S3 Fig. SDS PAGE analysis of isolated needle complexes of SpaP and SpaR *p*Bpa mutants with and without UV photocrosslinking for mass spectrometrical identification of crosslinking partners. (A) Immunodetection of $SpaP^{FLAG}$ and $SpaR^{FLAG}$, respectively, on Western blots of purified needle complexes of *S*. Typhimurium expressing indicated SpaP or SpaR *p*Bpa

mutants separated by SDS PAGE. Each sample is shown with and without UV-irradiation to induce photocrosslinking of the *p*Bpa to neighboring interaction partners. Identified interaction partners are indicated at the respective bands. A summary of the MS identifications is shown in S2 Table. (B) Coomassie stained SDS PAGE gels of the UV-irradiated samples shown in (A). Gel pieces were cut out at positions of crosslinking adducts identified by Western blotting and immunodetection for subsequent in gel Trypsin digestion and MS analysis.
(TIF)

S4 Fig. Class averages of negative-stained isolated SpaPR complexes imaged by electron microscopy. 91 classes are shown. The length of the scale bar in the upper left corner represents 50 Å.
(TIF)

S5 Fig. Controls for general bacterial lysis for biotin maleimide labeling experiments. (A) Coomassie-stained gel (left) and immunodetection (cytoplasmic marker RNA polymerase (RNApol), periplasmic marker maltose binding protein (MBP), right) of SDS PAGE-separated whole cell lysates and cell culture supernatants, respectively, of *S*. Typhimurium Δ*prgHIJK*, *flhD*::*tet* moderately overexpressing indicated proteins from a medium copy number plasmid (pT12). Equal culture volumes were loaded in each well. (B) Immunodetection of SDS PAGE-separated cell culture supernatants, periplasmic fractions, and cytoplasmic fractions, respectively, of *S*. Typhimurium Δ*prgHIJK*, *flhD*::*tet* moderately overexpressing indicated proteins from a medium copy number plasmid (pT12). Equal culture volumes were loaded in each well. RNApol serves as a marker protein for cytoplasmic proteins, MBP serves as a marker protein for periplasmic proteins. (C) Growth curves of *S*. Typhimurium Δ*prgHIJK*, *flhD*::*tet* overexpressing indicated proteins from a medium copy number plasmid (pT12) with the indicated concentrations of rhamnose.
(TIF)

S6 Fig. Prediction of topology and of the propensity of membrane integration of SpaR. (A) Topcons prediction of SpaR (topcons.cbr.su.se). (B) Prediction of ΔG for membrane integration propensity of SpaR using a sliding window between 18 and 31 amino acids (dgpred.cbr.su.se). (C) Protter visualization of the topology model of SpaR comprising 3 TM helices and an N-out/C-in orientation. Positions of detected crosslinks of SpaR to other T3SS components are indicated in color.
(TIF)

S7 Fig. Position and sequence of epitope tags used in SpaP, SpaR, and SpaS.
(PDF)

S8 Fig. Contact map of top 291 residue couplings. Abbreviations: norm. normalized, exp. experimentally.
(PNG)

S1 File. SEC-MALLS ASTRA calculations.
(PDF)

S2 File. Input alignment in fasta format.
(A2M)

S3 File. Notebook containing couplings analysis.
(HTML)

Acknowledgments

We acknowledge Ewa Folta-Stogniew and the Biophysics Resource of Keck Facility at Yale University for performing size exclusion chromatography—multi angle laser light scattering analysis.

Author Contributions

Conceptualization: JEG SW.

Data curation: MFW.

Formal analysis: TD MTM MJB CS OK TCM SW.

Funding acquisition: JEG SW.

Investigation: TD MTM MJB PA JY MFW CS SW.

Methodology: TD MTM MJB PA SZ IG MFW SL BM CVR SW.

Software: CS OK.

Validation: TD MTM SZ.

Visualization: TD MTM MJB JY CS SW.

Writing – original draft: TD MTM MJB PA JY MFW CS SW.

Writing – review & editing: JEG SW.

References

1. Galán JE, Lara-Tejero M, Marlovits TC, Wagner S. Bacterial type III secretion systems: specialized nanomachines for protein delivery into target cells. Annu Rev Microbiol. 2014; 68: 415–438. doi: 10.1146/annurev-micro-092412-155725 PMID: 25002086
2. Galán JE. SnapShot: effector proteins of type III secretion systems. Cell. 2007; 130: 192–192.e2. doi: 10.1016/j.cell.2007.06.042 PMID: 17632065
3. Schraidt O, Marlovits TC. Three-dimensional model of Salmonella's needle complex at subnanometer resolution. Science. 2011; 331: 1192–1195. doi: 10.1126/science.1199358 PMID: 21385715
4. Kubori T, Matsushima Y, Nakamura D, Uralil J, Lara-Tejero M, Sukhan A, et al. Supramolecular structure of the *Salmonella typhimurium* type III protein secretion system. Science. 1998; 280: 602–605. PMID: 9554854
5. Radics J, Königsmaier L, Marlovits TC. Structure of a pathogenic type 3 secretion system in action. Nat Struct Mol Biol. 2014; 21: 82–87. doi: 10.1038/nsmb.2722 PMID: 24317488
6. Akeda Y, Galán JE. Chaperone release and unfolding of substrates in type III secretion. Nature. 2005; 437: 911–915. doi: 10.1038/nature03992 PMID: 16208377
7. Lara-Tejero M, Kato J, Wagner S, Liu X, Galán JE. A sorting platform determines the order of protein secretion in bacterial type III systems. Science. 2011; 331: 1188–1191. doi: 10.1126/science.1201476 PMID: 21292939
8. Fan F, Ohnishi K, Francis NR, Macnab RM. The FliP and FliR proteins of Salmonella typhimurium, putative components of the type III flagellar export apparatus, are located in the flagellar basal body. Mol Microbiol. 1997; 26: 1035–1046. PMID: 9426140
9. Wagner S, Königsmaier L, Lara-Tejero M, Lefebre M, Marlovits TC, Galán JE. Organization and coordinated assembly of the type III secretion export apparatus. Proc Natl Acad Sci USA. 2010; 107: 17745–17750. doi: 10.1073/pnas.1008053107 PMID: 20876096
10. Burkinshaw BJ, Strynadka NCJ. Assembly and structure of the T3SS. Biochim Biophys Acta. 2014; 1843: 1649–1663. doi: 10.1016/j.bbamcr.2014.01.035 PMID: 24512838
11. Abrusci P, McDowell MA, Lea SM, Johnson S. Building a secreting nanomachine: a structural overview of the T3SS. Curr Opin Struct Biol. Elsevier Ltd; 2014; 25: 111–117.

12. Zilkenat S, Franz-Wachtel M, Stierhof Y-D, Galán JE, Macek B, Wagner S. Determination of the stoichiometry of the complete bacterial type III secretion needle complex using a combined quantitative proteomic approach. Molecular & Cellular Proteomics. 2016; 15: 1598–1609.

13. Zarivach R, Deng W, Vuckovic M, Felise HB, Nguyen HV, Miller SI, et al. Structural analysis of the essential self-cleaving type III secretion proteins EscU and SpaS. Nature. Nature Publishing Group; 2008; 453: 124–127.

14. Worrall LJ, Vuckovic M, Strynadka NCJ. Crystal structure of the C-terminal domain of the Salmonella type III secretion system export apparatus protein InvA. Protein Sci. 2010; 19: 1091–1096. doi: 10.1002/pro.382 PMID: 20306492

15. Abrusci P, Vergara-Irigaray M, Johnson S, Beeby MD, Hendrixson DR, Roversi P, et al. Architecture of the major component of the type III secretion system export apparatus. Nat Struct Mol Biol. 2012; 20: 99–104. doi: 10.1038/nsmb.2452 PMID: 23222644

16. Hirano T, Mizuno S, Aizawa S-I, Hughes KT. Mutations in flk, flgG, flhA, and flhE that affect the flagellar type III secretion specificity switch in Salmonella enterica. J Bacteriol. 2009; 191: 3938–3949. doi: 10.1128/JB.01811-08 PMID: 19376867

17. Minamino T, Shimada M, Okabe M, Saijo-Hamano Y, Imada K, Kihara M, et al. Role of the C-terminal cytoplasmic domain of FlhA in bacterial flagellar type III protein export. J Bacteriol. American Society for Microbiology; 2010; 192: 1929–1936.

18. Hara N, Namba K, Minamino T. Genetic characterization of conserved charged residues in the bacterial flagellar type III export protein FlhA. PLoS ONE. 2011; 6: e22417. doi: 10.1371/journal.pone.0022417 PMID: 21811603

19. Ferris HU, Minamino T. Flipping the switch: bringing order to flagellar assembly. Trends Microbiol. 2006; 14: 519–526. doi: 10.1016/j.tim.2006.10.006 PMID: 17067800

20. Monjarás Feria JV, Lefebre MD, Stierhof Y-D, Galán JE, Wagner S. Role of autocleavage in the function of a type III secretion specificity switch protein in *Salmonella enterica* serovar Typhimurium. MBio. American Society for Microbiology; 2015; 6: e01459–15.

21. Diepold A, Wiesand U, Cornelis GR. The assembly of the export apparatus (YscR,S,T,U,V) of the *Yersinia* type III secretion apparatus occurs independently of other structural components and involves the formation of an YscV oligomer. Mol Microbiol. 2011; 82: 502–514. doi: 10.1111/j.1365-2958.2011.07830.x PMID: 21923772

22. Yerushalmi G, Litvak Y, Gur-Arie L, Rosenshine I. Dynamics of expression and maturation of the type III secretion system of enteropathogenic Escherichia coli. J Bacteriol. 2014; 196: 2798–2806. doi: 10.1128/JB.00069-14 PMID: 24837293

23. Diepold A, Wagner S. Assembly of the bacterial type III secretion machinery. FEMS Microbiol Rev. 2014; 38: 802–822. doi: 10.1111/1574-6976.12061 PMID: 24484471

24. Collazo CM, Galan JE. Requirement for exported proteins in secretion through the invasion-associated type III system of *Salmonella* typhimurium. Infection and Immunity. 1996; 64: 3524–3531. PMID: 8751894

25. Farrell IS, Toroney R, Hazen JL, Mehl RA, Chin JW. Photo-cross-linking interacting proteins with a genetically encoded benzophenone. Nat Methods. 2005; 2: 377–384. doi: 10.1038/nmeth0505-377 PMID: 16170867

26. Marks DS, Colwell LJ, Sheridan R, Hopf TA, Pagnani A, Zecchina R, et al. Protein 3D structure computed from evolutionary sequence variation. Sali A, editor. PLoS ONE. Public Library of Science; 2011; 6: e28766.

27. Morcos F, Pagnani A, Lunt B, Bertolino A, Marks DS, Sander C, et al. Direct-coupling analysis of residue coevolution captures native contacts across many protein families. Proc Natl Acad Sci USA. National Acad Sciences; 2011; 108: E1293–301.

28. Hopf TA, Schärfe CPI, Rodrigues JPGLM, Green AG, Kohlbacher O, Sander C, et al. Sequence co-evolution gives 3D contacts and structures of protein complexes. Elife. 2014; 3: 65.

29. Park E, Rapoport TA. Preserving the membrane barrier for small molecules during bacterial protein translocation. Nature. Nature Publishing Group; 2011; 473: 239–242.

30. Marlovits TC, Kubori T, Sukhan A, Thomas DR, Galán JE, Unger VM. Structural insights into the assembly of the type III secretion needle complex. Science. 2004; 306: 1040–1042. doi: 10.1126/science.1102610 PMID: 15528446

31. Van Arnam JS, McMurry JL, Kihara M, Macnab RM. Analysis of an engineered Salmonella flagellar fusion protein, FliR-FlhB. J Bacteriol. 2004; 186: 2495–2498. doi: 10.1128/JB.186.8.2495-2498.2004 PMID: 15060055

32. Marlovits TC, Kubori T, Lara-Tejero M, Thomas D, Unger VM, Galán JE. Assembly of the inner rod determines needle length in the type III secretion injectisome. Nature. 2006; 441: 637–640. doi: 10.1038/nature04822 PMID: 16738660

33. Lefebre MD, Lefebre MD, Galan JE, Galán JE. The inner rod protein controls substrate switching and needle length in a Salmonella type III secretion system. Proc Natl Acad Sci USA. 2014; 111: 817–822. doi: 10.1073/pnas.1319698111 PMID: 24379359

34. Ohnishi K, Fan F, Schoenhals GJ, Kihara M, Macnab RM. The FliO, FliP, FliQ, and FliR proteins of Salmonella typhimurium: putative components for flagellar assembly. J Bacteriol. 1997; 179: 6092–6099. PMID: 9324257

35. Berger C, Robin GP, Bonas U, Koebnik R. Membrane topology of conserved components of the type III secretion system from the plant pathogen Xanthomonas campestris pv. vesicatoria. Microbiology (Reading, Engl). 2010; 156: 1963–1974.

36. Allaoui A, Woestyn S, Sluiters C, Cornelis GR. YscU, a Yersinia enterocolitica inner membrane protein involved in Yop secretion. J Bacteriol. 1994; 176: 4534–4542. PMID: 8045883

37. Hoiseth SK, Stocker BA. Aromatic-dependent *Salmonella typhimurium* are non-virulent and effective as live vaccines. Nature. 1981; 291: 238–239. PMID: 7015147

38. Folta-Stogniew E. Oligomeric states of proteins determined by size-exclusion chromatography coupled with light scattering, absorbance, and refractive index detectors. Methods Mol Biol. New Jersey: Humana Press; 2006; 328: 97–112.

39. Pringle SD, Giles K, Wildgoose JL, Williams JP, Slade SE, Thalassinos K, et al. An investigation of the mobility separation of some peptide and protein ions using a new hybrid quadrupole/travelling wave IMS/oa-ToF instrument. International Journal of Mass Spectrometry. 2007; 261: 1–12.

40. Hernández H, Robinson CV. Determining the stoichiometry and interactions of macromolecular assemblies from mass spectrometry. Nat Protoc. 2007; 2: 715–726. doi: 10.1038/nprot.2007.73 PMID: 17406634

41. Tsirigos KD, Peters C, Shu N, Käll L, Elofsson A. The TOPCONS web server for consensus prediction of membrane protein topology and signal peptides. Nucleic Acids Res. Oxford University Press; 2015; 43: W401–7.

42. Hessa T, Meindl-Beinker NM, Bernsel A, Kim H, Sato Y, Lerch-Bader M, et al. Molecular code for transmembrane-helix recognition by the Sec61 translocon. Nature. 2007; 450: 1026–1030. doi: 10.1038/nature06387 PMID: 18075582

43. Omasits U, Ahrens CH, Müller S, Wollscheid B. Protter: interactive protein feature visualization and integration with experimental proteomic data. Bioinformatics. Oxford University Press; 2014; 30: 884–886.

44. Borchert N, Dieterich C, Krug K, Schütz W, Jung S, Nordheim A, et al. Proteogenomics of Pristionchus pacificus reveals distinct proteome structure of nematode models. Genome Res. Cold Spring Harbor Lab; 2010; 20: 837–846.

45. Rappsilber J, Mann M, Ishihama Y. Protocol for micro-purification, enrichment, pre-fractionation and storage of peptides for proteomics using StageTips. Nat Protoc. Nature Publishing Group; 2007; 2: 1896–1906.

46. Franz-Wachtel M, Eisler SA, Krug K, Wahl S, Carpy A, Nordheim A, et al. Global detection of protein kinase D-dependent phosphorylation events in nocodazole-treated human cells. Molecular & Cellular Proteomics. American Society for Biochemistry and Molecular Biology; 2012; 11: 160–170.

47. Cox J, Mann M. MaxQuant enables high peptide identification rates, individualized p.p.b.-range mass accuracies and proteome-wide protein quantification. Nat Biotechnol. Nature Publishing Group; 2008; 26: 1367–1372.

48. Cox J, Neuhauser N, Michalski A, Scheltema RA, Olsen JV, Mann M. Andromeda: a peptide search engine integrated into the MaxQuant environment. J Proteome Res. American Chemical Society; 2011; 10: 1794–1805.

49. Carpy A, Krug K, Graf S, Koch A, Popic S, Hauf S, et al. Absolute proteome and phosphoproteome dynamics during the cell cycle of Schizosaccharomyces pombe (Fission Yeast). Molecular & Cellular Proteomics. American Society for Biochemistry and Molecular Biology; 2014; 13: 1925–1936.

50. Balakrishnan S, Kamisetty H, Carbonell JG, Lee S-I, Langmead CJ. Learning generative models for protein fold families. Proteins. Wiley Subscription Services, Inc., A Wiley Company; 2011; 79: 1061–1078.

51. Ekeberg M, Lövkvist C, Lan Y, Weigt M, Aurell E. Improved contact prediction in proteins: using pseudolikelihoods to infer Potts models. Phys Rev E Stat Nonlin Soft Matter Phys. American Physical Society; 2013; 87: 012707.

52. Kamisetty H, Ovchinnikov S, Baker D. Assessing the utility of coevolution-based residue-residue contact predictions in a sequence- and structure-rich era. Proc Natl Acad Sci USA. National Acad Sciences; 2013; 110: 15674–15679.

53. Johnson LS, Eddy SR, Portugaly E. Hidden Markov model speed heuristic and iterative HMM search procedure. BMC Bioinformatics. BioMed Central; 2010; 11: 431.

54. Suzek BE, Wang Y, Huang H, McGarvey PB, Wu CH, UniProt Consortium. UniRef clusters: a comprehensive and scalable alternative for improving sequence similarity searches. Bioinformatics. Oxford University Press; 2015; 31: 926–932.

55. Perez F, Granger BE. IPython: A system for interactive scientific computing. Comput Sci Eng. 2007; 9: 21–29.

56. Suloway C, Pulokas J, Fellmann D, Cheng A, Guerra F, Quispe J, et al. Automated molecular microscopy: the new Leginon system. J Struct Biol. 2005; 151: 41–60. doi: 10.1016/j.jsb.2005.03.010 PMID: 15890530

57. Tang G, Peng L, Baldwin PR, Mann DS, Jiang W, Rees I, et al. EMAN2: an extensible image processing suite for electron microscopy. J Struct Biol. 2007; 157: 38–46. doi: 10.1016/j.jsb.2006.05.009 PMID: 16859925

58. Sorzano COS, Marabini R, Velázquez-Muriel J, Bilbao-Castro JR, Scheres SHW, Carazo JM, et al. XMIPP: a new generation of an open-source image processing package for electron microscopy. J Struct Biol. 2004; 148: 194–204. doi: 10.1016/j.jsb.2004.06.006 PMID: 15477099

Publication 2

PLOS BIOLOGY

RESEARCH ARTICLE

A flagellum-specific chaperone facilitates assembly of the core type III export apparatus of the bacterial flagellum

Florian D. Fabiani[1‡], Thibaud T. Renault[1,2‡], Britta Peters[3☯], Tobias Dietsche[4☯], Eric J. C. Gálvez[5☯], Alina Guse[1], Karen Freier[1], Emmanuelle Charpentier[2], Till Strowig[5], Mirita Franz-Wachtel[6], Boris Macek[6], Samuel Wagner[4,7], Michael Hensel[3], Marc Erhardt[1]*

1 Junior Research Group Infection Biology of *Salmonella*, Helmholtz Centre for Infection Research, Braunschweig, Germany, **2** Max Planck Institute for Infection Biology, Berlin, Germany, **3** Abteilung Mikrobiologie, Fachbereich Biologie/Chemie, University of Osnabrück, Osnabrück, Germany, **4** Interfaculty Institute of Microbiology and Infection Medicine (IMIT), Section of Cellular and Molecular Microbiology, University of Tübingen, Tübingen, Germany, **5** Junior Research Group Microbial Immune Regulation, Helmholtz Centre for Infection Research, Braunschweig, Germany, **6** Proteome Center Tübingen, University of Tübingen, Tübingen, Germany, **7** German Center for Infection Research (DZIF), Partner-site Tübingen, Tübingen, Germany

☯ These authors contributed equally to this work.
‡ These authors are joint first authors on this work.
* marc.erhardt@helmholtz-hzi.de

OPEN ACCESS

Citation: Fabiani FD, Renault TT, Peters B, Dietsche T, Gálvez EJC, Guse A, et al. (2017) A flagellum-specific chaperone facilitates assembly of the core type III export apparatus of the bacterial flagellum. PLoS Biol 15(8): e2002267. https://doi.org/10.1371/journal.pbio.2002267

Academic Editor: Ann Stock, UMDNJ/Robert Wood Johnson Medical School, United States of America

Received: February 22, 2017

Accepted: June 30, 2017

Published: August 3, 2017

Data Availability Statement: The mass spectrometry data have been deposited to the ProteomeXchange Consortium (http://proteomecentral.proteomexchange.org) via the PRIDE partner repository with the data set identifier PXD005597.

Funding: Deutsche Forschungsgemeinschaft (grant number SFB 944 projects P4 and Z). Received by M.H.. The funder had no role in study design, data collection and analysis, decision to

Abstract

Many bacteria move using a complex, self-assembling nanomachine, the bacterial flagellum. Biosynthesis of the flagellum depends on a flagellar-specific type III secretion system (T3SS), a protein export machine homologous to the export machinery of the virulence-associated injectisome. Six cytoplasmic (FliH/I/J/G/M/N) and seven integral-membrane proteins (FlhA/B FliF/O/P/Q/R) form the flagellar basal body and are involved in the transport of flagellar building blocks across the inner membrane in a proton motive force-dependent manner. However, how the large, multi-component transmembrane export gate complex assembles in a coordinated manner remains enigmatic. Specific for most flagellar T3SSs is the presence of FliO, a small bitopic membrane protein with a large cytoplasmic domain. The function of FliO is unknown, but homologs of FliO are found in >80% of all flagellated bacteria. Here, we demonstrate that FliO protects FliP from proteolytic degradation and promotes the formation of a stable FliP–FliR complex required for the assembly of a functional core export apparatus. We further reveal the subcellular localization of FliO by super-resolution microscopy and show that FliO is not part of the assembled flagellar basal body. In summary, our results suggest that FliO functions as a novel, flagellar T3SS-specific chaperone, which facilitates quality control and productive assembly of the core T3SS export machinery.

Author summary

Many bacteria use the bacterial flagellum for directed movement in various environments. The assembly and function of the bacterial flagellum and the related virulence-associated

publish, or preparation of the manuscript. Deutsche Forschungsgemeinschaft (grant number SFB 766 project B14). Received by S.W.. The funder had no role in study design, data collection and analysis, decision to publish, or preparation of the manuscript. Helmholtz Association (grant number VH-GS-202). Received by F.D.F.. The funder had no role in study design, data collection and analysis, decision to publish, or preparation of the manuscript. Alexander von Humboldt Foundation. Received by T.T.R.. The funder had no role in study design, data collection and analysis, decision to publish, or preparation of the manuscript. Europeans Unions FP7 (grant number 334030). Received by M.E.. The funder had no role in study design, data collection and analysis, decision to publish, or preparation of the manuscript. Deutsche Forschungsgemeinschaft (grant number ER 778/2-1). Received by M.E.. The funder had no role in study design, data collection and analysis, decision to publish, or preparation of the manuscript. Helmholtz Association (grant number VH-NG-932). Received by M.E.. The funder had no role in study design, data collection and analysis, decision to publish, or preparation of the manuscript.

Competing interests: The authors have declared that no competing interests exist.

Abbreviations: BN-PAGE, blue native PAGE; C ring, cytoplasmic ring; DDM, n-dodecyl-β-D-maltoside; dSTORM, direct stochastic optical reconstruction microscopy; fT3SS, flagellar-specific type III secretion system; HA, 3×hemagglutinin; HBB, hook-basal-body; HMM, Hidden Markov Model; LB, lysogeny broth; LC-MS/MS, liquid chromatography-tandem mass spectrometry; MSD, Mean square displacement; Pfam, protein family; pmf, proton motive force; SIM, structured illumination microscopy; SMT, Single-molecule tracking; T3SS, type III secretion system; TIRF, total internal reflection fluorescence; VC, vector control; vT3SS, virulence-associated type III secretion system; WT, wild type.

injectisome relies on protein export via a conserved type III secretion system (T3SS). The multicomponent transmembrane core export apparatus of the flagellar T3SS consists of FlhA/B and FliP/Q/R and must assemble in a highly coordinated manner. In the present study, we determined the role of the transmembrane protein FliO in the maturation of the flagellar core protein export apparatus. We show that FliO functions as a flagellum-specific chaperone during the initial step of export apparatus assembly. FliO facilitates the efficient formation of a stable FliP–FliR core complex and is thus required for quality management and productive assembly of the flagellar export apparatus. Our results suggest a coordinated assembly process of the flagellar core export apparatus that nucleates with the FliO-dependent formation of a FliP–FliR complex. Subsequent incorporation of FliQ, FlhB, and FlhA leads to the assembly of a secretion-competent flagellar T3SS.

Introduction

The ability of many bacteria to move on surfaces and swim through liquid environments depends on the function of a rotating nanomachine, the bacterial flagellum. The flagellum is highly conserved among bacterial species and is best characterized in *Salmonella enterica* serovar Typhimurium. The structure of the flagellum can be divided into 3 main parts: a basal body, a flexible hook, and a long rigid filament [1,2]. The basal body itself is composed of several substructures located in the cytosol or spanning the bacterial cell envelope. The inner membrane MS ring, the periplasmic P ring, and the outer membrane L ring assemble using the Sec-pathway. The self-assembly of all other axial parts of the flagellum is dependent on protein export through the flagellar-specific type III secretion system (fT3SS) [3]. The core integral-membrane components of the flagellar export apparatus (FlhA/B and FliP/Q/R) are closely related to the virulence-associated T3SS (vT3SS) of the injectisome device used by many gram-negative bacteria to inject toxins into host cells [4]. Protein export via both fT3SS and vT3SS is primarily dependent on the proton motive force (pmf) [5–9]. How the bacterial cell coordinates the self-assembly of the multicomponent export apparatus complex in the inner membrane remains elusive.

Six cytoplasmic and seven membrane proteins are essential for the export of the majority of the extra-cytoplasmic building blocks of the flagellum. The MS ring is made of 26 subunits of FliF and likely assembles after the completion of the core integral membrane export apparatus, similar to the injectisome system [10–13]. Tightly associated with the MS ring is a cytoplasmic ring (C ring) made of FliG/M/N. The C ring functions as a rotor/switch complex and serves also as a docking platform for cargo [14] and the FliH/I/J ATPase complex [15,16], which facilitates export via ATP hydrolysis [7,17]. Within the MS ring, the integral membrane proteins FlhB/A and FliO/P/Q/R are thought to form the export gate. FlhA was reported to form a nonameric ring and presumably energizes export using the pmf [11,18–20]. FlhB is involved in the switch of secretion specificity between late and early substrates [21]. FliO (17.5 kDa), FliP (25 kDa), FliQ (9 kDa), and FliR (26 kDa) are integral membrane proteins and essential for the export of flagellar substrates [22]. FliP/Q/R are highly conserved in all fT3SS and have homologs in the vT3SS [23]. Interestingly, FliO homologs are apparently absent in the vT3SS, suggesting an important fT3SS-specific role [24]. FliO is a bitopic membrane protein with a large cytosolic C-terminal domain. While FliO is required for flagella formation and motility under physiological conditions, upregulation of flagellar secretion substrates and a secondary-site suppressor mutation in FliP restored partial motility of a Δ*fliO* strain, indicating a functional link between FliO and FliP [25–27].

Here, we determined the molecular function of FliO in maturation of the flagellar type III secretion system (T3SS). We propose that FliO functions as a flagellum-specific, integral membrane chaperone that stabilizes FliP protein and facilitates the formation of a stable FliP–FliR core complex, which is essential for the productive assembly of a functional flagellar basal body.

Results

Phylogenetic distribution of FliO reveals widespread conservation

Homologs of FliO are absent in vT3SS of the injectisome and were also thought to be absent in many flagellated species. However, Pallen et al. [28] suggested that FliO homologs are misannotated as FliZ in some bacterial species and identified several potential FliO homologs through PSI-BLAST searches: Cj0352 in *Campylobacter jejuni*, LA2612 in *Leptospira interrogans*, RB9276 in *Rhodopirellula baltica*, and TP0719 in *Treponema pallidum*.

This suggested that FliO homologs are more widespread than previously thought, and we thus performed a detailed phylogenetic analysis of the distribution of FliO proteins across different bacterial phyla (Fig 1). We retrieved the full collection of representative genomes from the *refseq* NCBI repository ($n = 4771$) and queried the genomes for the presence of flagellin, FliO, FliP, FliQ, and FliR homologs using regular annotations. We found that FliO homologs in particular were poorly annotated and in fact sometimes misannotated as FliZ, as previously noted by Pallen et al. [28]. This suggested that a large proportion of FliO homologs are missed by the automated annotation algorithms.

We next performed a de novo prediction of flagellin, FliO, FliP, FliQ, and FliR homologs using Hidden Markov Models (HMMs) based on curated Pfam (protein family) database models (Fig 1, S1 Fig). We screened all genomes using the HMM and identified a large number of FliO homologs in genomes in which also FliP and other flagella components were predicted. The majority of predicted FliO hits corresponded to hypothetical proteins, and we identified possible FliO homologs in >80% of flagellated bacteria across most bacterial phyla (Fig 1).

FliO protects FliP from proteolytic degradation

The gene encoding for FliP is frequently encoded in an operon with *fliO*, and a previous study suggested a functional link between FliO and FliP based on genetic evidence [26]. FliP is strongly conserved in both fT3SS and vT3SS (S2 Fig) and essential for protein export [22]. Accordingly, we hypothesized that the flagellum-specific protein FliO evolved to facilitate efficient production or assembly of FliP, a core component of the fT3SS. In an attempt to validate the presumed functional link between FliO and FliP, we analyzed the effect of excess FliP and FliO in wild-type (WT) and Δ*fliO* backgrounds. In the WT background, neither expression of FliP nor FliO increased motility compared to the empty vector control (VC) (Fig 2 + S3 Fig). In the *fliO* deletion background, overproduction of FliP but not of any other fT3SS integral membrane protein restored motility (S4 Fig). These results confirmed that FliO is functionally related to FliP.

The dispensability of FliO upon FliP overexpression led us to speculate that FliO was involved in maintaining FliP stability. To follow this idea, we monitored FliP protein levels after the arrest of de novo protein synthesis. We replaced the native *fliP* gene with epitope-tagged FliP variants to facilitate the detection of FliP protein. The 3×hemagglutinin (HA)- or 3×FLAG-tagged FliP proteins were expressed from the physiological *fliP* locus and retained WT function in a swimming plate motility assay (S5 Fig).

In a WT background, FliP remained stable after synthesis inhibition during the duration of the experiment. In a Δ*fliO* mutant, however, FliP protein levels degraded rapidly (Fig 3A). This

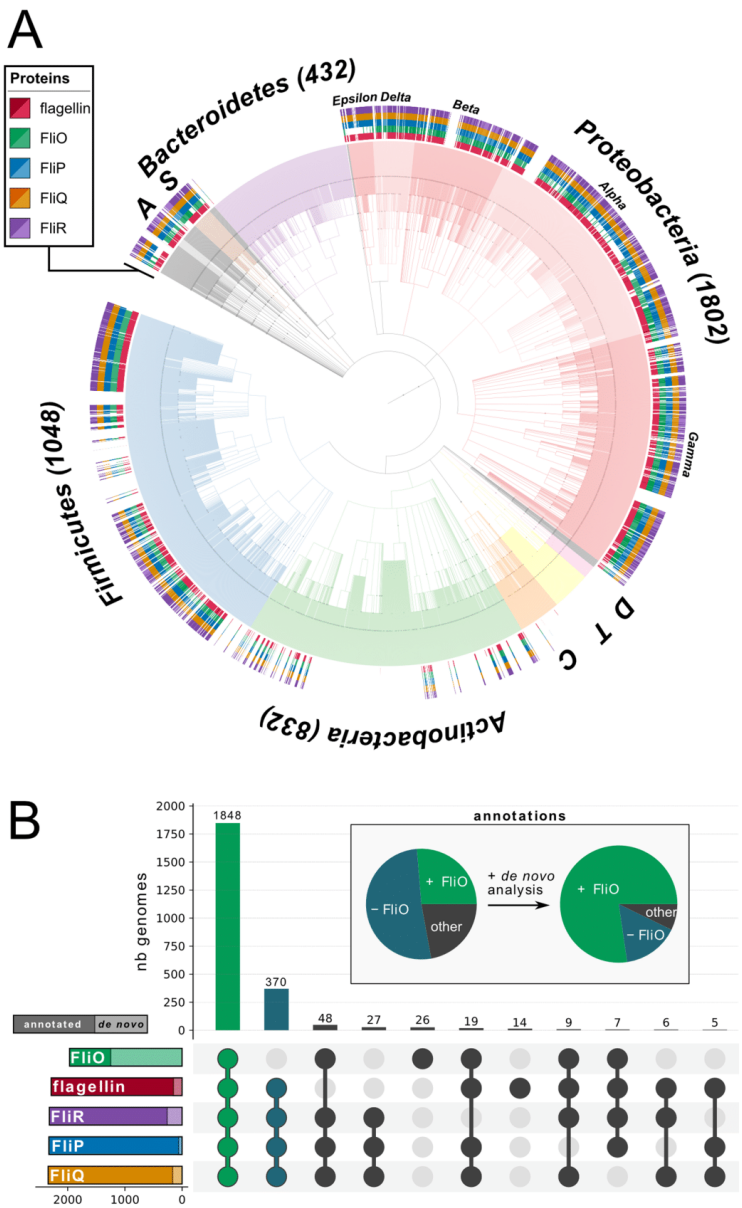

Fig 1. Computational prediction and phylogenetic distribution of FliO, FliP, FliQ, FliR, and flagellin across all bacterial phyla. The distribution of FliO, FliP, FliQ, FliR, and flagellin in all The National Center for

Biotechnology Information (NCBI) reference genomes ($n = 4771$) was analyzed according to NCBI annotation and de novo prediction using a Hidden Markov Model (HMM) based on curated Pfam (protein family) database models. (A) Phylogenetic tree based on NCBI taxonomy—outer rings indicate the presence/absence of flagellin, FliO, FliP, FliQ, and FliR. Each colored branch highlights a bacterial phylum. The number of retrieved genomes is indicated for the major phyla; C = Cyanobacteria (119), T = Tenericutes (116), S = Spirochaetes (60), D = Deinococcus-Thermus (39), A = Acidobacteria (24). (B) Gene set representation of de novo predicted FliO, FliP, FliQ, FliR, and flagellin. Left bars show the total number of predicted proteins including previously annotated (dark color) and newly predicted ones (light color) across the NCBI reference genomes. The top bars represent the number of genomes for each combination of predicted FliO, FliP, FliQ, FliR, and flagellin. The pie chart highlights the improved annotation of FliO through the HMM de novo prediction.

https://doi.org/10.1371/journal.pbio.2002267.g001

suggested that FliO was involved in stabilizing FliP protein. To exclude polar effects of the *fliO* deletion, we monitored protein stability of episomally expressed FliP in Δ*fliP* and Δ*fliOP* mutant backgrounds and observed a similar degradation pattern of FliP in the absence of FliO (Fig 3B). Reminiscent of the FliP degradation pattern in a Δ*fliO* mutant, we observed rapid degradation of FliP in nonfunctional FliO point mutants (V72G, L91R, and ΔL91-L94) (S6 Fig). Similar FliO point mutations (L91A, ΔL91) were previously shown to be expressed but not able to complement a *fliO* null mutant [26].

As mentioned above, FliP harbors a signal peptide of the Sec-system, and this raised the possibility that FliO participated in efficient cotranslational membrane integration of FliP. We thus assessed the effects of a *fliO* deletion in respect to the level of membrane-integrated FliP. Crude membranes were collected by ultracentrifugation and washed with urea to discriminate properly integrated proteins from aggregated proteins associated with the

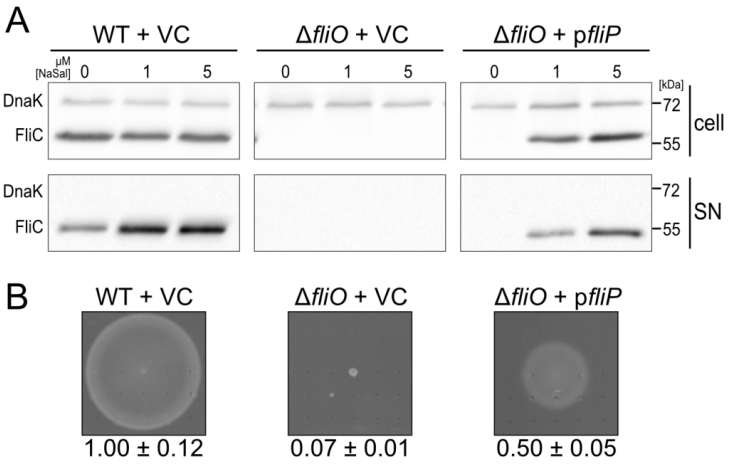

Fig 2. Excess FliP bypasses the requirement of FliO for flagellar-specific type III secretion system (fT3SS) function and motility. (A) Flagellin secretion in the wild-type (WT) (EM2320) and the Δ*fliO* mutant (EM2323, EM2324) harboring an empty (vector control [VC]) or *fliP* (p*fliP*)-expressing vector. Complementation was induced by the addition of 0 μM, 1 μM, and 5 μM sodium salicylate (NaSal). Secreted flagellin was detected by Western blot using anti-FliC antibodies. DnaK was used as loading control. (B) Motility of the WT and the Δ*fliO* mutant complemented with the empty (VC) or *fliP* (p*fliP*)-expressing vector in 0.3% swim agar plates after 5 h at 37˚C. Expression of *fliP* was induced using 5 μM NaSal. Relative motility reports the mean ± SD, $n = 4$.

https://doi.org/10.1371/journal.pbio.2002267.g002

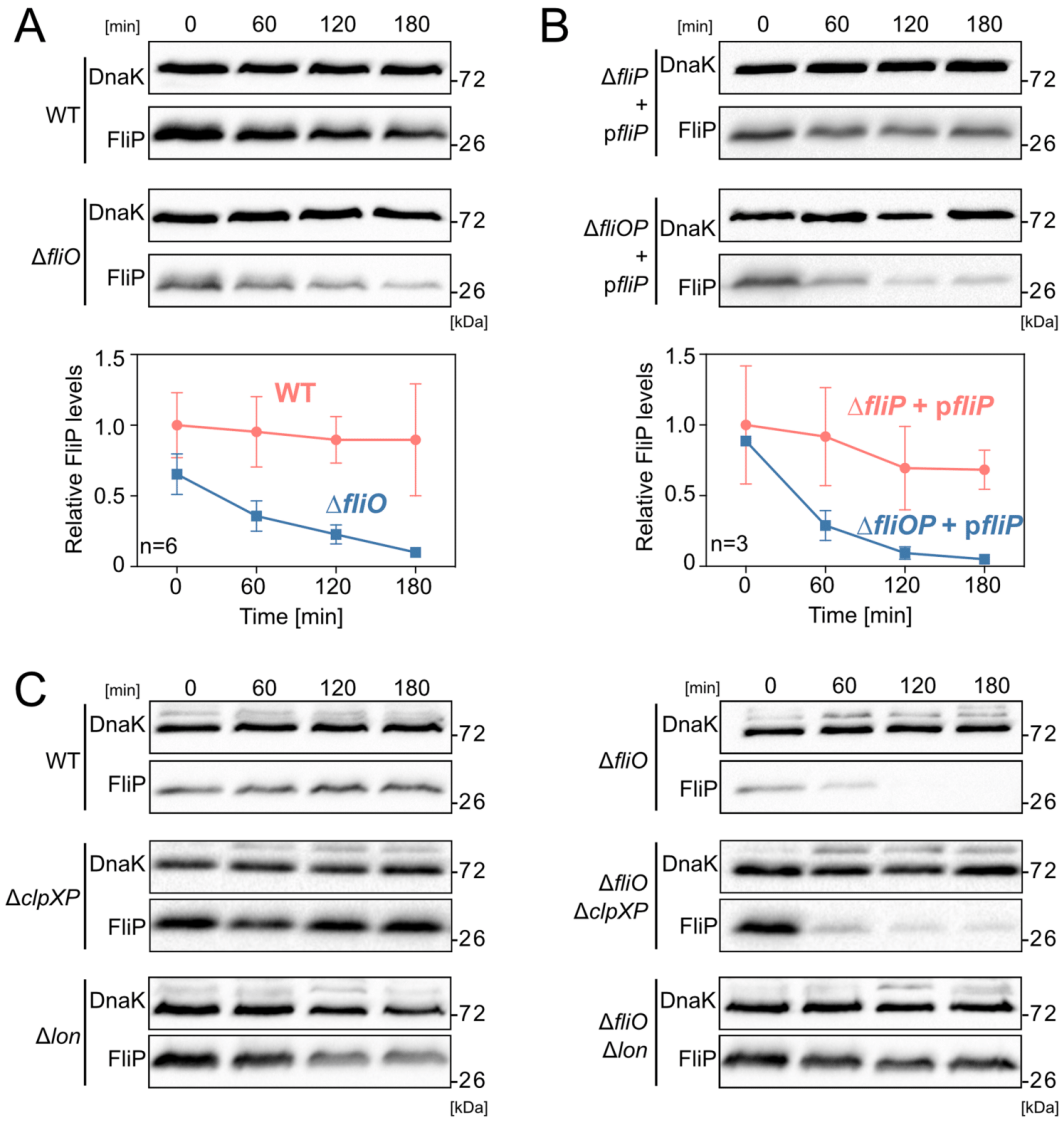

Fig 3. FliP protein is unstable in the absence of FliO. (A) FliP protein stability in the presence and absence of FliO. Protein levels of chromosomally expressed FliP-3×FLAG were monitored at 0, 60, 120, and 180 min after arrest of de novo protein synthesis. Wild-type (WT) (EM2225), Δ*fliO* (EM3201). FliP protein levels were normalized to DnaK, and relative FliP levels report the mean ± SD, $n = 6$. (B) Stability of episomally expressed FliP-3×HA protein in Δ*fliP* and Δ*fliOP* mutants after arrest of de novo protein synthesis. Δ*fliP* + p*fliP* (TH17448), Δ*fliOP* + p*fliP* (EM1610). Relative FliP levels report the mean ± SD, $n = 3$. (C) Protein stability of chromosomally expressed FliP-3×HA in presence or absence of FliO in the WT (TH17323), Δ*fliO* (EM1274), Δ*clpXP* (EM4018), Δ*clpXP* Δ*fliO* (EM4019), Δ*lon* (EM4478), and Δ*lon* Δ*fliO* (EM4479) mutants.

https://doi.org/10.1371/journal.pbio.2002267.g003

cytoplasmic membrane. FliP protein levels were determined in both the presence and absence of FliO (S7 Fig). As expected for a polytopic integral membrane protein, we detected FliP only in the membrane fractions but not in the cytosol. FliP steady-state protein levels were comparable in the presence and absence of FliO, indicating that FliO did not influence FliP incorporation into the inner membrane.

In order to understand the mechanisms underlying FliO stabilization of FliP, we aimed to identify the protease responsible for FliP degradation. We first analyzed the contribution of the integral membrane protease FtsH, which is involved in quality control of membrane protein complexes, such as the SecYEG translocase [29]. As a deletion of FtsH is lethal, we monitored FliP protein stability under conditions overproducing an inhibitor of FtsH, STM1085 (YccA in *Escherichia coli*) [30,31]. YccA has been shown to limit the suicidal degradation of jammed Sec-translocon complexes by inhibiting FtsH activity [31]. LamB-LacZ hybrids are commonly used to study jammed Sec-translocons. In order to verify the functionality of our YccA expression construct, we thus monitored bacterial growth after jamming of the Sec-translocon using a LamB-LacZ hybrid in the presence or absence of excess YccA. Expression of YccA from a medium-copy plasmid rescued the lethal growth defect after induction of the LamB-LacZ hybrid (S8A Fig). We next analyzed FliP protein stability in the absence of FliO in the presence or absence of YccA, the inhibitor of FtsH. As shown in S8B Fig, the FliP degradation pattern did not change, which suggested that FtsH might not be primarily responsible for the observed proteolytic degradation of FliP in the absence of FliO. We therefore analyzed FliP stability in the absence of FliO in mutants defective for the cytoplasmic ClpP and Lon proteases. In the Δ*clpXP* mutant, the presence of FliO was required to maintain FliP stability. In the Δ*lon* mutant, however, FliP was also significantly more stable in the absence of FliO, suggesting that Lon is the primary protease responsible for FliP degradation (Fig 3C).

FliO is not located in the basal body of the flagellum

Previous studies suggested that FliO, FliP, FliQ, and FliR were integral parts of the basal body complex [22,32]. However, the subcellular localization of the fT3SS components has only been experimentally determined for FliP and FliR [23]. As we demonstrated above, overproduction of FliP readily bypassed the requirement of FliO for the formation of functional flagella, which suggested that FliO might not be part of the completed fT3SS. To determine the subcellular localization of FliO, we performed single-molecule super-resolution microscopy of FliO-HaloTag and FliN-HaloTag protein fusions using structured illumination microscopy (SIM) and direct stochastic optical reconstruction microscopy (dSTORM) [27,33]. The chromosomal HaloTag fusions to FliO and FliN did not impair the protein export function of the fT3SS (S9 Fig), and the FliN-HaloTag construct has previously been shown to display normal flagellation patterns [27]. The C ring protein FliN was localized in clusters corresponding to the C rings of flagellar basal bodies, as previously reported [14,34], but not in the absence of the MS ring needed for C ring assembly (Fig 4, Fig 5A). FliO, however, was evenly distributed in smaller clusters in the cytoplasmic membrane, and the observed FliO-HaloTag clusters were not affected in mutant strains defective in MS-ring or fT3SS assembly (Fig 4, Fig 5A). Single-molecule tracking (SMT) revealed that FliN remained stably attached in the cell envelope with an apparent diffusion coefficient of 0.03 $\mu m^2\ s^{-1}$. FliO followed long trajectories in the cell envelope with a 6-fold higher apparent diffusion coefficient of 0.2 $\mu m^2 \cdot s^{-1}$ (Fig 5B and 5C), which is consistent with previous reports ranging from 0.02 to 0.2 $\mu m^2 \cdot s^{-1}$ for freely diffusing inner-membrane proteins [35,36]. We next performed colocalization studies of FliO-HaloTag and the C ring protein FliM-mEos (S10 Fig) and FliO-HaloTag or FliN-HaloTag with the flagellar hook (S10 Fig, Fig 5D). The hook-basal-body (HBB) components FliM, FliN, and epitope-

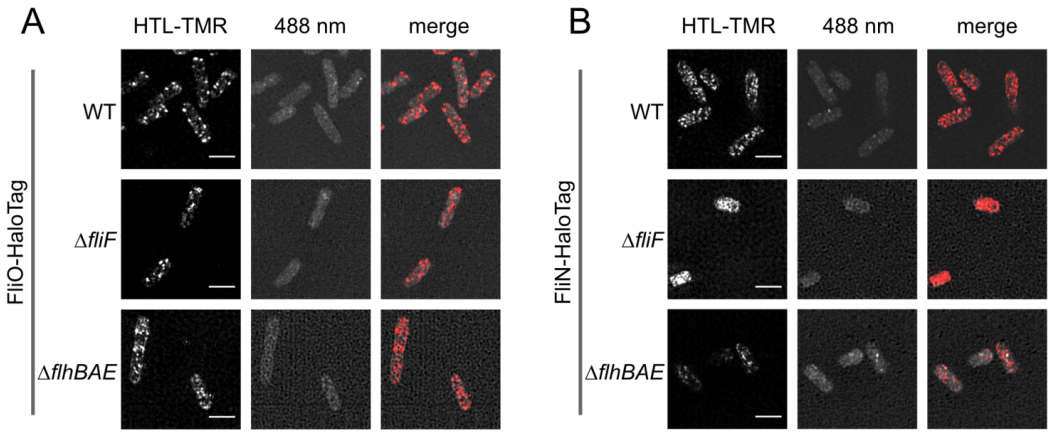

Fig 4. Subcellular localization of FliO revealed by structured illumination microscopy. The subcellular localization of FliO-HaloTag (A) or FliN-HaloTag (B) fusions expressed from their native chromosomal locus was analyzed in the wild-type (WT) and mutant backgrounds defective in MS-ring assembly (Δ*fliF*) or flagellar-specific type III secretion system (fT3SS) function (Δ*flhBAE*). WT FliO-HaloTag (EM1077), WT FliN-HaloTag (EM1081), Δ*fliF* FliO-HaloTag (EM6254), Δ*fliF* FliN-HaloTag (EM2640), Δ*flhBAE* FliO-HaloTag (EM6256), and Δ*flhBAE* FliN-HaloTag (EM6258). Strains were treated with 20 nM HaloTag ligands (HTL tetramethylrhodamine [TMR]) and observed using structured illumination microscopy (SIM). The autofluorescence of bacteria upon excitation with a 488 nm laser is shown in the middle panels. Scale bar 2 μm.

https://doi.org/10.1371/journal.pbio.2002267.g004

tagged hook protein FlgE localized in discrete spots similar to FliN-HaloTag as described above, and, consistently, FliN-HaloTag complexes were readily identified in the vicinity of extracellular hook structures (S10 Fig). In contrast, we did not observe colocalization of FliO-HaloTag with HBB components (S10 Fig, Fig 5D). These results indicated that FliO is not part of the final assembled fT3SS within the basal body complex. We thus hypothesized that FliO does not actively participate in the protein export process but acts as an accessory protein during the assembly of the core export apparatus.

FliO is required for FliP complex formation and basal body assembly

In order to study the effect of the absence of FliO on core fT3SS export apparatus formation and basal body assembly, we performed blue native PAGE (BN-PAGE) on crude membrane extracts solubilized in n-dodecyl-β-D-maltoside (DDM) (Fig 6). In a WT background, we detected 3×FLAG epitope–tagged FliP expressed from its native chromosomal locus in several low, intermediate, and high-molecular-weight complexes. We additionally performed liquid chromatography-tandem mass spectrometry (LC-MS/MS) analysis of selected bands corresponding to FliP-containing complexes, as detected by BN-PAGE Western blotting (S11 Fig). According to the BN-PAGE migration pattern and mass spectrometry analysis, FliP is present in several complexes in the WT: in a high-molecular-weight complex (complex 1), which presumably corresponds to finished, completed HBB complexes; in a minor (less abundant), intermediate molecular weight precursor complex (complex 3); and in a major (more abundant), intermediate molecular weight precursor complex (complex 4) (Fig 6A). LC-MS/MS analysis of the intermediate-molecular-weight FliP-containing complexes 3 and 4 further suggested the presence of FliO (in complex 3 and 4) and FliR (in complex 4). We note that we did not detect FliP in complex 4 by LC-MS/MS analysis, which is likely explained by well-known difficulties in detecting hydrophobic membrane proteins by LC-MS/MS (S11A Fig).

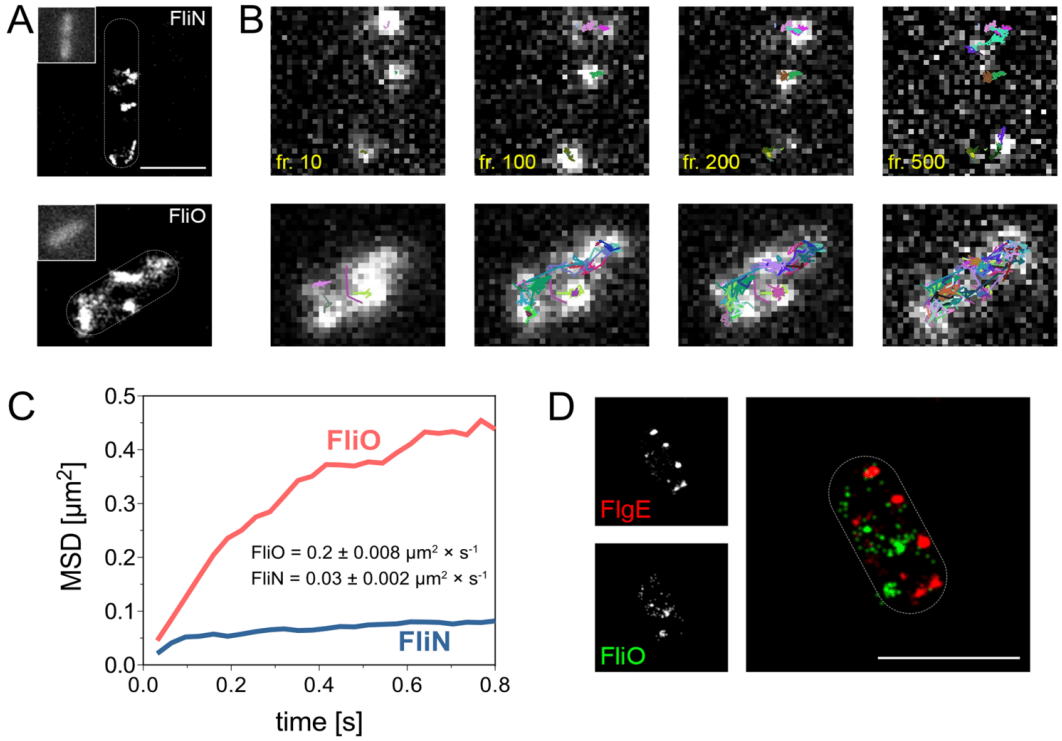

Fig 5. Single-particle tracking of FliO and colocalization with the flagellar basal body. (A) Strains expressing chromosomal FliN-HaloTag (EM1081) or FliO-HaloTag (EM1077) fusions were treated with 20 nM HaloTag ligands (HTL tetramethylrhodamine [TMR]) and analyzed by total internal reflection fluorescence (TIRF) microscopy. As described before, 500 frames were acquired with 5 mW laser power at the focal plane. The autofluorescence of bacteria upon excitation with a 488 nm laser is shown in the upper left corner. Scale bar 1 μm. (B) Single-molecule tracking (SMT) of TMR-labeled FliN and FliO. Selected frames from a series of 500 frames are shown, and frame numbers are indicated. (C) Mean square displacement (MSD) plots of pooled trajectories of at least 25 bacteria recorded under the same conditions. The diffusion coefficient *D* was calculated using the Jaqaman algorithm. (D) Dual-color direct stochastic optical reconstruction microscopy (dSTORM) of fixed bacteria expressing chromosomal FlgE-3×HA and FliO-HaloTag fusions (EM1214). Scale bar 1 μm.

https://doi.org/10.1371/journal.pbio.2002267.g005

In a mutant strain deficient for FliO, however, we neither detected FliP in complex 1 corresponding to the completed HBB, nor at the molecular weight of the intermediate-molecular-weight FliP precursor complexes 3 and 4. However, monomeric FliP was substantially more abundant in the Δ*fliO* mutant than in the WT. We also observed the formation of another FliP-containing high-molecular-weight complex in the Δ*fliO* mutant, which apparently migrated slightly below the completed basal body complexes of the WT and could correspond to aggregated FliP subassemblies (complex 2) (Fig 6A).

We next analyzed the assembly of FliP complexes in a mutant strain defective in MS-ring assembly (Δ*fliF*). Interestingly, the formation of the intermediate-molecular-weight FliP-containing subcomplexes 3 and 4 was not dependent on the presence of the MS ring, in contrast to the presence of FliP in the high-molecular-weight basal body complex (complex 1) (Fig 6A). Importantly, in a Δ*fliO* Δ*fliF* double mutant, we observed the formation of a FliP-containing

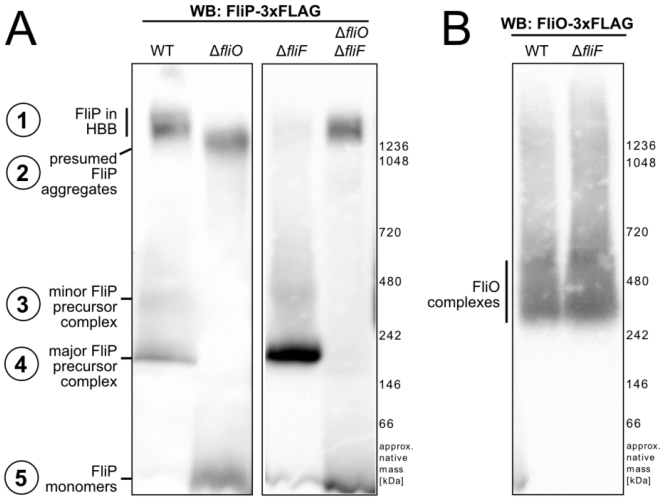

Fig 6. FliP subcomplex formation revealed by blue native PAGE (BN-PAGE). A. Anti-FLAG Western blot of BN-PAGE of crude membrane extracts prepared from the wild-type (WT) (EM2225), Δ*fliO* (EM3201), Δ*fliF* (EM4909), and Δ*fliO* Δ*fliF* (EM4910) mutant strains encoding for chromosomal FliP-3×FLAG. (B) Anti-FLAG Western blot of BN-PAGE of crude membrane extracts prepared from the WT (EM2269) and Δ*fliF* (EM3910) mutant strains encoding for chromosomal FliO-3×FLAG.

https://doi.org/10.1371/journal.pbio.2002267.g006

aggregation complex (complex 2) but not the intermediate-molecular-weight FliP precursor complexes 3 and 4. This suggested that complex 2 corresponds to aggregated FliP and demonstrates that the complex 2 is not related to the completed basal body complex observed in the WT (complex 1). In summary, these results suggested a sequence of assembly of the flagellar core export apparatus, which nucleates with the formation of a FliP-containing subcomplex, followed by subsequent assembly of additional transmembrane export apparatus components, and concluded by the assembly of the MS ring. Similar to the assembly of FliP, the formation of a FlhA-containing high-molecular-weight complex, which presumably corresponds to the finished HBB, was dependent on the presence of FliO and FliF (S12 Fig).

We next performed BN-PAGE of crude membrane extracts of a strain encoding for a functional FliO–FLAG fusion protein to corroborate the mass spectrometry and subcellular localization results. FliO showed a very heterogeneous size distribution in the BN-PAGE analysis, indicating complexes of different compositions (Fig 6B). The presence of FliO in intermediate-molecular-weight FliP-containing complexes—but not in completed HBB complexes—was also supported by LC-MS/MS analysis (S11A Fig) and is consistent with the super-resolution subcellular localization studies of FliO-HaloTag described above.

To validate the presence of FliO in FliP precursor complexes, we performed a FLAG-pull down of chromosomally encoded FliP-3×FLAG in a rod$^-$ background (Δ*flgBC*) under native conditions, followed by BN-PAGE protein separation and LC-MS/MS analysis (S11B Fig, S13A Fig). A rod$^-$ background was used to facilitate access of the 3×FLAG–tag located in the periplasmic domain of FliP. We observed several high-molecular-weight complexes, which corresponded to different FliP-containing subassemblies of the export gate and the basal body. Mass spectrometry analysis of the FliP-containing complexes suggested the presence of basal

body components (FliF, FliG, FlhA) in the high-molecular-weight complexes A and B, and of FlhA, FliO, and FliR in the intermediate-molecular-weight complexes C and D that copurified with FliP. In support, a pull down of chromosomally encoded FliO-3×FLAG using crude membrane extracts of a rod$^-$ background copurified chromosomally encoded FliP-3×HA (S13B Fig). We further expressed a plasmid-based FliO His_6-FliP construct in *E. coli* and performed His_6-FliP affinity purification followed by size exclusion chromatography. High molecular weight, pore-like FliP-containing complexes copurified with FliO, suggesting a direct or indirect interaction between these proteins (S13C Fig).

We next followed up on the presumed presence of the core integral membrane fT3SS component FliR in FliP-containing intermediate-molecular-weight complexes. We purified crude membrane extracts of rod$^-$ strains expressing FliP-3×FLAG and FliR-3×FLAG constructs from their native chromosomal locus and performed 2D BN-PAGE analysis (Fig 7). In the WT, we detected FliP and FliR in a high-molecular-weight complex corresponding to the flagellar basal body and in similar intermediate-molecular-weight complexes, which presumably corresponded to FliP–FliR subassemblies. Consistent with the 1D BN-PAGE results of Fig 6, the formation of FliP- and FliR-containing basal body complexes, but not the assembly of the intermediate-molecular-weight FliP–FliR complex (complex 4, Fig 6A), was dependent on the MS-ring protein FliF. We also note that the formation of stable FliP–FliR subassemblies is reminiscent to the previously observed SpaP–SpaR complex of the vT3SS [13,37].

Our results, presented above, suggested that the observed major, intermediate-molecular-weight FliP precursor complex (complex 4, Fig 6A) contained FliR and that the formation of a stable FliP–FliR complex was dependent on FliO. To test whether formation of the major FliP-containing precursor complex also involves FliQ, whose gene is encoded between *fliP* and *fliR*, we next analyzed formation of the major FliP precursor complex in mutants of the core fT3SS. As shown in Fig 8, the assembly of stable FliP-containing subassemblies was dependent on the presence of FliO and FliR but not on FliQ or FliF. These observations corroborate the hypothesis that FliO facilitates the assembly of a stable FliP–FliR intermediate-molecular-weight complex, which subsequently recruits FliQ and other components of the fT3SS for the assembly of a functional protein export apparatus.

Discussion

In *Salmonella* and other gram-negative bacteria, the flagellum and virulence-associated injectisome complexes play a crucial role during the infection process. The injectisome is believed to have evolved from the flagellum [39], and both nanomachines share many structural and functional similarities. In particular, the proteins forming the core T3SS protein export apparatus are highly conserved. One of the most striking differences is the absence of a FliO homolog in the injectisome vT3SS. Assembly of the flagellum and bacterial motility is dramatically impaired in the absence of FliO [26]; however, the molecular function of FliO remained elusive. Mutations in *fliP* have been shown to partially restore motility of a Δ*fliO* strain, and overexpression of FliO increased FliP expression, suggesting a functional relationship between these 2 proteins [26]. Here, we show that the nonmotile phenotype of a *fliO* deletion mutant was readily bypassed by moderate overproduction of FliP, which indicated that FliO was involved in FliP stability or complex assembly. To test this hypothesis, we monitored FliP protein stability after arrest of de novo protein synthesis and showed that the presence of FliO prevented FliP degradation. We demonstrate that Lon is the primary protease responsible for FliP degradation. The degradation of FliP as an integral membrane protein by a cytosolic protease is surprising, but LonB of *B. subtilis* is membrane-localized, and in yeast, the respective Lon homolog has been shown to degrade proteins of the mitochondrial membrane [40,41]. This

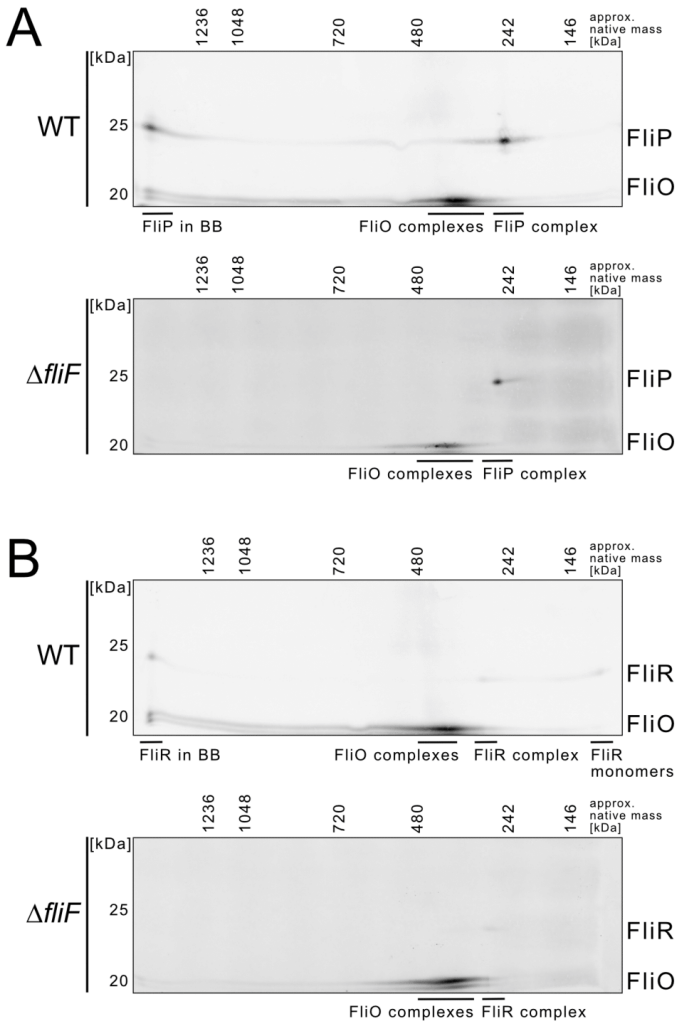

Fig 7. Evidence for FliP–FliR complex formation revealed by 2D blue native PAGE (BN-PAGE). (A) Anti-FLAG Western blot of a 2D BN-PAGE of crude membrane extracts prepared from rod$^-$ (Δ*flgBC*) strains encoding for chromosomal FliO-3×FLAG and FliP-3×FLAG. The strains additionally harbored a deletion of *rflP*, a negative regulator of the flagellar master regulator FlhDC and responsible for the phenotypic heterogeneity of flagellar gene expression in lysogeny broth (LB) medium [38]. The deletion of *rflP* results in homogeneous flagella production for cultures grown in LB and thus facilitates detection of the chromosomally encoded epitope-tagged transmembrane export apparatus components, which are expressed at low levels. Wild-type (WT) (EM6229) and Δ*fliF* (EM6195). (B) Anti-FLAG Western blot of a 2D BN-PAGE of crude membrane extracts prepared from Δ*flgBC* Δ*rflP* strains encoding for chromosomal FliO-3×FLAG and FliR-3×FLAG. WT (EM6228) and Δ*fliF* (EM6196).

https://doi.org/10.1371/journal.pbio.2002267.g007

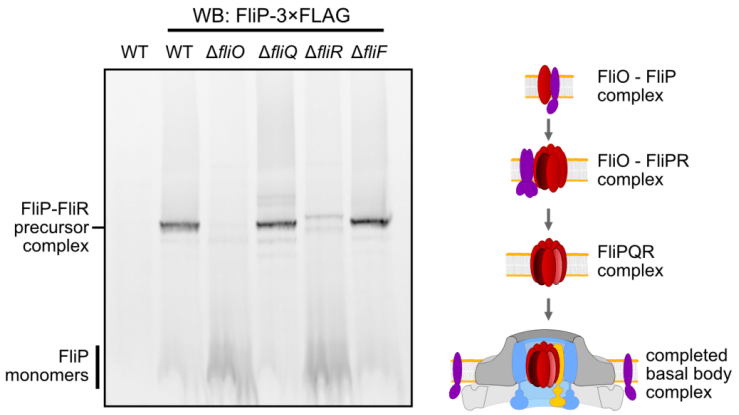

Fig 8. Assembly of FliP subassemblies in core export apparatus mutants and model of the coordinated assembly of the flagellar-specific type III secretion system (fT3SS). Left: The assembly of stable FliP subassemblies is dependent on FliO and FliR but not on FliQ or FliF. Anti-FLAG Western blot of blue native PAGE (BN-PAGE) of crude membrane extracts prepared from the wild-type (WT) harboring untagged FliP (LT2, TH437) and mutant strains encoding for chromosomal FliP-3×FLAG: WT (EM6221), Δ*fliO* (EM6222), Δ*fliQ* (EM6223), Δ*fliR* (EM6224), Δ*fliF* (EM4859). Strains EM6221, EM6222, EM6223, and EM6224 additionally harbored a deletion of the proximal rod components *flgBC* in order to arrest flagellar synthesis after assembly of the core export apparatus. Right: Model of the coordinated assembly of the core flagellar export apparatus. Upon initiation of flagellum assembly, the flagellar type III secretion system (T3SS)-specific chaperone FliO facilitates formation of an oligomeric complex containing FliP and FliR. FliO then presumably dissociates from the stable FliP–FliR core complex. The FliP–FliR core complex forms the nucleus for the assembly of FliQ, FlhB, and FlhA [11], followed by MS-ring (FliF) polymerization and formation of the completed protein export-competent flagellar T3SS.

https://doi.org/10.1371/journal.pbio.2002267.g008

result suggests that Lon is able to tightly interact with the cytoplasmic membrane in order degrade misassembled FliP.

It has been thought that FliO was part of the fT3SS within the basal body complex [22,23,32], and we performed super-resolution microscopy analyses to determine the subcellular localization of FliO. FliO did not colocalize with components of the basal body, and single-molecule analysis revealed that FliO complexes are evenly distributed and freely diffusing in the cytoplasmic membrane. We thus hypothesized that FliO is not part of the fT3SS in the assembled basal body and does not actively participate in the export process but rather has a function as an accessory protein during assembly of the core export apparatus.

We tested this hypothesis by performing 1D and 2D BN-PAGE and LC-MS/MS analyses of crude membrane extracts to determine the composition of the basal body complex under native conditions. We did not detect FliO in completed basal body complexes, but FliO was associated with FliP and FliR-containing subcomplexes. The formation of stable FliP–FliR subassemblies required the presence of FliO, but not the MS-ring protein FliF. These observations indicate that precursors of the flagellar export gate assemble prior and independently from the MS ring, as previously shown for vT3SS assembly of the injectisome [37,42]. Finally, FliP monomers detected using BN-PAGE analysis were strikingly more abundant in the absence of FliO, which was consistent with the absence of FliP-containing higher-molecular-weight complexes in the *fliO* mutant.

In summary, we propose that FliO functions as a flagellum-specific chaperone required for productive assembly of the core flagellar export apparatus. We suggest that assembly of the

flagellar core T3SS initiates with the formation of FliP–FliR oligomers, which is facilitated by FliO. Upon assembly of a stable FliP–FliR core complex, FliO is released and possibly replaced with other export gate components. The FliP–FliR core complex might subsequently serve as platform for the recruitment of FliQ, FlhB, and the FlhA nonamer, resulting in the formation of a secretion-competent export apparatus needed for flagellar assembly (Fig 8). Both the bacterial flagellum and the homologous vT3SS of the injectisome device are important virulence factors of many pathogenic bacteria. Thus, understanding the principles and molecular mechanisms of the assembly of large, multicomponent transmembrane protein complexes might have important implications for the rational design of novel anti-infectives that interfere with the assembly and function of these nanomachines.

Materials and methods

Bacterial strains, plasmids, and growth conditions

Bacterial strains and plasmids used in this study are listed in S1 Table. All strains were derivatives of *S. enterica* serovar Typhimurium LT2. Cultures were grown in lysogeny broth (LB) at 37˚C under continuous shaking to mid-log phase except when stated otherwise.

Strain constructions

Chromosomal fusions or clean deletions of genes were created using λ-Red recombination either by *tetRA* cassette replacement using pKD46 plasmid [43] or by *aph*-I-SceI cassette replacement using pWRG730. One-step gene inactivation was performed as described by Datsenko and Wanner [44]. Insertion of a chromosomal LacZ-Frt-aminoglycoside phosphotransferase (Kanamycin resistance)-Frt (FKF) through homologous recombination was performed as described [45]. Mutations, fusions, and deletions were transferred between strains using P22 phage transduction. For STM1085 (*yccA*) cloning, the gene was amplified by PCR from genomic DNA and subcloned blunt end into pBR322 before cloning with DraIII and BstEII into the IPTG-inducible expression plasmid pTr99FFA.

Phylogenetic analysis and de novo prediction of FliO, FliP, FliQ, FliR, and flagellin homologs

In order to characterize the distribution of FliO, FliP, FliQ, FliR, and flagellin proteins across different bacterial phyla, proteomes (.faa files) of representative genomes were downloaded from *refseq* NCBI: https://www.ncbi.nlm.nih.gov/refseq/about/prokaryotes/.

A total of 4,771 genomes (date: 01.05.2017) were retrieved, and the proteomes were queried based on regular NCBI annotations for the presence of FliO, FliP, FliQ, FliR, and flagellin proteins. For the de novo prediction of homologs of FliO, FliP, FliQ, FliR, and flagellin proteins, HMMs were generated using the curated Pfam database models for FliO (PF04347), FliP (PF00813), FliQ (PF01313), FliR (PF01311), and flagellin (PF00669+PF00700), and all representative genomes were screened using the *hmmsearch* function in HMMER3 [46] with the default Pfam database gathering cutoff (GA) per domain. This HMM approach identified a large number of FliO proteins for genomes in which FliP and the other flagella components have been predicted. The majority of novel FliO proteins corresponded to hypothetical genes. Results from the annotated FliO, FliP, FliQ, FliR, and flagellin proteins and the de novo prediction were integrated using custom Python scripts. For the phylogenetic representation, the NCBI taxonomy IDs were extracted using ETEtools [47], and the tree topology was obtained for a given list of TaxIDs. For tree visualization and rendering, iTOL [48] was used, and set comparison was visualized using the UpSet tool [49].

Motility assay

Equal amounts of an overnight culture were inoculated in 0.3% swim agar plates supplemented with appropriate additives. Plates were incubated at 37˚C and scanned after 4 h to 7 h. The sizes of the motility halos were measured using ImageJ.

Protein secretion assay

Cells were grown in LB at 37˚C until OD_{600} reached 0.8–0.9, and 1.9 ml of culture was harvested and cooled down on ice. Cells and supernatant were separated by 3 × 3 min centrifugation at 18,000 × g at 4˚C. The pellet and 1.5-ml supernatant of each strain were precipitated with 10% TCA. After normalization to the OD_{600}, samples were loaded on a 15% SDS-PAGE and analyzed by Western blot.

Protein stability assay

Overnight cultures of chromosomally encoded $FliP_{Q22}$3×HA/$FliP_{G157}$3×FLAG were diluted 1:100 into 25 ml of fresh LB and grown at 37˚C under shaking until OD_{600} reached 0.6. Protein synthesis was inhibited by the addition of 0.5 mg ml^{-1} spectinomycin and 12.5 μg ml^{-1} chloramphenicol (Cm). The equivalent of 1 ml at OD_{600} 0.6 was collected at 0, 30, 60, 90, 120, and 180 min after synthesis inhibition. Samples were precipitated in 10% TCA, spun down (30 min at 20,000 x g), washed with ice-cold acetone, and resuspended in 40 μl 2 × SDS loading buffer (300 mM Tris-HCl pH 6.8, 4% SDS, 20% glycerol, 25 mM EDTA, 0.04% bromophenol blue, 2% β-mercaptoethanol). 10 μl of each sample was run on 15% SDS-PAGE and analyzed by Western blot. To assess the effect of STM1085, cultures were grown in LB supplemented with ampicillin and with 1 mM IPTG. Synthesis was stopped and samples were collected after 0 min and 180 min, as described above. For plasmid-encoded $FliP_{Q22}$-3×HA, overnight cultures of Δ*fliOP* and Δ*fliP* harboring pKG116-$FliP_{Q22}$-3×HA were diluted 1/100 into 25-ml LB containing 12.5 μg ml^{-1} Cm and 2.5 μM sodium salicylate (NaSal) and grown at 37˚C for 2.5 h until OD_{600} 0.6. Protein synthesis was inhibited by the addition of 0.5 mg ml^{-1} spectinomycin [50]. Samples were collected and treated as described above.

Western blot

Following SDS-PAGE, proteins were transferred onto a nitrocellulose membrane. Directly after transfer, membranes were stripped at 60˚C for 20 min to enhance signal as described previously [51]. Blots were then blocked with 5% milk and probed for 1 h with appropriate antibodies: Anti-HA (Sigma-Aldrich; dilution 1:2,000), Anti-FLAG (Sigma-Aldrich; dilution 1:3,000), Anti-DnaK (Abcam; dilution 1:10,000) mouse monoclonal antibodies, rabbit anti-FliC serum (dilution 1:10,000), and rabbit anti-FlhA serum (dilution 1:10,000), respectively. Membranes were then incubated 30 min in Immun-Star Goat anti-mouse HRP and goat anti-HRP secondary antibodies (1:20,000; BioRad). After washing, membranes were developed using Clarity Western ECL (BioRad) and imaged with a ChemiDoc imaging system (BioRad).

TCE staining

Total protein amounts were detected before transfer with 2,2,2-Trichloroethanol (TCE), as described previously [52]. Gels were imaged with a ChemiDoc imaging system after 1-min activation.

Crude and washed membrane preparation for cell fractionation assay

Overnight cultures were diluted 1:50 into fresh LB until OD_{600} 0.7–0.8. The equivalent of 8 OD units was harvested at 8,000 × g for 10 min, resuspended in 750 μl Buffer K (50 mM TEA, 250 mM sucrose, 2 mM EDTA, 10 μg ml^{-1} lysozyme, 10 μg ml^{-1} DNase, 1 mM $MgCl_2$, complete protease inhibitors), and incubated for 30 min at 4˚C. Cells were lysed using glass beads, and lysates were spun at 10,000 × g for 10 min to eliminate nonlysed cells. Supernatants were then spun down at 150,000 × g at 4˚C for 50 min. 900 μl of supernatant was collected and precipitated with 10% TCA, washed, and resuspended in 2 × SDS loading buffer (cytosolic fraction). Pellets were resuspended into 100 μl cold PBS. Half of the suspension was directly mixed with 50 μl 2 × SDS-loading buffer (unwashed membrane fraction). The rest was washed with 1 ml of urea solution (50 mM TAE, 1 mM EDTA pH 7.5) for 1 h at room temperature and centrifuged at 120,000 × g for 1.5 h at 23˚C. The supernatant was discarded, and the pellet was resuspended in 100 μl of 1 × SDS loading buffer (washed membrane fraction). All fractions were run on SDS-PAGE and analyzed by Western blots.

Super-resolution microscopy

(i) Sample preparation and microscopy: Bacteria were subcultured from overnight cultures (1:100) in fresh LB medium and grown for 2.5 h at 30˚C. After 1 h 45 min of subculture, fluorescent ligands were added, i.e., 20 nM HTL-TMR (Promega) or 150 nM HTL-Atto655 (self-synthesized) for HaloTag fusions. At least 5 washing steps were performed with minimal medium to remove unbound ligand and LB medium by centrifugation at 8,000 × g for 2 min. Bacteria are diluted to approximately OD_{600} 0.5, and 15 μl was added to freshly prepared agarose-coated glass cover slips prepared with 1% agarose. Another glass slide was positioned on the agarose. Total internal reflection fluorescence (TIRF) microscopy was performed using an inverted microscope (IX71, Olympus) equipped with a motorized 4-line TIRF condenser (cell^TIRF, Olympus), a 150× oil immersion TIRF objective (UAPON 150x OTIRF, Olympus), and high-power lasers: 488 nm, 150 mW (LuxX, Omicron, Germany); 561 nm, 150 mW (Jive, Cobolt, Sweden); 640 nm, 140 mW (LuxX, Omicron, Germany). Images were acquired by an electron-multiplying back-illuminated frame transfer CCD camera (iXon Ultra 897, Andor). A fluorescence filter cube containing a polychroic beamsplitter (R405/488/561/647, Semrock), and a quad-band emission/blocking filter (FF01 446/523/600/677, Semrock) was used. For each cell, 500 frames were recorded with an exposure time of 31 ms for 561 nm and 640 nm laser and laser power of 5 mW. For dual-color dSTORM, bacteria were stained as indicated, washed, and fixed with 3% PFA in PBS for 15 min at RT. After fixation, bacteria were washed again 3 times and were then immobilized on PLL-coated cover slides. As redox system 100 mM β-mercaptoethylamine, 4.5 mg × 10^{-1} ml D-glucose, 40 μg × 10^{-1} ml catalase, and 0.5 μg × 10^{-1} ml glucose-oxidase were added in 1-ml PBS. Five hundred frames were recorded with an exposure time of 31 ms for 561 nm and 640 nm laser, with a laser power of 40 mW and 50 mW, respectively, and a cycle time of 67. SIM was performed using a Nikon Eclipse T_i N-SIM super-resolution microscope equipped with a 100× SR ApoTIRF objective and 488 nm and 561 nm lasers. Using an ORCA FLASH 4.0 camera, 100-nm z-stack images were acquired, and the SIM stacks were reconstructed using the Nikon NIS-Elements 4.5.1 software on auto settings. The pixel data of individual z-stacks were subsequently projected on a single plane using maximum intensity settings. (ii) Single molecule localization and tracking: Localization of single molecules as well as SMT were carried out by a self-written graphical user interface written in Matlab R2012 (MathWorks). Single-molecule localization is based on the multiple-target tracing algorithm, and SMT was performed using the utrack algorithm (online available:

MTT: http://ciml-e12.univ-mrs.fr/App.Net/mtt/, utrack: http://lccb.hms.harvard.edu/doc/u-track-2.1.3.zip).

Large-scale crude membrane preparation

In order to perform BN-PAGE, crude membranes were prepared on a large scale as described by Zilkenat et al. [53]. Overnight cultures were diluted 1:100 into 1 liter of fresh LB, and cells were grown at 37˚C until OD_{600} 0.8–0.9. All steps were performed at 4˚C except when stated otherwise. Eight hundred OD units of culture were harvested and centrifuged at 6,000 × g for 15 min. The supernatant was discarded, and the pellet was washed with cold PBS and centrifuged 10 min at 6,000 × g. Cells were resuspended in 15 ml of buffer K (50 mM TEA, 250 mM sucrose, 1 mM EDTA, pH 7.5) and supplemented with cOmplete mini EDTA free protease inhibitors cocktail, 10 μg ml^{-1} DNase, 10 μg ml^{-1} lysozyme, and 1 mM EDTA. After 30-min incubation, cells were lysed using a French Press at 18,000 psi. After lysis, 1-mM $MgCl_2$ was added, and lysates were centrifuged at 24,000 × g for 20 min to eliminate cell debris. Crude membranes were pelleted at 200,000 × g for 50 min, resuspended in 500 μl of buffer M (1×), and homogenized in a 1-ml dounce homogenizer. Membranes were then stored on ice before separation on sucrose gradient or pull down.

1D and 2D BN-PAGE

Crude membranes or pull-down elations were prepared as described above. An aliquot of solubilized membranes (45 μl) were collected and mixed to 5 μl of 5% coomassie G (Serva) in 250-mM n-amino-caproic-acid, 50% glycerol and 25 μl were loaded on a 3%–12% Native-PAGE (Thermo Fisher scientific) and run for 50 min at 130 V. The cathode buffer was exchanged and the gel was run for an additional 1 h 30 min at 250 V at 4˚C. Electrotransfer onto a PVDF membrane was performed at 30 V for 2 h. As previously described [13], 2D BN/SDS PAGE of crude membranes was carried out.

Sucrose gradient

Previously homogenized crude membrane extracts were carefully deposed at the surface of a 30%–55% sucrose gradient and were centrifuged for 14 h at 150,000 g. All steps were performed at 4˚C. Eight fractions of 1 ml were collected and diluted 1:3 with buffer M (50 mM TEA, 1 mM EDTA at pH 7.5) and centrifuged at 200,000 × g for 45 min. The supernatant was discarded, and the membranes were resuspended in 200-μl buffer L (50 mM TEA, 250 mM sucrose at pH 7.5). After SDS-PAGE and Western blot analysis, the purest fractions were pooled together. Protein concentration was measured using Bradford protein assay (BioRad), and the concentration of each sample was adjusted to 3.0 mg ml^{-1}. Membranes were then solubilized with 1% DDM for 1 h under gentle shaking and centrifuged 20 min at 20,000 × g to eliminate nonsolubilized membranes. The supernatant was collected, and a 25-μl sample was loaded on a 3%–12% BN-PAGE as described below.

FliO/FliP-3×FLAG pull down

A strain lacking the rod proteins (Δ*flgBC*) was used to ensure that the FLAG tag was accessible from the periplasm. Crude membranes were prepared as described above from a 1-L culture. Membranes were solubilized for 1 h with 0.5% DDM and centrifuged at 20,000 for 20 min to eliminate cell debris. Solubilized membranes were then incubated for 4 h with 25-μl anti-FLAG M2 affinity gel (Sigma) at 4˚C in PBS with 0.1% DDM, washed with 4 column volumes,

and eluted by addition of FLAG peptide. After analysis on SDS-PAGE, the purest fractions were pulled together and loaded on a BN-PAGE as described above.

$FliP_{His6}$ affinity purification

Purification of $FliP_{His6}$ expressed from pTrc99a-*fliO-fliP*$_{His6}$ was performed by Ni-NTA chromatography as detailed in Fukumura et al. [54].

Protein in-gel digestion

Coomassie-stained gel bands were excised and in-gel digested using ProteaseMAX Surfactant (Promega). Sample preparation was done according to the instruction manual with the following modifications: digestions were performed overnight using the enzymes trypsin and chymotrypsin (12.5 ng μl^{-1} each in 20 mM ammonium bicarbonate, 0.01% ProteaseMAX Surfactant). Extracted peptides were desalted using C18 StageTips [55] and subjected to LC-MS/MS analysis.

Mass spectrometry

LC-MS/MS analyses were performed on an Easy nano-LC (Thermo Scientific) coupled to an LTQ Orbitrap XL mass spectrometer (Thermo Scientific) [56]. The peptide mixtures were injected onto the column in HPLC solvent A (0.1% formic acid) at a flow rate of 500 nl min^{-1} and subsequently eluted with a 57-min gradient of 5-33-50-90% HPLC solvent B (80% ACN in 0.1% formic acid). During peptide elution, the flow rate was kept constant at 200 nl min^{-1}. The 10 most intense precursor ions were sequentially fragmented in each scan cycle using collision-induced dissociation (CID). In all measurements, sequenced precursor masses were excluded from further selection for 90 s. The target values for MS/MS fragmentation were 5,000 charges and 10^6 charges for the MS scan.

Mass spectrometry data processing

The mass spectrometry data were processed with MaxQuant software suite v.1.5.2.8 [57]. The database search was performed using the Andromeda search engine [58], which is a module of the MaxQuant. MS/MS spectra were searched against a database consisting of 10,152 protein entries from *S*. Typhimurium and 285 commonly observed contaminants. In a database search, full specificity was required for trypsin. Cleavage specificity C-terminal of phenylalanine, tryptophan, tyrosine, leucine, and methionine was set for chymotrypsin, and up to 5 missed cleavages were allowed. Carbamidomethylation of cysteine was set as fixed modification, protein N-terminal acetylation, and oxidation of methionine were set as variable modifications. Initial precursor mass tolerance was set to 4.5 parts per million (ppm) and at the fragment ion level 0.5 dalton (Da) was set for CID fragmentation. Peptide, protein, and modification site identifications were filtered using a target-decoy approach at a false discovery rate (FDR) set to 0.01 [59]. The mass spectrometry data have been deposited to the ProteomeXchange Consortium (http://proteomecentral.proteomexchange.org) via the PRIDE partner repository with the data set identifier PXD005597.

The numerical data used in all figures are included in S1 Data.

Supporting information

S1 Fig. Quality score assessment of de novo predictions of FliO, FliP, FliQ, and FliR homologs. Hits are sorted by decreasing score on the x-axis. Black dots represent previously annotated proteins, red dots the newly predicted ones. Darker shades of grey indicate increasing

degree of homology.
(TIFF)

S2 Fig. Fingerprint alignment of FliP homologs of flagellar T3SS and virulence-associated T3SS. Increasing shades of grey indicate the degree of amino acid conservation.
(TIFF)

S3 Fig. Effects of excess FliP and FliO on motility and flagellin secretion. A. Motility of the wild type (WT) and a Δ*fliO* strain carrying pKG116-*fliO* (p*fliO*), pKG116-*fliP* (p*fliP*) or pKG116 empty vector control (VC) was analyzed in the presence or absence of inducer (1 μM and 10 μM NaSal). Expression of *fliO* from pKG116 is leaky also in the absence of inducer. Halo sizes were measured using ImageJ and expressed relative to the WT + VC in the absence of inducer. B. Flagellin secretion in the WT and the Δ*fliO* mutant harboring p*fliO*, p*fliP* or the empty vector control. Secreted flagellin was detected by Western blot using anti-FliC antibodies.
(TIFF)

S4 Fig. Cross-complementation of a *fliO* mutant by overproduction of T3SS core integral membrane proteins. Δ*fliO* strains carrying pKG116-*fliO/P/Q/R*, pKG116-*flhB/A* or pKG116 empty vector control (VC) were incubated in LB + Cm for 5 h in the presence or absence of inducer (5 μM−10 μM NaSal). Expression of *fliO* from pKG116 is leaky also in the absence of inducer. Halo sizes were measured using ImageJ and expressed relative to the WT + VC without inducer.
(TIFF)

S5 Fig. Motility phenotype of epitope tagged mutants. A. Example of motility in 0.3% agar at 37˚C of strain harboring FliP-3×FLAG (WT, EM2225; Δ*fliO*, EM3201; Δ*fliF*, EM4909; Δ*fliF* Δ*fliO*, EM4910) or FliP-3×HA FliO-3×FLAG (WT, EM2269; Δ*fliF*, EM3910) chromosomal fusions. Relative motility and standard deviation 4 h and 7 h after inoculation are indicated below (n = 4). B. Shows representative example of motility of episomally encoding FliP-3×HA strains (WT, TH437; Δ*fliP*, TH17448; Δ*fliOP*, EM1610) grown 5 h at 37˚C in LB + Cm + 0.3% agar non-induced (top row) or induced with 1 μM of NaSal (bottom row). Relative motility and standard deviation 5 h after inoculation are indicated below (n = 9).
(TIFF)

S6 Fig. FliP degradation in FliO point mutants. Chromosomally encoded $FliP_{Q22}$-3×HA protein levels were monitored at 0, 60, 120 and 180 min after protein synthesis arrest in the wild type (WT, TH17323) and FliO point mutants ($FliO^{L91R}$, EM2742; $FliO^{V72G}$, EM2743; $FliO^{\Delta L91\text{-}L94}$, EM2744). Western blot was performed using anti-HA antibody and DnaK was used as loading control.
(TIFF)

S7 Fig. The absence of FliO does not affect FliP membrane integration. Membrane and cytosol fractions of the WT (EM2225) and Δ*fliO* mutant (EM3201) were collected 0 min and 120 min after synthesis arrest and separated by ultracentrifugation. Unwashed, solubilized membranes, urea-washed membranes and precipitated cytosols were separated on a 15% SDS-PAGE and FliP protein was detected by Western blot using anti-FLAG antibodies. TCE staining shows total protein levels. DnaK was used as cytosolic protein control.
(TIFF)

S8 Fig. Stability of FliP upon overproduction of YccA, an inhibitor of FtsH. A. Bacterial growth analysis to test the functionality of the pTrc99a-YccA(STM1085)$_{\Delta aa5\text{-}12}$ expression

plasmid. Expression of YccA from a moderate copy plasmid by addition of 1 mM IPTG rescued the lethal growth defect of a $LamB_{181}$-LacZ hybrid (EM6396, pEM3191 (YccA); EM6399, pTrc99AFF4 vector control (VC)) in the presence of maltose due to jamming of the Sec-translocon. A short $LamB_{26}$-LacZ fusion (EM6394, pEM3191 (YccA); EM6397, pTrc99AFF4 vector control (VC)) is not targeted to the Sec translocon and bacterial growth is not affected by addition of maltose (Mal). B. The wild type (WT, TH17323) and Δ*fliO* mutant harboring a IPTG-inducible pTrc99a empty vector control (VC, EM3192) and pTrc99a-$YccA_{\Delta aa5\text{-}12}$ (YccA, EM3193) were grown in LB + Amp. Expression of YccA was induced by addition of 1 mM IPTG. Samples were taken at 0 and 180 min after synthesis stop and separated on 15% SDS-PAGE. $FliP_{Q22}$-3×HA protein was detected by Western blot using anti-HA antibodies. TCE staining indicates total protein levels.
(TIFF)

S9 Fig. Flagellin secretion in HaloTag fusion strains. FliC locked strains (FliN-HaloTag, EM1330; FliN-SNAP-tag, EM1331; FliM-HaloTag, EM1328; FliM-SNAP-tag, EM1329; FliO-HaloTag, EM1326; FliO-SNAP-tag, EM1327; Δ*fliO*, EM2272, wild type (WT), TH5861) were grown in LB at 37˚C. Cells (top) and supernatants (bottom) were harvested and separated by centrifugation. Samples were analyzed by Western blot using anti-FliC antibodies. TCE staining was used to determine total protein levels.
(TIFF)

S10 Fig. Analysis of co-localization of FliO and flagellar basal body complexes by structured illumination microscopy (SIM). The sub-cellular co-localization of chromosomal FliO-HaloTag (EM1204, EM1214) and FliN-HaloTag (EM3202) with hook-basal-body components was analyzed using structured illumination microscopy. Strain EM1204 additionally harbored a chromosomal FliM-mEos fusion. Strains EM1214 and EM3202 additionally harbored a chromosomal epitope-tagged variant of the hook protein (FlgE-3×HA). Scale bar 2 μm.
(TIFF)

S11 Fig. LC-MS/MS analysis of FliP containing complexes separated by BN-PAGE. A. LC-MS/MS analysis of prominent FliP-containing complexes revealed after BN-PAGE separation. The heat map represents the relative abundance of peptides from relevant proteins detected in the indicated FliP-containing complexes. B. LC-MS/MS analysis of prominent FliP-containing bands after immunoprecipitation of chromosomal FliP-3xFLAG in a rod^- (Δ*flgBC*) strain background. The heat map represents the relative abundance of peptides from relevant proteins detected in the indicated FliP-containing complexes.
(TIFF)

S12 Fig. BN-PAGE analysis of FlhA-containing complexes. Anti-FlhA (left panel) and anti-HA (middle panel) Western blot of BN-PAGE of crude membrane extracts prepared from the WT (TH17323), Δ*fliO* (EM1274), Δ*fliF* (EM3910), and Δ*fliO* Δ*fliF* (EM1618) mutant strains encoding for chromosomal FliP-3×HA. The merged anti-FlhA and anti-HA Western blots are shown in the right panel.
(TIFF)

S13 Fig. Co-purification of FliO and FliP. A. Immunoprecipitation of chromosomal FliP-3xFLAG. LC-MS/MS analysis on the indicated FliP-containing bands was performed and the results are summarized in S11B Fig. B. Immunoprecipitation of chromosomal FliO-3xFLAG specifically pulls down FliP. C. Co-purification of FliO and FliP complexes. FliO-$FliP_{His6}$ was expressed in *Escherichia coli* and affinity purified after solubilisation of crude membrane

extracts in DDM. Top: size exclusion chromatography after $FliP_{His6}$ affinity purification and electron microscopy analysis of indicated elution fractions. Bottom: SDS-PAGE analysis of input and size exclusion chromatography elution fractions. Proteins were visualized using coomassie staining and polyclonal anti-FliP / anti-FliO Western blot analysis.
(TIFF)

S1 Table. List of strains and plasmids used in this study. All strains are derivative of Salmonella enterica servovar Typhimurium LT2 unless noted otherwise.
(DOCX)

S1 Data. Numerical data used in all figures.
(XLSX)

Acknowledgments

We are grateful to Nadine Körner for expert technical assistance and members of the Erhardt lab for useful discussions of the manuscript. We thank Frederik Czarniak for preliminary analyses of HaloTag fusion proteins. We are also grateful to Kelly T. Hughes for generous donation of strains, to David F. Blair for discussions, Roman Gerlach for the *lacZ*-FKF template plasmid and Tohru Minamino for the kind gift of antibodies and *fliO-fliP*$_{His6}$ expression plasmid.

Author Contributions

Conceptualization: Florian D. Fabiani, Thibaud T. Renault, Britta Peters, Samuel Wagner, Michael Hensel, Marc Erhardt.

Data curation: Eric J. C. Gálvez.

Formal analysis: Thibaud T. Renault, Britta Peters, Eric J. C. Gálvez, Alina Guse, Mirita Franz-Wachtel, Samuel Wagner, Michael Hensel, Marc Erhardt.

Funding acquisition: Emmanuelle Charpentier, Till Strowig, Boris Macek, Samuel Wagner, Michael Hensel, Marc Erhardt.

Investigation: Florian D. Fabiani, Thibaud T. Renault, Britta Peters, Tobias Dietsche, Eric J. C. Gálvez, Alina Guse, Karen Freier, Mirita Franz-Wachtel, Marc Erhardt.

Methodology: Thibaud T. Renault, Britta Peters, Tobias Dietsche, Eric J. C. Gálvez, Mirita Franz-Wachtel, Boris Macek, Samuel Wagner, Michael Hensel.

Project administration: Michael Hensel, Marc Erhardt.

Resources: Emmanuelle Charpentier, Till Strowig.

Supervision: Thibaud T. Renault, Boris Macek, Samuel Wagner, Michael Hensel, Marc Erhardt.

Visualization: Florian D. Fabiani, Thibaud T. Renault, Britta Peters, Eric J. C. Gálvez, Marc Erhardt.

Writing – original draft: Florian D. Fabiani, Marc Erhardt.

Writing – review & editing: Florian D. Fabiani, Thibaud T. Renault, Britta Peters, Tobias Dietsche, Karen Freier, Emmanuelle Charpentier, Till Strowig, Mirita Franz-Wachtel, Boris Macek, Samuel Wagner, Michael Hensel, Marc Erhardt.

References

1. Macnab RM. How bacteria assemble flagella. Annual Review of Microbiology. 2003; 57:77–100. https://doi.org/10.1146/annurev.micro.57.030502.090832 PMID: 12730325.
2. Chevance FF, Hughes KT. Coordinating assembly of a bacterial macromolecular machine. Nature Reviews Microbiology. 2008; 6(6):455–65. https://doi.org/10.1038/nrmicro1887 PMID: 18483484.
3. Macnab RM. Type III flagellar protein export and flagellar assembly. Biochimica et biophysica acta. 2004; 1694(1–3):207–17. https://doi.org/10.1016/j.bbamcr.2004.04.005 PMID: 15546667.
4. Cornelis GR. The type III secretion injectisome. Nature Reviews Microbiology. 2006; 4(11):811–25. https://doi.org/10.1038/nrmicro1526 PMID: 17041629.
5. Galperin M, Dibrov PA, Glagolev AN. ΔμH+ is required for flagellar growth in *Escherichia coli*. FEBS letters. 1982; 143(2):319–22. PubMed PMID: 6811323.
6. Wilharm G, Lehmann V, Neumayer W, Trcek J, Heesemann J. *Yersinia enterocolitica* type III secretion: evidence for the ability to transport proteins that are folded prior to secretion. BMC Microbiology. 2004; 4:27. https://doi.org/10.1186/1471-2180-4-27 PMID: 15248901; PubMed Central PMCID: PMC471551.
7. Paul K, Erhardt M, Hirano T, Blair DF, Hughes KT. Energy source of flagellar type III secretion. Nature. 2008; 451(7177):489–92. https://doi.org/10.1038/nature06497 PMID: 18216859.
8. Minamino T, Namba K. Distinct roles of the FliI ATPase and proton motive force in bacterial flagellar protein export. Nature. 2008; 451(7177):485–8. https://doi.org/10.1038/nature06449 PMID: 18216858.
9. Lee PC, Stopford CM, Svenson AG, Rietsch A. Control of effector export by the *Pseudomonas aeruginosa* type III secretion proteins PcrG and PcrV. Molecular Microbiology. 2010; 75(4):924–41. https://doi.org/10.1111/j.1365-2958.2009.07027.x PMID: 20487288; PubMed Central PMCID: PMC3124366.
10. Li H, Sourjik V. Assembly and stability of flagellar motor in *Escherichia coli*. Molecular Microbiology. 2011; 80(4):886–99. https://doi.org/10.1111/j.1365-2958.2011.07557.x PMID: 21244534.
11. Morimoto YV, Ito M, Hiraoka KD, Che YS, Bai F, Kami-Ike N, et al. Assembly and stoichiometry of FliF and FlhA in *Salmonella* flagellar basal body. Molecular Microbiology. 2014; 91(6):1214–26. https://doi.org/10.1111/mmi.12529 PMID: 24450479.
12. Diepold A, Amstutz M, Abel S, Sorg I, Jenal U, Cornelis GR. Deciphering the assembly of the *Yersinia* type III secretion injectisome. The EMBO Journal. 2010; 29(11):1928–40. https://doi.org/10.1038/emboj.2010.84 PMID: 20453832; PubMed Central PMCID: PMC2885934.
13. Wagner S, Konigsmaier L, Lara-Tejero M, Lefebre M, Marlovits TC, Galan JE. Organization and coordinated assembly of the type III secretion export apparatus. Proceedings of the National Academy of Sciences of the United States of America. 2010; 107(41):17745–50. https://doi.org/10.1073/pnas.1008053107 PMID: 20876096; PubMed Central PMCID: PMC2955140.
14. Erhardt M, Hughes KT. C-ring requirement in flagellar type III secretion is bypassed by FlhDC upregulation. Molecular Microbiology. 2010; 75(2):376–93. https://doi.org/10.1111/j.1365-2958.2009.06973.x PMID: 19919668; PubMed Central PMCID: PMC3194100.
15. Paul K, Harmon JG, Blair DF. Mutational analysis of the flagellar rotor protein FliN: identification of surfaces important for flagellar assembly and switching. Journal of Bacteriology. 2006; 188(14):5240–8. https://doi.org/10.1128/JB.00110-06 PMID: 16816196; PubMed Central PMCID: PMC1539977.
16. Gonzalez-Pedrajo B, Minamino T, Kihara M, Namba K. Interactions between C ring proteins and export apparatus components: a possible mechanism for facilitating type III protein export. Molecular Microbiology. 2006; 60(4):984–98. https://doi.org/10.1111/j.1365-2958.2006.05149.x PMID: 16677309.
17. Erhardt M, Mertens ME, Fabiani FD, Hughes KT. ATPase-independent type-III protein secretion in *Salmonella enterica*. PLoS Genet. 2014; 10(11):e1004800. https://doi.org/10.1371/journal.pgen.1004800 PMID: 25393010; PubMed Central PMCID: PMC4230889.
18. Abrusci P, Vergara-Irigaray M, Johnson S, Beeby MD, Hendrixson DR, Roversi P, et al. Architecture of the major component of the type III secretion system export apparatus. Nature Structural & Molecular Biology. 2013; 20(1):99–104. https://doi.org/10.1038/nsmb.2452 PMID: 23222644; PubMed Central PMCID: PMC3537844.
19. Hara N, Namba K, Minamino T. Genetic characterization of conserved charged residues in the bacterial flagellar type III export protein FlhA. PLoS ONE. 2011; 6(7):e22417. https://doi.org/10.1371/journal.pone.0022417 PMID: 21811603; PubMed Central PMCID: PMC3139655.
20. Erhardt M, Wheatley P, Kim EA, Hirano T, Zhang Y, Sarkar MK, et al. Mechanism of type-III protein secretion: Regulation of FlhA conformation by a functionally critical charged-residue cluster. Molecular Microbiology. 2017. https://doi.org/10.1111/mmi.13623 PMID: 28106310.
21. Fraser GM, Hirano T, Ferris HU, Devgan LL, Kihara M, Macnab RM. Substrate specificity of type III flagellar protein export in *Salmonella* is controlled by subdomain interactions in FlhB. Molecular Microbiology. 2003; 48(4):1043–57. PubMed PMID: 12753195.

22. Minamino T, Macnab RM. Components of the *Salmonella* flagellar export apparatus and classification of export substrates. Journal of Bacteriology. 1999; 181(5):1388–94. PubMed PMID: 10049367; PubMed Central PMCID: PMC93525.

23. Ohnishi K, Fan F, Schoenhals GJ, Kihara M, Macnab RM. The FliO, FliP, FliQ, and FliR proteins of *Salmonella typhimurium*: putative components for flagellar assembly. Journal of Bacteriology. 1997; 179 (19):6092–9. PubMed PMID: 9324257; PubMed Central PMCID: PMC179513.

24. Liu R, Ochman H. Stepwise formation of the bacterial flagellar system. Proceedings of the National Academy of Sciences of the United States of America. 2007; 104(17):7116–21. https://doi.org/10.1073/pnas.0700266104 PMID: 17438286; PubMed Central PMCID: PMC1852327.

25. Barker CS, Meshcheryakova IV, Inoue T, Samatey FA. Assembling flagella in *Salmonella* mutant strains producing a type III export apparatus without FliO. Journal of Bacteriology. 2014; 196(23):4001–11. https://doi.org/10.1128/JB.02184-14 PMID: 25201947; PubMed Central PMCID: PMC4248865.

26. Barker CS, Meshcheryakova IV, Kostyukova AS, Samatey FA. FliO regulation of FliP in the formation of the *Salmonella enterica* flagellum. PLoS Genet. 2010; 6(9):e1001143. https://doi.org/10.1371/journal.pgen.1001143 PMID: 20941389; PubMed Central PMCID: PMC2947984.

27. Barlag B, Beutel O, Janning D, Czarniak F, Richter CP, Kommnick C, et al. Single molecule super-resolution imaging of proteins in living *Salmonella enterica* using self-labelling enzymes. Scientific Reports. 2016; 6:31601. https://doi.org/10.1038/srep31601 PMID: 27534893.

28. Pallen MJ, Penn CW, Chaudhuri RR. Bacterial flagellar diversity in the post-genomic era. Trends in Microbiology. 2005; 13(4):143–9. https://doi.org/10.1016/j.tim.2005.02.008 PMID: 15817382.

29. Langklotz S, Baumann U, Narberhaus F. Structure and function of the bacterial AAA protease FtsH. Biochimica et biophysica acta. 2012; 1823(1):40–8. https://doi.org/10.1016/j.bbamcr.2011.08.015 PMID: 21925212.

30. Kihara A, Akiyama Y, Ito K. Different pathways for protein degradation by the FtsH/HflKC membrane-embedded protease complex: an implication from the interference by a mutant form of a new substrate protein, YccA. Journal of Molecular Biology. 1998; 279(1):175–88. https://doi.org/10.1006/jmbi.1998.1781 PMID: 9636708.

31. van Stelten J, Silva F, Belin D, Silhavy TJ. Effects of antibiotics and a proto-oncogene homolog on destruction of protein translocator SecY. Science. 2009; 325(5941):753–6. https://doi.org/10.1126/science.1172221 PMID: 19661432; PubMed Central PMCID: PMC2832214.

32. Fan F, Ohnishi K, Francis NR, Macnab RM. The FliP and FliR proteins of *Salmonella typhimurium*, putative components of the type III flagellar export apparatus, are located in the flagellar basal body. Molecular Microbiology. 1997; 26(5):1035–46. PubMed PMID: 9426140.

33. Liss V, Barlag B, Nietschke M, Hensel M. Self-labelling enzymes as universal tags for fluorescence microscopy, super-resolution microscopy and electron microscopy. Scientific Reports. 2015; 5:17740. https://doi.org/10.1038/srep17740 PMID: 26643905; PubMed Central PMCID: PMC4672345.

34. Delalez NJ, Wadhams GH, Rosser G, Xue Q, Brown MT, Dobbie IM, et al. Signal-dependent turnover of the bacterial flagellar switch protein FliM. Proceedings of the National Academy of Sciences of the United States of America. 2010; 107(25):11347–51. https://doi.org/10.1073/pnas.1000284107 PMID: 20498085; PubMed Central PMCID: PMC2895113.

35. Kumar M, Mommer MS, Sourjik V. Mobility of cytoplasmic, membrane, and DNA-binding proteins in *Escherichia coli*. Biophysical Journal. 2010; 98(4):552–9. https://doi.org/10.1016/j.bpj.2009.11.002 PMID: 20159151; PubMed Central PMCID: PMC2820653.

36. Dajkovic A, Hinde E, MacKichan C, Carballido-Lopez R. Dynamic Organization of SecA and SecY Secretion Complexes in the B. subtilis Membrane. PLoS ONE. 2016; 11(6):e0157899. https://doi.org/10.1371/journal.pone.0157899 PMID: 27336478; PubMed Central PMCID: PMC4918944.

37. Dietsche T, Tesfazgi Mebrhatu M, Brunner M, Abrusci P, Yan J, Franz-Wachtel M, et al. Structural and Functional Characterization of the Bacterial Type III Secretion Export Apparatus. PLoS Pathog. 2016; 12(12):e1006071. https://doi.org/10.1371/journal.ppat.1006071 PMID: 27977800

38. Koirala S, Mears P, Sim M, Golding I, Chemla YR, Aldridge PD, et al. A nutrient-tunable bistable switch controls motility in *Salmonella enterica* serovar Typhimurium. mBio. 2014; 5(5):e01611–14. https://doi.org/10.1128/mBio.01611-14 PMID: 25161191; PubMed Central PMCID: PMC4173784.

39. Abby SS, Rocha EP. The non-flagellar type III secretion system evolved from the bacterial flagellum and diversified into host-cell adapted systems. PLoS Genet. 2012; 8(9):e1002983. https://doi.org/10.1371/journal.pgen.1002983 PMID: 23028376; PubMed Central PMCID: PMC3459982.

40. Simmons LA, Grossman AD, Walker GC. Clp and Lon proteases occupy distinct subcellular positions in *Bacillus subtilis*. Journal of Bacteriology. 2008; 190(20):6758–68. https://doi.org/10.1128/JB.00590-08 PMID: 18689473; PubMed Central PMCID: PMC2566193.

41. Rep M, van Dijl JM, Suda K, Schatz G, Grivell LA, Suzuki CK. Promotion of mitochondrial membrane complex assembly by a proteolytically inactive yeast Lon. Science. 1996; 274(5284):103–6. PubMed PMID: 8810243.

42. Diepold A, Wagner S. Assembly of the bacterial type III secretion machinery. FEMS Microbiology Reviews. 2014; 38(4):802–22. https://doi.org/10.1111/1574-6976.12061 PMID: 24484471.

43. Karlinsey JE. lambda-Red genetic engineering in *Salmonella enterica* serovar Typhimurium. Methods in Enzymology. 2007; 421:199–209. https://doi.org/10.1016/S0076-6879(06)21016-4 PMID: 17352924.

44. Datsenko KA, Wanner BL. One-step inactivation of chromosomal genes in *Escherichia coli* K-12 using PCR products. Proceedings of the National Academy of Sciences of the United States of America. 2000; 97(12):6640–5. https://doi.org/10.1073/pnas.120163297 PMID: 10829079; PubMed Central PMCID: PMC18686.

45. Gerlach RG, Holzer SU, Jackel D, Hensel M. Rapid engineering of bacterial reporter gene fusions by using Red recombination. Applied and Environmental Microbiology. 2007; 73(13):4234–42. https://doi.org/10.1128/AEM.00509-07 PMID: 17513596; PubMed Central PMCID: PMC1932792.

46. Eddy SR. Accelerated Profile HMM Searches. PLoS Comput Biol. 2011; 7(10):e1002195. https://doi.org/10.1371/journal.pcbi.1002195 PMID: 22039361; PubMed Central PMCID: PMC3197634.

47. Huerta-Cepas J, Serra F, Bork P. ETE 3: Reconstruction, Analysis, and Visualization of Phylogenomic Data. Molecular Biology and Evolution. 2016; 33(6):1635–8. https://doi.org/10.1093/molbev/msw046 PMID: 26921390; PubMed Central PMCID: PMC4868116.

48. Letunic I, Bork P. Interactive tree of life (iTOL) v3: an online tool for the display and annotation of phylogenetic and other trees. Nucleic Acids Research. 2016; 44(W1):W242–5. https://doi.org/10.1093/nar/gkw290 PMID: 27095192; PubMed Central PMCID: PMC4987883.

49. Lex A, Gehlenborg N, Strobelt H, Vuillemot R, Pfister H. UpSet: Visualization of Intersecting Sets. IEEE Transactions on Visualization and Computer Graphics. 2014; 20(12):1983–92. https://doi.org/10.1109/TVCG.2014.2346248 PMID: 26356912; PubMed Central PMCID: PMC4720993.

50. Aldridge P, Karlinsey JE, Becker E, Chevance FF, Hughes KT. Flk prevents premature secretion of the anti-sigma factor FlgM into the periplasm. Molecular Microbiology. 2006; 60(3):630–43. https://doi.org/10.1111/j.1365-2958.2006.05135.x PMID: 16629666; PubMed Central PMCID: PMC3471667.

51. Kaur J, Bachhawat AK. A modified Western blot protocol for enhanced sensitivity in the detection of a membrane protein. Analytical Biochemistry. 2009; 384(2):348–9. https://doi.org/10.1016/j.ab.2008.10.005 PMID: 18952039.

52. Ladner CL, Yang J, Turner RJ, Edwards RA. Visible fluorescent detection of proteins in polyacrylamide gels without staining. Analytical Biochemistry. 2004; 326(1):13–20. https://doi.org/10.1016/j.ab.2003.10.047 PMID: 14769330.

53. Zilkenat S, Dietsche T, Monjarás Feria JV, Torres-Vargas CE, Mebrhatu MT, Wagner S. Blue Native PAGE Analysis of Bacterial Secretion Complexes. Methods Molecular Biology. 2017; 1615. doi: 978-1-4939-7031-5.

54. Fukumura T, Makino F, Dietsche T, Kinoshita M, Kato T, Wagner S, et al. Assembly and stoichiometry of the core structure of the bacterial flagellar type III export gate complex. PLoS Biol. 2017;15(8):e2002281. https://doi.org/10.1371/journal.pbio.2002281

55. Rappsilber J, Mann M, Ishihama Y. Protocol for micro-purification, enrichment, pre-fractionation and storage of peptides for proteomics using StageTips. Nature Protocols. 2007; 2(8):1896–906. https://doi.org/10.1038/nprot.2007.261 PMID: 17703201.

56. Franz-Wachtel M, Eisler SA, Krug K, Wahl S, Carpy A, Nordheim A, et al. Global detection of protein kinase D-dependent phosphorylation events in nocodazole-treated human cells. Molecular & Cellular Proteomics: MCP. 2012; 11(5):160–70. https://doi.org/10.1074/mcp.M111.016014 PMID: 22496350; PubMed Central PMCID: PMC3418846.

57. Cox J, Mann M. MaxQuant enables high peptide identification rates, individualized p.p.b.-range mass accuracies and proteome-wide protein quantification. Nature Biotechnology. 2008; 26(12):1367–72. https://doi.org/10.1038/nbt.1511 PMID: 19029910.

58. Cox J, Neuhauser N, Michalski A, Scheltema RA, Olsen JV, Mann M. Andromeda: a peptide search engine integrated into the MaxQuant environment. Journal of Proteome Research. 2011; 10(4):1794–805. https://doi.org/10.1021/pr101065j PMID: 21254760.

59. Elias JE, Gygi SP. Target-decoy search strategy for increased confidence in large-scale protein identifications by mass spectrometry. Nature Methods. 2007; 4(3):207–14. https://doi.org/10.1038/nmeth1019 PMID: 17327847.

Publication 3

PLOS BIOLOGY

RESEARCH ARTICLE

Assembly and stoichiometry of the core structure of the bacterial flagellar type III export gate complex

Takuma Fukumura[1], Fumiaki Makino[1], Tobias Dietsche[2], Miki Kinoshita[1], Takayuki Kato[1], Samuel Wagner[2,3], Keiichi Namba[1,4]*, Katsumi Imada[5]*, Tohru Minamino[1]*

1 Graduate School of Frontier Biosciences, Osaka University, Suita, Osaka, Japan, **2** Interfactulty Institute of Microbiology and Infection Medicine, Section of Cellular and Molecular Microbiology, Eberhard Karls University Tübingen, Tübingen, Germany, **3** German Center for Infection Research (DZIF), Partner-site Tübingen, Tübingen, Germany, **4** Quantitative Biology Center, Riken, Suita, Osaka, Japan, **5** Department of Macromolecular Science, Graduate School of Science, Osaka University, Toyonaka, Osaka, Japan

* keiichi@fbs.osaka-u.ac.jp (KN); kimada@chem.sci.osaka-u.ac.jp (KI); tohru@fbs.osaka-u.ac.jp (TM)

Citation: Fukumura T, Makino F, Dietsche T, Kinoshita M, Kato T, Wagner S, et al. (2017) Assembly and stoichiometry of the core structure of the bacterial flagellar type III export gate complex. PLoS Biol 15(8): e2002281. https://doi.org/10.1371/journal.pbio.2002281

Academic Editor: Ann Stock, UMDNJ/Robert Wood Johnson Medical School, United States of America

Received: February 22, 2017

Accepted: June 30, 2017

Published: August 3, 2017

Data Availability Statement: All relevant data are within the paper and its Supporting Information files. The atomic coordinates of the periplasmic domain of FliP derived from *Thermotoga maritia* have been deposited in Protein Data Bank under the accession code 5H72. Amino acid sequences of FliP derived from *Salmonella* and *Thermotoga* are available from the UniProt database. Uniprot accession numbers are P54700 for *Salmonella* FliP and Q9WZG2 for *Thermotoga* FliP.

Abstract

The bacterial flagellar type III export apparatus, which is required for flagellar assembly beyond the cell membranes, consists of a transmembrane export gate complex and a cytoplasmic ATPase complex. FlhA, FlhB, FliP, FliQ, and FliR form the gate complex inside the basal body MS ring, although FliO is required for efficient export gate formation in *Salmonella enterica*. However, it remains unknown how they form the gate complex. Here we report that FliP forms a homohexameric ring with a diameter of 10 nm. Alanine substitutions of conserved Phe-137, Phe-150, and Glu-178 residues in the periplasmic domain of FliP ($FliP_P$) inhibited $FliP_6$ ring formation, suppressing flagellar protein export. FliO formed a 5-nm ring structure with 3 clamp-like structures that bind to the $FliP_6$ ring. The crystal structure of $FliP_P$ derived from *Thermotoga maritia*, and structure-based photo-crosslinking experiments revealed that Phe-150 and Ser-156 of $FliP_P$ are involved in the FliP–FliP interactions and that Phe-150, Arg-152, Ser-156, and Pro-158 are responsible for the FliP–FliO interactions. Overexpression of FliP restored motility of a Δ*fliO* mutant to the wild-type level, suggesting that the $FliP_6$ ring is a functional unit in the export gate complex and that FliO is not part of the final gate structure. Copurification assays revealed that FlhA, FlhB, FliQ, and FliR are associated with the FliO/FliP complex. We propose that the assembly of the export gate complex begins with $FliP_6$ ring formation with the help of the FliO scaffold, followed by FliQ, FliR, and FlhB and finally FlhA during MS ring formation.

Author summary

The bacterial flagellar type III export gate complex is a membrane-embedded nanomachine responsible for flagellar protein export and exits in a patch of membrane within the central pore of the basal body MS ring. In this work, we investigate how formation of the export gate complex is initiated. The export gate complex is composed of 5 highly

Funding: This research has been supported in part by JSPS KAKENHI Grant Numbers JP26650021 (to TK), JP15H02386 (to KI), JP25000013 (to KN) and JP26293097 (to TM) from the Japan Society for the Promotion of Science (http://www.jsps.go.jp/english/index.html) and MEXT KAKENHI Grant Numbers JP23115008 (to K.I.) and JP24117004, JP25121718 and JP15H01640 (to TM) from the Ministry of Education, Culture, Sports, Science and Technology of Japan (http://www.mext.go.jp/english/index.htm) and by the Deutsche Forschungsgemeinschaft (DFG) as part of the Collaborative Research Center (SFB) 766 "Bacterial cell envelope", project B14 (to SW) (http://www.dfg.de). The funders had no role in study design, data collection and analysis, decision to publish, or preparation of the manuscript.

Competing interests: The authors have declared that no competing interests exist.

Abbreviations: pBPA, *p*-benzoyl-phenylalanine; CBB, Coomassie Brilliant Blue; CM, cytoplasmic membrane; DDM, n-dodecyl β-D-maltoside; EM, electron microscopy; LMNG, lauryl maltose neopentyl glycol; NTA, nitrilotriacetic acid; PDB, Protein Data Bank; SEC, size exclusion chromatography; T3SS, type III secretion system; TM, transmembrane; WT, wild type.

conserved transmembrane proteins: FlhA, FlhB, FliP, FliQ, and FliR. Each subunit protein assembles into the gate during MS ring formation in a well-coordinated manner. The transmembrane protein FliO is required for efficient assembly of the export gate complex in *S. enterica* but is not essential for flagellar protein export. Here we carry out biochemical and structural analyses of FliP and provide direct evidence suggesting that FliP forms a trimer-of-dimer structure with a diameter of 10 nm. The assembly of the export gate complex begins with $FliP_6$ ring formation with the help of the FliO scaffold, followed by FliQ, FliR, and FlhB and finally FlhA during MS ring formation. Given the structural and functional similarities between the flagellar and the virulence-factor-delivering injectisome machineries, we propose that the periplasmic domain of FliP homologues of the injectisome could be a good target for novel antibiotics.

Introduction

The bacterial flagellum is supramolecular motility machinery consisting of basal body rings and an axial structure consisting of the rod, the hook, the hook-filament junction, the filament, and the filament cap. Flagellar axial proteins are translocated across the cytoplasmic membrane by a type III protein export apparatus and assemble at the distal end of the growing structure. The export apparatus consists of an export gate complex formed by 5 highly conserved transmembrane proteins (FlhA, FlhB, FliP, FliQ, and FliR) and a cytoplasmic ATPase complex consisting of FliH, FliI, and FliJ [1–4]. These flagellar proteins are evolutionarily related to the components of the type III secretion system (T3SS) of pathogenic bacteria, also known as the injectisome [5]. The transmembrane protein, FliO, which is not conserved in flagellar and virulence-associated T3SS family, is required for efficient assembly of the export gate complex in *S. enterica* (hereafter referred to as *Salmonella*) but is not essential for flagellar protein export [6–8].

The flagellar type III export apparatus utilizes ATP and proton motive force across the cytoplasmic membrane to drive protein export [2,3]. Recently, it has been shown that ATP hydrolysis by the FliI ATPase and the following rapid protein translocation by the export gate complex are both linked to efficient proton translocation through the gate, suggesting that the export apparatus acts as a proton/protein antiporter to couple the proton flow through the gate with protein export [9]. Interestingly, the structure of the cytoplasmic ATPase complex looks similar to those of F- and V-type rotary ATPases [10–12].

The export gate complex is located inside the basal body MS ring formed by a transmembrane protein, FliF [13,14]. FlhA forms a homononamer [8,13] and acts as an energy transducer along with the cytoplasmic ATPase complex [15–19]. The C-terminal cytoplasmic domains of FlhA and FlhB form a docking platform for the ATPase complex, flagellar type III export chaperones, and export substrates [20–22] and coordinate flagellar protein export with assembly [23–26]. Genetic analyses have suggested possible interactions of the N-terminal transmembrane domain of FlhA ($FlhA_{TM}$) with FliF [27], FliR [28] and FlhB [29]. Since a FlhB–FliR fusion protein is partially functional in *Salmonella*, FlhB presumably associates with FliR in a 1-to-1 fashion [30]. FliP and FliR are incorporated into the basal body at the earliest stage of MS ring formation [31,32]. The transmembrane export gate complex of the *Salmonella* SPI-1 T3SS is composed of SpaP (FliP homologue), SpaQ (FliQ homologue), SpaR (FliR homologue), SpaS (FlhB homologue), and InvA (FlhA homologue) in a 5:1:1:1:9 stoichiometry [33]. Recently, it has been shown that 5 copies of SpaP and 1 copy of SpaR form a donut-shaped structure with a diameter of about 8 nm [34]. Since the assembly of the export apparatus begins

with SpaP, SpaQ, and SpaR, followed by the assembly of SpaS and finally of InvA in the *Salmonella* SPI-1 T3SS [34,35], the assembly of the flagellar export gate complex is postulated to occur in a way similar to the *Salmonella* SPI-1 T3SS [8].

FliP is a 25-kDa transmembrane protein that has a cleavable N-terminal signal peptide, 4 transmembrane (TM) helices, and a relatively large periplasmic domain ($FliP_P$) between TM-2 and TM-3 (S1 Fig) [36]. The number of FliP molecules has been estimated to be 4 to 5 per basal body in *Salmonella* [32]. $FliP_P$ of *T. maritia* (*Tm*-$FliP_P$) forms a homotetramer in solution [37], raising the possibility that *Salmonella* FliP (*St*-FliP) forms an oligomer through interactions between $FliP_P$ domains. To study the oligomeric structure of FliP, we purified *St*-FliP from the membrane fraction by solubilizing it with 1% n-dodecyl β-D-maltoside (DDM) and analyzed it by electron microscopy (EM) and image analysis. We show that FliP forms a homohexameric ring with a diameter of about 10 nm. We also determined the structure of *Tm*-$FliP_P$ at 2.4 Å resolution and carried out structure-based photo-crosslinking experiments. We will discuss the assembly mechanism of the transmembrane export gate complex.

Results

Oligomeric state of full-length *St*-FliP

To study the oligomeric state of mature form of FliP, we expressed, solubilized, and purified *St*-FliP. A hexahistidine tag (LHHHHHH) was inserted between Gln-22 and Leu-23 of *St*-FliP (His-*St*-FliP) for rapid and efficient purification (S1 Fig). The membrane fraction of *Salmonella* cells expressing His-*St*-FliP was solubilized by 1% DDM, and His-*St*-FliP was purified by Ni affinity chromatography (Fig 1A), followed by size exclusion chromatography (SEC) with a Superdex 200 10/300 column (Fig 1B, first row). The SEC elution profile of His-*St*-FliP showed 2 distinct peaks (S2A Fig). Many ring-shaped structures were observed by EM of negatively stained particles in the earlier peak fraction (S2B Fig, Peak 2) but not in the later one (S2B Fig, Peak 4).

An apparent molecular mass of the FliP ring structure was estimated to be about 200 kDa by SEC (S2A Fig). Since the deduced molecular weight of His-*St*-FliP is approximately 25 kDa, the FliP ring structure presumably contains several copies of FliP together with a DDM micelle covering the transmembrane helices of FliP. To estimate the stoichiometry of the FliP ring more precisely, we carried out 2D classification EM image analysis of negatively stained FliP ring particles, followed by autocorrelation analysis for the rotational symmetry (Fig 2 and S3 Fig). The *St*-FliP rings exhibiting clear blob features were mostly hexameric with a diameter of about 10 nm (Fig 2 and S3A, S3B and S3C Fig). Autocorrelation analysis also showed that 5,333 of the 11,736 FliP ring particles analyzed were assigned to the 6-fold rotational symmetry and the rest, which did not show proper ring-shaped structures, were assigned to 5-fold or other rotational symmetries (S3D and S3E Fig), suggesting either that the ring structure is flexible or that they could be side views or incomplete partial rings.

Interaction between FliP and FliO

Previous genetic analyses of a *Salmonella* Δ*fliO* mutant have suggested possible interactions between FliO and FliP [6,7]. To clarify this, we coexpressed FliO with His-FliP and purified them by Ni affinity chromatography and finally by SEC. In agreement with a previous report [6], FliO was expressed as 2 forms: $FliO_L$ and $FliO_S$ (Fig 1A). Both forms copurified with His-FliP from a SEC column (Fig 1B, second row). EM observation of the FliO/FliP complex revealed that 2 to 3 $FliP_6$ rings are connected to each other through an interaction between FliP and FliO (Fig 2 and S2B and S4 Figs). Since the inner diameter of the M ring of the flagellar basal body is about 20 nm [3] and is too small to accommodate such multiring complexes of FliO and FliP, it is likely that only 1 $FliP_6$ ring exists in the final structure of the export gate

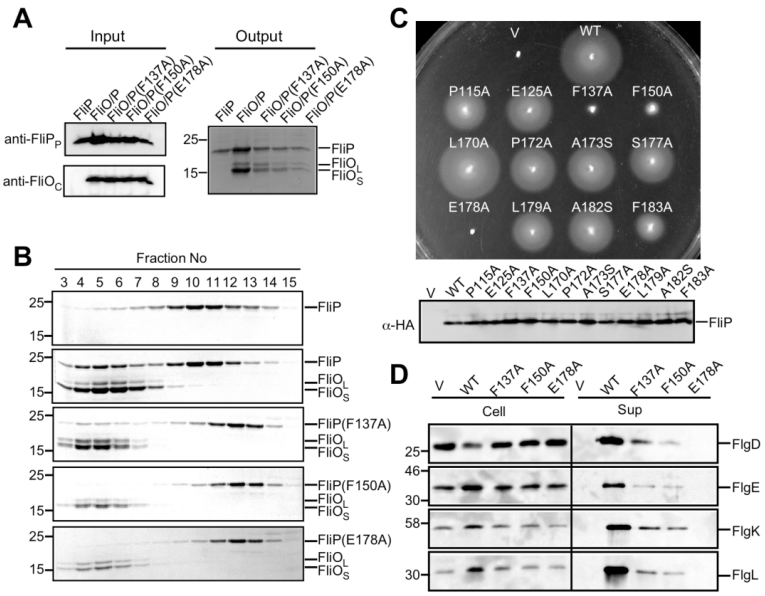

Fig 1. Genetic and biochemical characterization of *St*-FliP. (A) Ni affinity chromatography. The membrane fractions were prepared from SJW1368 expressing His-FliP (FliP), FliO and His-FliP (FliO/P), FliO and His-FliP (F137A) [FliO/P(F137A)], FliO and His-FliP(F150A) [FliO/P(F150A)], or FliO and His-FliP(E178A) [FliO/P(E178A)], solubilized by 1% n-dodecyl β-D-maltoside (DDM) and analyzed by immunoblotting with polyclonal anti-FliP$_P$ or anti-FliO$_C$ antibody (Input). The solubilized membranes were loaded onto a Ni–nitrilotriacetic acid (NTA) column. After washing the column extensively, proteins were eluted with a 50–400 mM imidazole gradient. Fractions containing His-FliP with or without FliO were analyzed by SDS-PAGE with Coomassie Brilliant Blue (CBB) staining (Output). Molecular mass markers (kDa) are shown on the left. (B) Size exclusion chromatography (SEC) analysis with a Superdex 200 10/300 column. Eluted factions were monitored by SDS-PAGE with CBB staining. (C) Motility of a *Salmonella* Δ*fliP* mutant transformed with pBAD24-based plasmids encoding wild-type FliP and its mutant variants in soft agar at 30˚C for 6 h (upper panel). Immunoblotting, using monoclonal anti-HA antibody, of whole cell lysates prepared from the Δ*fliP* mutant transformed with pUC19-based plasmids encoding wild-type FliP and its mutant variants. (D) Effect of the F137A, F150A, and E178A mutations on flagellar protein export. Whole cell proteins (Cell) and culture supernatant fractions (Sup) were prepared from the Δ*fliP* mutant transformed with pBAD24 (indicated as V), pKY041 (indicated as WT), pKY041(F137A) (indicated as F137A), pKY041(F150A) (indicated as F150A), or pKY014(E178A) (indicated as E178A) and then analyzed by immunoblotting with polyclonal anti-FlgD (first row), anti-FlgE (second row), anti-FlgK (third row), or anti-FlgL (fourth row) antibody. The positions of molecular mass markers are indicated on the left.

https://doi.org/10.1371/journal.pbio.2002281.g001

complex. To test this, we investigated whether overexpression of *St*-FliP restores motility of a *Salmonella* Δ*fliO* mutant. To monitor the expression level of *St*-FliP, we inserted a HA tag between Gln-22 and Leu-23 of *St*-FliP (HA-*St*-FliP). The motility of the Δ*fliO* mutant overexpressing HA-*St*-FliP was essentially the same as that of the Δ*fliO* mutant transformed with a pTrc99A-based plasmid encoding FliO (S5 Fig). This indicates that FliO is not essential for flagellar protein export.

We next tested whether FliO itself forms an oligomer. We found that the FliP$_6$ ring dissociates from FliO during storage of the purified FliO/FliP complexes at 4˚C (S6A Fig). Thus, we ran purified FliO/His-FliP complex samples on a Ni– nitrilotriacetic acid (NTA) column to

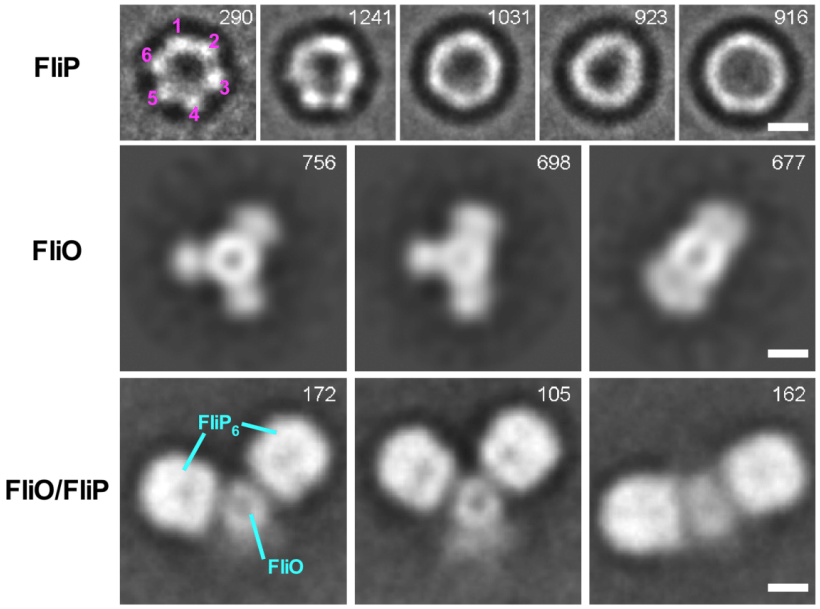

Fig 2. Enlarged views of representative 2D class averages of the $FliP_6$ ring, the FliO complex, and the FliO/FliP complex. Reference-free 2D class average images were calculated by e2refine2d.py. All scale bars show 50 Å. The number of particles for each class is indicated in the top-right corner. FliP forms a ring structure with a diameter of about 10 nm (first row). The FliP ring has the 6-fold rotational symmetry as judged by autocorrelation analysis (see S3A, S3B and S3C Fig). FliO forms a ring structure of 5 nm in diameter with 3 flexible clamp-like structures (second row) that bind to the FliP ring with their ring axes perpendicular to the axis of the FliO ring (third row). Thus, the FliP rings in the first row are end-on views, and those in the third row are side views.

https://doi.org/10.1371/journal.pbio.2002281.g002

remove His-$FliP_6$ rings and the FliO/His-FliP complex, followed by SEC to purify FliO (S6B Fig). EM observation and image analysis showed that FliO forms a 5-nm ring structure with 3 flexible clamp-like structures (Fig 2 and S2 and S4 Figs). These observations led us to conclude that the FliO ring complex is not incorporated into the MS ring.

Mutational analysis of *St*-$FliP_P$

The FliP(R143H) mutation, which is located in *St*-$FliP_P$, can bypass the FliO defect to some extent [6,7], raising the possibility that *St*-$FliP_P$ is required for $FliP_6$ ring formation. To test this, we selected relatively well-conserved residues of FliP, Pro-115, Glu-125, Phe-137, Phe-150, Leu-170, Phe-172, Ala-173, Ser-177, Glu-178, Leu-179, Ala-182, and Phe-183 (S1B Fig); replaced each residue with alanine, except for Ala-173 and Ala-182, which we replaced with serine; and then analyzed the motility of mutant strains in soft agar (Fig 1C, upper panel). These substitutions did not significantly affect the steady cellular level of FliP as judged by immunoblotting with monoclonal HA-tag antibody (Fig 1C, lower panel). HA-*St*-FliP fully restored the motility of a Δ*fliP* mutant. The L170A mutant variant complemented the Δ*fliP* mutant to the wild-type level. The P115A, E125A, P172A, A173S, S177A, L179A, A182S, and F183A mutant variants restored the motility to a considerable degree, although not to the

wild-type level. The F137A and F150A mutant variants complemented the Δ*fliP* mutant to some degree, and the E178A mutant variant did not at all. In agreement with these results, the F137A and F150A mutations in FliP significantly reduced the secretion levels of the hook-capping protein FlgD, the hook protein FlgE, and the hook-filament junction proteins FlgK and FlgL, and the E178A substitution inhibited the export of these flagellar proteins (Fig 1D). These results indicate that highly conserved Phe-137, Phe-150, and Glu-178 residues of $FliP_P$ are critical for the protein export activity.

To investigate whether the F137A, F150A, and E178A mutations affect the FliP–FliO interaction, we carried out copurification assays by Ni-NTA affinity chromatography. FliO coeluted with His-FliP(F137A), His-FliP(F150A), and His-FliP(E178A) from a Ni-NTA column (Fig 1A, Output), indicating that they retain the ability to bind to FliO. To test whether these FliP mutations inhibit $FliP_6$ ring formation, we ran FliO/His-FliP(F137A), FliO/His-FliP(F1507A), and FliO/His-FliP(E178A) complexes on a SEC column and then analyzed the pooled fractions by EM. His-FliP(F137A), His-FliP(F150A), and His-FliP(E178A) dissociated from the FliO complex during SEC and eluted at the same position as peak 4 of wild-type FliP (Fig 1B and S2A Fig), indicating that these mutations reduced the binding affinity of FliP for FliO. The FliO ring structures were seen in their peak 3 fractions, but neither FliP(F137A), FliP(F150A), nor FliP(E178A) formed the homohexamer ring (S2B Fig, Peak 4). These results suggest that Phe-137, Phe-150, and Glu-178 in $FliP_P$ contribute to the FliP–FliP interactions in the 6-fold rotational symmetry ring as well as the FliO–FliP interaction.

Crystal structure of *Tm*-$FliP_P$

To clarify the role of $FliP_P$ in $FliP_6$ ring formation, we determined the crystal structure of $FliP_P$. Although no *St*-$FliP_P$ crystal was obtained, the *Tm*-$FliP_P$ crystals were grown [37], and its structure was solved at 2.4 Å resolution. *Tm*-$FliP_P$ formed a homotetramer in the crystal (Mol A, Mol B, Mol C, and Mol D) related by pseudo D2 symmetry (Protein Data Bank [PDB] ID: 5H72) (Fig 3A). There are 2 tetramers in the asymmetric unit, and their structures are essentially identical. The 8 *Tm*-$FliP_P$ molecules in the asymmetric unit show no significant structural difference (root mean square distances for Cα atoms are less than 0.46 Å for the 8 molecules). *Tm*-$FliP_P$ monomer consists of 3 α-helices: α1, α2 and α3 (Fig 3B). The N-terminal 13 residues are invisible in the electron density map presumably because of their conformational flexibility. Therefore, the atomic model of *Tm*-$FliP_P$ contains residues from Thr-122 to Lys-188. Since each subunit of the *Tm*-$FliP_P$ tetramer is related by D2 symmetry, we studied 3 possible intermolecular interactions: between Mol A and Mol B (Mol C and Mol D), between Mol A and Mol C (Mol B and Mol D), and between Mol A and Mol D (Mol B and Mol C) (Fig 3A). The A–B interaction is hydrophobic, and Tyr-124, Phe-128, Met-154, Leu-155, Pro-176, and Leu-180 are involved in this interaction (S7A, S7C, S7D and S7E Fig). The A–C interaction contains both hydrophilic and hydrophobic nature, and Met-127, Arg-130, Val-131, Arg-134, Phe-138, Glu-142, Glu-182, Val-185, Ala-186, and Phe-187 are responsible (S7B, S7F, S7G and S7H Fig). Arg-134 forms a salt bridge with Glu-142 and Glu-182. Ala-186 and Phe-187 make hydrophobic interactions with Met-127, Val-131, and the side chain arm of Arg-130. There is no direct contact between Mol A and Mol D. Since sedimentation equilibrium analytical ultracentrifugation measurements have revealed that *Tm*-$FliP_P$ forms a homotetramer in solution [37], we conclude that the tetramer structure observed in the crystal appears to be equivalent to that in solution.

Physical contacts between *St*-$FliP_P$ monomers

Although the *Tm*-$FliP_P$ tetramer in the crystal is inconsistent with the *St*-$FliP_6$ ring structure, it is possible that the dimer units seen in the tetramer are responsible for the hexameric ring

formation of *St*-FliP if the hexamer is a trimer-of-dimer structure. Two distinct dimers are present in the *Tm*-FliP$_P$ crystal: A–B dimer and A–C dimer (Fig 3A and S7 Fig). Although the sequence identity between *Tm*-FliP$_P$ and *St*-FliP$_P$ is only about 30% (Fig 3C), we constructed a homology model of *St*-FliP$_P$ based on the *Tm*-FliP$_P$ tetramer structure (Fig 3D and 3E). The interface residues are not well conserved, but the properties of the interface of *St*-FliP$_P$ are similar to those of *Tm*-FliP$_P$ (S8 Fig). The A–B interface of *St*-FliP$_P$ is hydrophobic, and Met-123, Leu-127, Leu-149, Phe-150, and Pro-172 form the hydrophobic surface (S8A, S8B and S8C Fig). The A–C interface of *St*-FliP$_P$ shows an elongated shape with both hydrophilic and hydrophobic properties (S8D, S8E and S8F Fig). Arg-140 and Gln-141 form a hydrogen-bonding network with those in the other molecule. Phe-137 is in contact with Tyr-174 and the side chain arm of Glu-178. Considering the hydrophobic nature of the A–B interface, the A–B dimer is more likely to be a dimer unit of the FliP$_6$ ring structure, although the area of the A–B interface is smaller than that of the A–C interface. The C-termini of the A–B dimer can be connected to the periplasmic end of TM-3 without any steric hindrances with the cytoplasmic

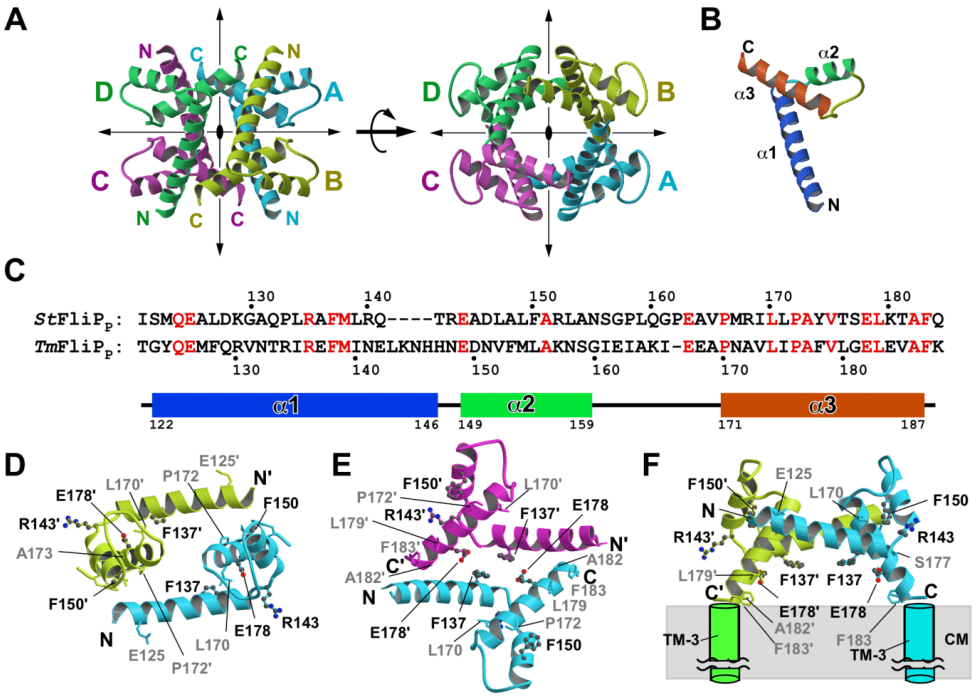

Fig 3. Structure of FliP$_P$. (A) Ribbon diagram of the *Tm*-FliP$_P$ tetramer in the crystal (Protein Data Bank [PDB] ID: 5H72). Two different views are shown. Mol A, Mol B, Mol C, and Mol D are colored in cyan, yellow green, magenta, and green, respectively. Each subunit of the *Tm*-FliP$_P$ tetramer is related by D2 symmetry. (B) Cα ribbon drawing of the *Tm*-FliP$_P$ monomer. The secondary structure elements are labeled with α for α-helix. (C) Structure-based sequence alignment of *Salmonella* FliP$_P$ (*St*FliP$_P$) and *Tm*-FliP$_P$. The secondary structure of *Tm*-FliP$_P$ is shown below the sequence. Identical residues are highlighted in red. Uniprot accession numbers: *Salmonella* (P54700) and *Thermotoga* (Q9WZG2). (D) Homology model of the A–B dimer of *St*-FliP$_P$. (E) Homology model of the A–C dimer of *St*-FliP$_P$. (F) The model of the A–B dimer connected to the TM-3 helices. Both C-termini of the A–B dimer can be directly connected to the TM-3 helices. CM, cytoplasmic membrane. Residues selected for mutational analyses are mapped and labeled in (D), (E), and (F). The residues whose substitution affected the FliP function are shown in ball-and-stick with black labels, and those that did not are in stick with gray labels.

https://doi.org/10.1371/journal.pbio.2002281.g003

membrane, suggesting that the A–B dimer contributes to trimer-of-dimer ring formation (Fig 3F). Because the N-terminal 13 residues are invisible, it is possible that both of the 2 N-termini of the dimer can connect to the periplasmic ends of TM-2 helices. In contrast, if the C-termini of the A–C dimer are directly connected to TM-3, the hydrophilic surface of the dimer core region would be buried in the cytoplasmic membrane (S7H and S8F Figs), which is unlikely.

In vivo photo-crosslinking

To investigate which dimer form is actually present in the $FliP_6$ ring structure, we carried out structure-based photo-crosslinking experiments. We introduced an amber mutation at positions of 123, 124, 127, 137, 150, 152, 156, or 158 of *St*-FliP to incorporate *p*-benzoyl-phenylalanine (pBPA), which is a photoreactive phenylalanine. Since Ser-14 and Thr-15 in TM-1 of SpaP—which correspond to Leu-51 and Thr-52 in TM-1 of *St*-FliP, respectively—provide strong SpaP-SpaP photo-crosslinked products [34], we also introduced an amber mutation at positions of 51 or 52. We introduced 2 plasmids into the *Escherichia coli* BL21(DE3) strain, 1 encoding FliO, FLAG-tagged FliP (FliP-FLAG) with an amber mutation, FliQ, and FliR and the other encoding the amber suppressor tyrosyl tRNA and the engineered tyrosyl-tRNA synthetase to incorporate pBPA at the positions of amber codons. We used wild-type FliP-FLAG as a negative control. As expected, UV irradiation of pBPA at positions of 51 or 52 led to the formation of a photo-crosslinked FliP homodimer (Fig 4A, indicated by a red dot), indicating that TM-1 of FliP is responsible for the FliP–FliP interaction in a way similar to the SpaP–SpaP interaction. Both FliP(F150pBPA)-FLAG and FliP(S156pBPA)-FLAG also reproducibly gave a photo-crosslinked FliP homodimer, whereas the others did not (Fig 4A, indicated by a red dot). This photo-crosslinked product was also observed when only FliO and FliP-FLAG with an amber mutation were expressed in the presence of pBPA (Fig 4B). These results indicate that both FliP-TM1 and $FliP_P$ are involved in the FliP–FliP interactions in the hexameric ring structure. Phe-150 and Ser-156 are located at the A–B interface, whereas Phe-137 is located at the A–C interface (Fig 3D and 3E and S8B and S8E Fig). Since we found that both Phe-137 and Phe-150 are required for $FliP_6$ ring formation, protein export, and motility (Fig 1), the A–B dimer unit seen in the *Tm*-$FliP_P$ crystal structure is likely to exist in the *St*-$FliP_6$ ring structure, and it is likely that Phe-137 contributes to its trimer-of-dimer formation.

UV irradiating pBPA at positions of Phe-150, Arg-152, Ser-156, or Pro-158 produced a 30-kDa crosslinked band, suggesting the presence of a FliP-FliO crosslinked product (indicated by blue dot). This band was also present when only FliO and FliP were expressed (Fig 4B). To confirm the FliO–FliP interaction, we labeled FliO and FliP(R152pBPA) with a 3 x FLAG tag and a 3 x HA tag, respectively. FliO-FLAG formed a crosslinked band with FliP (R152pBPA)-HA but not with wild-type FliP-HA, proving the presence of the FliO–$FliP_P$ interaction (Fig 4C). These results indicate that Phe-150, Arg-152, Ser-156, and Pro-158 of $FliP_P$ are in relatively close proximity to FliO (Fig 4D). This is in agreement with our finding that the F150A mutation reduced the binding affinity of FliP for FliO (Fig 1). Interestingly, the UV irradiation of pBPA at a position of 52 also produced a 30-KDa crosslinked product in the absence of FliQ and FliR (Fig 4B) but not in their presence (Fig 4A), indicating that the TM-1 helix of FliP is in close proximity to FliO when FliQ and FliR are absent.

The intensity of the FliO-FliP crosslinked band formed by the introduction of pBPA at positions of Phe-150, Ser-156, or Pro-158 was weaker in the presence of FliQ and FliR (Fig 4A) than in their absence (Fig 4B), whereas the intensity of the FliP-FliP crosslinked band at positions of Phe-150 or Ser-156 was somehow stronger in the presence of FliQ and FliR (Fig 4A) than in their absence (Fig 4B). Therefore, we suggest that FliO appears to facilitate oligomerization of FliP and maintain its stability until FliQ and FliR assemble into the $FliP_6$ ring and that the

binding of FliQ and FliR to FliP probably induces conformational rearrangements of the FliP ring in the FliO complex.

Interaction of the $FliP_6$ ring with FliQ, FliR, FlhB, and FlhA

To analyze the interactions of the $FliP_6$ ring with other export gate proteins, we constructed plasmids coexpressing His-FliP with FliR-FLAG, with HA-FliQ and FliR-FLAG, with FliO and

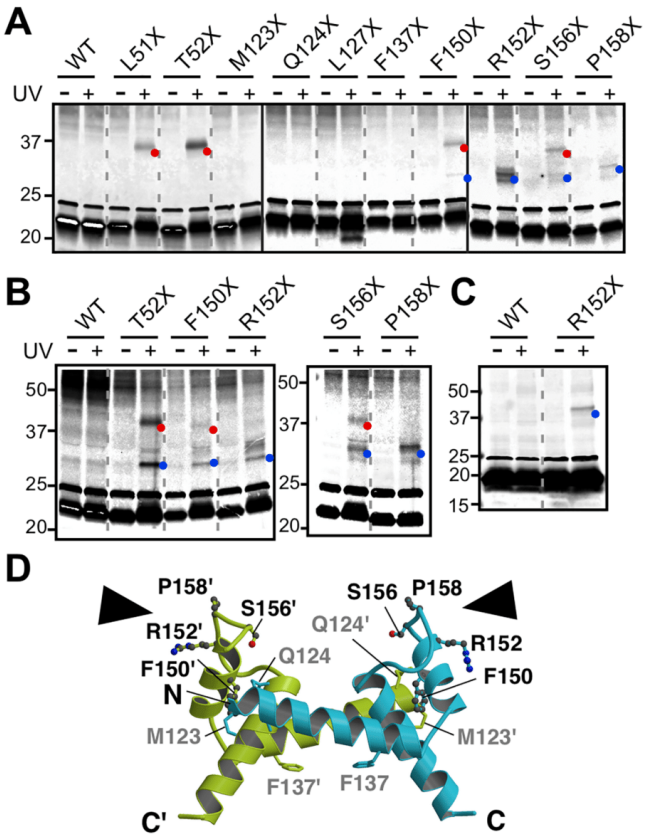

Fig 4. In vivo photo-crosslinking. *E. coli* BL21 (DE3) cells coexpressing (A) FliP-FLAG with an amber mutation at indicated positions with FliO, FliQ, and FliR, (B) FliP-FLAG with an amber mutation with FliO, or (C) FliP-HA with an amber mutation with FliO-FLAG were grown in the presence of *p*-benzoyl-phenylalanine (pBPA) and then treated with (+) or without (−) UV irradiation. Wild-type FliP-FLAG (WT) was used as a negative control. Crude membrane fractions were prepared, followed by SDS-PAGE and finally immunoblotting with monoclonal anti-FLAG antibody. Red and blue dots indicate FliP-FliP and FliP-FliO photo-crosslinked products, respectively. Each cropped blot is shown within a box. (D) The residues selected for the photo-crosslinking experiment are mapped on the A–B dimer model of *St*-$FliP_P$. The residues that formed crosslinking products by the substitution with pBPA are shown in ball-and-stick with black labels, and those that did not are in stick with gray labels. Black arrowheads indicate possible interaction sites of *St*-$FliP_P$ with FliO.

https://doi.org/10.1371/journal.pbio.2002281.g004

FliR-FLAG, with FliO, HA-FliQ, and FliR-FLAG, or with FlhA, FlhB, FliO, HA-FliQ, and FliR-FLAG. These tags did not affect the export function of export gate proteins considerably. To simplify the examination of their interactions, we expressed these proteins from a single pTrc99A-based plasmid in the *Salmonella* SJW1368 strain, in which no flagellar genes are expressed because of loss of the master regulator complex, $FlhD_4FlhC_2$ [1]. The membrane fractions of *Salmonella* cells coexpressing His-FliP with other export gate proteins were solubilized by 1% DDM, and then the proteins were purified by Ni affinity chromatography, followed by FLAG affinity chromatography (S9 Fig) and finally SEC (Fig 5A). FliR-FLAG and FlhB copurified with His-FliP and FliO, whereas neither HA-FliQ nor FlhA did (Fig 5A and S9A Fig).

It has been shown that SpaR of the *Salmonella* SPI-1 T3SS directly binds to the $SpaP_5$ ring [34]. Therefore, we investigated if FliR directly binds to FliP. When only FliR-FLAG was coexpressed with His-FliP, FliR coeluted with the $FliP_6$ ring from a SEC column (S9B Fig), indicating that FliR tightly associates with the $FliP_6$ ring structure.

We found that FliQ and FlhA were easily dissociated from the FlhB/FliO/FliP/FliR complex. Therefore, we investigated whether the MS ring, which is made of 26 copies of a single transmembrane protein FliF, stabilizes the structure of the entire export gate complex. Since a C ring protein FliG is required for efficient MS ring formation in the cytoplasmic membrane [8], we attached a His tag to the C-terminus of FliG for efficient and rapid purification of the MS ring. To carry out copurification assay, we constructed a pTrc99A-based plasmid encoding 8 flagellar proteins: FlhA, FlhB, FliF, FliG-His, FliO, FliP, HA-FliQ, and FliR-FLAG (S10A Fig). Immunoblotting revealed that they were expressed in the *Salmonella* SJW1368 strain (S10B Fig). The membranes were solubilized by 1% DDM, and then the proteins were purified by Ni affinity chromatography. Only FlhA and FliF copurified with His-FliG from DDM-solubilized membranes of the cells expressing FlhA, FlhB, FliF, FliG-His, FliO, FliP, HA-FliQ, and FliR-FLAG (Fig 5A), indicating that the FliO/FliP/FliR-FLAG/FlhB complex and HA-FliQ dissociate from the FlhA/FliF/FliG complex. The FlhA/FliF/FliG complex was further purified by SEC, and then the main peak fraction containing FlhA, FliF, and FliG was analyzed by EM with negative staining. Many MS rings were observed in the pooled fractions (Fig 5B), indicating that FlhA associates with the MS ring.

It has been shown by in vivo photo-crosslinking experiments that SpaQ interacts with SpaP and SpaR in the final assembled export gate complex. However, an assembly intermediate complex isolated from DDM-solubilized membranes contains only SpaP and SpaR, which may be due to loss of SpaQ in response to DDM extraction [33–35]. FliQ is an essential export component of the flagellar type III export apparatus [38]. FlhA requires FliQ for efficient assembly of the FlhA ring structure inside the MS ring [8], raising the possibility that DDM affects interactions of FlhA and FliQ with other export gate proteins. To test this, we solubilized the membrane fractions of *Salmonella* cells expressing FlhA, FlhB, FliO, His-FliP, HA-FliQ, and FliR-FLAG by 1% lauryl maltose neopentyl glycol (LMNG) instead of DDM and purified it by Ni affinity chromatography, followed by SEC with a Superdex 200 10/300 column (Fig 6). The SEC elution profile of the FlhA/FlhB/FliO/FliP/FliQ/FliR complex showed 2 distinct peaks (Fig 6A). The first peak (10.3 ml, Fig 6A) mainly contained FliO, FlhB, and FlhA along with a much smaller amount of His-FliP (Fig 6B). Since FlhB copurified with His-FliP, FliO, and FliR-FLAG upon membrane solubilization by DDM (Fig 5A and S8 Fig), we suggest that LMNG weakens the interactions of FliO and FlhB with FliP and FliR. The second peak (12.6 ml, Fig 6A) mainly contained FliP, FliQ, FliR, and FlhA (Fig 6B), indicating that FliQ and FlhA bind to the FliP/FliR complex, although some of the FlhA molecules are dissociated from the complex along with FliO and FlhB.

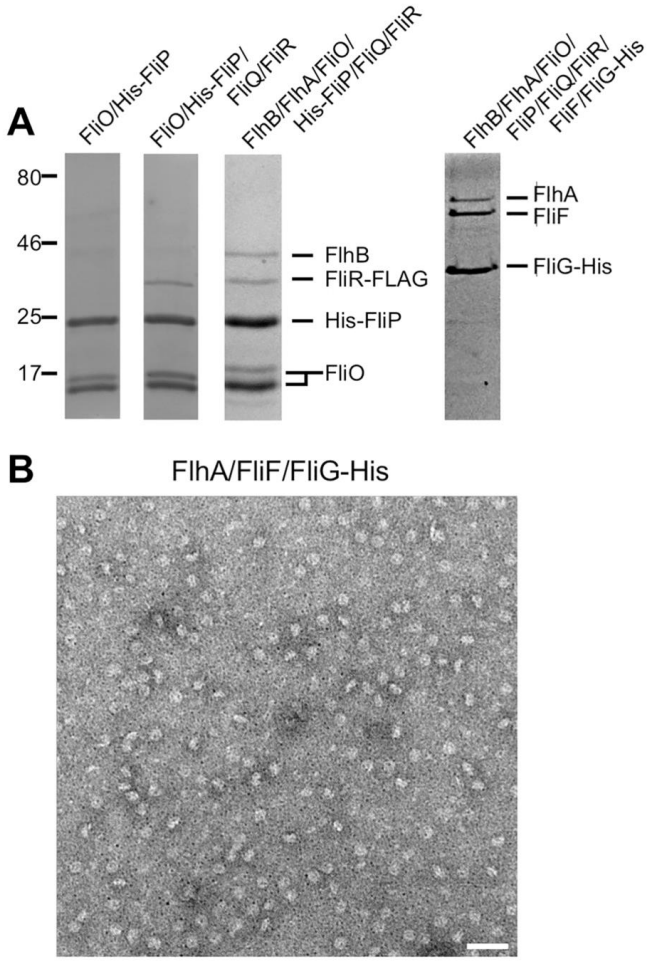

Fig 5. Interactions of the $FliP_5$ ring with other export gate proteins. (A) SDS-PAGE of pooled fractions after size exclusion chromatography (SEC) with a Superdex 200 10/300 column. Membrane fractions were prepared from SJW1368 expressing FliO and His-FliP (lane 1); FliO, His-FliP, HA-FliQ, and FliR-FLAG (lane 2); FlhA, FlhB, FliO, His-FliP, HA-FliQ, and FliR-FLAG (lane 3); or FlhA, FlhB, FliF, FliG-His, FliO, FliP, HA-FliQ, and FliR-FLAG (lane 4) and solubilized by 1% n-dodecyl β-D-maltoside (DDM), followed by Ni affinity chromatography. For purification of the FliO/His-FliP/FliR-FLAG and FliO/His-FliP/FliR-FLAG/FlhB complexes, pooled fractions were subjected to FLAG affinity chromatography (see S9 Fig), followed by SEC with a Superdex 200 10/300 column (lanes 2 and 3). For purification of the FlhA/FliF/FliG-His complex, pooled fractions were subjected to SEC (lane 4). (B) Representative negatively stained electron microscopy (EM) images of purified FlhA/FliF/FliG-His complexes. Scale bar shows 100 nm.

https://doi.org/10.1371/journal.pbio.2002281.g005

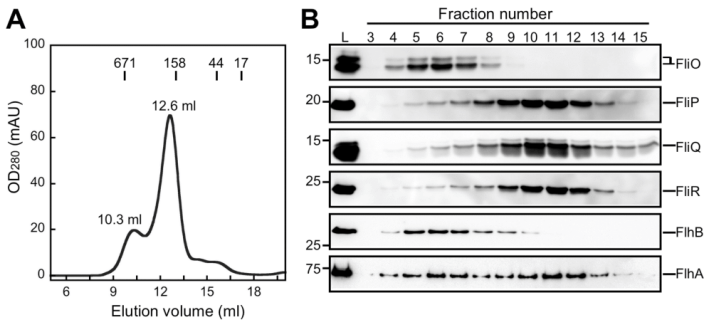

Fig 6. Effect of lauryl maltose neopentyl glycol (LMNG) on the interactions of the $FliP_6$ ring with other export gate proteins. (A) Elution profiles of the FlhA/FlhB/FliO/FliP/FliQ/FliR complex from a Superdex 200 10/300 column equilibrated with 20 mM Tris-HCl, pH 8.0, 150 mM NaCl, 2 mM EDTA, 5% glycerol, and 0.01% LMNG. Membrane fractions were prepared from SJW1368 expressing FlhA, FlhB, FliO, His-FliP, HA-FliQ, and FliR-FLAG and were solubilized by 1% LMNG. Then, the protein complex was purified by Ni affinity chromatography, followed by size exclusion chromatography (SEC). (B) Immunoblotting of elution fractions from A, using anti-FliO (first row), anti-His (second row), anti-HA (third row), anti-FLAG (fourth row), anti-$FlhB_C$ (fifth row), or anti-$FlhA_C$ (sixth row) antibody. (Note: The C-terminal cytoplasmic domain of FlhB undergoes autocleavage between conserved Asp-269 and Pro270 residues [2–4], and hence, the molecular size of the FlhB band recognized by polyclonal anti-$FlhB_C$ antibody is smaller than that of full-length FlhB). These proteins treated with LMNG showed slightly distinct running behavior on SDS gels compared to those with n-dodecyl β-D-maltoside (DDM), presumably due to the detergent effect. The lane marked L represents the material loaded onto the SEC column.

https://doi.org/10.1371/journal.pbio.2002281.g006

Discussion

The export gate complex is composed of 5 highly conserved transmembrane proteins—namely, FlhA, FlhB, FliP, FliQ, and FliR—although the transmembrane protein FliO is required for efficient assembly of the export gate in *Salmonella* [6,7]. FliP and FliR are postulated to form a core structure for the assembly of other export gate proteins [31,32]. Recently, it has been reported that SpaP of the *Salmonella* SPI-1 T3SS forms a homopentamer [34]. In contrast to SpaP, we showed that *St*-FliP forms a homohexamer with a diameter of about 10 nm (Fig 2). The F137A, F150A, and E178A substitutions in $FliP_P$ interfered with $FliP_6$ ring formation (S2 Fig) and reduced the export function considerably (Fig 1D). Therefore, we suggest that the $FliP_6$ ring is a functional unit in the export gate complex and that Phe-137, Phe-150, and Glu-178 are responsible for $FliP_6$ ring formation. Thus, it seems that the core structure of the flagellar export gate complex is somewhat different from that of the T3SS of pathogenic bacteria. However, 3,780 of the 11,736 FliP ring particles analyzed were assigned to the 5-fold rotational symmetry (S3E Fig), raising the possibility that FliP forms a homopentamer in a way similar to the $SpaP_5$ ring.

We have solved the crystal structure of the *Tm*-$FliP_P$ tetramer and have built 2 *St*-$FliP_P$ dimer models on the basis of the *Tm*-$FliP_P$ structure (Fig 3). We have also mapped 3 functionally important residues—namely, Phe-137, Phe-150, and Glu-178 —onto the *St*-$FliP_P$ model. Although the A–B and A–C dimers are found in the crystal, the A–B dimer seems to be the dimer unit of the ring structure, as supported by photo-crosslinking experiments (Fig 4). However, since Phe-137 and Glu-178, which are involved in A–C dimer formation (Fig 3E) and are located on the bottom surface close to the rectangular corner of the A–B dimer (Fig 3F), are required for the ring formation and export function (Fig 1 and S2 Fig), they are likely to be involved in the ring formation by connecting the dimers.

The FliP(R143H) and FliP(F190L) mutations, which are located in $FliP_P$ and TM-3 of FliP, respectively, improve motility of the Δ*fliO* mutant to some extent [6,7]. This suggests the presence of FliO–FliP interaction. Here, we provided direct evidence that FliP binds to FliO (Figs 1 and 4). Negatively stained EM analysis revealed that FliO forms a 5-nm ring structure with 3 clamp-like structures that bind to the $FliP_6$ ring (Fig 2 and S4 Fig). Photo-crosslinking experiments revealed direct interactions of FliO with FliP-TM1 and $FliP_P$ (Fig 4). Overexpression of FliP restored motility of the Δ*fliO* mutant to the wild-type level (S5 Fig), suggesting that the FliO ring complex does not exist in the final structure of the export gate complex. In agreement with this, FliO homologues are absent in nonflagellar T3SSs [5]. Therefore, we propose that the FliO ring complex acts as a scaffold to catalyze $FliP_6$ ring formation and that the interactions of FliO with FliP may induce structural rearrangements of the $FliP_P$ dimer to facilitate $FliP_6$ ring formation. Because Arg-143 is located on the rectangular corner surface of the A–B dimer and near Phe-137 and Glu-178 (Fig 3F), we suggest that the R143H and F190L mutations in FliP increase the probability of $FliP_6$ ring formation in the absence of FliO. Since the virulence-associated T3SS apparatus does not have the FliO homologue, we assume that FliP homologues may have a self-scaffolding function to facilitate their own ring formation.

The export gate complex of the SPI1-T3SS contains 5 SpaP molecules, 1 SpaQ, 1 SpaR, 1 SpaS and 9 InvA subunits [33–35]. SpaQ, SpaR, and SpaS assemble onto the SpaP pentamer and closely interact with each other [34]. Here we showed that FliR and FlhB copurified with the FliO/FliP ring complex when isolated from DDM-solubilized membrane of *Salmonella* cells expressing FlhA, FlhB, FliO, FliP, FliQ, and FliR (Fig 5 and S9 Fig). Relative band intensities of FliP, FliR, and FlhB in the FlhB/FliO/FliP/FliR complex allowed us to roughly estimate that the complex contains 6 copies of FliP, 2 copies of FliR, and 2 copies of FlhB. This is in good agreement with 2 sets of previous experimental data that FlhB forms a homodimer in the basal body [39] and that FliR and FlhB associate with each other in a 1 to 1 fashion [30]. When we used LMNG as a detergent instead of DDM, both FlhA and FliQ coeluted with the FlhB/FliO/FliP/FliR complex from a Ni-NTA column (Fig 6B, the lane marked L), indicating that they bind to the FlhB/FliO/FliP/FliR complex. In contrast to the complex solubilized by DDM, FliO and FlhB dissociated from the complex during SEC. However, FlhA and FliQ were associated with the FliP/FliR complex, although some of the FlhA molecules were dissociated from the complex along with FliO and FlhB (Fig 6B). Taken all together, we suggest that FlhA, FlhB, FliQ, and FliR assemble onto the $FliP_6$ ring in complex with FliO to form the export gate complex.

When FliF, FliO, FliP, FliQ, FliR, FlhA, and FlhB were coexpressed with His-FliG (S10 Fig), only FlhA copurified with the FliF-FliG ring complex from the DDM-solubilized membrane (Fig 5), indicating that FlhA directly associates with the MS ring. This is in agreement with a previous report that a *Salmonella fliF(Δ174-175)* mutant gives rise to extragenic suppressor mutations in $FlhA_{TM}$ [27]. It has been shown that FlhA forms a homononamer inside the MS ring [8,13,14] and that the assembly of FlhA to the MS ring is required for FliO, FliP, FliQ, and FliR [8]. Since we found that some FlhA molecules associate with the FliP/FliQ/FliR complex (Fig 6B), we propose that the assembly of the export gate complex begins with $FliP_6$ ring formation with the help of the FliO scaffold, followed by the assembly of FliQ, FliR, and FlhB and finally of 9 FlhA molecules during MS ring formation in the cytoplasmic membrane (Fig 7).

In summary, we have presented direct evidence that FliP forms a homohexamer with the help of the FliO complex and that $FliP_P$–$FliP_P$ and $FliP_P$–FliO interactions are required for efficient $FliP_6$ ring formation. Our most important findings are that $FliP_6$ ring formation is essential for flagellar type III protein export (Fig 1). Since there are many structural and functional similarities between the flagellar and T3SS proteins, the periplasmic domain of FliP homologues of the T3SSs could be a good target for inhibitors specific for bacterial infection.

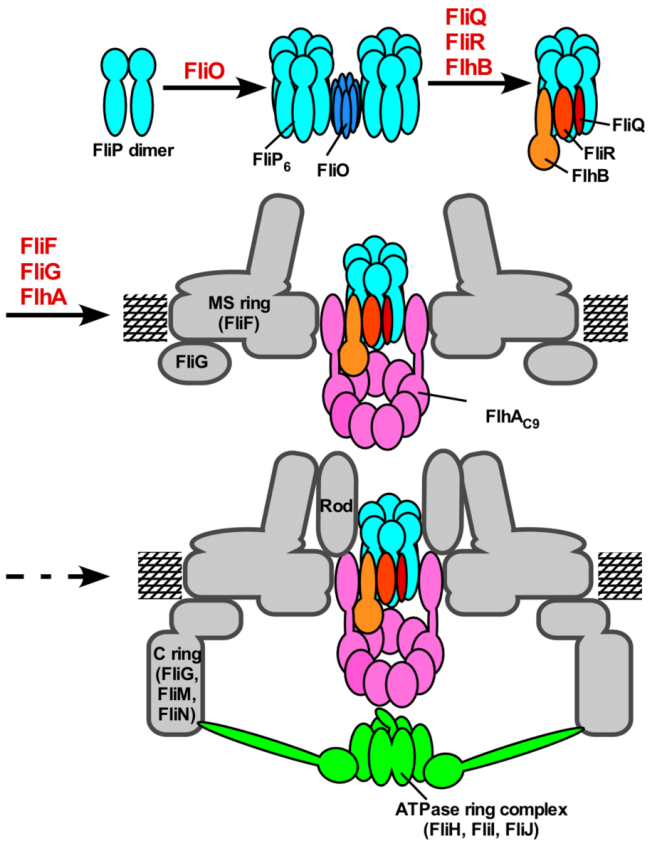

Fig 7. Model for the assembly process of the flagellar type III export apparatus. The export apparatus is composed of a transmembrane export gate complex made of FlhA, FlhB, FliP, FliQ, and FliR and a cytoplasmic ATPase ring complex consisting of FliH, FliI, and FliJ. The FliP dimers form a homohexamer with the help of the FliO complex, followed by the assembly of FliQ, FliR, and FlhB and finally of FlhA during MS ring formation in the cytoplasmic membrane. Then, the FliM/FliN complex binds to FliG to form the C ring on the cytoplasmic face of the MS ring. Finally, the FliH/FliI/FliJ ATPase ring complex is formed at the flagellar base through interactions of FliH with FlhA and FliN [2–4], allowing export substrates to go into the central cavity of the $FliP_6$ ring complex.

https://doi.org/10.1371/journal.pbio.2002281.g007

Materials and methods

Bacterial strains, plasmids, DNA manipulations, and media

Bacterial strains and plasmids used in this study are listed in S1 Table. DNA manipulations, site-directed mutagenesis, and DNA sequencing were carried out as described previously [40]. L-broth (LB) and soft tryptone agar plates were used as described before [38,41]. The 2×YT medium contained 1.6% (w/v) Bacto-tryptone, 1.0% (w/v) Bacto-yeast extract, and 0.5% (w/v) NaCl.

Purification of FliP alone and FliP in complex with FliO

For expression and purification of FliP, *Salmonella* SJW1368 cells harboring pKY069 were grown in 2×YT medium containing 100 μg ml^{-1} ampicillin at 30˚C until the cell density had reached an OD_{600} of about 0.4–1.0 and then were incubated at 16˚C for another 24 h. Cells were harvested by centrifugation (6,400 g, 10 min, 4˚C) and stored at −80˚C. The cells were thawed, resuspended in 20 mM Tris-HCl, pH 8.0, 3 mM EDTA, and disrupted by sonication. The cell lysates were centrifuged (20,000 g, 15 min, 4˚C) to remove cell debris. The supernatants were ultracentrifuged (110,000 g, 1 h, 4˚C). The harvested membranes were stored at −80˚C. The membranes were solubilized in 50 mM Tris-HCl, pH 8.0, 300 mM NaCl, 5% glycerol, 20 mM imidazole, and 1% DDM at 4˚C for 30 min and ultracentrifuged (110,000 g, 30 min, 4˚C) to remove the insoluble membrane fractions. Solubilized membranes were loaded onto a Ni-NTA agarose column (GIAGEN) and washed extensively with 50 mM Tris-HCl, pH 8.0, 300 mM NaCl, 5% glycerol, 20 mM imidazole, and 0.1% DDM. Proteins were eluted with a 50–400 mM imidazole gradient. Fractions containing His-FliP were concentrated and further purified by SEC with a Superdex 200 10/300 column (GE Healthcare) equilibrated with 20 mM Tris-HCl, pH 8.0, 300 mM NaCl, 2 mM EDTA, 5% glycerol, and 0.1% DDM.

For purification of the FliO/His-FliP complex, the membrane fractions were prepared from the SJW1368 cells carrying pKY070 or its mutant variant plasmids in a way similar to His-FliP. After solubilization with 1% DDM, the FliO/His-FliP complex and its mutant variants were purified by Ni-NTA chromatography, followed by SEC with a Superdex 200 10/300 column equilibrated with 20 mM Tris-HCl, pH 8.0, 300 mM NaCl, 2 mM EDTA, 5% glycerol, and 0.1% DDM.

EM and image processing

Samples were applied to carbon-coated copper grids and negatively stained with 1.0% (w/v) uranyl acetate. Micrographs were recorded at a magnification of ×50,000 with a JEM-1011 transmission electron microscope (JEOL, Tokyo, Japan) operated at 100 kV. To carry out 2D class averaging of the FliP ring structure and the FliO/FliP complex, 11,736 and 1,961 particle images, respectively, were boxed out with e2boxer.py [42], aligned, classified, and averaged using the e2refine2d.py program [42]. To estimate the stoichiometry of the FliP ring, a typical class averaged image was converted from cartesian to polar coordinates, and then the autocorrelation function was calculated. The rotational symmetry was analyzed from Fourier transformation of the autocorrelation function. To carry out 2D class averaging of the FliO structure, 14,915 particle images were boxed out with e2boxer.py [42], aligned, classified, and averaged using the RELION program [43].

Multiple sequence alignment

Multiple sequence alignment was performed by CLUSTAL-Ω (http://www.ebi.ac.uk/Tools/msa/clustalo/).

Purification and crystallization of *Tm*-$FliP_P$

Details of the expression, purification, and crystallization of *Tm*-$FliP_P$ have been described previously [37].

Data collection and structure determination

X-ray diffraction data were collected at the synchrotron beamline BL41XU in SPring-8 (Harima, Japan) with the approval of the Japan Synchrotron Radiation Research Institute (JASRI)

(Proposal No. 2013B1305). Details of the X-ray data collection and processing are described previously [37]. Crystals were frozen in liquid nitrogen and mounted in nitrogen gas flow at 100 K. The X-ray diffraction data were collected on an MX225HE CCD detector (Rayonix), were processed with iMOSFLM [44], and were scaled using SCALA [45]. The statistics of the diffraction data have been described previously [37]. The experimental phase was calculated using the SAD data of the Se-Met derivative with the program Phenix [46]. The atomic model was built with Coot [47] and refined to 2.4 Å with Phenix [46] against the native crystal data that showed the best resolution limit. The refinement R factor and the free R factor were converged to 21.5% and 26.2%, respectively. The Ramachandran plot indicated that 96.5% and 3.5% residues were located in the most favorable and allowed region, respectively. Structural refinement statistics are summarized in S2 Table. The atomic coordinates have been deposited in PDB under the accession code 5H72.

Homology modeling

The structure of *St*-FliP$_P$ was modeled by using SWISS-MODEL [48]. The amino acid sequence from Ile-121 to Phe-183 of *St*-FliP was used for the target sequence, and the crystal structure of *Tm*-FliP$_P$ was used for a template to construct the homology model.

Motility assay

Fresh transformants were inoculated onto soft tryptone agar plates containing 100μg ml^{-1} ampicillin and 0.2% arabinose and incubated at 30˚C. At least 7 independent measurements were carried out.

Secretion assays

Details of sample preparation have been described previously [49]. After SDS-PAGE, immunoblotting with polyclonal anti-FlgD, anti-FlgE, anti-FlgK, or anti-FlgL antibody was carried out as described previously [38]. Detection was done with an ECL immunoblotting detection kit (GE Healthcare). At least 3 independent experiments were carried out.

In vivo photo-crosslinking

E. coli BL21 (DE3) cells were transformed with a low-copy-number pTACO10-based plasmid [35] and the amber suppressor plasmid pSup-pBpa [50]. The transformed BL21 (DE3) cells were cultured at 37˚C in LB containing 10 μg ml^{-1} chloramphenicol and 25 μg ml^{-1} kanamycin. Cultures were supplemented with 500 μM rhamnose to induce the expression of FliO/FliP-FLAG/FliQ/FliR, FliO/FliP-FLAG, or FliO-FLAG/FliP-HA from the pTACO10-based plasmid. Additionally, the cultures were supplemented with pBPA to a final concentration of 1 mM and afterwards incubated for 5.5 h. Two OD units of bacterial cells were harvested and washed once with 1 ml cold PBS (8 g of NaCl, 0.2 g of KCl, 3.63 g of Na_2HPO_4 $12H_2O$, 0.24 g of KH_2PO_4, pH 7.4 per liter). Cells were resuspended in 1 ml PBS and transferred into 6-well cell culture dishes for 30 min UV irradiation (λ = 365 nm) using a UV transilluminator table (UVP).

Two OD units of bacterial lysates of *E. coli* were resuspended in 750 μl buffer K (50 mM triethanolamine, pH 7.5, 250 mM sucrose, 1 mM EDTA, 1 mM $MgCl_2$, 10 μg/ml DNAse, 2 mg/ml lysozyme, 1:100 protease inhibitor cocktail) and incubated for 30 min on ice. Samples were bead milled, and beads, unbroken cells, and debris were removed by centrifugation (10,000 g, 10 min, 4˚C). Crude membranes contained in the supernatant were precipitated by ultracentrifugation using a Beckman TLA 55 rotor (100,000 g, 45 min, 4˚C). Pellets containing

crude membranes were frozen until use. For protein detection, samples were subjected to SDS-PAGE using SERVAGel TG PRiME 8%–16% or SERVAGel TG PRiME 12% precast gels, transferred onto a PVDF membrane (Bio-Rad), and probed with M2 anti-FLAG antibody (Sigma). Anti-mouse IgG DyLight 800 (Thermo Fisher) was used as a secondary antibody. Scanning of the PVDF membrane and image analysis were performed with a Li-Cor Odyssey system and Image Studio 2.1.10 (Li-Cor).

Copurification assays

His-FliP/FliR-FLAG, His-FliP/HA-FliQ/FliR-FALG, FliO/His-FliP/FliR-FLAG, FliO/His-FliP/HA-FliQ/FliR-FLAG, FliO/His-FliP/HA-FliQ/FliR-FLAG/FlhB/FlhA, or FliO/ FliP/HA-FliQ/FliR-FLAG/FlhB/FlhA/FliF/His-FliG was expressed in *Salmonella* SJW1368 cells harboring a pTrc99A-based plasmid, solubilized by 1% DDM or 1% LMNG, and purified by Ni-NTA chromatography, followed by FLAG affinity chromatography. Proteins were eluted from anti-FLAG affinity gels (Sigma) with 100 μg ml^{-1} of FLAG peptide (Sigma). The His-FliP/FliR-FLAG, FliO/His-FliP/FLAG-FliR, and FliO/His-FliP/FLAG-FliR/FlhB complexes were further purified by SEC.

Supporting information

S1 Fig. Topological model of *St*-FliP. (A) St-FliP is a transmembrane membrane protein with a cleavable signal peptide (SP) at its N-terminus. The signal peptide of FliP (Met-1 to Gln-22) is cleaved during its membrane insertion [36]. The mature form of St-FliP has four transmembrane (TM) helices and a periplasmic domain ($FliP_P$) between TM-2 and TM-3. (B) Amino acid sequence of St-FliP. Conserved residues in $FliP_P$ are highlighted in red. Colored regions are matched in A and B.
(TIF)

S2 Fig. Purification of FliP and the FliO/FliP complex by size exclusion chromatography. (A) Elution profiles of FliP, the FliO/FliP complex, the FliO/FliP(F137A) complex, the FliO/FliP(F150A) complex and the FliO/FliP(E178A) complex from a Superdex 200 10/300 column equilibrated with 20 mM Tris-HCl pH 8.0, 150 mM NaCl, 2 mM EDTA, 5% glycerol and 0.1% DDM. The elution positions are shown by peaks 1, 2, 3 and 4. Peak fractions of molecular mass markers (670 kDa, 158 kDa and 44 kDa) are shown. (B) Representative negatively stained EM images of each peak fraction. Scale bar shows 50 nm. Peaks 1, 2, 3 and 4 contained the $FliO/FliP_6$ ring complex, the $FliP_6$ ring, the FliO ring and the FliP dimer, respectively.
(TIF)

S3 Fig. Stoichiometry of the FliP ring. (A) A representative reference-free 2D class average images of the FliP ring calculated from e2refine2d.py (EMAN2). (B) Polar coordinates conversion from area sandwiched by two green dashed lines in A. (C) Auto-correlation plots calculated from the image obtained by polar coordinates conversion. (D) Result of reference-free 2D class average images of the FliP ring calculated from e2refine2d.py (EMAN2). The number of particles for each class is shown in the top right corner. (E) Histogram of the number of particles between three and eight symmetries, resulted from auto-correlation analysis.
(TIF)

S4 Fig. 2D class averaging of the FliO ring complex and the FliO/FliP complex. (A) Reference-free 2D class average images of the FliO ring complex calculated from RELION. (B) Reference-free 2D class average images of the FliO/FliP complex calculated from e2refine2d.py (EMAN2). The number of particles for each class is shown in the top right corner.
(TIF)

S5 Fig. Multicopy effect of FliP on motility of a *Salmonella* Δ*fliO* mutant. Motility of TH10548 transformed with pTrc99A (V), pKY073 (FliO), pKY074 (P_{ara}-HA-FliP) or pKY010 (P_{lac}-HA-FliP) in soft agar (upper panel). Immunoblotting, using polyclonal anti-FliOC (middle panel) or monoclonal anti-HA antibody (lower panel), of whole cell lysates prepared form the above strains. (Note: the level of HA-FliP expressed from the pBAD24 vector was not detected at all.).
(TIF)

S6 Fig. Purification of the FliO ring complex. (A) Stability of the FliO/FliP ring complex during storage at 4˚C. The FliO/FliP complex stored at 4˚C for 1 day was run on a Superdex 200 10/300 column. SDS-PAGE of elution fractions. Molecular mass markers (kDa) are shown on the left. (B) SEC analysis of the FliO complex. Fractions containing the FliO complex was pooled and analyzed by SDS-PAGE with CCB staining.
(TIF)

S7 Fig. Surface properties of the A–B and A–C dimers of *Tm*-FliP$_P$. (A) A–B dimer form of Tm-FliP$_P$ (B) A–C dimer form of Tm-FliP$_P$. Residues involved in the dimer interaction are indicated with ball-and-stick representation. (C), (D) A–B dimer interface. (F), (G) A–C dimer interface. The A subunit is shown in surface representation painted with yellow and white for hydrophobic and the other residues, respectively. The B and C subunits are shown by Cα-trace colored with pink in (C) and (F), respectively. Residues involved in the dimer interaction are labeled in (D) and (G). (E), (H) The A–B (E) and A–C dimers (H) are viewed from the opposite side of both C-termini (viewed from the top of the model in (C) and in (F), respectively). The hydrophobic [same color as (C)] and the electrostatic potential (red, negative; blue, positive) surfaces are shown in left and right panels, respectively. The Cα-trace of the dimer is in the middle panel.
(TIF)

S8 Fig. Surface properties of the A–B and A–C dimers of *St*-FliP$_P$. (A), (B) A–B dimer interface. (D), (E) A–C dimer interface. The A subunit is shown in surface representation painted with yellow and white for hydrophobic and the other residues, respectively. The B and C subunits are shown by Cα-trace colored with pink in (A) and (D), respectively. Residues involved in the dimer interaction are labeled in (B) and (E). (C), (F) The A–B (C) and A–C (F) dimers viewed from the opposite side of both C-termini (viewed from the top of the model in (A) and in (D), respectively). The hydrophobic (same color as (A)) and the electrostatic potential (red, negative; blue, positive) surfaces are shown in left and right panels, respectively. The Cα-trace of the dimer is in the middle panel.
(TIF)

S9 Fig. Interactions of the FliP$_6$ ring with other export gate components. (A) Co-purification assays by anti-FLAG M2 affinity chromatography. Membranes were prepared from SJW1368 expressing His-FliP and FliR (P/R), His-FliP, FliQ and FliR (P/Q/R), FliO, His-FliP and FliR (O/P/R), FliO, His-FliP, FliQ and FliR (O/P/Q/R), or FlhA, FlhB FliO, His-FliP, FliQ and FliR (O/P/Q/R/B/A) and solubilized by 1% DDM, followed by Ni affinity chromatography and finally anti-FLAG M2 affinity chromatography. "Input" indicates pooled fractions after Ni affinity chromatography. "Flow through" and "Elution" indicate the flow through and elution fractions, respectively. Each fraction obtained by anti-FLAG M2 affinity chromatography was analyzed by SDS-PAGE with CBB staining. Molecular mass markers (kDa) are shown on the left. (B) Analysis of purified FliP/FliR by SEC with a Superose 6 10/300 column. SDS-PAGE of pooled fractions shown by grey line. Representative negatively stained EM image of the peak

fraction. Scale bar shows 50 nm.
(TIF)

S10 Fig. Co-expression system of flagellar type III export gate proteins. (A) Schematic diagram of plasmid construction of pKY079. (B) Expression of FlhA, FlhB, FliF, FliG-His, FliO, FliP, HA-FliQ and FliR-FLAG as judged by immunoblotting with anti-$FlhA_C$, anti-$FlhB_C$, anti-FliF, anti-His, anti-$FliO_C$, anti-$FliP_P$, anti-HA and anti-FLAG antibodies, respectively.
(TIF)

S1 Table. Strains and plasmids used in this study.
(DOCX)

S2 Table. X-ray refinement statistics.
(DOCX)

Acknowledgments

We thank Naoya Terahara for technical assistance for purification of membrane protein complexes, Kazuya Hasegawa at SPring-8 for technical help in the use of beamline BL41XU, Kelly T. Hughes for kind gifts of the *Salmonella* TH10548 (Δ*fliO*) and TH10549 (Δ*fliP*) strains, and Marc Erhardt for providing the *Salmonella* EM2269 strain (*fliO22348*::*3xFLAG*, *fliP8004*::*3xHA*).

Author Contributions

Formal analysis: Takuma Fukumura, Fumiaki Makino, Tobias Dietsche, Miki Kinoshita, Samuel Wagner, Katsumi Imada, Tohru Minamino.

Funding acquisition: Takayuki Kato, Samuel Wagner, Keiichi Namba, Katsumi Imada, Tohru Minamino.

Investigation: Takuma Fukumura, Tobias Dietsche, Miki Kinoshita, Katsumi Imada, Tohru Minamino.

Methodology: Takayuki Kato.

Software: Takayuki Kato.

Supervision: Samuel Wagner, Keiichi Namba, Katsumi Imada, Tohru Minamino.

Writing – original draft: Takuma Fukumura, Tohru Minamino.

Writing – review & editing: Samuel Wagner, Keiichi Namba, Katsumi Imada, Tohru Minamino.

References

1. Macnab RM. How bacteria assemble flagella. Annu Rev Microbiol. 2003; 57: 77–100. https://doi.org/10.1146/annurev.micro.57.030502.090832 PMID: 12730325
2. Minamino T, Imada K, Namba K. Mechanisms of type III protein export for bacterial flagellar assembly. Mol BioSyst. 2008; 4:1105–1115. https://doi.org/10.1039/b808065h PMID: 18931786
3. Minamino T. Protein export through the bacterial flagellar type III export pathway. Biochim Biophys Acta. 2014; 1843: 1642–1648. https://doi.org/10.1016/j.bbamcr.2013.09.005 PMID: 24064315
4. Minamino T, Imada K. The bacterial flagellar motor and its structural diversity. Trends Microbiol. 2015; 23: 267–274. https://doi.org/10.1016/j.tim.2014.12.011 PMID: 25613993
5. Galán JE, Lara-Tejero M, Marlovits TC, Wagner S, Bacterial type III secretion systems: specialized nanomachines for protein delivery into target cells. Annu Rev Microbiol. 2014; 68: 415–438. https://doi.org/10.1146/annurev-micro-092412-155725 PMID: 25002086

6. Barker CS, Meshcheryakova IV, Kostyukova AS, Samatey FA. FliO regulation of FliP in the formation of the *Salmonella enterica* flagellum. PLoS Genet. 2010; 6: e1001143. https://doi.org/10.1371/journal.pgen.1001143 PMID: 20941389
7. Barker CS, Meshcheryakova IV, Inoue T, Samatey FA. Assembling flagella in *Salmonella* mutant strains producing a type III export apparatus without FliO. J Bacteriol. 2014; 196: 4001–4011. https://doi.org/10.1128/JB.02184-14 PMID: 25201947
8. Morimoto YV, Ito M, Hiraoka KD, Che YS, Bai F, Kami-Ike N, et al. Assembly and stoichiometry of FliF and FlhA in *Salmonella* flagellar basal body. Mol Microbiol. 2014; 91: 1214–1226. https://doi.org/10.1111/mmi.12529 PMID: 24450479
9. Morimoto YV, Kami-ike N, Miyata T, Kawamoto A, Kato T, Namba K, et al. High-resolution pH imaging of living bacterial cell to detect local pH differences. mBio. 2016; 7: 01911–16. https://doi.org/10.1128/mBio.01911-16
10. Imada K, Minamino T, Tahara A, Namba K. Structural similarity between the flagellar type III ATPase FliI and F-1-ATPase subunits. Proc Natl Acad Sci USA. 2007; 104:485–490. https://doi.org/10.1073/pnas.0608090104 PMID: 17202259
11. Ibuki T, Imada K, Minamino T, Kato T, Miyata T, Namba K. Common architecture between the flagellar protein export apparatus and F- and V-ATPases. Nat Struct Mol Biol. 2011; 18: 277–282. https://doi.org/10.1038/nsmb.1977 PMID: 21278755
12. Imada K, Minamino T, Uchida Y, Kinoshita M, Namba K. Insight into the flagella type III export revealed by the complex structure of the type III ATPase and its regulator. Proc Natl Acad Sci USA. 2016; 113: 3633–3638. https://doi.org/10.1073/pnas.1524025113 PMID: 26984495
13. Abrusci P, Vergara-Irigaray M, Johnson S, Beeby MD, Hendrixson DR, Roversi P, et al. Architecture of the major component of the type III secretion system export apparatus. Nat Struct Mol Biol. 2013; 20: 99–104. doi:10.1038/nsmb.2452. https://doi.org/10.1038/nsmb.2452 PMID: 23222644
14. Kawamoto A, Morimoto YV, Miyata T, Minamino T, Hughes KT, Kato T, et al. Common and distinct structural features of *Salmonella* injectisome and flagellar basal body. Sci Rep. 2013; 3: 3369. https://doi.org/10.1038/srep03369 PMID: 24284544
15. Minamino T, Namba K. Distinct roles of the FliI ATPase and proton motive force in bacterial flagellar protein export. Nature. 2008; 451: 485–488. https://doi.org/10.1038/nature06449 PMID: 18216858
16. Minamino T, Morimoto YV, Hara N, Namba K. An energy transduction mechanism used in bacterial flagellar type III protein export. Nat Commun. 2011; 2: 475. https://doi.org/10.1038/ncomms1488 PMID: 21934659
17. Minamino T, Morimoto YV, Kinoshita M, Aldridge PD, Namba K. The bacterial flagellar protein export apparatus processively transports flagellar proteins even with extremely infrequent ATP hydrolysis. Sci Rep. 2014; 4: 7579. https://doi.org/10.1038/srep07579 PMID: 25531309
18. Minamino T, Kinoshita M, Inoue Y, Morimoto YV, Ihara K, Koya S, et al. FliH and FliI ensure efficient energy coupling of flagellar type III protein export in *Salmonella*. MicrobiologyOpen. 2016; 5: 424–435. https://doi.org/10.1002/mbo3.340 PMID: 26916245
19. Minamino T, Morimoto YV, Hara N, Aldridge PD, Namba K. The bacterial flagellar type III export gate complex is a dual fuel engine that can use both H^+ and Na^+ for flagellar protein export. PLoS Pathog. 2016; 12: e1005495. https://doi.org/10.1371/journal.ppat.1005495 PMID: 26943926
20. Minamino T, Shimada M, Okabe M, Saijo-Hamano Y, Imada K, Kihara M, et al. Role of the C-terminal cytoplasmic domain of FlhA in bacterial flagellar type III protein export. J Bacteriol. 2010; 192: 1929–1936. https://doi.org/10.1128/JB.01328-09 PMID: 20118266
21. Bange G, Kümmerer N, Engel C, Bozkurt G, Wild K, Sinning I. FlhA provides the adaptor for coordinated delivery of late flagella building blocks to the type III secretion system. Proc Natl Acad Sci USA. 2010; 107: 11295–11300. https://doi.org/10.1073/pnas.1001383107 PMID: 20534509
22. Minamino T, Kinoshita M, Hara N, Takeuchi S, Hida A, Koya S, et al. Interaction of a bacterial flagellar chaperone FlgN with FlhA is required for efficient export of its cognate substrates. Mol Microbiol. 2012; 83: 775–788. https://doi.org/10.1111/j.1365-2958.2011.07964.x PMID: 22233518
23. Minamino T, Macnab RM. Domain structure of *Salmonella* FlhB, a flagellar export component responsible for substrate specificity switching. J Bacteriol. 2000; 182: 4906–4919. https://doi.org/10.1128/JB.182.17.4906-4914.2000 PMID: 10940035
24. Fraser GM, Hirano T, Ferris HU, Devgan LL, Kihara M, Macnab RM. Substrate specificity of type III flagellar protein export in *Salmonella* is controlled by subdomain interactions in FlhB. Mol Microbiol. 2003; 48: 1043–1057. https://doi.org/10.1046/j.1365-2958.2003.03487.x PMID: 12753195
25. Hirano T, Mizuno S, Aizawa S, Hughes KT. Mutations in *flk*, *flgG*, *flhA*, and *flhE* that affect the flagellar type III secretion specificity switch in *Salmonella enterica*. J Bacteriol. 2009; 191: 3938–3949. https://doi.org/10.1128/JB.01811-08 PMID: 19376867

26. Kinoshita M, Hara N, Imada K, Namba K, Minamino T. Interactions of bacterial flagellar chaperone-substrate complexes with FlhA contribute to co-ordinating assembly of the flagellar filament. Mol Microbiol. 2013; 90: 1249–1261. https://doi.org/10.1111/mmi.12430 PMID: 24325251

27. Kihara M, Minamino T, Yamaguchi S, Macnab RM. Intergenic suppression between the flagellar MS ring protein FliF of *Salmonella* and FlhA, a membrane component of its export apparatus. J Bacteriol. 2001; 183: 1655–1662. https://doi.org/10.1128/JB.183.5.1655-1662.2001 PMID: 11160096

28. Hara N, Namba K, Minamino T. Genetic characterization of conserved charged residues in the bacterial flagellar type III export protein FlhA. PLoS ONE. 2011; 6: e22417. https://doi.org/10.1371/journal.pone.0022417 PMID: 21811603

29. Barker CS, Samatey FA. Cross-complementation study of the flagellar type III export apparatus membrane protein FlhB. PLoS ONE. 2012; 7: e44030. https://doi.org/10.1371/journal.pone.0044030 PMID: 22952860

30. Van Arnam JS, McMurry JL, Kihara M, Macnab RM. Analysis of an engineered *Salmonella* flagellar fusion protein, FliR-FlhB. J Bacteriol. 2004; 186: 2495–2498. https://doi.org/10.1128/JB.186.8.2495-2498.2004 PMID: 15060055

31. Jones CJ, Macnab RM. Flagellar assembly in *Salmonella typhimurium*: analysis with temperature-sensitive mutants. J. Bacteriol. 1990; 172: 3022–3028. https://doi.org/10.1128/jb.172.3.1327-1339.1990

32. Fan F, Ohnishi K, Francis NR, Macnab RM. The FliP and FliR proteins of *Salmonella typhimurium*, putative components of the type III flagellar export apparatus, are located in the flagellar basal body. Mol Microbiol. 1997; 26: 1035–1046. https://doi.org/10.1046/j.1365-2958.1997.6412010.x PMID: 9426140

33. Zilkenat S, Franz-Wachtel M, Stierhof YD, Galán JE, Macek B, Wagner S. Determination of the stoichiometry of the complete bacterial type III secretion needle complex using a combined quantitative proteomic approach. Mol Cell Proteomics. 2016; 15: 1598–1609. https://doi.org/10.1074/mcp.M115.056598 PMID: 26900162

34. Dietsche T, Tesfazgi Mebrhatu M, Brunner MJ, Abrusci P, Yan J, Franz-Wachtel M, et al. Structural and functional characterization of the bacterial type III secretion export apparatus. PLoS Pathog. 2016; 12: e1006071. https://doi.org/10.1371/journal.ppat.1006071 PMID: 27977800

35. Wagner S, Königsmaier L, Lara-Tejero M, Lefebre M, Marlovits TC, Galán JE Organization and coordinated assembly of the type III secretion export apparatus. Proc Natl Acad Sci USA. 2010; 107: 17745–17750. https://doi.org/10.1073/pnas.1008053107 PMID: 20876096

36. Ohnishi K, Fan F, Schoenhals GJ, Kihara M, Macnab RM. The FliO, FliP, FliQ, and FliR proteins of *Salmonella typhimurium*: putative components for flagellar assembly. J Bacteriol. 1997; 179: 6092–6099. https://doi.org/10.1128/jb.179.19.6092-6099.1997 PMID: 9324257

37. Fukumura T, Furukawa Y, Kawaguchi T, Saijo-Hamano Y, Namba K, Imada K, et al. Crystallization and preliminary X-ray analysis of the periplasmic domain of FliP, an integral membrane component of the bacterial flagellar type III protein export apparatus. Acta Crystallogr Sect F Struct Biol Cryst Commun. 2014; 70: 1215–1218. https://doi.org/10.1107/S2053230X14014678

38. Minamino T, Macnab RM. Components of the *Salmonella* flagellar export apparatus and classification of export substrates. J Bacteriol. 1999; 181: 1388–1394. PMID: 10049367

39. McMurry JL, Minamino T, Furukawa Y, Francis JW, Hill SA, Helms KA, et al. Weak interactions between *Salmonella enterica* FlhB and other flagellar export apparatus proteins govern type III secretion dynamics. PLoS One 2015; 10: e0134884. https://doi.org/10.1371/journal.pone.0134884 PMID: 26244937

40. Saijo-Hamano Y, Minamino T, Macnab RM, Namba K. Structural and functional analysis of the C-terminal cytoplasmic domain of FlhA, an integral membrane component of the type III flagellar protein export apparatus in *Salmonella*. J Mol Biol. 2004; 343: 457–466. https://doi.org/10.1016/j.jmb.2004.08.067 PMID: 15451673

41. Minamino T, Macnab RM. Interactions among components of the *Salmonella* flagellar export apparatus and its substrates. Mol Microbiol. 2000; 35: 1052–1064. https://doi.org/10.1046/j.1365-2958.2000.01771.x PMID: 10712687

42. Tang G, Peng L, Baldwin PR, Mann DS, Jiang W, Rees I, et al. EMAN2: an extensible image processing suite for electron microscopy. J Struct Biol. 2007; 157: 38–46. https://doi.org/10.1016/j.jsb.2006.05.009 PMID: 16859925

43. Scheres SH. RELION: implementation of a Bayesian approach to cryo-EM structure determination. J Struct Biol. 2012; 180: 519–530. https://doi.org/10.1016/j.jsb.2012.09.006 PMID: 23000701

44. Battye TG, Kontogiannis L, Johnson O, Powell HR, Leslie AG. iMOSFLM: a new graphical interface for diffraction-image processing with MOSFLM. Acta Crystallogr D Biol Crystallogr. 2011; 67: 271–281. https://doi.org/10.1107/S0907444910048675 PMID: 21460445

45. Evans P. Scaling and assessment of data quality. Acta Crystallogr D Biol Crystallogr. 2006; 62: 72–82. https://doi.org/10.1107/S0907444905036693 PMID: 16369096

46. Adams PD, Grosse-Kunstleve RW, Hung LW, Ioerger TR, McCoy AJ, Moriarty NW, et al. PHENIX: building new software for automated crystallographic structure determination. Acta Crystallogr D Biol Crystallogr. 2002; 58:1948–1954. doi:10.1107/S0907444902016657. PMID: 12393927

47. Emsley P, Cowtan K. Coot: model-building tools for molecular graphics. Acta Crystallogr D Biol Crystallogr. 2004; 60: 2126–2132. https://doi.org/10.1107/S0907444904019158 PMID: 15572765

48. Schwede T, Kopp J, Guex N, Peitsch MC. SWISS-MODEL: an automated protein homology-modeling server. Nucleic Acids Res. 2003; 31: 3381–3385. PMID: 12824332.

49. Minamino T, Kinoshita M, Namba K. Fuel of the bacterial flagellar type III protein export apparatus. Methods Mol Biol. 2017; 1593: 3–16. https://doi.org/10.1007/978-1-4939-6927-2_1 PMID: 28389941

50. Ryu Y, Schultz PG. Efficient incorporation of unnatural amino acids into proteins in *Escherichia coli*. Nat Methods. 2006; 3: 263–265. https://doi.org/10.1038/nmeth864 PMID: 16554830